Proceedings of the

11th "Patras" Workshop on Axions, WIMPs and WISPs PATRAS2015

June 22–26, 2015
Zaragoza, Spain

Editors: Igor G. Irastorza, Javier Redondo, José Manuel Carmona, Susana Cebrián, Theopisti Dafní, Francisco J. Iguaz, Gloria Luzón.

Verlag Deutsches Elektronen-Synchrotron

Impressum

Proceedings of the 11th "Patras" Workshop on Axions, WIMPs and WISPs (Patras2015)

June 22–26, 2015, Zaragoza, Spain

Conference homepage
`http://axion-wimp2015.desy.de/`

Slides at
`https://indico.desy.de/conferenceTimeTable.py?confId=11832#all`

Online proceedings at
`http://www-library.desy.de/preparch/desy/proc/proc15-02.pdf`

Editors:
Steve Miller, Mary Smith (————————-)
November 2015 (————————-)
DESY-PROC-2015-02
ISBN 978-3-935702-43-0 (————————-)
ISSN 1435-8077 (————————-)

Published by
Verlag Deutsches Elektronen-Synchrotron
Notkestraße 85
22607 Hamburg
Germany

Printed by
Kopierzentrale Deutsches Elektronen-Synchrotron

Local Organizing Committee (University of Zaragoza)

Igor G. Irastorza (Chair)
Jose M. Carmona
Susana Cebrián
Theopisti Dafní
Diego González-Díaz
Francisco Iguaz
Gloria Luzón
Javier Redondo
Jose A. Villar

International Organizing Committee

Igor G Irastorza (Chair, University of Zaragoza)
Vassilis Anastassopoulos (University of Patras)
Laura Baudis (University of Zurich)
Joerg Jaeckel (University of Heidelberg)
Axel Lindner (DESY)
Andreas Ringwald (DESY)
Marc Schumann (AEC Bern)
Konstantin Zioutas (University of Patras & CERN)

Preface

The 11th Patras Workshop on Axions, WIMPs and WISPs took place in Zaragoza, on June 22nd to 26th, 2015. After the successful 10th-anniversary edition of the conference last year at CERN, this edition broke again the record with 125 attendants, proof of the good health of the field and the increasing interest that axion physics is attracting. The participants enjoyed an intense program of science, comprising both theory and experiments, many interesting discussions, but also good gastronomy and sightseeing in Zaragoza. The presentations took place in the Aula Magna of the Paraninfo building of the Universidad de Zaragoza, famous for having hosted the lessons of Nobel-prize-winner Santiago Ramón y Cajal about a century ago, as well as one of the few lectures of Albert Einstein in Spain. For the 24th, the conference moved to Canfranc in the Spanish Pyrenees, where the attendants visited the Laboratorio Subterráneo de Canfranc (LSC), a singular facility in Spain, of which the local organizers are associated researchers.

As it is customary in the series, the workshop reviewed the latest advances in the physics case of WIMPs, axions and WISPs, including the latest theoretical developments as well as their link to astrophysics and cosmology, e.g. their potential role in our understanding of dark matter and dark energy. The current experimental efforts, as well as new proposals to detect these particles were also presented and discussed. The vitality of the field was patent in the scientific program of the workshop, including more than 80 oral presentations, as well as a poster session on the first afternoon of the week, in which 15 posters were presented and discussed. As a novelty this year, a prize for the best poster was organized, mostly addressed to the younger colleagues of the community. A prize committee was constituted (chaired by José Manuel Carmona and including also Axel Lindner, Babette Doebrich and Theopisti Dafni). The committee evaluated both the formal and scientific contents of the posters, as well as their presentation during the session. The decision was difficult due to the good quality of the posters, but the prize was finally awarded jointly to Doyu Lee (50%), Patricia Villar (25%) and Adrián Ayala (25%). We want to congratulate them all again.

We want to express our gratitude to all the participants of the workshop for their contribution to its success, and most especially to those colleagues who accepted our invitation to give one of the review talks of the conference.

Given the rapid evolution of our field, with new ideas and projects emerging constantly, the issuing of proceedings (for a meeting that is organized yearly!) is always a delicate issue. The question was exposed during the last day of the conference, and the community answered overwhelmingly in favour of the preparation of proceedings. In order to keep the novelty and freshness of the talks of the conference, we tried to arrange a publication process as fast as possible. Despite the strict deadline set, encompassing only the two summer months, 50 written contributions made it through to the present volume of proceedings, which we believe is another record for the series. We sincerely think that the present volume is a very good witness of the excitement and good quality of the research being done in our field. We hope you enjoy it!

Acknowledgements

The local organising committee would like to thank the University of Zaragoza for supporting the workshop and for providing the magnificent premises of the Paraninfo building; in particular, we would like to thank Luis Miguel García Vinuesa, Vice-president of Research of the University, and Luis Oriol Langa, Dean of the Science Faculty, for their warm welcome of the workshop on the first day, as well as the LSC management and staff for their help with the visit on the 24th of June. The organisers wish also to acknowledge economical support from the following institutions: CERN, DESY, University of Bern, University of Zurich and University of Patras, that greatly helped the organisation of the workshop. In addition, support from the Spanish Ministry of Economy and Competitiveness, as well as from the European Research Council is acknowledged, through the research grants to the local groups. Special thanks also to the students of the local group and the secretariat of the Theoretical Physics Department for the help with the logistics of the organisation.

The local organising committee


FACULTADES DE MEDICINA Y CIENCIAS DE ZARAGOZA
campus iberus de Excelencia Internacional
Universidad Zaragoza
upna

Contents

Chapter 1

Contributed Talks

Cosmological Search for Ultra-Light Axions

Daniel Grin[1], *Renée Hložek*[2], *David J. E. Marsh*[3], *Pedro G. Ferreira*[4]

[1]University of Chicago, Chicago, Illinois, U.S.A.,
[2]Princeton University, Princeton, NJ, USA,
[3]Perimeter Institute, Waterloo, ON, Canada,
[4]University of Oxford, Oxford, UK.

DOI: http://dx.doi.org/10.3204/DESY-PROC-2015-02/grin_daniel

Ultralight axions (ULAs) with masses in the range 10^{-33} eV $\leq m_a \leq 10^{-18}$ eV (motivated by string theory) might contribute to the dark-matter or dark-energy density of the Universe. ULAs would suppress the growth of structure on small scales and change the shape of the cosmic microwave background (CMB) anisotropy power spectra. In this work, we compute cosmological observables over the full ULA mass range and then use them to search for evidence of ULAs using CMB temperature data from the *Planck* satellite, large-scale CMB polarization data from Wilkinson Microwave Anisotropy Probe (WMAP), smaller-scale CMB experiments, as well as the WiggleZ galaxy-redshift survey. In the mass range 10^{-32} eV $\leq m_a \leq 10^{-25.5}$ eV, the ULA relic-density must obey the constraint $\Omega_a h^2 \leq 0.006$ at 95%-confidence. For $m_a \gtrsim 10^{-24}$ eV, ULAs are indistinguishable from standard cold dark matter on the length scales probed while for $m_a \lesssim 10^{-32}$ eV, ULAs are allowed to compose a significant fraction of the dark energy. If primordial gravitational waves are detected, limits to the primordial isocurvature fraction will put severe constraints on ULA dark matter. In the future, weak-lensing measurements of the CMB will yield even more powerful probes of the ULA hypothesis.

1 Motivation

Originally introduced to solve the strong *CP* problem [1, 2, 3], axions are a well-motivated dark-matter candidate [4, 5]. In the context of the axiverse scenario, in which there are many axions with masses spanning many orders-of-magnitude covering the range 10^{-33} eV $\lesssim m_a \lesssim 10^{-18}$ eV, ultra-light axions (ULAs) could compose significant fractions of both the dark matter and the dark energy [6, 7, 8]. More generally, axion-like particles (ALPs) arise in string theory [9, 10, 11, 12], often as the Kaluza-Klein zero modes of anti-symmetric tensors compactified on extra dimensions. As discussed in many of the other workshop contributions, a variety of creative laboratory techniques have emerged to probe a wide swathe of ULA/ALP parameter space. All these techniques depend, however, on the highly model-dependent two-photon couplings of ULAs/ALPs.

The gravitational imprint of ULAs [for example, on the cosmic microwave background (CMB) or the distribution of galaxies at redshifts $z \lesssim 1$], however, is nearly model-independent, once their mass and density is specified [8]. For masses $m_a \lesssim 10^{-20}$ eV, ULA dark matter exhibits suppressed structure formation on cosmological length scales. If the ULA is the Goldstone boson of a global symmetry broken during inflation (and not subsequently restored) the relative

entropy fluctuation between ULAs and radiation yields a detectable *isocurvature* imprint on the CMB.

Here we apply these effects to search for evidence of ULA dark matter or dark energy using *Planck* CMB data and the WiggleZ survey. These proceedings are a summary of Ref. [13], whose results are reproduced with permission (Copyright 2012 by The American Physical Society). We built on past work (in which constraints are obtained without a Boltzmann code [14]) by extending the standard CMB Boltzmann code CAMB[1] to include the evolution of cosmological perturbations in the presence of ULAs with any m_a value.

2 Ultra-light axion cosmology

As a first step in exploring the axiverse, we consider a single ULA, described by a real scalar field ϕ_0 (subject to a harmonic potential) with equation of motion

$$\ddot{\phi}_0 + 2\mathcal{H}\dot{\phi}_0 + m_a^2 a^2 \phi_0 = 0. \tag{1}$$

Here $\mathcal{H} = aH$ is the conformal Hubble parameter, where a is the usual cosmological scale factor and H the usual Hubble parameter with respect to physical time. Early on, when $m_a \ll 3H$, the scalar field rolls slowly, has equation-of-state parameter $w \simeq -1$, and constant energy density. A transition when $m_a = 3H$, defining the transition scale factor $a \equiv a_{\rm osc}$. Thenceforth, on timescales longer than the oscillation period $\sim m^{-1}$, the ULA field is well described as a non-relativistic fluid with $\rho \propto a^{-3}$ and $w \simeq 0$. The ULA relic abundance is then readily obtained to be

$$\Omega_a = \begin{cases} \frac{1}{6}(9\Omega_r)^{3/4}\left(\frac{m_a}{H_0}\right)^{1/2}\left(\frac{\phi_{0,i}}{M_{pl}}\right)^2 \text{ if } a_{\rm osc} < a_{\rm eq}\,, \\ \frac{9}{6}\Omega_m\left(\frac{\phi_{0,i}}{M_{pl}}\right)^2 \text{ if } a_{\rm eq} < a_{\rm osc} \lesssim 1\,, \\ \frac{1}{6}\left(\frac{m_a}{H_0}\right)^2\left(\frac{\phi_{0,i}}{M_{pl}}\right)^2 \text{ if } a_{\rm osc} \gtrsim 1\,, \end{cases} \tag{2}$$

where $\phi_{0,i}$ is the initial scalar field displacement, $M_{pl}^2 = 1/(8\pi G)$ is the Planck mass. Here Ω_r and Ω_m are the radiation and matter energy-densities today relative to the critical density.

The observed dark matter or dark-energy relic densities can be obtained for the ULA mass-range 10^{-33} eV $\lesssim m_a \lesssim 10^{-18}$ eV for sub-Planckian axion global $U(1)$-symmetry breaking scales and initial field misalignments [16, 8]. One important moment is the epoch of matter-radiation equality, which occurs when $a = a_{\rm eq} = (1 + z_{\rm eq})^{-1} \simeq 2.93 \times 10^{-4}$. If $a_{\rm osc} \lesssim a_{\rm eq}$, the homogeneous piece of the ULA homogeneous field behaves as a non-relativistic relic while most observed cosmological large-scale structure (LSS) forms, and we call such ULAs "dark-matter like." If $a_{\rm osc} \gtrsim a_{\rm eq}$, the homogeneous piece of the ULA field behaves as a cosmological constant while LSS forms [7], and we call such ULAs "dark-energy like." Both regimes are evident in Fig. 1, where energy densities from the full (scalar-field+matter+cosmological constant) evolution are shown. To actually obtain field histories for our exploration of parameter space (which also requires perturbation evolution), we solve the exact Klein-Gordon equation [Eq. (1)] including all components in $\mathcal{H}$ until $a = a_{\rm osc}$, and then use a simple $w \simeq 0$, $\rho_a \propto a^{-3}$ solution afterwards.

[1] CAMB is distributed and described at http://camb.info/.

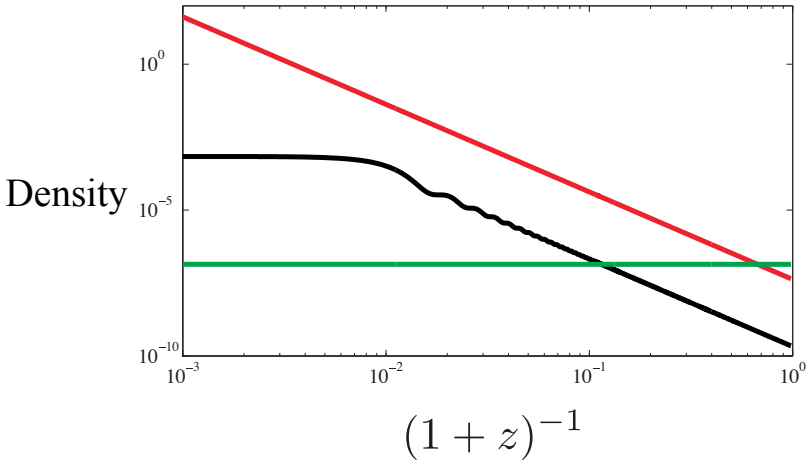

Figure 1: Time evolution of ULA density in arbitrary units (shown in black) for an $m_a = 10^{-30}$ eV axion comprising 1% of the dark matter, as a function of cosmological scale factor a. The red curve shows the matter density while the green curve shows the energy density associated with the cosmological constant. Modified and reproduced (with permission) from Ref. [15]. Copyright 2012 by The American Physical Society.

3 Perturbation evolution and observables

For the low values of m_a we consider, the ULA de Broglie wavelength is macroscopic, and so is the ULA "Jeans" scale $k_J \sim \sqrt{m_a H}$, which today corresponds to a wavelength [6, 7, 17, 18, 20, 8]

$$\lambda_J \simeq 2.5 \text{ Mpc } h^{-1/2} \left(\frac{m_a}{10^{-25} \text{ eV}}\right)^{-1/2}. \tag{3}$$

For ULA in the "dark-matter like" regime, structure formation is suppressed at length scales $l < \lambda_J$ and in proportion to Ω_a/Ω_d, where $\Omega_d = (\Omega_a + \Omega_c)$ and Ω_c is the relic density of standard cold dark-matter (CDM). This fact is evident in the suppressed amplitude of the matter power-spectrum at small scales, as seen in Fig. 2. CMB anisotropies are altered in this regime for modes which enter the horizon when ULAs are still not redshifting as $\rho \propto a^{-3}$. In this case, gravitational potential wells decay more rapidly than they usually do, leading to enhanced higher-l acoustic peak heights in the observed CMB power spectra, as seen in Fig. 2.

At lower masses still ($m_a \lesssim 10^{-25}$ eV), in the "dark-energy like" ULA regime, the expansion rate (and thus the growth rate of structure) is altered from its behavior in a $w = -1$ dark-energy cosmology. This leads to shifts of the CMB acoustic peak locations in l at fixed values of other parameters, due to the altered angular-diameter distance to the surface of last-scattering, as seen in Fig. 2. Matter-radiation equality also occurs at a different time, changing the shape and amplitude of the matter power-spectrum, as seen in Fig. 2.

Our modified Boltzmann code, AXICAMB, handles perturbation evolution by solving the perturbed Klein-Gordon equation exactly when $a \leq a_{\rm osc}$. Later, when $a > a_{\rm osc}$, we treat ULAs as a fluid with an unusual sound speed, a result which can be rigorously justified using

a WentzelKramersBrillouin (WKB) approximation. The resulting sound speed is [20]

$$c_a^2 = \frac{k^2/m_a^2}{4/\left(1+z\right)^2 + k^2/m_a^2}, \tag{4}$$

where k is the perturbation wave number. This scale-dependent c_a^2 captures the suppression of small-scale structure by ULAs. This code is nearly ready for public release, and we will make it publicly available in coming months, so that observers can include new data in the search for ULAs.

4 Data and constraints

To determine the allowed parameter space, we use *Planck* 2013 temperature anisotropy data, WMAP large-scale CMB polarization data (to break the degeneracy between the perturbation amplitude A_s and the optical depth to reionization τ), as well as small-scale CMB data from the Atacama Cosmology Telescope (ACT) and South-Pole Telescope (SPT) [21, 22, 23, 24]. To complement this data, we also include measurements of the galaxy clustering power-spectrum from the WiggleZ galaxy survey [25]. We vary the standard 6Λ CDM parameters, in addition to the ULA parameters m_a and $\Omega_a h^2$. The degeneracy of ULA parameters with the standard 6 is strongly dependent on the mass, making the parameter space difficult to sample. To address this difficulty, we use a nested sampling technique, as described in Ref. [13]. We ultimately obtain the constraints to ULA parameter space shown in Fig. 3. Marginalizing over all other parameters, we find that in the constrained region of parameter space (10^{-32} eV $\lesssim m_a \lesssim 10^{-25.5}$ eV), $\Omega_a h^2 \lesssim 6 \times 10^{-3}$ at 95%-confidence, while at higher and lower masses, ULAs can compose nearly all of the dark matter or dark energy, respectively.

5 Conclusions and future work

There are many exciting possibilities for future cosmological tests of ULAs and standard QCD axions. The most powerful is related to the phase structure of the CMB acoustic peaks. These reflect the initial conditions of the primordial plasma, which are now known to be predominantly adiabatic. This is consistent with simple inflationary models. If the Peccei-Quinn symmetry is broken during the inflationary era and not restored, the axion will carry *isocurvature* perturbations, altering the phase structure of the CMB acoustic peaks [26]. The 2013 *Planck* satellite data impose a limit (through the lack of isocurvature) of $\left(H_I/\phi_{i,0}\right)\left[\Omega_a/\left(\Omega_a+\Omega_c\right)\right] \lesssim 4\times10^{-5}$, where H_I is the Hubble parameter during inflation [27, 28]. In the "dark-matter like" ULA mass range, or for QCD axions, the relic density may then be related to the initial field value using standard expressions.

This then yields the limits

$$\frac{\Omega_a}{\Omega_a+\Omega_c} \lesssim 10^{-3}\left(\frac{10^{14}\text{ GeV}}{H_I}\right) \tag{5}$$

for ULA dark matter and

$$\frac{\Omega_a}{\Omega_a+\Omega_c} \lesssim 10^{-12}\left(\frac{10^{14}\text{ GeV}}{H_I}\right)^{7/2} \tag{6}$$

for QCD axions. The fractional slope in the QCD case results from temperature-dependent corrections to the axion mass during the onset of coherent oscillation of the field. It is important to note that the corresponding limits are not known in the "dark-energy like" ULA mass regime, because the isocurvature transfer function of such ULAs, while known from our AXICAMB code using analytic initial conditions we have derived, has not yet been self-consistently included in a cosmological Monte-Carlo Markov chain analysis of CMB data. A robust detection of primordial gravitational waves at the level of the current limits [$H_I \sim 10^{14}$ GeV] would thus either severely constrain the cosmic relic density of axions/ULAs, or require a non-canonical scenario for their production. Alternatively, robust evidence for ULA or standard QCD axion dark matter could indicate a very dim forecast for experiments targeting primordial CMB B-mode polarization.

We note that our limits from the matter power-spectrum result from a simple treatment of the bias between the galaxy density field and the ULA density field which we will work to improve once a complete treatment of nonlinear structure formation from ULAs is developed. In the meantime, we will use our code with new data sets, such as the nearly 40σ observation [29] by *Planck* of weak lensing of the CMB by foreground structure. This data set tests both the kinematics of cosmic expansion when ULAs replace some of the dark matter or dark energy, and also the altered growth of structure in such a cosmology. We show an example case in Fig. 4, where the effect of low and high ULA mass-fractions is contrasted with observations of the lensing deflection-angle dimensionless power-spectrum by the ACT experiment. The era of precision cosmology promises ever more sensitive tests of axionic dark matter and dark energy.

References

[1] R. D. Peccei and H. R. Quinn, Phys. Rev. Lett. **38**, 1440 (1977).

[2] S. Weinberg, Phys. Rev. Lett. **40**, 223 (1978).

[3] F. Wilczek, Phys. Rev. Lett. **40**, 279 (1978).

[4] M. B. Wise, H. Georgi and S. L. Glashow, Phys. Rev. Lett. **47**, 402 (1981).

[5] P. J. Steinhardt and M. S. Turner, Phys. Lett. B **129**, 51 (1983).

[6] J. A. Frieman, C. T. Hill, A. Stebbins and I. Waga, Phys. Rev. Lett. **75**, 2077 (1995) [astro-ph/9505060].

[7] K. Coble, S. Dodelson and J. A. Frieman, Phys. Rev. D **55**, 1851 (1997) [astro-ph/9608122].

[8] A. Arvanitaki, S. Dimopoulos, S. Dubovsky, N. Kaloper and J. March-Russell, Phys. Rev. D **81**, 123530 (2010) [arXiv:0905.4720].

[9] E. Witten, Phys. Lett. B **149**, 351 (1984).

[10] P. Candelas, G. T. Horowitz, A. Strominger and E. Witten, Nucl. Phys. B **258**, 46 (1985).

[11] P. Svrcek and E. Witten, JHEP **0606**, 051 (2006) [hep-th/0605206].

[12] S. Dimopoulos, S. Kachru, J. McGreevy and J. G. Wacker, JCAP **0808**, 003 (2008) [hep-th/0507205].

[13] R. Hlozek, D. Grin, D. J. E. Marsh and P. G. Ferreira, Phys. Rev. D **91**, no. 10, 103512 (2015) [arXiv:1410.2896].

[14] L. Amendola and R. Barbieri, Phys. Lett. B **642**, 192 (2006) [hep-ph/0509257].

[15] D. J. E. Marsh, E. Macaulay, M. Trebitsch and P. G. Ferreira, Phys. Rev. D **85**, 103514 (2012) [arXiv:1110.0502].

[16] J. A. Frieman and A. H. Jaffe, Phys. Rev. D **45**, 2674 (1992).

[17] M. Khlopov, B. A. Malomed and I. B. Zeldovich, Mon. Not. Roy. Astron. Soc. **215**, 575 (1985).

[18] W. Hu, R. Barkana and A. Gruzinov, Phys. Rev. Lett. **85**, 1158 (2000) [astro-ph/0003365].

[19] D. J. E. Marsh and P. G. Ferreira, Phys. Rev. D **82**, 103528 (2010) [arXiv:1009.3501].

[20] J.-C. Hwang and H. Noh 2009, Physics Letters B, 680, 1.

[21] P. A. R. Ade *et al.* [Planck Collaboration], Astron. Astrophys. **571**, A1 (2014) [arXiv:1303.5062].

[22] C. L. Bennett *et al.* [WMAP Collaboration], Astrophys. J. Suppl. **208**, 20 (2013) [arXiv:1212.5225].

[23] S. Das *et al.*, JCAP **1404**, 014 (2014) [arXiv:1301.1037].

[24] R. Keisler *et al.*, Astrophys. J. **743**, 28 (2011) [arXiv:1105.3182].

[25] C. Blake, S. Brough, M. Colless et al. 2012, Mon. Not. R. Astron. Soc., **425**, 405.

[26] M. Axenides, R. H. Brandenberger and M. S. Turner, Phys. Lett. B **126**, 178 (1983).

[27] L. Visinelli and P. Gondolo, Phys. Rev. Lett. **113**, 011802 (2014) [arXiv:1403.4594].

[28] D. J. E. Marsh, D. Grin, R. Hlozek and P. G. Ferreira, Phys. Rev. Lett. **113**, no. 1, 011801 (2014) [arXiv:1403.4216].

[29] P. A. R. Ade *et al.* [Planck Collaboration], arXiv:1502.01591 [astro-ph.CO].

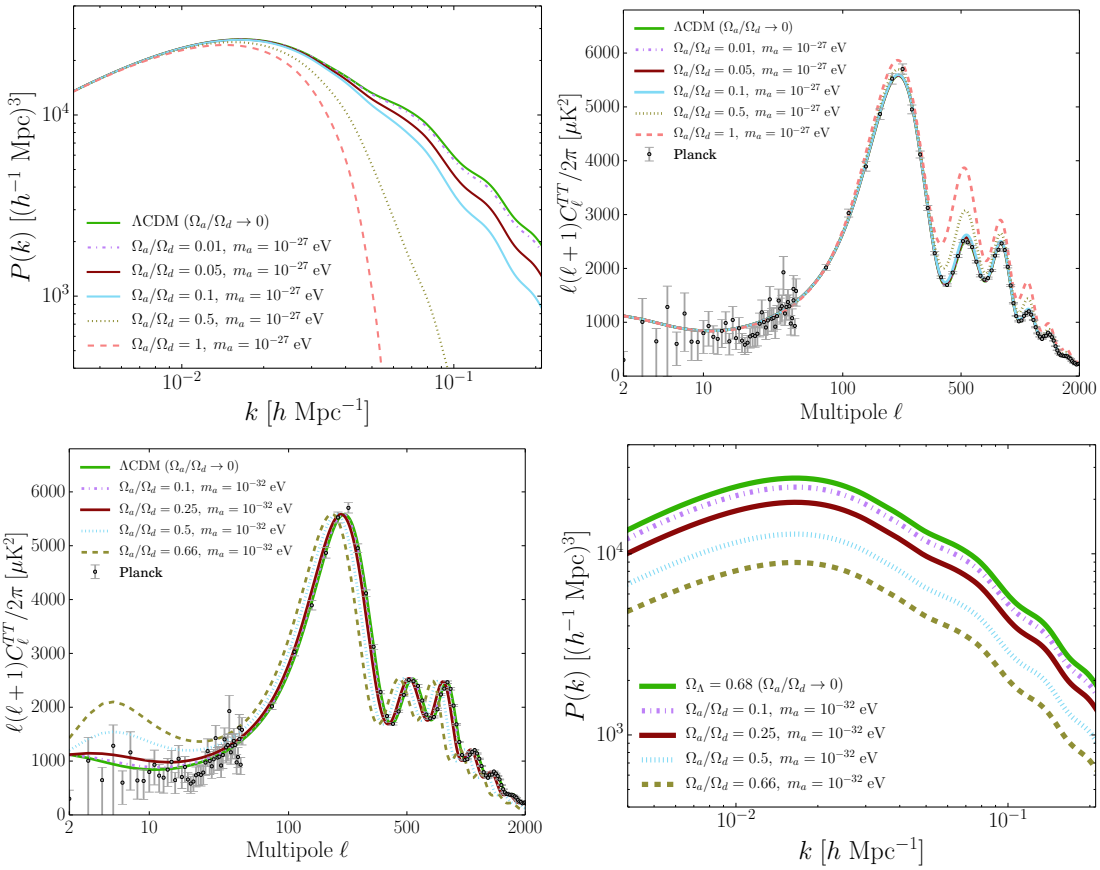

Figure 2: Top left panel shows total theoretical matter power-spectra when $m_a = 10^{-27}$ eV ULAs replace the indicated fraction of matter (CDM). The fraction is normalized as Ω_a/Ω_d, where $\Omega_d = \Omega_a + \Omega_c$, with Ω_c denoting the fractional density of ordinary CDM relative to the critical density. Top right panel shows theoretical CMB TT power spectra in the same ULA regime, along with *Planck* measurements of the TT power spectrum. Bottom left panel shows theoretical CMB TT power spectra when $m_a = 10^{-32}$ eV, deep into the "dark-energy like" ULA mass range. ULAs replace the indicated fraction of Ω_d. Bottom right panel shows theoretical matter power-spectra over the same parameter range. Reproduced (with permission) from Ref. [13]. Copyright 2015 by The American Physical Society.

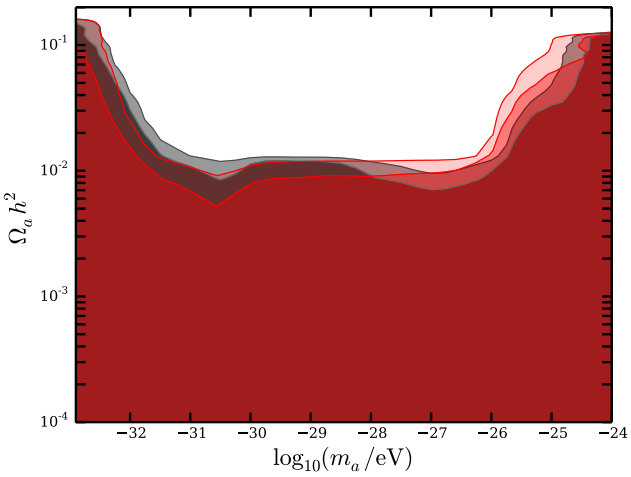

Figure 3: Marginalized 2 and 3σ contours in the $m_a - \Omega_a h^2$ plane for both the CMB-only and CMB+WiggleZ (large-scale structure survey) combinations of data sets. We obtain constraints of $\Omega_a h^2 \leq 0.006$ at 95% confidence level over some seven orders of magnitude in ULA mass m_a. Reproduced (with permission) from Ref. [13]. Copyright 2015 by The American Physical Society. Theoretical curves are compared here with TT power spectra from the *Planck* 2013 data release [21].

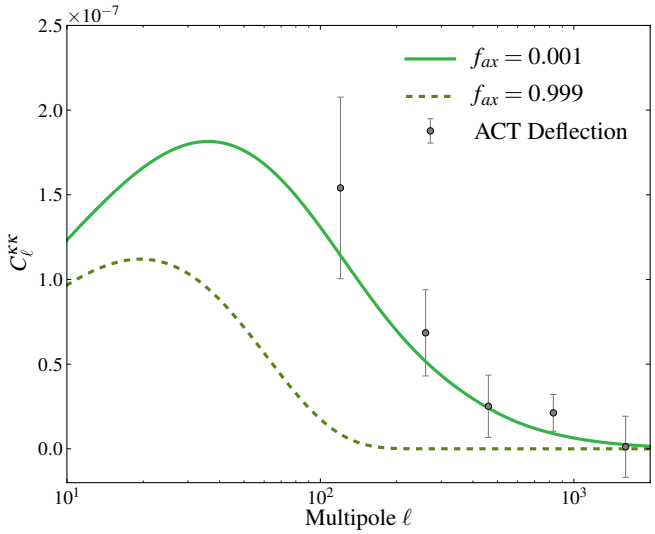

Figure 4: Dimensionless CMB-lensing deflection angle power-spectrum in ULA models [for $m_a = 10^{-28}$ eV and varying axion mass fraction $f_{ax} = \Omega_a/(\Omega_a + \Omega_c)$] compared with ACT data.

Dark Matter Searches with the LUX Experiment

Paolo Beltrame, on behalf of the LUX Collaboration

School of Physics & Astronomy, University of Edinburgh, Edinburgh, UK

DOI: http://dx.doi.org/10.3204/DESY-PROC-2015-02/beltrame_paolo

The Large Underground Xenon (LUX) experiment is a 350 kg liquid xenon time projection chamber (TPC) whose primary goal is to directly detect galactic Dark Matter in form of Weakly Interacting Massive Particles (WIMPs). The first LUX science search results based on 85.3 day of data (Run3) collected in 2013 has set the best limit on spin-independent WIMP-nucleon cross section, reaching a minimum of 7.6×10^{-46} cm^2 90% CL for WIMP mass of 33 GeV/c^2. While presently collecting a 300-day data set (Run4), the LUX collaboration is also performing the re-analysis of the Run3 sample with new calibration measurements for nuclear and electronic recoil events, and additional improvements of the analysis methods. Dual phase xenon based TPCs, although optimised to observe WIMPs, are particularly suitable for exploration of alternative Dark Matter scenarios, such as axions and axion-like particles. The present status of the ongoing searches in LUX is also described.

1 Introduction and LUX Experiment

Consistent evidence from multiple astrophysical observations suggests that cold Dark Matter is the dominant form of matter in our galaxy [1]. Weakly interacting massive particles (WIMPs) are a generic class of particle candidates, arising from extensions to the Standard Model of particle physics. They could be detected via Weak-force-mediated nuclear recoils (NR) in detectors on Earth [2, 3]. Direct search experiments look for the low NR energy expected when WIMPs scatter elastically off target nuclei in the active detector material. The small interaction cross sections and low velocities of galactic WIMPs impose the detectors to be sensitive to few keV and at the same time to exploit large exposures of many kg·years.

The Large Underground Xenon (LUX) experiments is a 350 kg dual-phase xenon time-projection chamber (TPC) located 4850 feet underground at the Sanford Underground Research Facility (SURF) in Lead, South Dakota. Energy deposited from the particle interaction in the xenon creates a primary scintillation signal ($S1$) and ionization charge which is drifted by an electric field (181 V/cm) to the liquid-gas interface at the top of the detector. The electrons are then extracted into the gas phase (6.0 kV/cm), where they produce electroluminescence ($S2$). Both signals are read out by two arrays of photomultipler tubes (PMTs): 61 viewing the TPC from above, and 61 from below. The precise (few mm) 3D position reconstruction of the particle scattering point enables to exploit the self-shielding capability of the liquid xenon selecting for the Dark Matter search only inner radioactively-quiet fiducial volume. The $S1$ and $S2$ signals are also used to estimate the deposited energy and their ratio is exploited as particle identification to discriminate WIMP-like NR from background electron recoils (ER) at the 99.6% level at a 50% NR acceptance in the energy range of the LUX analysis. Description of

the detector technology, underground laboratory and deployment can be found in [4].

2 WIMP search

LUX completed its first physics run in 2013, collecting a total of 85.3 day of WIMP search data. During this period the ER background rate inside the 118 kg selected fiducial volume was 3.6 ± 0.3 mDRU (mDRU $= 10^{-3}$ counts/day/kg/keV) between 2 – 30 photoelectrons $S1$, the energy range of interest. A non-blind analysis was conducted in which only a minimal set of high-acceptance data quality cuts were used. Single scatter events containing exactly one $S1$ within the maximum drift time preceding a single $S2$ were selected for further analysis. In total 160 events were observed, being consistent with the predicted background of ER. Confidence intervals on the spin-independent WIMP-nucleon cross section were set using a Profile Likelihood Ratio analysis (PLR), based on distributions in radius, depth and $S1$ and $S2$. The 90% upper CL is shown in Fig. 1 with a minimum of 7.6×10^{-46} cm^2 at a WIMP mass of 33 GeV/c^2. These remain the strongest constraints over a wide range of WIMP mass [5]. However, the analysis was performed under the conservative assumption of zero efficiency for NR events below the 3 keV, corresponding to the minimum energy of previous liquid xenon calibrations.

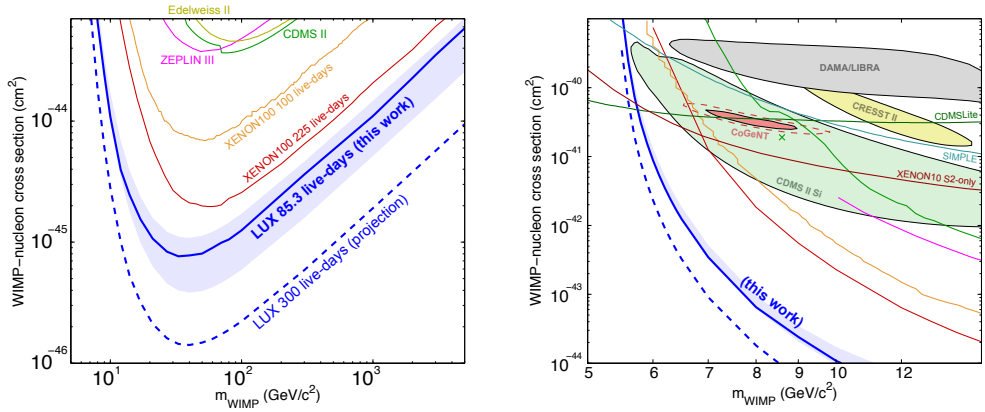

Figure 1: *Left*: The LUX 90% confidence limit on the spin-independent elastic WIMP-nucleon cross section for the 85.3-day exposure (blue) and projected limit for the upcoming 300-day run (dashed blue). *Right*: Close-up of the low mass region. The results use the conservative assumption of zero efficiency for NR events below the 3 keV.

2.1 Electron and nuclear recoil calibrations

The detector has been extensively calibrated with internal sources (for ER) and both external sources and DD neutron generator (for NR).
The internal sources, ^{83m}Kr and tritiated methane (CH_3T), injected into the xenon circulation stream, have the advantage of spreading evenly throughout the active volume, providing a homogeneous calibration. The mono-energetic 9.4 keV and 32.1 keV energy depositions of

^{83m}Kr were used to constantly monitor the electron drift attenuation length, the light yield and the corrections in x, y, z for detector effects. The novel CH_3T (β^- source with endpoint of ∼18 keV) provided the ER response of the detector at low energies and information on the background shape. This also enabled to study the light and charge yields down to ∼1 keV. The precise determination of ER events "leaking" down into NR $S2/S1$ region has been also evaluated between 0.2 and 5 keV, as a function of $S1$. A combined study with ^{83m}Kr and CH_3T enabled for a precise estimation of the fiducial volume.
To estimate the detector response to NR, in addition to AmBe and ^{252}Cf, a DD neutron generator was employed. This generates an almost monochromatic neutron beam, enabling through an analysis of multiple-scatter events to perform calibration down to 0.8 keV for the NR ionization and to 1.2 keV for the scintillation channels.

2.2 Re-analysis and Run4

Following the first WIMP-search results LUX underwent a period of preparation for the final 300-day WIMP-search run. This included a campaign of cathode and grid wire conditioning aimed at increasing the applied drift and extraction fields and improvements to the krypton calibration system. While collecting new data, the collaboration is also re-analysing the Run3 sample. The improved detector response calibration at very low energy, the better modelling of the background, a more accurate event position reconstruction for events close to the radial edge of the TPC, the updated fiducial volume (with an increased mass up to ∼140 kg), and the more advanced PLR analysis (with the inclusion of nuisance parameters and an update energy scale), all this will lead to a considerable improved results, in particular in the low WIMP mass region, already in the re-analysis. As for the Run4, the increased exposure and the reduced background (because of the ^{127}Xe decaying away) will improve the sensitivity by more then a factor of 4 compared to the current limit.

3 Axion and Axion Like Particle searches

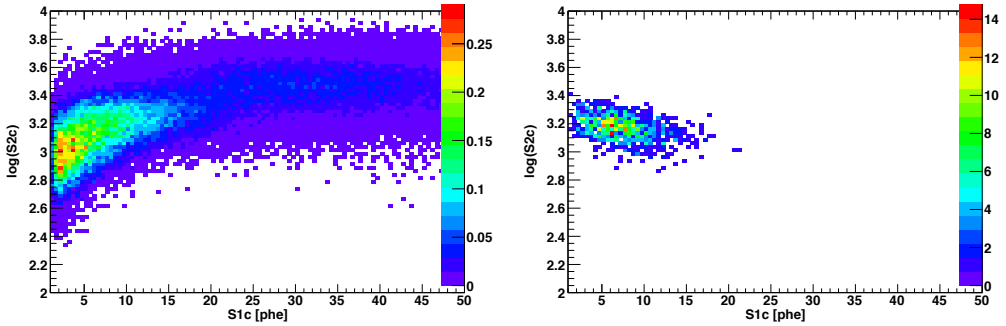

Figure 2: *Left*: Expected event rate in the LUX discrimination phase space from solar axions, assuming the axio-electric effect with coupling $g_{Ae} = 1.5 \times 10^{-12}$. *Right*: Expected signal from 2 keV ALPs and $g_{Ae} = 1.5 \times 10^{-13}$. The "c" subscript denotes that the $S1$ and $S2$ variables have been corrected by the detector effects at the position of the interaction point.

Astrophysical observations are thought to be the most sensitive technique for detecting axions and Axion Like Particles (ALPs) [7]. The Sun would constitute an intense source and searches can be conducted for ALPs. The latter may have been generated via a non-thermal production mechanism in the early universe, in which case they would be now slowly moving within our galaxy, and might constitute the Dark Matter.
Axions and ALPs may give rise to observable signatures in liquid xenon TPCs through their coupling to electrons (g_{Ae}), scattering off the electrons of an atom target, through the axio-electric effect [8, 9, 10]. This process is the analogue of the photo-electric effect with the absorption of an axion instead of a photon.
LUX is currently performing two specific analyses for axions and ALPs, based on the Run3 data sample. LUX is expected to surpass the current best limit on g_{Ae} set by the XENON100 collaboration [11] because of the very low ER background rate at low recoil energies, and the low energy threshold. Figure 2 shows the expected signal event rate in the LUX discrimination phase space for Solar axion (left) and ALPs (right). A dedicated PLR test statistic has been developed, exploiting the re-analysis background and detector response model implemented with the new ER calibrations data.

4 Conclusion and Outlook

During an 85.3 live-day (Run3) commissioning run with a 118 kg of fiducial xenon mass, the LUX experiment has achieved the most sensitive spin-independent WIMP exclusion limits over a wide range of masses. LUX commenced a 300-day data taking (Run4) in 2014 that will further improve the WIMP sensitivity by a factor of 4. A re-analysis of the Run3 data is ongoing, exploiting the new calibration campaign and various improvements which will significantly enhance the sensitivity at low mass. Publications will come soon.
Along with the standard WIMP searches, exploiting the low ER background rate and energy threshold of the LUX detector, the collaboration is conducting dedicated searches for alternative signals, primarily for axions and axion-like particles.

Acknowledgments

This work was partially supported by the U.S. Department of Energy (DOE) under award numbers DE-FG02-08ER41549, DE-FG02-91ER40688, DE-FG02-95ER40917, DE-FG02-91ER40674, DE-NA0000979, DE-FG02-11ER41738, DE-SC0006605, DE-AC02-05CH11231, DE-AC52-07NA 27344, and DE-FG01-91ER40618; the U.S. National Science Foundation under award numbers PHYS-0750671, PHY-0801536, PHY-1004661, PHY-1102470, PHY-1003660, PHY-1312561, PHY-1347449; the Research Corporation grant RA0350; the Center for Ultra-low Background Experiments in the Dakotas (CUBED); and the South Dakota School of Mines and Technology (SDSMT). LIP-Coimbra acknowledges funding from Fundao para a Cincia e Tecnologia (FCT) through the project-grant CERN/FP/123610/2011. Imperial College and Brown University thank the UK Royal Society for travel funds under the International Exchange Scheme (IE120804). The UK groups acknowledge institutional support from Imperial College London, University College London and Edinburgh University, and from the Science & Technology Facilities Council for PhD studentship ST/K502042/1 (AB). The University of Edinburgh is a charitable body, registered in Scotland, with registration number SC005336.

References

[1] D. Harvey *et al.*, Science **347**, 1462 (2015).
[2] M. W. Goodman and E. Witten, Phys. Rev. D **31**, 3059412 (1985).
[3] J. L. Feng, Ann. Rev. Astr. Astrophys. **48**, 495 (2010).
[4] D. Akerib et al. (LUX coll.), Nucl. Instrum. Meth. A **704**, 111 (2013)
[5] D. Akerib et al. (LUX coll.), Phys. Rev. Lett. **112**, 091303 (2014).
[6] M. Szydagis, A. Fyhrie, D. Thorngren and M. Tripathi, JINST **8**, C10003 (2013).
[7] P. Sikivie, Phys. Rev. Lett. **51**, 1415 (1983).
[8] S. Dimopoulos and G. D. Starkman and B. W. Lynn, Phys. Rev. **B 168**, 145 (1986).
[9] M. Pospelov and A. Ritz and M. Voloshin, Phys. Rev. D **78**, 115012 (2008).
[10] K. Arisaka et al., Astropart. Phys. **44**, 59 (2013).
[11] E. Aprile et al. (XENON100 coll.), Phys. Rev. D **90**, 062009 (2014).

Axions at the International AXion Observatory

Javier Redondo

University of Zaragoza, Zaragoza, Spain
Max Planck Institut für Physik, Munich, Germany

DOI: http://dx.doi.org/10.3204/DESY-PROC-2015-02/redondo_javier

QCD axions with meV mass can be behind some stellar cooling anomalies and form all or part of the cold dark matter of the universe. We discuss on a proposed experiment to discover the solar flux of meV mass axions: the International AXion Observatory (IAXO).

1 The meV mass axion frontier

The really low energy frontier of fundamental physics [1] offers several pressing questions that have received much attention in the recent years [2]. Very weakly-interacting sub-eV particles (WISPs) can arise as low energy manifestations of high energy completions of the standard model of particle physics and tend to be generically good dark matter candidates [3]. A central target is to discover the QCD axion, hypothetical particle predicted in the Peccei-Quinn mechanism to explain the puzzling absence of CP violation in the strong interactions, and only later realised as suitable for constituting the cold dark matter (CDM) and found to appear generically in string theories, prime candidates for describing quantum gravity. Actually, if the QCD axion exists, a sizeable amount of axion CDM is unavoidable (it turns out to be more natural for axion-like particles to solve the DM puzzle than to solve the strong CP problem).

The axion CDM density produced in the Big Bang depends on the axion mass, m_a, and the details of early cosmology. There are two basic scenarios: the axion field taking its initial conditions (typically after a phase transition) either *after* cosmic inflation or *before*. In the *after* scenario, the initial conditions are random in causally disconnected regions and a network of global strings forms through the Kibble mechanism. QCD instantons generate a potential for the axion with a set of N CP-conserving minima (N depends on the UV completion of the axion model), which is strongly suppressed at high temperatures but becomes relevant close to the color confinement phase transition, $T_{\rm QCD}$. By then, the field relaxes to one minimum and oscillates around it with its amplitude damped by the universe expansion. The harmonically oscillating field is a coherent state of very non-relativist quanta (axions), a cold dark matter fluid. The network of strings and domain walls developed around $T_{\rm QCD}$ is unstable if $N = 1$ and decays into a second population of CDM axions. The first contribution is computable but the second (which seems to dominate) has to be extrapolated over many orders of magnitude from numerical simulations. The latest simulations [4] give[1],

$$\Omega_a h^2 = 0.12 \left(\frac{1}{3.4} + \frac{2.4 \pm 1.12}{3.4}\right) \left(\frac{108\,\mu{\rm eV}}{m_a}\right)^{1.187} \quad ; \quad \text{(misalignment + strings)} \qquad (1)$$

[1] A recent analysis [5] challenges the interpretation of the simulations, adding to a longstanding controversy.

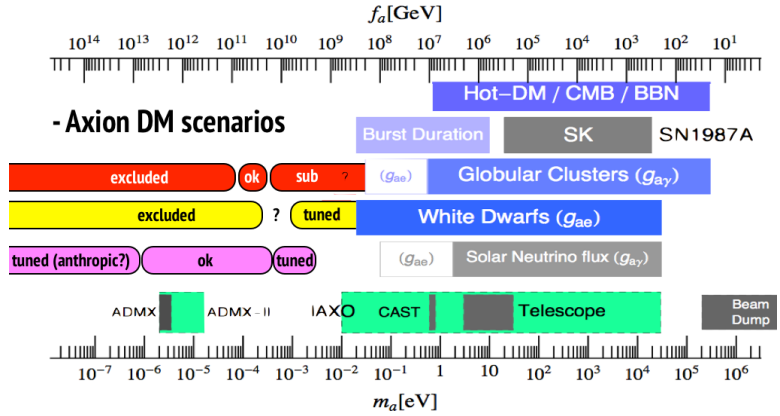

Figure 1: Axion mass bands in the main CDM scenarios: *after* (red for $N = 1$, yellow for $N > 1$) and *before* (purple). Shown also are excluded bands from cosmology, stellar evolution and experiments together with sensitivities from ADMX-II and IAXO (green), from [6].

suggesting an axion CDM mass $m_a = 105 \pm 25\,\mu$eV labelled 'ok' in Fig. 1 in red. Smaller values overproduce DM and are excluded, and larger ones imply a subdominant fraction of the CDM $\gtrsim (0.11/20)^{1.187} = 0.2\%$ for $m_a \lesssim 20$ meV. If $N > 1$ the string-wall network is stable and thus ruled out unless a small energy breaks the degeneracy of vacua. This breaking needs to be extremely small because it tends to displace the minimum away from CP conserving and spoil the solution of the strong CP problem. The hecatomb of strings and walls gets delayed by the small degeneracy breaking, making CDM axions less diluted and more abundant today, favouring much larger axion CDM masses (see yellow labelled 'tuned' in Fig. 1). Finally, in the *before* scenario, inflation makes homogeneous the axion field in our observable universe and dilutes away strings and walls. The observed amount of CDM can be obtained for any $m_a <$ meV by invoking the appropriate axion initial condition. Excluding fine tunings of 10% to the bottom or top of the potential the preferred range is 1 μeV$< m_a <$ 0.5 meV (purple band labelled 'ok').

Figure 1 shows the CDM regions together with the exclusion bounds from cosmology astrophysics and experiments and makes a very clear point: would DM be made of ∼meV mass axions, we shall then expect some effects in astrophysics too. Indeed, for several years now, there have been increasing claims of anomalies in the cooling of certain types of stars that could be attributable to QCD axions. We shall here briefly name them and show that a consistent axion model exists which fits every claim, constituting a prime target for a next generation helioscope: IAXO. The axion Lagrangian defines conventions for the axion coupling to photons and fermions,

$$\mathcal{L}_a = \frac{1}{2}(\partial_\mu a)(\partial^\mu a) - \frac{1}{2}m_a^2 a^2 - \frac{g_{a\gamma}}{4}F_{\mu\nu}\tilde{F}^{\mu\nu}a + \sum_f \frac{g_{af}}{2}\bar{\Psi}_f\gamma^\mu\gamma_5\Psi_f\partial_\mu a. \qquad (2)$$

In UV-complete axion models the couplings are related through a few parameters. Here we use KSVZ and DSFZ (with variants 1 and 2) models as exposed in Ref. [7] and show the electron, proton and neutron couplings in Fig. 2.

White dwarfs (WDs) are degenerate stars not massive enough to fuse C and O into heavier nuclei, which just cool down by neutrino thermal emission from the core and surface electromag-

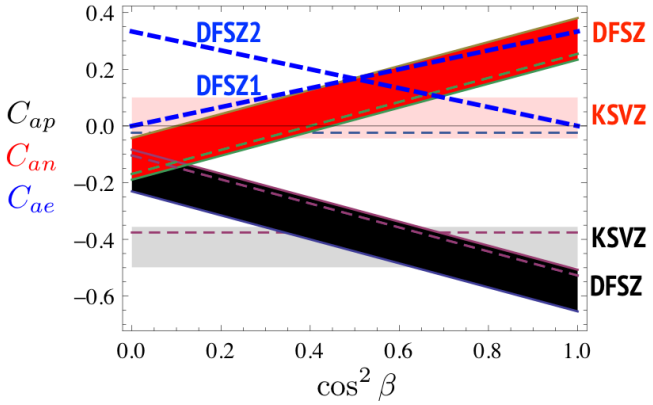

Figure 2: Axion-proton, neutron and electron couplings (black, red, and blue resp.) with low-energy-QCD error bars ($m_u/m_d = 0.56^{+0.04}_{-0.26}$) in the KSVZ and DFSZ 1 and 2 models. Here C_{af} is the coupling normalised with the axion decay constant f_a and the fermion mass m_f: $C_{af} = g_{af} \times f_a/m_f$ ($\tan\beta$ is the ratio of extra Higgs fields in the model [7]).

netic radiation. The WD luminosity function (number of WDs per unit luminosity) decreases if there is an extra channel for plasma energy loss [8]. Recently compiled luminosity functions tend to fit better expectations if the emission of axions in nucleus-electron bremsstrahlung is added[2] with a coupling strength [9],

$$g_{ae} = (1.4 \pm 1.4) \times 10^{-13}. \tag{3}$$

Axion emission from the red giant star cores cools the plasma delaying the Helium flash, which happens at a larger core mass and thus becomes brighter. The study of the red giant branch of M5 [10] yields a 95% CL upper bound $g_{ae} < 4.3 \times 10^{-13}$ but a 1-σ preferred region,

$$g_{ae} = (2 \pm 1.5) \times 10^{-13}. \tag{4}$$

The swift cooling of the neutron star CAS A observed for 10 years by CHANDRA seems to confirm neutrino pair emission in neutron Cooper pair formation, $n + n \to {}^3\mathrm{P}_2 + \bar{\nu}\nu$, as the responsible cooling mechanism but theoretical emission rates fall short by a factor of two [11], accountable among others [12] by a similar axion emission process, $n + n \to {}^3\mathrm{P}_2 + a$ if the axion-neutron coupling were [11],

$$g_{an} = (3.8 \pm 3) \times 10^{-13}. \tag{5}$$

Other interesting anomalies have been presented in this workshop [13] and elsewhere [14]. A full analysis is in progress and shall be reported elsewhere [15]. We advance that some of them are not quantitative enough and some others cannot be directly attributable to QCD axions because of the strong constraint on the axion-proton coupling derived from the duration of the detected neutrino pulse from SN1987a [16],

$$g_{ap} < 8 \times 10^{-10}, \tag{6}$$

certainly in need of refinement from new simulations and data from a next galactic SN.

We can now use a χ^2 function of the different exotic energy losses which led to constraints (3)-(6) to estimate the microscopic parameters of the axion models. The KSVZ model has

[2]The anomalous cooling of the variables G117-B15A and R548 could also be due to axion emission, but the interpretation depends on the proper identification of the oscillating mode, so we have not included it in this analysis.

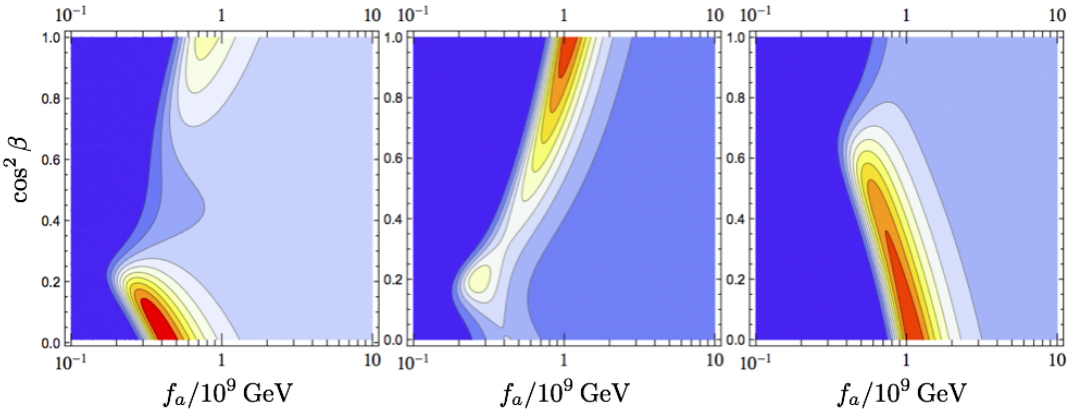

Figure 3: Isocontours of relative χ^2 (blue to red from max to min) for DFSZ models as function of the axion decay constant f_a and $\cos^2\beta$ ($\tan\beta$ is the ratio of extra Higgs fields in the model [7]).

$C_{ae} \simeq 0$ so in principle it could only fit the NS cooling anomaly (5) while respecting the SN constraint (6) but this is not the case because g_{an} is larger than g_{ap}, see Fig. 2. For DFSZ models, the χ^2 including only NS and SN data (Fig. 3 left) is maximal at two points, which correspond to large neutron to proton coupling happening at $\cos^2\beta = 1, 0$ for large f_a ($\sim 10^9$ GeV) and small f_a solutions ($\sim 3\times 10^8$ GeV). Including WD and RG data in DFSZ1 (Fig. 3 center) we see all fitting in both the small and large f_a points, with a larger tension in the small f_a. The DFSZ2 scenario (Fig 3 right) fits also the WD and RG anomalies respecting the SN constraint but cannot fit the NS simultaneously. In summary, there are two interesting targets

$$\begin{aligned} &\text{P1}: \quad f_a \sim 10^9\,\text{GeV} \quad \text{explains} \quad \text{RG}+\text{WD}+\text{NS}\,(\text{DFSZ1}),\ \text{RG}+\text{WD}\,(\text{DFSZ2}),\\ &\text{P2}: \quad f_a \sim 3\times 10^8\,\text{GeV} \quad \text{explains} \quad \text{RG}+\text{WD}+\text{NS}\,(\text{DFSZ1}), \end{aligned}$$

which correspond to masses $m_a \simeq 0.6$ and 20 meV resp.

2 IAXO: International AXion Observatory

Searching for meV mass axions seems to be within the reach of a future helioscope [17], or perhaps a future generation of 5th force searches [18] but the direct detection of meV DM axions seems extremely challenging. The helioscope technique [19] aims at detecting the copious flux of axions produced in the solar core via either Primakoff process ($\propto g^2_{a\gamma}$) or the ABC processes ($\propto g^2_{ae}$) [20]. Solar axions of energy ω convert coherently into detectable X-rays along an homogeneous transverse magnetic field B of length L with a probability

$$P(a\to\gamma) \simeq \frac{(2g_{a\gamma}B\omega)^2}{m_a^4}\sin^2\left(\frac{m_a^2 L}{4\omega}\right). \tag{7}$$

The most successful helioscope to date, CAST, uses a 9 T, 10 m long LHC decommissioned magnet mounted on a movable platform to track the Sun for ~ 2 h/day with CCD and micromegas detectors at its bore ends. It mostly suffers from a small bore aperture ($\sim 14.5\,\text{cm}^2$) and issues

to track the Sun far outside horizontal positions, consequences of the dipole being designed as part of a proton collider unaware of its today's axionic duties.

Members of the CAST collaboration are seeding a collaboration to build the first right-to-scale axion helioscope: the International AXion Observatory [21]. The central target is to build a new magnet dedicated solely to axion physics not to suffer from any of the constraints inherited from a recycling experiment. In [17], a preliminary study based on the CAST experience demonstrated that the technologies matured in CAST would allow for an improvement of up to 6 orders of magnitude in signal/noise beyond CAST with the use of a new toroidal magnet operated with X-ray focusing optics and state of the art Micromegas. Since then, the collaboration has grown to $\mathcal{O}(100)$ scientists from $\mathcal{O}(40)$ institutions, a conceptual design report was produced [22] and a LOI presented at CERN [23] (although the site of IAXO is by no means yet decided). A 20-m long, 5-m diameter toroid to be operated in a fully steerable platform has been designed [24] in collaboration with the CERN magnet labs. It would have 8 warm bores of 0.6 m diameter with an average field of 2.5 T (5 T peak field). The X-ray optics to be mounted at the bore's ends has been designed [25] by the IAXO groups at LLNL, Columbia U. and DTU Denmark. Micromegas detectors have been shown levels of 8×10^{-7}counts/(keV cm^2 s) in the CAST 2014 run and 10^{-7}counts/(keV cm^2 s) in a dedicated prototype at the Canfranc underground lab [26], which advance the ambitious goal 10^{-8}counts/(keV cm^2 s) as realistic. New groups in IAXO have brought expertise in other detection technologies such as Gridpix/InGrid, MMCs and low-noise CCDs, presented also in this workshop.

In Fig. 4 we show in dark gray the sensitivity of a 3-year data campaign of IAXO to solar axions of Primakoff (left) and ABC (right) origin, with the parameters shown to be Conservative in the CDRs [22, 24] but a background figure of 10^{-8}counts/(keV cm^2 s). The ABC flux of target P2 is in the discoverable region and of P1 only in the DFSZ2 model. We are considering improvements over the base design to raise the signal to noise up to a maximal factor of ~ 20 ("Not so" lightgray region), which would cover all the interesting points at high confidence and consistently improve over the SN1987a constraint scanning unconstrained parameter space where, as we argued before, axions can constitute all or part of the CDM of the universe.

IAXO has a large potential impact beyond discovering solar QCD axions. The flux of axions from the core collapse of Betelgueuse could be detected if IAXO is pointed at it with an early warning [27]. Other WISPs from the Sun could be detected, such as axion-like particles or hidden-photons [28]. Axion-like particles with a photon-coupling $\sim 10^{-11}$GeV^{-1} have been invoked as a solution for the anomalous transparency of the universe to high-energy photons [13] and will be either found or excluded by IAXO. Finally, we are studying the possibility of hosting direct axion CDM experiments in the IAXO magnet [29].

References

[1] J. Jaeckel and A. Ringwald, Ann. Rev. Nucl. Part. Sci. **60**, 405 (2010) [arXiv:1002.0329].

[2] K. Baker *et al.*, Annalen Phys. **525**, A93 (2013) [arXiv:1306.2841].

[3] P. Arias *et al.*, JCAP **1206**, 013 (2012) [arXiv:1201.5902].

[4] M. Kawasaki, K. Saikawa and T. Sekiguchi, Phys. Rev. D **91**, no. 6, 065014 (2015) [arXiv:1412.0789].

[5] L. Fleury and G. D. Moore, "Axion dark matter: strings and their cores," [arXiv:1509.00026].

[6] R. Essig *et al.*, "Working Group Report: New Light Weakly Coupled Particles," [arXiv:1311.0029].

[7] A. G. Dias *et al.*, JHEP **1406**, 037 (2014) [arXiv:1403.5760].

[8] G. G. Raffelt, Phys. Lett. B **166**, 402 (1986).

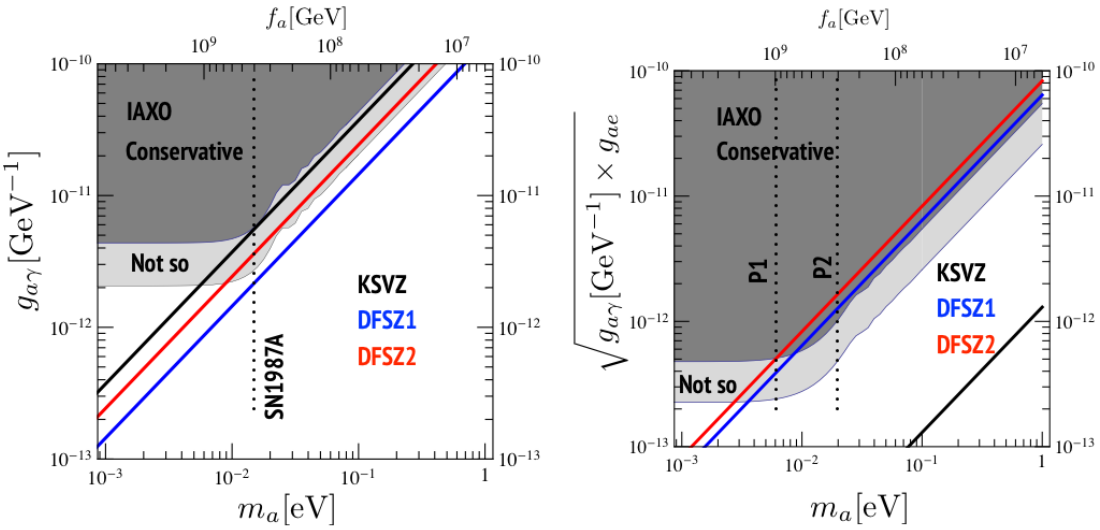

Figure 4: IAXO sensitivity for Primakof (left) and ABC (right) solar axions in the "conservative" and "not so" configurations. Axion models KSVZ, DFSZ1 and 2 as black, blue and red lines and the target points P1 and P2 motivated by astro-hints.

[9] M. M. Miller Bertolami *et al.* JCAP **1410**, no. 10, 069 (2014) [arXiv:1406.7712].

[10] N. Viaux, M. Catelan, P. B. Stetson, G. Raffelt, J. Redondo, A. A. R. Valcarce and A. Weiss, Astron. Astrophys. **558**, A12 (2013) [arXiv:1308.4627]; Phys. Rev. Lett. **111**, 231301 (2013) [arXiv:1311.1669].

[11] L. B. Leinson, JCAP **1408**, 031 (2014) [arXiv:1405.6873].

[12] L. B. Leinson, Phys. Lett. B **741**, 87 (2015) [arXiv:1411.6833].

[13] Talks of M. Giannotti, S. Troitsky, M. Roncadelli and M. Meyer in these proceedings.

[14] A. Ayala *et al.* Phys. Rev. Lett. **113** 19, 191302 (2014) [arXiv:1406.6053]. S. Aoyama and T. K. Suzuki, [arXiv:1502.02357].

[15] M. Giannotti, A. Payez, A. Ringwald, J. Redondo *et al.*, in preparation.

[16] G. G. Raffelt, Lect. Notes Phys. **741**, 51 (2008) [arXiv:hep-ph/0611350].

[17] I. G. Irastorza *et al.*, JCAP **1106**, 013 (2011) [arXiv:1103.5334].

[18] A. Arvanitaki and A. A. Geraci, Phys. Rev. Lett. **113**, no. 16, 161801 (2014) [arXiv:1403.1290].

[19] P. Sikivie, Phys. Rev. Lett. **51**, 1415 (1983) [Phys. Rev. Lett. **52**, 695 (1984)].

[20] J. Redondo, JCAP **1312**, 008 (2013) [arXiv:1310.0823].

[21] `http://iaxo.web.cern.ch/`

[22] E. Armengaud *et al.*, JINST **9**, T05002 (2014) [arXiv:1401.3233].

[23] I. Irastorza *et al.*, "The International Axion Observatory IAXO. Letter of Intent to the CERN SPS committee, " CERN-SPSC-2013-022 ; SPSC-I-242.

[24] I. Shilon, A. Dudarev, H. Silva and H. H. J. ten Kate, IEEE Trans. Appl. Supercond. **23**, no. 3, 4500604 (2013) [arXiv:1212.4633].

[25] A. C. Jakobsen, M. J. Pivovaroff, F. E. Christensen *et al.*, "X-ray optics for axion helioscopes," Proc. SPIE **8861**, Optics for EUV, X-Ray, and Gamma-Ray Astronomy VI, 886113, DOI: 10.1117/12.2024476.

[26] J. A. García, in these proceedings.

[27] G. G. Raffelt, J. Redondo and N. V. Maira, Phys. Rev. D **84**, 103008 (2011) [arXiv:1110.6397].

[28] J. Redondo, JCAP **0807**, 008 (2008) [arXiv:0801.1527]; JCAP **1507**, no. 07, 024 (2015) [arXiv:1501.07292].

[29] J. Redondo, "Axion Dark Matter searches @ IAXO" (e-link), talk at the 10th Patras Workshop on Axions, WIMPs and WISPs, 29th June-4th July, CERN, Switzerland.

EDELWEISS-III: Status and First Data

Maryvonne De Jésus[1] for the EDELWEISS Collaboration

[1]Université de Lyon, F-69622, Lyon, France; Université de Lyon 1, Villeurbanne; CNRS/IN2P3, Institut de Physique Nucléaire de Lyon

DOI: http://dx.doi.org/10.3204/DESY-PROC-2015-02/maryvonne_dejesus

EDELWEISS is an experiment dedicated to the direct detection of WIMPs, installed in the Underground Laboratory of Modane. It has accumulated WIMP data from July 2014 to April 2015 after important upgrades. The detectors are bolometers made of germanium crystals equiped with Full InterDigitized electrodes (FID). We present a preliminary analysis for a subset of the data (35 kg·d) giving a sensitivity of 1.57×10^{-5} pb for a WIMP mass of 7 GeV/c^2, as well as near future prospects in the low WIMP mass region.

1 The EDELWEISS-III experiment

Despite the tremendous theoretical and experimental efforts for more than eighty years we still do not know the exact nature of dark matter. Nevertheless there is strong evidence from recent precise measurements of the Planck satellite [1] that a large fraction of all matter of the Universe is invisible and predominantly non-baryonic. Among a large panel of theories sustaining the existence of Dark Matter, WIMPs (Weakly Interacting Massive Particles) are a generic class of particles with unknown mass ranging from 1 GeV to hundreds GeV [2].

The direct detection principle consists in the detection of the energy deposited due to elastic scattering off target nuclei. The expected event rate is extremely low ($<$ 1 evt/kg/year) due to the very small interaction cross-section of WIMPs with ordinary matter, along with the relatively small deposited energy ($<$ few tens of keV). The main challenges are to build a detector with a very low energy threshold and a good energy resolution, a large mass and running in a very low background environment.

EDELWEISS (Expérience pour Détecter les WIMPs en Site Souterrain), is an experiment dedicated to the direct detection of WIMPs, located in the Modane Underground Laboratory (LSM) in the Fréjus highway tunnel, where an overburden of about 1700 m of rock reduces the cosmic muon flux down to 5 μ m^{-2} day^{-1}.

The experimental set-up is mounted in a clean room (class 10,000) with a constant flow of deradonised air which reduces the radon level down to 30 mBq/m^3. The outermost shell is an active muon veto with a geometrical coverage of more than 98 % tagging muons crossing the experimental setup producing neutrons [3]. A polyethylene (PE) shielding (50 cm thick) attenuates the neutron flux from the laboratory walls by more than five orders of magnitude. The gamma-ray background is reduced by a 20 cm thick lead shielding around the cryostat.
The EDELWEISS-III setup was notably improved with respect to the previous phase of the experiment. A new internal PE shielding was added between the detection volume and the warm electronics, while the copper used for the cryostat thermal shields was replaced by a

much purer (NOSV Electronic Tough Pitch copper produced by Norddeutsche Affinerie) [4]. The cryogenics have been upgraded as well: thermal machines are now placed outside the external overall shields, allowing microphonics reduction. The feedback and bias resistances at 100 K were replaced with mechanical relays and the ionisation read-out was improved, yielding a 30% improvement for the baseline resolution.

To reduce environmental background, all materials used in the vicinity of the detectors have been tested for their radiopurity, using a dedicated high purity Ge (HPGe) detector [4].

The EDELWEISS-III detectors are 800 g germanium crystals (Figure 1, left) operating at very low temperatures (18 mK), equiped with a set of interleaved electrodes on all surfaces (Full Interdigitized : FID800) and two neutron transmutation doping (NTD) thermometers glued on each planar surface. The ionization signal, corresponding to the collection of electron-hole pairs on electrodes, depends on the particle type whereas the heat signal reflects the total energy deposit. The simultaneous measurements of heat and ionization allow an event by event discrimination between electronic recoils from γ's and β's and nuclear recoils from neutrons and WIMPs. With the FID detector technology, surface events are tagged by the presence of charge on only one side of the detector: the charge collection is shared between one veto and its neighbor fiducial electrodes, whereas for events occurring in the bulk of the crystal, the charge is collected on fiducial electrodes of both sides. The surface event rejection factor of FID has been measured with a dedicated ^{210}Pb calibration to be better than 4×10^{-5} at 90 % C.L., with a recoil energy threshold of 15 keV [5].

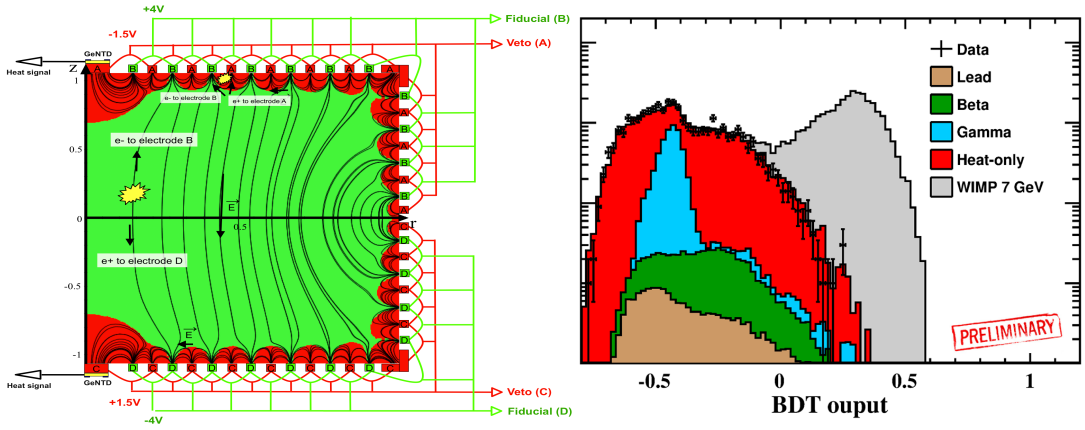

Figure 1: Left: EDELWEISS-III Full Inter-Digitized (FID) detector. Right: Boosted Desicion Tree discriminating variable. The colored histograms show the background contributions, the grey histogram shows the expected WIMP signal from a 7 GeV WIMP and the black dots are data.

2 Low-Mass WIMP

The interest for light dark matter has increased in the past few years with the recent excesses of events reported by different collaborations, (DAMA [6, 7], CRESST [8], CoGeNT [9] and CDMS [10]) supported by the observations of diffuse gamma-ray emission from the galactic

center, interpreted as evidence for annihilation of light WIMPs [11]. Due to the very steep shape of the energy recoil spectrum at low energy low mass WIMPs are particularly hard to identify in direct detection experiments and require a very low experimental threshold. Event discrimination is also compromised in the low recoil energy region as the different background populations overlap.

The data selection procedure, as well as the background and signal modeling are described in detail in [12, 13]. To summarize we used only a small fraction (35 kg·days) of the whole data: single standard detector is unblinded to tune the analysis and build data-driven background models.

A Boosted Decision Tree (BDT) analysis method is used for the event discrimination. This is a multivariate method which combines several inputs into a single discriminating variable (Figure 1, right). The BDT score can be more background like (close to -1) or more signal-like (close to 1). A cut is applied on the BDT output, the optimal value being derived from simulations by maximising the signal over noise ratio, effectively rejecting all backgrounds (<1 background event expected). A BDT was trained for each WIMP mass. The resulting limit is shown in Figure 2 (left), showing competitive results in spite of the small exposure and relatively high threshold. A clear separation between signal and background events can be achieved. This is a tribute to the new FID detector design which allows for remarkable surface event rejection. This clearly demonstrates the potential of EDELWEISS detectors for low mass WIMP searches.

The EDELWEISS collaboration is working on improving baseline resolutions and thresholds. The ionization baseline resolutions can be improved down to 100 eV RMS using HEMT (high-electron-mobility transistor) technology for charge readout electronics [14]. The heat signal can be amplified using the boosted Neganov-luke effect by increasing the bias voltage up to 100 V [15]. The effects can be seen in Figure 2 (right). At low WIMP masses we have to optimize the bias voltage to balance the background discrimination and the gain in sensitivity. Indeed, for WIMP masses $M_W < 4\,\mathrm{GeV/c^2}$, very high voltage will give the lower threshold and for $M_W > 4\,\mathrm{GeV/c^2}$ low voltage will keep the discrimination capability.

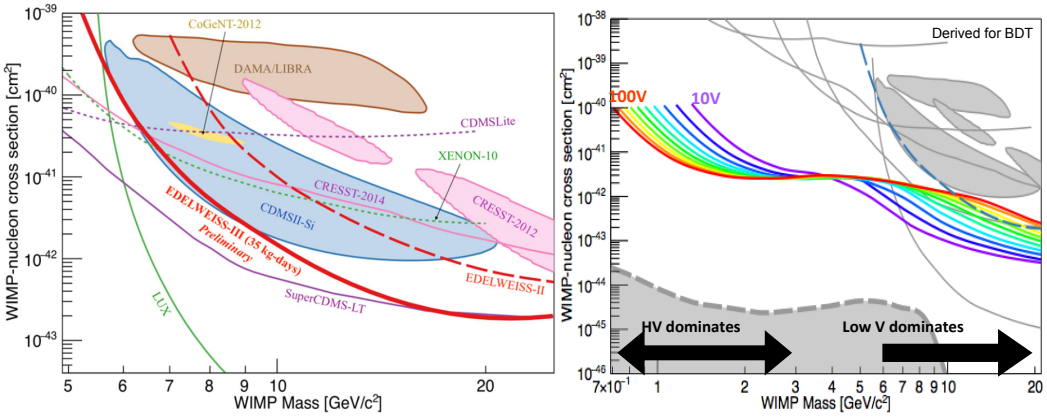

Figure 2: Left: Limit on the WIMP cross section, given the WIMP masses. EDELWEISS-II is dashed-red and EDELWEISS-III 35 kg.d in red (this work). Right: Voltage impact on the low mass WIMP search for the EDELWEISS FID detectors.

3 Conclusions

We analyzed the first data from the EDELWEISS-III experiment for a low mass WIMP search. The results are very promising for future searches: improvements in the baseline resolution allow a single detector (35 kg·d) to improve the published EDELWEISS-II low mass limit (113 kg·d)[16]. The experimental sensitivity will further increase by pushing the analysis in two directions: increasing the available statistics by combining several detectors and decreasing the analysis threshold in order to improve the sensitivity to very low mass WIMPs (< 5 GeV/c^2).

Acknowledgments

The help of the technical staff of the Laboratoire Souterrain de Modane and the participant laboratories is gratefully acknowledged. The EDELWEISS project is supported in part by the German ministry of science and education (BMBF Verbundforschung ATP Proj.-Nr.05A14VKA), by the Helmholtz Alliance for Astroparticle Phyics (HAP), by the French Agence Nationale pour la Recherche and the Labex Lyon Institute of Origins (ANR-10-LABX-0066) of the Université de Lyon within the program Investissement d'Avenir (ANR-11-IDEX-00007), by Science and Technology Facilities Council (UK) and the Russian Foundation for Basic Research (grant No. 07-02-00355-a).

References

[1] P. Ade *et al.*, arXiv:1502.01589(2015).

[2] P. Gondolo, "Theory of low mass WIMPs: Light dark matter Weakly-interacting 2-10 GeV/c2 mass", Dark Matter Conference, UCLA 2012

[3] B. Schmidt *et al.*, Astroparticle Physics 44, 28 **39** (2013).

[4] S. Scorza *et al.*, LRT conferencce (2015), AIP Conference Proceedings, vol. **1672** (2015).

[5] A. Juillard *et al.*, LTD16 conference (2015) to be published.

[6] R. Bernabei *et al.*, Eur. Phys. J. C67, 39(2010).

[7] C. Savage, G. Gelmini, P. Gondolo, and K. Freese, J. Cosmol. Astropart. P. **0904**, 010(2009).

[8] G. Angloher *et al.*, Eur. Phys. J. C **72**, 1(2012).

[9] C. E. Aalseth *et al.*, Phys. Rev. D **88**, 012002(2013).

[10] R. Agnese *et al.*, Phys. Rev. Lett. (2013), arXiv:1304.4279[hep-ex].

[11] D. Hooper and T. R. Slatyer, (2013), arXiv:1302.6589[astro-ph.HE].

[12] Th. Main de la Boissière , PhD Thesis Université Paris Sud, July 3rd 2015, to be published in https://tel.archives-ouvertes.fr

[13] Th. Main de la Boissière , "Low mass WIMP searc with EDELWEISS-III: first results", Moriond 2015 proceedings.

[14] Q. Dong *et al.*, Appl. Phys. Lett. **105**,013504(2014)

[15] A. Broniatovski *et al.*, "Voltage-assisted calorimetric detection of gamma interactions in cryogenic Ge detectors for dark matter search", LTD16 conference (2015) to be published.

[16] E. Armengaud *et al.*, Phys. Rev. D **86**, 2012.

ALP Hints from Cooling Anomalies

Maurizio Giannotti

Barry University, Miami Shores, US

DOI: http://dx.doi.org/10.3204/DESY-PROC-2015-02/giannotti_maurizio

We review the current status of the anomalies in stellar cooling and argue that, among the new physics candidates, an axion-like particle would represent the best option to account for the hinted additional cooling.

1 Introduction

For over two decades, observations of different stellar systems have shown deviations from the expected behavior, indicating in all cases an over-efficient cooling.

Statistically, each of these anomalies is not very significant. Taken together, however, they do seem to suggest the possibility of a common systematic problem in the modeling of the stellar evolution, in particular of the cooling mechanisms.

Is this a hint of physics beyond the Standard Model? If so, what kind of new physics? As we shall see, among the various options the axion, or Axion-Like-Particle (ALP), solution is the most appealing and, in fact, the one most frequently considered in the past.

The axion [1, 2] is a light pseudoscalar particle predicted by the most widely accepted solution of the strong CP problem [3, 4] and a prominent dark matter candidate [5, 6, 7]. Its interactions with photons and fermions are described by the Lagrangian terms

$$L_{\rm int} = -\frac{1}{4} g_{a\gamma}\, a F_{\mu\nu} \tilde{F}^{\mu\nu} - \sum_{\rm fermions} g_{ai}\, a \overline{\psi}_i \gamma_5 \psi_i \,, \tag{1}$$

where $g_{a\gamma} = C_\gamma \alpha / 2\pi f_a$ and $g_{ai} = C_i m_i / f_a$, with C_γ and C_i model-dependent parameters and f_a a phenomenological scale known as the Peccei-Quinn symmetry breaking scale.

Moreover, in the so called QCD axion models, mass and interaction scale (Peccei-Quinn constant) are related as $(m_a/1\ \text{eV}) = 6 \times 10^6 \text{GeV}/f_a$. This describes a band (the width given by the possible values of the model dependent parameters) in the mass-coupling (e.g., to photons) parameter space, known as the QCD axion line. Belonging to this band, however, is not a requirement for the solution of the strong CP problem [8, 9, 10].

More general models of pseudoscalar particles, known as ALPs, which couple to photons (and, possibly, to fermions) but do not satisfy the above mass-coupling relation, emerge naturally in various extensions of the Standard Model though, in general, their existence is not related to the strong CP problem [11].

If appropriately coupled to electrons, photons, and nucleons, ALPs could explain the stellar cooling anomalies. Additionally, light ALPs have been invoked to explain other astrophysical anomalies, such as the seeming transparency of the universe to very high energy (TeV) gamma rays in the galactic and extragalactic medium [12] and some anomalous redshift-dependence of

AGN gamma-ray spectra [13] (though this last hypothesis currently shows some conflict with the SN bound on the axion-photon coupling [14]). More recently, it was also pointed out that anomalous X-ray observations of the active Sun suggest an ALP-photon coupling [15] of the same size hinted by the other analyses.

Interestingly, the required couplings are not excluded by experiments nor by phenomenological considerations and are accessible to the new generation ALP detectors, in particular ALPS II [16] and the International Axion Observatory (IAXO) [17, 18].

2 Observational anomalies is stellar cooling and ALPs

2.1 White dwarfs

For over two decades, observations of the period decrease ($\dot{P}/P$) of particular white dwarf (WD) variables have shown discrepancies (at 1σ) with the expected behavior. In particular, all the variables studied (two pulsating DA WDs, G117-B15A [19, 20] and R548 [21], and one pulsating DB WD, PG 1351+489 [22]) show an unexpectedly fast cooling ($\dot{P}/P$ is practically proportional to the cooling rate $\dot{T}/T$), suggesting the possibility of additional energy loss channels. The results from the two DA WD show a preference for an axion coupled to electrons with $g_{ae} \simeq 4.8 \times 10^{-13}$ [19, 21] (see Fig. 1). The no-axion solution is recovered at 2σ.

Additionally, various studies of the WD luminosity function (WDLF), which represents the WD number density per brightness interval, also seem to indicate a preference for an additional cooling channel and, in particular, for an axion-electron coupling $g_{ae} \simeq (1.4 \pm 0.3) \times 10^{-13}$ (at 1σ) [23]. A more recent study of the hot part of the WDLF [24] did not confirm this anomalous behavior. However, the hotter section of the WDLF has much larger observational errors and the ALP production would be almost completely hidden by standard neutrino cooling in the hottest WDs.

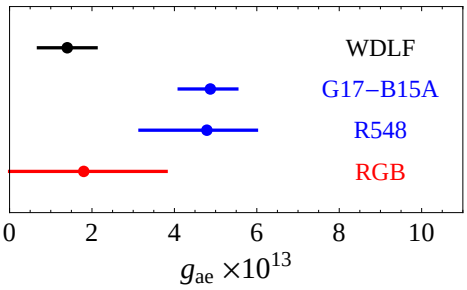

Figure 1: Summary of hints on the ALP-electron coupling from WD and RGB stars (at 1σ).

It should also be noted that the hints on the axion-electron coupling from the WDLF and the WD pulsation disagree at 1σ indicating, perhaps, an underestimate of the errors. In particular, the results from the pulsating WDs are based on assumptions on the analyzed oscillating mode that should be independently verified (see, e.g., discussion in [23]).

2.2 Red giants

Further hints to anomalous energy loss in stars emerge from the recent analysis of the Red Giant Branch (RGB) stars in [25, 26]. This showed a brighter than expected tip of the RG branch in the M5 globular cluster, indicating a somewhat over-efficient cooling during the evolutionary phase preceding the helium flash.

The anomalous brightness, $\Delta M_{I,\mathrm{tip}} \simeq 0.2$ mag in absolute $I-$band magnitude, is within the calculated observational and modeling errors, which include uncertainties in the mass loss,

treatment of convection, equation of state and cluster distance. However, the error budget seems to just barely compensate for the difference between observed and expected brightness. A better agreement would require an anomalous cooling of a few 10^{33} erg/s, which could be accounted for by a neutrino magnetic moment $\mu_\nu \sim (1-2)\times 10^{-12}\mu_{\rm B}$ [25], where $\mu_{\rm B}$ is the Bohr magneton, or an axion-electron coupling $g_{ae} \sim (1-2)\times 10^{-13}$ [26].

A reduction of the uncertainties, particularly a better determination of the cluster distance, which may become possible with the GAIA mission, will certainly help clarifying the physical significance of this discrepancy.

2.3 Horizontal branch stars

A recent analysis [27] showed a mild disagreement (at 1σ) between the observed and the expected R-parameter, $R = N_{\rm HB}/N_{\rm RGB}$, which compares the numbers of stars in the horizontal branch (HB) ($N_{\rm HB}$) and in the upper portion of the RGB ($N_{\rm RGB}$). More specifically, the observed value, $R = 1.39 \pm 0.03$ is somewhat smaller than the expected one $1.44 \leq R \leq 1.50$.

The higher than expected value of R indicates a surplus of HB stars with respect to RGB in the examined clusters, suggesting that HB stars are cooling more efficiently, and therefore are less numerous, than expected.

This result may be due to an ALP coupled to photons with $g_{a\gamma} = (0.29-0.57)\times 10^{-10}{\rm GeV}^{-1}$. A more recent analysis (see [28]) indicates a slightly smaller value for the hinted coupling but preserves the discrepancy at the 1σ level.

2.4 Massive He-burning stars

Another long standing puzzle is the smaller than predicted number ratio of blue over red supergiants in open clusters (see [29] and references therein).

Stars of mass a few times larger than the Sun, during their helium burning stage evolve from red (cold) to blue (hot) and back. This journey is called the blue loop and is very sensitive to the microphysics governing the stellar evolution, in particular its cooling mechanism. The observation of less blue stars indicates a shorter than expected blue stage, which can be attributed to a more efficient than expected cooling of the core [30, 31, 32].

The analysis in [30] indicated that an axion-photon coupling of a few $10^{11}{\rm GeV}^{-1}$, in the same range as the one hinted by the HB anomaly, would reduce the number of expected blue stars, alleviating or perhaps solving the anomaly. However, in this case the uncertainties in the microphysics and in the observations are, essentially, unquantifiable.

2.5 Neutron stars

Finally, X-rays observations of the surface temperature of a neutron star in Cassiopeia A also showed a cooling rate considerably faster than expected. The effect may be interpreted in terms of an axion-nucleon coupling of the order of $g_{an} \sim 4\times 10^{-10}$ [33].

However, the uncertainties in the physics of neutron stars cooling make this only a marginal hint. Indeed, the effect could have a different origin, for example as a phase transition of the neutron condensate into a multicomponent state [34].

3 Is this an ALP?

Among the *new physics* explanations, the existence of ALPs is the most appealing and the most frequently invoked. To explain the cooling anomalies, ALPs should couple to photons and fermions, as in Eq. (1) with, for example, $f_a \simeq 10^7$GeV, $C_\gamma \sim 1$ and $C_e \sim C_n \sim 10^{-2}$ [35].

A study (in preparation) shows that none of the other common candidates can explain the combined observed deviations from the standard cooling of the diverse stellar systems. In particular, an anomalous neutrino magnetic moment has essentially no effects on the WDLF [36]. Moreover, even if equipped with a magnetic moment as large as the currently allowed by experimental limits and astrophysical observations, neutrinos would not be effectively produced in low density stars, such as HB or massive He burning stars.

Analogously, preliminary results show that the regions of the hidden photon (HP) parameter space necessary to explain the HB and RGB anomalies do not overlap and the region in which HP could reconcile the WDLF observations is phenomenologically excluded.

4 Summary and conclusion

Numerous independent observations seem to indicate an excessive energy loss in several stellar system. The combination of the anomalous observations of WD, RG and HB stars, strongly favors ALPs with respect to other possible candidates.

Additionally, ALPs have been invoked for the solution of other unexplained astrophysical observations. Most importantly, the quest for dark matter, of which the axion provides an excellent candidate (see [37]). Additionally, a light ALP coupled to photons has been proposed to explain observations of the seeming transparency of the universe to very high-energy gamma-rays and an anomalous redshift-dependence of AGN gamma-ray spectra.

Remarkably, the most important section of the hinted ALP parameter space could be investigated with the next generation of axion detectors. A discovery of an ALP in the parameter region discussed would be revolutionary not only for particle physics and probably for cosmology, but also for TeV gamma ray astronomy and for stellar evolution.

References

[1] S. Weinberg, Phys. Rev. Lett. **40**, 223 (1978).

[2] F. Wilczek, Phys. Rev. Lett. **40**, 279 (1978).

[3] R. D. Peccei and H. R. Quinn, Phys. Rev. Lett. **38**, 1440 (1977).

[4] R. D. Peccei and H. R. Quinn, Phys. Rev. D **16**, 1791 (1977).

[5] L. F. Abbott and P. Sikivie, Phys. Lett. B **120**, 133 (1983).

[6] M. Dine and W. Fischler, Phys. Lett. B **120**, 137 (1983).

[7] J. Preskill, M. B. Wise and F. Wilczek, Phys. Lett. B **120**, 127 (1983).

[8] V. A. Rubakov, JETP Lett. **65**, 621 (1997) [hep-ph/9703409].

[9] Z. Berezhiani, L. Gianfagna and M. Giannotti, Phys. Lett. B **500**, 286 (2001) [hep-ph/0009290].

[10] L. Gianfagna, M. Giannotti and F. Nesti, JHEP **0410**, 044 (2004) [hep-ph/0409185].

[11] A. Ringwald, Phys. Dark Univ. **1**, 116 (2012) [arXiv:1210.5081 [hep-ph]].

[12] D. Horns and M. Meyer, JCAP **1202**, 033 (2012) [arXiv:1201.4711 [astro-ph.CO]].

[13] G. Galanti, M. Roncadelli, A. De Angelis and G. F. Bignami, arXiv:1503.04436 [astro-ph.HE].

[14] A. Payez, C. Evoli, T. Fischer, M. Giannotti, A. Mirizzi and A. Ringwald, JCAP **1502**, no. 02, 006 (2015) [arXiv:1410.3747 [astro-ph.HE]].

[15] V. D. Rusov, M. V. Eingorn, I. V. Sharph, V. P. Smolyar and M. E. Beglaryan, [arXiv:1508.03836 [astro-ph.SR]].

[16] R. Bahre *et al.*, JINST **8**, T09001 (2013) [arXiv:1302.5647 [physics.ins-det]].

[17] I. G. Irastorza, F. T. Avignone, S. Caspi, J. M. Carmona, T. Dafni, M. Davenport, A. Dudarev and G. Fanourakis *et al.*, JCAP **1106**, 013 (2011) [arXiv:1103.5334 [hep-ex]].

[18] J. K. Vogel *et al.*, arXiv:1302.3273 [physics.ins-det].

[19] A. H. Corsico, L. G. Althaus, M. M. M. Bertolami, A. D. Romero, E. Garcia-Berro, J. Isern and S. O. Kepler, Mon. Not. Roy. Astron. Soc. **424**, 2792 (2012) [arXiv:1205.6180 [astro-ph.SR]].

[20] A. Bischoff-Kim, M. H. Montgomery and D. E. Winget, Astrophys. J. **675**, 1512 (2008) [arXiv:0711.2041 [astro-ph]].

[21] A. H. Corsico, L. G. Althaus, A. D. Romero, A. S. Mukadam, E. Garcia-Berro, J. Isern, S. O. Kepler and M. A. Corti, JCAP **1212**, 010 (2012) [arXiv:1211.3389 [astro-ph.SR]].

[22] A. H. Crsico, L. G. Althaus, M. M. Miller Bertolami, S. O. Kepler and E. Garca-Berro, JCAP **1408**, 054 (2014) [arXiv:1406.6034 [astro-ph.SR]].

[23] M. M. Miller Bertolami, B. E. Melendez, L. G. Althaus and J. Isern, JCAP **1410**, no. 10, 069 (2014) [arXiv:1406.7712 [hep-ph]].

[24] B. Hansen, H. Richer, J. Kalirai, R. Goldsbury, S. Frewen and J. Heyl, arXiv:1507.05665 [astro-ph.SR].

[25] N. Viaux, M. Catelan, P. B. Stetson, G. Raffelt, J. Redondo, A. A. R. Valcarce and A. Weiss, Astron. Astrophys. **558**, A12 (2013) [arXiv:1308.4627 [astro-ph.SR]].

[26] N. Viaux, M. Catelan, P. B. Stetson, G. Raffelt, J. Redondo, A. A. R. Valcarce and A. Weiss, Phys. Rev. Lett. **111**, 231301 (2013) [arXiv:1311.1669 [astro-ph.SR]].

[27] A. Ayala, I. Dominguez, M. Giannotti, A. Mirizzi and O. Straniero, Phys. Rev. Lett. **113**, 191302 (2014) [arXiv:1406.6053 [astro-ph.SR]].

[28] O. Straniero, in these proceedings.

[29] K. B. W. McQuinn, E. D. Skillman, J. J. Dalcanton, A. E. Dolphin, J. Holtzman, D. R. Weisz and B. F. Williams, Astrophys. J. **740**, 48 (2011) [arXiv:1108.1405 [astro-ph.CO]].

[30] A. Friedland, M. Giannotti and M. Wise, Phys. Rev. Lett. **110**, 061101 (2013) [arXiv:1210.1271 [hep-ph]].

[31] G. Carosi, A. Friedland, M. Giannotti, M. J. Pivovaroff, J. Ruz and J. K. Vogel, arXiv:1309.7035 [hep-ph].

[32] M. Giannotti, arXiv:1409.7981 [astro-ph.HE].

[33] L. B. Leinson, JCAP **1408**, 031 (2014) [arXiv:1405.6873 [hep-ph]].

[34] L. B. Leinson, Phys. Lett. B **741**, 87 (2015) [arXiv:1411.6833 [astro-ph.SR]].

[35] A. Ringwald, arXiv:1506.04259 [hep-ph].

[36] M. M. Miller Bertolami, Astron. Astrophys. **562**, A123 (2014) [arXiv:1407.1404 [hep-ph]].

[37] P. Sikivie, in these proceedings.

Any Light Particle Search II - Status Overview

Noëmie Bastidon for the ALPS II collaboration

University of Hamburg, Hamburg, Germany

DOI: http://dx.doi.org/10.3204/DESY-PROC-2015-02/bastidon_noemie_talk

The Any Light Particle Search II (ALPS II) experiment (DESY, Hamburg) searches for photon oscillations into Weakly Interacting Sub-eV Particles (WISPs). This second generation of the ALPS light-shining-through-a-wall (LSW) experiment approaches the finalization of the preparation phase before ALPS IIa (search for hidden photons). In the last years, efforts have been put for the setting up of two optical cavities as well as the characterization of a single-photon Transition-Edge Sensor (TES) detector. In the following, we put some emphasis on the detector development. In parallel, the setting up of ALPS IIc (search for axion-like particles), including the unbending of 20 HERA dipoles, has been pursued. The latest progress in these tasks will be discussed.

1 Introduction

The Any Light Particle Search II (ALPS II) experiment (DESY, Hamburg) searches for photon oscillations into light fundamental bosons (e.g., axion-like particles, hidden photons and other WISPs) by shining light through a wall [1]. The aimed sensitivity increase for the coupling strength of axion-like particles to photons of the experiment is of a factor of 3000 compared to ALPS I. Such an improvement is due to the increase of the magnets' length, to two optical cavities as well as to the replacement of the single-photon detector. Indeed, the ALPS experiment sensitivity to the conversion of photons into axion-like particles depends on various parameters and is expressed as

$$S(g_{a\mu}) \quad \propto \quad (\frac{1}{BL})(\frac{DC}{T})^{\frac{1}{8}}(\frac{1}{\eta \dot{N}_{\mathrm{Pr}} \beta_{\mathrm{PC}} \beta_{\mathrm{RC}}})^{\frac{1}{4}}$$

with a strong dependency on the magnetic length L and field B. The effect of the optical setup depends on $\dot{N}_{\mathrm{Pr}}$, the number of injected photons as well as on β_{PC} and β_{RC}, the power build-ups of the production (PC) and regeneration cavities (RC). Finally, the reached sensitivity depends on the chosen detector's detection efficiency η and dark current (DC). The data-taking time is expressed as T. In the last years, preparation work has demonstrated the basics of the setup.

2 Optics

The ALPS IIa (search for hidden photons) optical setup includes two 10 m optical cavities separated by a ligth-tight barrier. A 30 W 1064 nm laser is injected inside the first cavity (Fig. 1). Such a system is technically challenging for two reasons: first, an alignment of both cavities

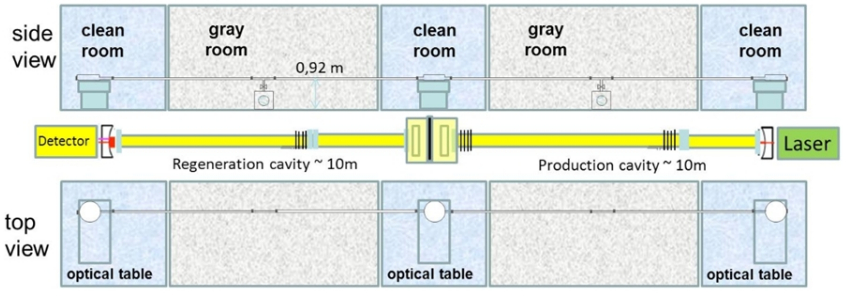

Figure 1: The ALPS IIa experiment.

towards each other is necessary to provide a larger spatial overlap of the modes resonating in both cavities. Second, high power buildups (PB) are required for both cavities in order to reach the ALPS IIa foreseen sensitivity. The aimed PB of the production cavity is of 5 000 and the regeneration cavity PB is of 40 000. In order to maximise this feature, the PC and RC need to be in the same modal phase with a mode-overlap of 95 %. The regeneration cavity is locked via an auxiliary green beam obtained via second harmonic generation (KTP crystal) of the PC infrared beam [2]. Latest tests showed a lower PB than required for the production cavity. Possible sources of such issues are the mirrors' coating, cleanliness of the mirrors, alignment of the cavity as well as a clipping in the beam pipes. Usage of a cavity ring-down technique demonstrated a good quality of the mirrors [3]. Measurements will be repeated with a larger beam radius in order to enlarge the tested region on the mirrors surface.

3 Coupling of the beam inside a fiber

The regeneration cavity will be connected via a fiber to a single-photon detector in order to detect possible regenerated photons. Efficient coupling of a 4.23 mm beam inside a 8.2 μm single-mode fiber is feasible but its stability over loner timescales still needs to be demonstrated.

The coupling of the beam inside a fiber setup includes two mirrors as well as an aspheric lens (Fig. 2). In the test setup, a class 1 $\lambda = 1064$ nm laser is shone to a mirror setup before being focused inside a standard single-mode fiber. It has been shown that the efficiency of the coupling depends highly on the alignement of the setup and on the focal length of the used lens (Fig. 2). During the preliminary tests, an efficiency higher than 80% was reached. The highest value for the final setup which has been currently obtained is of 53% for a focal length of 35 mm. This value is lower than what was expected for such a lens. In the near future, the beam quality will be studied with a knife-edge unit. Such a device allows the characterization and adjustement of the beam on micrometer-scale before it enters the fiber.

4 Detector

The detection of a low rate (one event every few hours) of low energetic (1.17 eV) photons requires both a high detection efficiency as well as a low dark count rate. Additionally, the ALPS II detection system is required to have a good energy and time resolution as well as a good long-term stability. To meet all of these criteria, the ALPS II setup includes a cryogenic

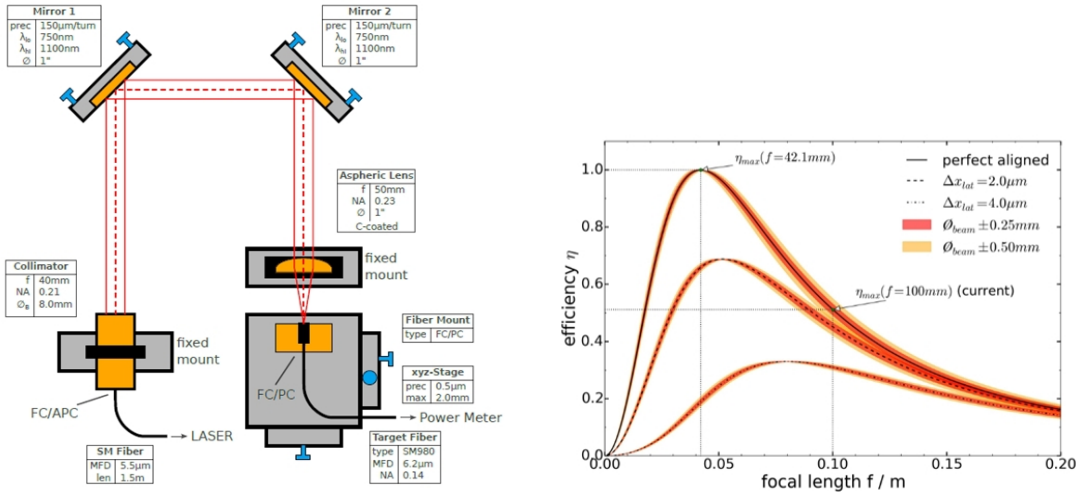

Figure 2: Coupling of the beam. On the left, a drawing of the coupling of the beam test setup. On the right, the theoretical efficiency of the coupling values η for different levels of alignment $\Delta\, x_{tot}$ and for different focal length f.

detector of the transition edge type (TES) developed by NIST (National Institute of Standard and Technology) [4].

Transition-Edge Sensors are superconductive microcalorimeters measuring the temperature difference ΔT induced by the absorption of a photon with R(T, I). The detector is positioned within its superconductive transition (TES set point corresponds to 30% of its normal resistance) through a thermal link to a heat bath at $T_b = 80mK$ and by applying a constant bias voltage accrss the TES. In order to obtain the cool-down of the detector, it is placed in an adiabatic demagnetization refrigerator (ADR) [5].

The ALPS detector module includes two TESs inductively coupled to a SQUID (Superconducting Quantum Interference Device). The ALPS detectors are optimized for 1064 nm photons. The sensitive area of each chip measures 25 x 25 μm^2 for a thickness of 20 nm. The substrate is surrounded by a standard fiber ceramic sleeve allowing connection of a single mode fiber ferrule [6].

NIST has demonstrated that such a detector can reach quantum efficiency higher than 95 % [7]. Latest measurements of the ALPS II detector efficiency led to a first approximation of 30 %. Optimization work is currently under progress.

5 ALPS IIc

The ALPS IIc experiment will allow the search for axion-like particles (ALPs). It is constituted in the same way as ALPS IIa with two 100 m cavities and the addition of 20 HERA (Hadron-Electron Ring Accelerator) dipoles [1] to allow the conversion of photons into ALPs and reconversion. The HERA dipoles were all bent during their design, leading to a small aperture of 35 mm. It was foreseen to unbend all of the dipoles by applying a force in their middle (cold

mass). The deformation of the first magnet was successful, yielding to an aperture of 50 mm allowing to set up the 100 m long cavities without any aperture limitations. The magnet is working according to its specifications with a slight increase of its quench current. Efforts to straighten further magnets are on-going.

6 Summary

The ALPS II experiment aims at an improvement of sensitivity by a factor of 3 000 compared to ALPS I for the coupling of axion-like particles to photons. This improvement is achieved mainly by implementing a regeneration cavity and a larger magnetic length. Basics of the optics setup have been demonstrated but not all of the specifications have been reached yet. A Tungsten Transition-Edge Sensor operated below 100 mK has been successfully used to detect single-photons in the near-infrared.

Acknowledgments

The author would like to thank all the members of the ALPS collaboration. The author also thanks the PIER Helmholtz Graduate School for their financial travel support.

References

[1] R. Bähre *et al.*, "Any light particle search II Technical Design Report," JINST **8** T09001 (2013) [arXiv:1302.5647v2 [hep-ex]].

[2] R. Hodajerdi, "Production Cavity and Central Optics for a Light Shining through a Wall Experiment," ISBN 1435-8085 (2015)

[3] T. Isogai *et al.*, "Loss in long-storage-time optical cavities," Optics Express **21**(24) 30114 (2013) [arXiv:1310.1820v2 [hep-ex]]

[4] N. Bastidon, D. Horns, A. Lindner, "Characterization of a Transition-Edge Sensor for the ALPS II Experiment," these proceedings (2015)

[5] G. K. White, P. J. Meeson, "Experimental techniques in low-temperature physics," Fourth Edition, Oxford University Press, (2002).

[6] J. Dreyling-Eschweiler *et al.*, "Characterization, 1064 nm photon signals and background events of a tungsten TES detector for the ALPS experiment," J. Mod. Opt. **62**, 14 (2005) [arXiv:1502.07878 [hep-ex]].

[7] A. E. Lita, A. J. Miller and S. W. Nam, "Counting near-infrared single-photons with 95% efficiency," Optics express **16**, 5 (2008).

Using an InGrid Detector to Search for Solar Chameleons with CAST

Klaus Desch, Jochen Kaminski, Christoph Krieger, Michael Lupberger

University of Bonn, Bonn, Germany

DOI: http://dx.doi.org/10.3204/DESY-PROC-2015-02/desch_klaus

We report on the construction, operation experience, and preliminary background measurements of an InGrid detector, i.e. a MicroMegas detector with CMOS pixel readout. The detector was mounted in the focal plane of the Abrixas X-Ray telescope at the CAST experiment at CERN. The detector is sensitive to soft X-Rays in a broad energy range (0.3–10) keV and thus enables the search for solar chameleons. Smooth detector operation during CAST data taking in autumn 2014 has been achieved. A preliminary analysis of background data indicates a background rate of $(1\text{–}5)\times10^{-5}$ keV^{-1}cm^{-2}s^{-1} above 2 keV and $\sim 3\times10^{-4}$ keV^{-1}cm^{-2}s^{-1} around 1 keV. An expected limit of $\beta_\gamma \lesssim 5\times10^{10}$ on the chameleon photon coupling is estimated in case of absence of an excess in solar tracking data. We also discuss the prospects for future operation of the detector.

1 The CAST experiment

The CERN Axion Solar Telescope (CAST) [1] is operating since 2003 in search for the emission of axions from the Sun through their conversion into soft X-Ray photons in the strong magnetic field of an LHC dipole prototype magnet. The experiment has been setting the strongest bounds on solar axion production to date [2]. More recently, CAST is extending its scope, making use of the versatility of the experimental setup. These extensions include the search for solar chameleons both through their coupling to photons [3] and through their coupling to matter [4] as well as the search for relic axions exploiting resonant microwave cavities immersed into the magnetic field [5]. In these proceedings we report about the progress in the search for solar chameleons using an InGrid detector, extending the preliminary results reported at the 2014 Axion-WIMP workshop [6].

2 Solar Chameleons

The observation of a non-vanishing cosmological constant, dubbed Dark Energy (DE), is arguably one of the greatest mysteries of modern physics. There exist only very few particle physics approaches to explain DE. The observed accelerated expansion of the universe may be explained by the existence of a scalar field. One such scenario is the so-called chameleon for which a low-energy effective theory has been formulated [7]. The chameleon field acquires an effective mass through a screening potential which establishes a non-zero vacuum expectation value depending on the surrounding matter density. The screening potential assures the

suppression of measurable fifth force effects and leads to a chameleon mass which depends on the ambient matter density. Chameleons, similar to axions, can be created via the Primakoff effect in strong electro-magnetic fields present in the Sun and observed on Earth through their back-conversion into detectable X-ray photons within a strong magnetic field via the inverse Primakoff effect. The energy of the photons is essentially equivalent to the chameleons' thermal energy during their production in the Sun. While axions may be created in the core of the Sun with a spectral maximum at approximately 3 keV, chameleons are predicted to be created in the solar tachocline [8] around 0.7 $R_\odot$ where intense magnetic fields are present. Thus, they are produced at lower temperature corresponding to a spectral maximum of only 600 eV, requiring photon detectors with sub-keV sensitivity. An initial search for solar chameleons with CAST has been conducted using a Silicon Drift Detector [3].

3 InGrid Detector

An InGrid ("Integrated Grid") is a gas-amplification device based on the MicroMegas principle. A thin aluminum mesh is mounted approximately 50 μm above a CMOS pixel chip, in our case the TimePix ASIC [9], via photolithographic wafer post-processing techniques [10]. The input pads of the pixels' charge-sensitive amplifiers serve as charge-collecting anodes and the collected charged is amplified and processed digitally in-situ. The pixel pitch is 55×55 μm^2. With this fine pitch, a typical gas amplification of ~ 3000 and a detection threshold of $\lesssim 1000$ electrons, a single electron efficiency $> 95\%$ is achieved. Given the diffusion of the ionization electrons from the photo electron, this allows for the counting of the total number of created electrons on the pixel chip and yields a direct measure of the energy, free of fluctuations in the amplification region. As the range of the photoelectron in the detector gas (97.7% Argon, 2.3% Isobutane) is only a few hundred microns, the image of an absorbed photon is an essentially circular cloud of hit pixels, where the cloud radius decreases with the absorption depth of the photon. This pattern provides an effective template which differs significantly from charged particle background (e.g. cosmic muons or electrons from β-decay) which produces typically a track-like pattern on the pixel chip. These differences are exploited to provide a powerful topological background suppression. The detector and its installation in CAST is explained in more detail in [6, 11] where also sensitivity of the detector down to below 300 eV has been demonstrated.

4 Results and Prospects

In autumn 2014, the detector has, for the first time, been taking data on 27 consective days including 1.5 h of daily solar tracking. While the solar tracking data are still blinded, the in-situ background data are being analysed using a simple three-variable likelihood for the photon hypothesis. In comparison to [6], the likelihood has been further tuned to reduce energy-dependent biases. A preliminary background spectrum is shown in Fig. 1. In the region above 2 keV two peaks around 3 keV and 8 keV are visible. The former corresponds to the known flourescence line of Argon while the latter is likely a superposition of Copper flourescence and cosmic tracks which traverse the detector parallel to the drift field. Such cosmics produce a m.i.p. signal which, due to the track's direction, is difficult to distinguish from a photon via topological supression alone. Outside these peaks, the background level is around $(1\text{–}2)\times10^{-5}$ $\mathrm{keV}^{-1}\mathrm{cm}^{-2}\mathrm{s}^{-1}$. There is a notable increase in background for energies

below 2 keV, reaching $\sim 3 \times 10^{-4}$ keV^{-1}cm^{-2}s^{-1} around 1 keV. The origin of this background needs further study.

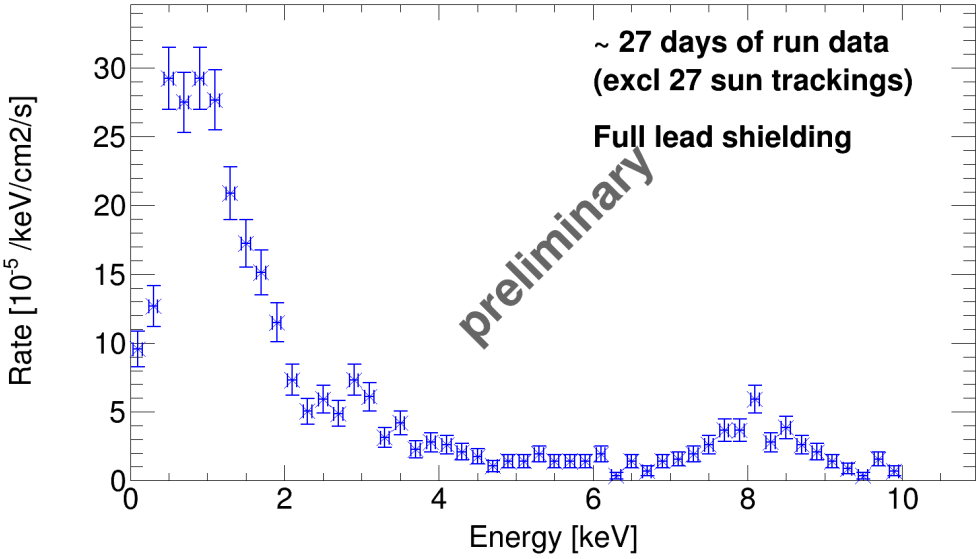

Figure 1: Preliminary background rate of InGrid Detector during operation in CAST in autumn 2014.

While the solar tracking data of the 2014 run have not yet been analyzed, one can already estimate an expected limit in case of non-observation of an excess. Our estimates are based on scaling the limit of the SDD detector [3] and accounting for scaling factors in exposure time, effective sensitive area, background, and efficiency. In Fig. 2 the estimated expected limit of the chameleon-photon coupling, β_γ, from the InGrid detector is shown together with the observed SDD limit and other experimental and astrophysical constraints. It can be seen that the 2014 InGrid data have the potential to set a limit $\beta_\gamma \lesssim 5 \times 10^{10}$, improving the SDD limit by almost a factor two under the same model assumptions as given in [3]. Also shown are prospects for data taking in 2015 and 2016. At the time of writing, the detector has been continously taking data in the 2015 CAST run using the same setup as in 2014. Further improvements in background suppression (external cosmic veto, additional readout of the grid signal) and photon detector efficiency (through thinner X ray windows) as well as improvements in the software rejection of background are currently being developed and will be implemented step-wise. Rough estimates for the potential of these improvements yield expected exclusions are also shown in Fig. 2.

Acknowledgments

We thank the organizers of the Axion-WIMP-Workshop 2015 for an exciting conference and their warm hospitality.

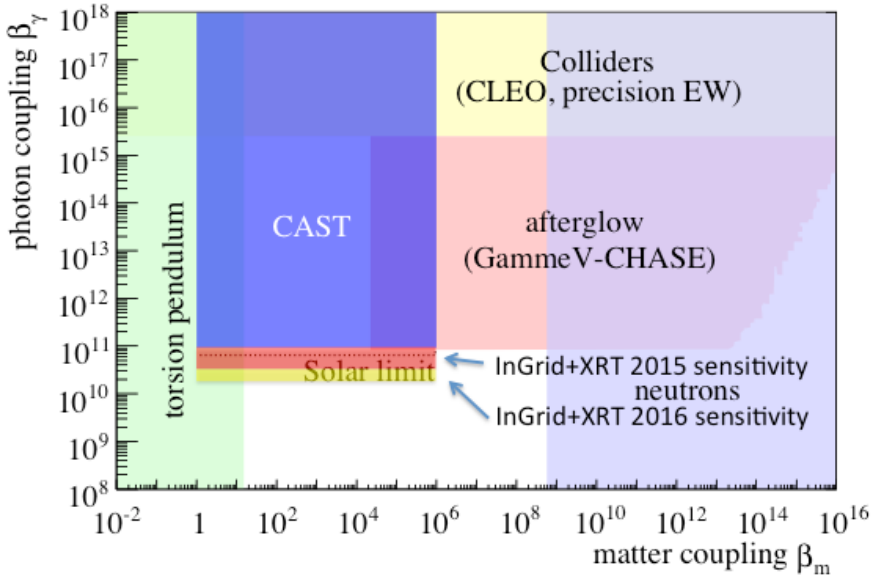

Figure 2: Exclusions in the plane of chameleon-matter coupling β_m vs. chameleon-photon coupling β_γ. Figure from [3] and modified to include InGrid detector prospects.

5 Bibliography

References

[1] K. Zioutas *et al.*, Nucl. Instrum. Meth. A **425**, 480 (1999) [astro-ph/9801176].

[2] M. Arik *et al.* [CAST Collaboration], Phys. Rev. Lett. **112**, 091302 (2014) [arXiv:1307.1985 [hep-ex]].

[3] V. Anastassopoulos *et al.* [CAST Collaboration], Phys. Lett. B **749**, 172-180 (2015) [arXiv:1503.04561 [astro-ph.SR]].

[4] G. Cantatore, these proceedings.

[5] L. Miceli, these proceedings.

[6] C. Krieger, K. Desch, J. Kaminski, M. Lupberger and T. Vafeiadis, arXiv:1410.0264 [physics.ins-det].

[7] J. Khoury and A. Weltman, Phys. Rev. Lett. **93**, 171104 (2004) [astro-ph/0309300] and Phys. Rev. D **69**, 044026 (2004) [astro-ph/0309411]; P. Brax, C. van de Bruck, A. C. Davis, J. Khoury and A. Weltman, Phys. Rev. D **70**, 123518 (2004) [astro-ph/0408415].

[8] P. Brax and K. Zioutas, Phys. Rev. D **82**, 043007 (2010) [arXiv:1004.1846 [astro-ph.SR]].

[9] X. Llopart *et al.*, Nucl. Instrum. Meth. **A 581**, 485-494 (2007).

[10] M. Chefdeville *et al.*, Nucl. Instrum. Meth. **A 556**, 490-494 (2006) ; T. Krautscheid, Y. Bilevych, K. Desch, J. Kaminski, C. Krieger, M. Lupberger and F. Mller, Nucl. Instrum. Meth. A **718**, 391 (2013) .

[11] C. Krieger, J. Kaminski and K. Desch, Nucl. Instrum. Meth. A **729**, 905 (2013).

Theoretical Prospects for Directional WIMP Detection

Ciaran A. J. O'Hare[1], *Julien Billard*[2], *Enectali Figueroa-Feliciano*[3], *Anne M. Green*[1], *Louis E. Strigari*[4]

[1]University of Nottingham, UK
[2]IPNL, Université de Lyon, France
[3]Massachusetts Institute of Technology, Cambridge, MA, USA
[4]Texas A & M University, College Station, TX, USA

DOI: http://dx.doi.org/10.3204/DESY-PROC-2015-02/ohare_ciaran

Direct detection of dark matter with directional sensitivity is a promising concept for improving the search for weakly interacting massive particles. With information on the direction of WIMP induced nuclear recoils one has access to the full 3-dimensional velocity distribution of the local dark matter halo and thus a potential avenue for studying WIMP astrophysics. Furthermore the unique angular signature of the WIMP recoil distribution provides a crucial discriminant from neutrinos which currently represent the ultimate background to direct detection experiments.

1 Introduction

The search for WIMPs by direct detection has in principle a strong directional signature. The motion of the Solar system within the non-rotating dark matter halo of the Milky Way gives rise to an apparent wind of WIMPs coming from a particular direction in the sky aligned with the constellation of Cygnus. The detection of the direction of laboratory-based nuclear recoils consistent with this predicted direction would hence be a smoking gun for the scattering of a particle with Galactic origin. If achievable at the scale of current non-directional experiments, directional detection would not only provide another way of making competitive exclusion limits on the WIMP parameter space but also for the discovery of an unequivocal WIMP signal [1]. Beyond this, directional detection is also a novel technique for studying the astrophysics of WIMPs as it probes the full local velocity distribution; without directional information one only has access to the 1-dimensional speed distribution.

Another area in which directional detection is promising is in the subtraction of the encroaching "irreducible background" due to coherent neutrino-nucleus scattering (CNS). For example a 1 keV threshold Xenon detector with a mass of 1 ton operated for a year will detect around 100 neutrino events from ^{8}B decay in the Solar core. Given that neutrinos cannot be shielded they represent the ultimate background to WIMP direct detection experiments. The limiting cross-section at which the neutrino background becomes important is known as the neutrino floor.

The content of this section of the proceedings has been drawn from Refs. [2, 3] in which further results and technical details can be found.

2 Directional detection

The rate of WIMP-nucleus elastic scattering events in the laboratory frame is a function of recoil energy, recoil direction and time. We can write the triple differential recoil rate per unit detector mass for spin-independent interactions with a single nucleus type of mass number A as [4],

$$\frac{\mathrm{d}^3 R}{\mathrm{d}E_r \mathrm{d}\Omega_r \mathrm{d}t} = \frac{\rho_0 \sigma_{\chi-n}}{4\pi m_\chi \mu_{\chi n}^2 \Delta t} A^2 F^2(E_r) \int \delta(\mathbf{v}\cdot\hat{\mathbf{q}} - v_{\min})\, f(\mathbf{v}+\mathbf{v}_{\mathrm{lab}}(t))\mathrm{d}^3 v\,, \tag{1}$$

where $\rho_0 = 0.3$ GeV cm^{-3} is the local astrophysical density of WIMPs, $\sigma_{\chi-n}$ is the spin-independent WIMP-nucleon cross-section, m_χ is the WIMP mass, $\mu_{\chi n}$ is the WIMP-nucleus reduced mass and Δt is the exposure time of the experiment. The function $F(E_r)$ is the nuclear form factor which describes the loss of coherence in the WIMP-nucleus interaction at high momentum transfer. The velocity distribution, $f(\mathbf{v})$, enters as its Radon transform and has been boosted into the laboratory frame by the time dependent lab velocity $\mathbf{v}_{\mathrm{lab}}(t)$. The angular dependence of the event rate is a dipole anisotropy peaking towards -$\mathbf{v}_{\mathrm{lab}}$.

The unique advantage given by directional information is the potential to make a WIMP "discovery" i.e., to claim that a detected particle is of Galactic origin. Once the initial assumption of isotropic backgrounds has been rejected which requires around $\mathcal{O}(10)$ events [5], a discovery can be made by checking the consistency of the direction of nuclear recoils with the direction of Solar motion. This can be done with either non-parametric tests on spherical data or with a likelihood analysis and requires as few as $\mathcal{O}(30)$ events [1, 6].

Once dark matter has been discovered the search enters the post-discovery phase when it becomes possible to study phenomena regarding the WIMP interaction and perform essentially "WIMP astronomy" by observing the velocity distribution of the local dark matter halo. An example of such a study is the detection of tidal streams of dark matter [3]. The hierarchical formation of the Milky Way is expected to give rise to a number of streams of dark matter matter wrapping around the Galaxy due to the tidal stripping of material from smaller satellite galaxies [7]. We have found that for a reasonably forecasted directional detector with a CF_4 target, a 30 kg-yr exposure and a threshold of 5 keV, a stream such as that expected from the Sagittarius dwarf galaxy would be detectable with either Bayesian parameter inference or a modified profile likelihood ratio test between a substructure free halo model and one containing a stream [3].

2.1 Experiments

Directional detection is a very exciting prospect theoretically but in practice is fraught with experimental limitations. The standard approach with low gas pressure Time Projection Chambers (TPCs) suffers from complications such as a limited sense recognition and an imprecise measurement of direction, as well as being inherently low in mass. In light of these restrictions it has become pertinent to consider possible solutions; for instance by compromising on the full 3-dimensional recoil track reconstruction. A 2-d readout for example could be obtained in a gas-TPC without time sampling the anode. A 1-d readout on the other hand consists of only measuring the projection of the recoil track onto the drift direction and currently has no experimental implementation. A 1-d readout strategy using dual-phase liquid noble detectors has been put forward conceptually in which columnar recombination is exploited to obtain directional sensitivity [8]. The advantage of such a technique is that it is possible to perform

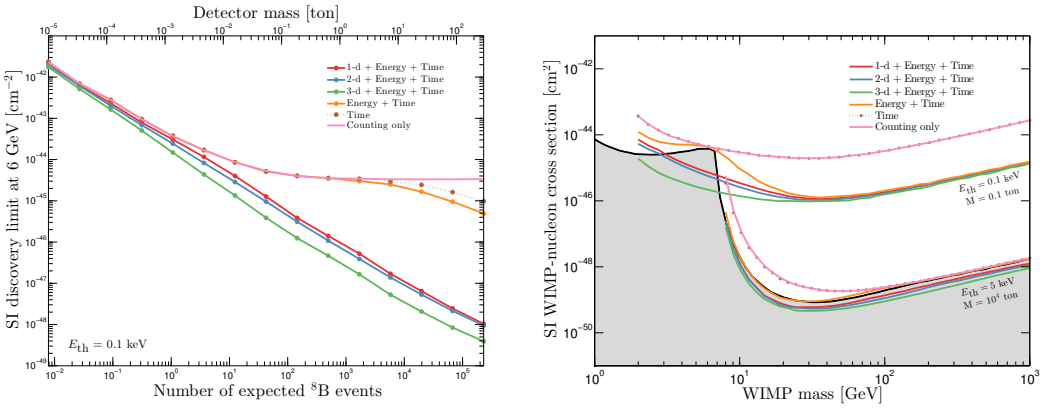

Figure 1: **Left:** The dependence of the discovery limit for the spin independent WIMP-nucleon cross-section, $\sigma_{\chi-n}$, on the mass of a Xe detector operated for 1 year using (from top to bottom) number of events only (pink line), time information (brown dotted), energy & time (orange), energy & time plus 1-d (red), 2-d (blue) and 3-d (green) directionality. **Right:** Discovery limits as a function of WIMP mass for fixed detector mass. The upper set of curves correspond to the limits obtained by a detector with a threshold of 0.1 keV and a mass of 0.1 ton, and the bottom set of curves for a 5 keV threshold detector with a 10^4 ton mass. The shaded region indicates the neutrino floor from Ref. [9].

with existing technology and in the liquid phase making it much more readily scalable to higher detector masses.

3 Directional detection and the neutrino floor

To follow Eq. (1) we can write the triple differential recoil rate per unit detector mass for coherent neutrino-nucleus scattering as the convolution of the double differential cross-section and the neutrino directional flux,

$$\frac{\mathrm{d}^3 R}{\mathrm{d}E_r \mathrm{d}\Omega_r \mathrm{d}t} = \frac{1}{m_N} \int_{E_\nu^{\rm min}} \frac{\mathrm{d}^2\sigma}{\mathrm{d}E_r \mathrm{d}\Omega_r} \times \frac{\mathrm{d}^3\Phi}{\mathrm{d}E_\nu \mathrm{d}\Omega_\nu \mathrm{d}t} \mathrm{d}E_\nu \mathrm{d}\Omega_\nu \,, \tag{2}$$

where $E_\nu^{\rm min}$ is the minimum neutrino energy required to generate a recoil of energy E_r and m_N the nucleus mass. The neutrino directional flux is dependent on the type of neutrino under consideration. For Solar neutrinos the flux is a delta function in direction with a cosine modulation in time due to the eccentricity of the Earth's orbit. For DSNB and atmospheric neutrinos the flux can be approximated as isotropic and constant in time.

Figure 1 shows the discovery limits for the spin-independent WIMP-nucleon cross-section obtained in a Xenon detector located in the Modane underground lab, operated for 1 year. The discovery limit is defined as the minimum cross-section for which 90% of hypothetical experiments can make a 3σ discovery [1] and are calculated using the standard profile likelihood ratio test. In the left hand plot we show the limits for a 6 GeV WIMP (which has a recoil

spectrum closest to that of ^{8}B neutrinos) as a function of detector mass for the 6 readout strategies. Firstly we have a counting only experiment, in such an experiment only the number of events above some energy threshold is measured. In this case the discovery limit plateaus at a value controlled by the ^{8}B neutrino flux uncertainty (around 15%). Including time information to a counting search only improves the discovery limit at very large detector masses/exposures due to the small amplitudes of the annual modulation effects. An energy + time experiment has a slight advantage due to the small differences in the tails of the WIMP and neutrino recoil spectra. Again, as this is a very small effect the detector masses needed to go beyond the neutrino floor are extremely large by directional detection standards. Including 1-d, 2-d and 3-d information the discovery limit cuts below the neutrino floor and retains a $1/M$ scaling due to the significant differences between the angular signatures of the WIMP and neutrino induced recoils. This proves that indeed directional information is a powerful tool for subtracting the Solar neutrino background.

The right hand plot in Fig. 1 shows the limits as a function of WIMP mass for two detector set-ups, a low threshold-low mass detector (0.1 keV and 0.1 ton), and a high threshold-high mass detector (5 keV and 10^4 ton). These numbers are well beyond the current and possibly even forseeable future of directional detection. However it is important to choose model experiments with a sizable neutrino background so that the advantage of a directional readout can be observed. In both the low and high mass WIMP ranges we see the directional limits cut below the non-directional neutrino floor, in the low mass range by a few orders of magnitude and in the high mass range by a factor of roughly 3. This is due to the fact that at low masses distinguishing WIMP from Solar neutrino recoils is much easier as they both possess unique directional signatures with little overlap between the two, whereas for distinguishing WIMP from atmospheric or diffuse supernova background neutrino recoils, the isotropic distibution of the latter two means there is much overlap between the two recoil signals and discriminating between the two to the same significance requires more WIMP events.

4 Summary

The detection of dark matter with directional information currently presents the most powerful approach for disentangling the WIMP signal from the ultimate neutrino background. The difference between the angular dependence of the neutrino and WIMP recoil spectra make the two signals distinct in a way that their recoil energies alone do not. We have shown the neutrino floor can be circumvented over the full range of WIMP masses, tackling both neutrinos from the Sun as well as atmospheric and diffuse supernova background neutrinos. Furthermore directional detection offers an exciting prospect for WIMP astronomy by observing features of the local velocity distribution such as tidal streams.

References

[1] J. Billard, F. Mayet and D. Santos, Phys. Rev. D **85** (2012) 035006 [arXiv:1110.6079 [astro-ph.CO]].

[2] C. A. J. O'Hare, A. M. Green, J. Billard, E. Figueroa-Feliciano and L. E. Strigari, arXiv:1505.08061 [astro-ph.CO].

[3] C. A. J. O'Hare and A. M. Green, Phys. Rev. D **90** (2014) 12, 123511 [arXiv:1410.2749 [astro-ph.CO]].

[4] P. Gondolo, Phys. Rev. D **66** (2002) 103513 [hep-ph/0209110].

[5] A. M. Green and B. Morgan, Astropart. Phys. **27** (2007) 142 [astro-ph/0609115].

[6] A. M. Green and B. Morgan, Phys. Rev. D **81** (2010) 061301 [arXiv:1002.2717 [astro-ph.CO]].

[7] C. W. Purcell, A. R. Zentner and M. Y. Wang, JCAP **1208** (2012) 027 [arXiv:1203.6617 [astro-ph.GA]].

[8] D. R. Nygren, J. Phys. Conf. Ser. **460** (2013) 012006.

[9] J. Billard, L. Strigari and E. Figueroa-Feliciano, Phys. Rev. D **89** (2014) 2, 023524 [arXiv:1307.5458 [hep-ph]].

Cross-Spectral Measurements for Cavity-based Axion and WISP Experiments

Stephen R. Parker, Ben McAllister, Eugene N. Ivanov, Michael E. Tobar
School of Physics, The University of Western Australia, Crawley 6009, Australia

DOI: http://dx.doi.org/10.3204/DESY-PROC-2015-02/tobar_michael

We introduce the basic concepts of the cross-spectrum measurement technique whereby two spectrums are cross-correlated together, allowing for rejection of uncorrelated noise processes. We apply these ideas to microwave cavity-based searches for Weakly Interacting Slim Particles and provide a proof-of-concept measurement.

1 Introduction

Weakly Interacting Slim Particles (WISPs) are a broad class of hypothetical particles with sub-eV masses that provide elegant and compelling solutions to a host of outstanding issues in particle physics and cosmology [1]. Experimental searches for these particles typically involve exploiting WISP-to-photon couplings, which provide a sensitive portal for detection with minimal model dependency. Some of the most sensitive and mature techniques for WISP searches utilize microwave and RF cavity structures, such that the converted WISP signal is resonantly enhanced and then read out via an amplification chain coupled to the cavity [2, 3, 4]. The challenge is to resolve the very weak power associated with WISP-to-photon conversion, P_W, against the intrinsic system noise generated by the cavity, P_C, and the first-stage amplifier, P_A.

2 Cross-spectral WISP measurements

The cross-spectrum [5] of two spectrums rejects uncorrelated signals while retaining those that are correlated. In each individual measurement channel the measurement error associated with a noise process is reduced at a rate proportional to $\sqrt{m}$ (m = number of averages), while in the associated cross-spectrum the mean of uncorrelated processes is suppressed at the rate $\sqrt{2m}$ while the associated error remains proportionally constant.

Figure 1 outlines the cross-spectral measurement scheme for cavity-based WISP searches. Two separate nominally identical cavities each have a measurement channel coupled to them. When the cross-spectrum is computed on the FFT the first-stage amplifier noise and the thermal cavity noise is rejected, while a signal due to a flux of WISPs is correlated between the two cavities and thus remains in the cross-spectrum. As the noise being rejected is thermal (random), the performance of the system should be independent of the relative phase of the two measurement channels.

Assuming that both cavities are frequency-tuned such that their resonances overlap then the

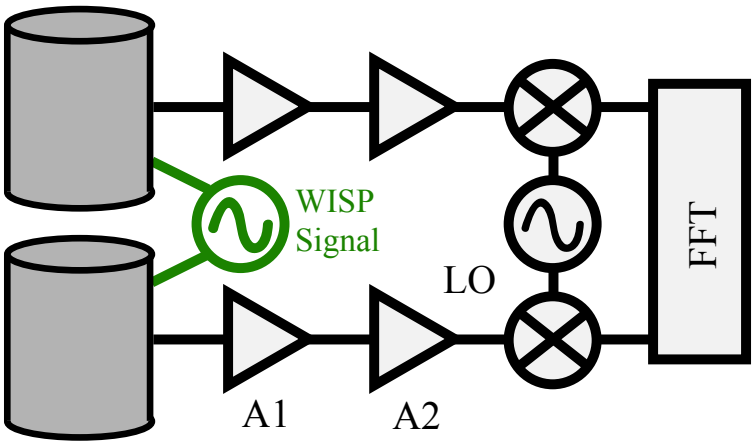

Figure 1: Schematic of the cross-spectral WISP measurement technique. The green signal source is used in the proof-of-concept measurements. A1 is the first-stage amplifier, LO is the local oscillator used to mix down the signal-of-interest to a lower frequency and FFT is the fast Fourier transform machine used to sample the spectrums.

expected Signal-to-Noise ratio for a correlated WISP signal is given by

$$\sqrt{2m}\frac{P_W}{P_C + P_A}. \tag{1}$$

This represents a $\sqrt{2}$ improvement compared to a single cavity measurement, owing to the addition of the second measurement system. It is important to note that the two cavities in Fig. 1 can be physically well-separated. This scheme therefore allows one to determine the coherence length of any candidate WISP signal.
Proof-of-concept measurements can be carried out using the system outlined in Fig. 1. A pair of nominally identical sapphire-loaded copper cavities with resonant frequencies of 9.3 GHz were housed in a vacuum chamber and connected to independent amplifier chains. The cavity resonance frequencies were tuned to overlap by adjusting the temperature control setpoint of the system. The spectrums from both channels were recorded as a function of averages taken with the cross-spectrum computed in-situ.

Figure 2 shows a single channel spectrum and the cross-spectrum of both measurement channels. The test WISP signal is resolvable in the single channel at the level 14σ, while in the cross-spectrum it is present at 20σ. This difference corresponds to a factor of $\sqrt{2}$ as outlined in Eq. (1). Fitting to the measured SNR as a function of averages indicates a starting SNR of $\sim$0.45, showing that the technique is valid for measurements with small initial SNRs, as is the typical situation in a WISP search.

Acknowledgments

This work was supported by Australian Research Council grant DP130100205.

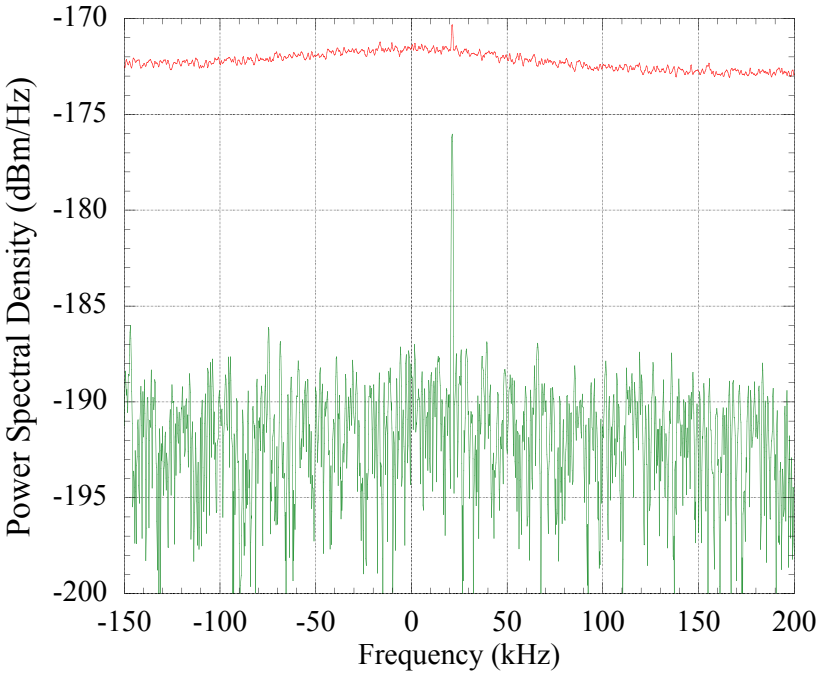

Figure 2: A 1600 point power spectrum after 1000 averages for the measurement scheme illustrated in Fig. 1. Single channel trace is shown in red and the cross-spectrum is shown in green.

References

[1] J. Jaeckel and A. Ringwald, "The Low-Energy Frontier of Particle Physics," Annual Review of Nuclear and Particle Science **60**, 405 (2010).

[2] S.J. Asztalos *et al.*, "SQUID-Based Microwave Cavity Search for Dark-Matter Axions," Phys. Rev. Lett. **104**, 041301 (2010).

[3] M. Betz *et al.*, "First results of the CERN Resonant Weakly Interacting sub-eV Particle Search (CROWS)," Phys. Rev. D **88**, 075014 (2013).

[4] S.R. Parker *et al.*, "Cryogenic resonant microwave cavity searches for hidden sector photons," Phys. Rev. D **88**, 112004 (2013).

[5] E. Rubiola and F. Vernotte, "The cross-spectrum experimental method," arXiv:1003.0113 [physics.ins-det].

Light Dark Matter in the NOνA Near Detector: First Look at the New Data

Athanasios Hatzikoutelis

University of Tennessee Knoxville, Knoxville, TN, USA

DOI: http://dx.doi.org/10.3204/DESY-PROC-2015-XX/hatzikoutelis_athanasios

The neutrino oscillations experiment NOνA is the flagship of Fermi National Laboratory. The neutrino source NuMI is delivering record numbers of protons-on-target surpassing the most stringent dark matter production upper limits of current models in the under-10 GeV mass range. We take advantage of the sophisticated particle identification algorithms of the experiment to interrogate the data from the 300-ton, off-axis, low-Z, Near Detector of NOvA during the first physics runs. We search for signatures of sub-GeV or Light Dark Matter (LDM), Axion-like-particles, and Heavy or Sterile Neutrinos that may scatter or decay in the volume of the detector.

1 Introduction

The NOνA (NuMI Off-axis electron-neutrino Appearance) [1] is the biggest particle physics experiment in the US currently and is hosted by Fermi National Accelerator Laboratory (Fermilab) and U. of Minnesota. It uses the most intense neutrino source in the world called NuMI (Neutrinos at the Main Injector). The ν_μ beam is produced by the 120 GeV protons of the Main Injector (MI) accelerator interacting in a carbon target at the NuMI target complex. Neutrinos are the tertiary beam coming out of this source that feeds the MINOS+ and MINERνA experiments as well.

The LDM title has been covering several types of New Physics candidate particles from Axion-like-particles that come from global broken symmetries, to Hidden Sectors interpreting SUSY models [2], all the way to some types of Heavy or Sterile Neutrino (Heavy Neutral Leptons -HNL) that come from the minimal extensions of SM [3]. They are not charged under SM and do not bind their mass with the Weak-scale couplings. The lowest dimension operators (*Portals*) that may couple both to SM and the lightest of the members of these structured *Sectors* may explain a very weak coupling of these particles to SM.

2 The NuMI-NOνA as a beam-dump experiment

The main function of the NOνA Near Detector (ND) [1] is to measure, near the source, the energy spectrum and profile of the ν_μ beam and the ν_e background expectation within the range of (1–3) GeV (Figure 1). Its segmented design of 4 cm×6 cm cells and its construction of low-Z plastic material gives it an estimated energy loss of about 10 MeV/cell or $0.18X_o$/plane. This

makes it very competitive for detecting electron tracks for a wide range of energies (0.1–60) GeV as shown in a study in [4].

Re-interpreting the NOνA ND as a beam-dump experiment opens the door to searches of rare events without any bias towards a particular model. The MI machine that feeds the NuMI source has been recently upgraded to 500 kW. It delivers multiple proton groups (bunches) stored in each burst (spill) of 10 μsec every 1.67 sec. Since September of 2013, it has delivered almost 3.25×10^{20} protons on the target (POT). About 1 km of earth is separating the NuMI-target from the 300-ton ND protecting it from any kind of products from the interactions at the target, besides the neutrinos and whatever other weakly-interacting LDM particles that may be produced.

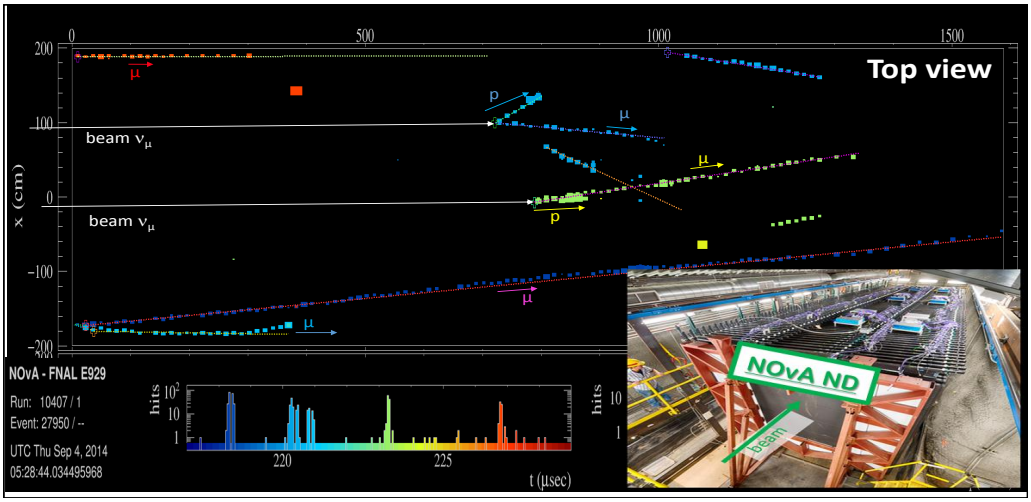

Figure 1: Event display of NOνA ND with a typical event (Top view) at 350 kW. (insert) The NOνA ND in its cavern at 11 meters from the beam center at left along the beam. It is usual to have events with five, identified, neutrino induced, interactions on nuclear targets in the detector and the surrounding walls of the cave (*rock muons*). The signatures from particles that are associated with neutrino interactions are highlighted (color denotes groupings in time) and labelled with two of the incident neutrinos artificially imposed on the display.

3 First look at the data

Even though we make every effort to use minimal assumptions and no model bias, we need to use a simple LDM model for illustration purposes. We choose here, a well-studied model [5] that assumes the Vector Portal model with a GeV-mass vector mediator which decays into a pair of scalar, MeV-mass, DM particles [4] that, in turn, fly to the ND where they may scatter elastically on atomic electrons. These events leave signatures of single, energetic, electron-induced, showers that are identical to the Neutral Current (NC) type of ν-induced interactions (the illustration in the insert of Figure 2 left). The NC events are the background to this LDM model signatures.

For this first look at the data we use the NOνA official preselection rules designed to identify

NC events. They have proven quite successful in identifying NC events in the primary energy range of (1–3) GeV that is the focus of the NOνA measurement [6]. We apply these rules to data from events covering the full energy range where events appear. For the small sample we are using in this work, the range extends up to little over 20 GeV. We search for spectral distortions (excess events) between the predicted distributions of the neutrino interactions that have no LDM channel included in the simulation (MC) and the data that may contain extra channels possibly from LDM. Identifying any regions of excess events and attempting to interpret them from their kinematics (energy transfer to the scattered particle, direction of the scattered product, time of flight with respect to the prompt neutrino beam coincident with the accelerator cycle, etc.) and then, attempt to compare which are the most probable models predicting such distributions.

For the size of the current sample used, and for pico-barn cross-section for scattering on atomic electrons, one would expect, for the range of (5–25) GeV, about $O(10)$ excess events to the simulated, pure neutrino, spectrum. In the right plot of Figure 2, we show the shape difference between the data spectrum and the simulated (MC) one. For all three studied energy bands, the average is consistent with no excess events.

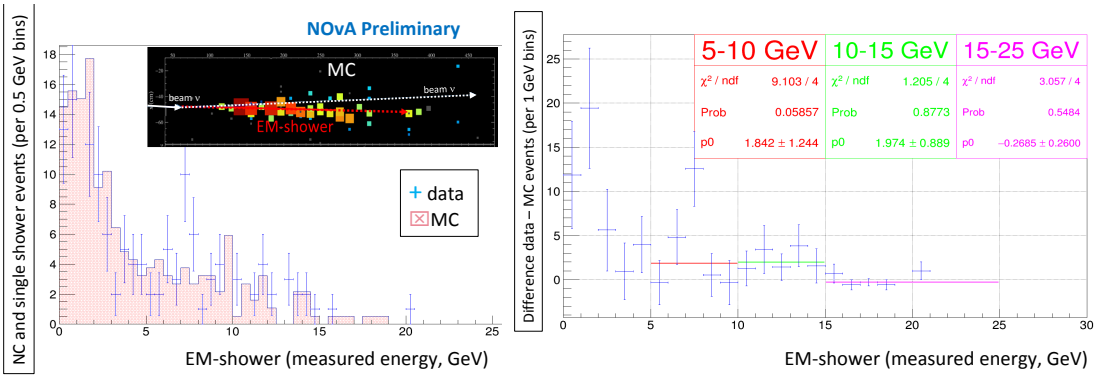

Figure 2: (left) The full energy range spectrum after the NC preselection cuts on data and simulated (MC) events. (left-insert) A simulated (MC) beam-ν_e scattered off of an atomic electron. The ν_e track is artificially displayed. Within the data we cannot distinguish signatures between beam-ν_e and LDM. (right) Shape difference by subtracting the simulated (MC) from the data spectrum. For all three studied energy bands, in this sample, the average is consistent with no excess events from any LDM candidates.

Further studies are warranted, with the full data-set of the first year NOνA run, as well as investigations to the stability of identification efficiency as a function of energy and the purity of the preselection cuts in the high sidebands from the ones they were designed for.

4 Outlook

Further upgrades will bring the intensity to 700 kW within 2016. The projected integral beam is 5×10^{21} POT within the 6 years of the NOνA run plan (see [4]). Regardless of what LDM model each favors, a model-agnostic attitude searching in the excess from the predicted rate

can help us probe LDM scattering down to pico-barn cross sections. Also, comparing with the recent results from MicroBooNE will be very interesting. There are also other motivated LDM channels producing particles that may decay in the near detector volume making these exotic searches a full research program at the NOνA-Near Detector and others future experiments. The searches with the NOνA ND though will be ten years in advance of any other [3, 7] proton beam-dump search at these LDM mass ranges.

Acknowledgments

Operated by Fermi Research Alliance, LLC under Contract No. De-AC02-07CH11359 with the United States Department of Energy.

References

[1] A. Hatzikoutelis, "Neutrino oscillations at the intensity frontier: The NOνA experiment," IOP Journal of Phys.: Conf. Series **410**, 012146 (2013).

[2] E. Rouven *et al.* "Dark Sectors and New, Light, Weakly-Coupled Particles," arXiv:1311.0029 [hep-ph]. B. Batell, W. Wester, P. deNiverville, R. Dharmapalan, A. Hatzikoutelis, D. McKeen, M. Pospelov, A. Ritz and R. Van de Water, "New, light, weakly-coupled particles with Project X" chapter VII pp 142-152 of the Project-X book, editor Henderson S *et al.* (Batavia, IL: Fermi National Accelerator Laboratory).

[3] S. Alekhin *et al.* "A facility to Search for Hidden Particles at the CERN SPS: the SHiP physics case." CERN-SPSC-2015-017 (SPSC-P-350-ADD-1) arXiv:1504.04855 [hep-ph].

[4] A. Hatzikoutelis, S. Kotelnikov, B. A. Bambah, S. P. Kasetti, "New light weakly-coupled particle searches in a neutrino detector," IOP Journal of Physics: Conference Series **490**, 012070 (2014). A. Hatzikoutelis, S. Kotelnikov, B. A. Bambah, S. P. Kasetti, "Search for Hidden Sector and Dark Matter Particles Produced at Fermilab's NuMI Target," Fermilab Technical Publications: FERMILAB-CONF-14-376-PPD.

[5] P. deNiverville *et al.*, Phys. Rev. D **86**, 035022 (2012)

[6] NOνA first results press release:
`http://www.fnal.gov/pub/presspass/press_releases/2015/NOvA-Neutrinos-Change-20150807.html`

[7] LBNE Collaboration, "LBNE Science Opportunities," arXiv:1307.7335 and `http://lbne.fnal.gov/`

Axions and CMB Spectral distortions in Cosmic Magnetic Field

Damian Ejlli

Theory group, INFN Laboratori Nazionali del Gran Sasso, 67100 Assergi, L'Aquila Italy
Department of Physics, Novosibirsk State University, Novosibirsk 630090, Russia

DOI: http://dx.doi.org/10.3204/DESY-PROC-2015-02/ejlli_damian

In this paper I discuss the impact of photon axion-mixing in the early Universe. Interaction of CMB photons with large scale cosmological magnetic fields can produce axions or other pseudoscalar particles. This process in the early Universe would distort the CMB spectrum and also create a measurable temperature anisotropy. New limits on axion mass and magnetic field strength are presented.

1 Introduction

One of the most striking predictions of the standard cosmology is the existence of the Cosmic Microwave Background (CMB) radiation. The CMB has been experimentally observed and its temperature has been measured with a great precision, $T = 2.725 \pm 0.001$ K by several experiments. An extremely important feature of the CMB is that it presents very small spatial temperature anisotropy of the order $\delta T/T \simeq 10^{-5}$. Apart from this observational fact, the CMB is expected to have additional features that are intrinsically connected with its spectrum.

Indeed, another prediction of the standard cosmology is that the CMB spectrum may present very small spectral distortions that may have been generated before or after the recombination epoch. In general these distortions are labelled as μ, i, y type distortions and are formed in different cosmological epochs. Until today there has not been observed any CMB spectral distortions but only upper limits on the distortion parameters exist. The COBE/FIRAS experiment [1] put only upper limits on μ and y with values $|\mu| < 9 \times 10^{-5}$ and $|y| < 1.5 \times 10^{-5}$.

Despite the fact that there has not been observed any CMB spectral distortions, the standard cosmological model predicts them and are generated by processes which heat, cool, scatter and create photons. Most of these processes are in general connected with new physics but there are also several ones that are connected with very well known physics. Mechanisms that might produce spectral distortions by injecting energy and photons in the plasma include: evaporating primordial black holes, decaying of relic particles, dark matter annihilation, tangled cosmological magnetic fields, etc. On the other hand, there are also processes that tend to erase any spectral distortion that might be created in the CMB and attempt to restore the full thermal equilibrium.

Obviously there is a competition between processes that tend to distort the CMB spectrum and those that tend to restore it. As shown in Ref. [2] the CMB spectrum would be distorted only if energy injection occurs after a certain cosmological time or cosmological redshift. In the

standard model of CMB spectral distortions, the spectrum will acquire a μ distortion if energy is injected in the redshift interval $2 \times 10^5 \lesssim z \lesssim 2 \times 10^6$. In this case the CMB spectrum is a Bose-Einstein distribution. For later times or cosmological redshifts, if there is any energy injection at $z \lesssim 1.5 \times 10^5$ the spectrum will acquire a y type distortion. Here the i type distortion is not discussed [3].

Among the sources that may generate spectral distortion, axion production in magnetic field is one of the best candidates. Indeed, in the presence of large scale magnetic fields axions may be efficiently produced before and after the decoupling time. At this point it would be natural to ask which is the impact of CMB photon-axion mixing on spectral distortions. If there is an impact, which is the mass range of axions that create spectral distortions, etc. Before answering to these questions it is important to first discuss the nature and strength of the cosmological magnetic field. This is done in Sec. 2, and in Sec. 3 we discuss the impact of photon-axion mixing on spectral distortions and temperature anisotropy.

2 Cosmological magnetic fields

One of the most fascinating problems in modern cosmology is whether primordial magnetic fields exist or not. Based on several astrophysical observations they seem to be everywhere in the Universe. They are present in our solar system, in stars, in the Milky way, in low and high redshift galaxies, in galaxy clusters, in superclusters and in voids of large scale structure (LSS). Their strength in galaxies is of the order of few to ten μG independently on the redshift while in clusters is of the order of μG. Their generation mechanism still remains an open question; however, the general consensus at present time is that they are thought to be produced by amplification of pre-existing weaker magnetic fields via different types of dynamo and via flux-conserving compression during the gravitational collapse of an accompanying structure formation.

The dynamo and amplification mechanisms can act only if an initially non-zero magnetic field is present. This seed field for the amplification might be very small, but it has to be generated by a different mechanism, which pre-dates the structure formation epoch or operates at the onset of structure formation. Two main models are widely accepted: either it is produced in the early Universe prior to the epoch of LSS or it is produced during gravitational collapse at the start of LSS. The existing data on magnetic fields in galaxies and galaxy clusters cannot provide direct constraints on the properties and origin of the seed fields. Therefore the only potential opportunity for understanding the nature of the initial seed fields is to search for places in the Universe where these fields might exist in their original form, namely in the intergalactic medium (IGM) and in the voids of LSS.

The spatial structure of large scale magnetic fields can be divided in two categories: large scale uniform magnetic fields (spatially homogeneous) and inhomogeneous magnetic fields (tangled magnetic fields). The former category was considered for the first time by Zel'dovich and Thorne [4]. Indeed, if there existed a large scale homogeneous magnetic field in the early Universe, it would induce a preferred direction during Universe expansion and therefore would break the Universe isotropy (every direction is the same). In this case the metric is not given anymore by a FRW one but by a Bianchi type IX metric.

The metric for a homogeneous magnetic directed along the z axis is given by:

$$ds^2 = dt^2 - a^2(t)(dx^2 + dy^2) - b^2(t)dz^2, \tag{1}$$

where $a(t)$ is the cosmological scale factor in the x, y direction and $b(t)$ is the scale factor along the z direction. In an anisotropic Universe, the energy momentum tensor of the electromagnetic field is also anisotropic. This implies that along the x, y axis there is a positive pressure induced that would tend to decelerate the Universe and there is a negative pressure induced along the z axis that tends to accelerate the Universe. Following Zel'dovich, one can formally calculate which is the induced temperature anisotropy by an anisotropic expansion of the Universe as follows:

$$\frac{T_x - T_z}{T_{rec}} \simeq -\frac{1}{2}\int_{t_{rec}}^{t_0} \sigma d(\ln t), \tag{2}$$

where $\alpha = \dot{a}/a, \beta = \dot{b}/b$ and $\sigma = \alpha - \beta$ and T_{rec} is the CMB temperature at the recombination time. If we use the present constraint on the CMB temperature anisotropy, it is possible to reverse Eq. 2 and use it as a constraint on the magnetic field strength at present epoch. For $\Delta T/T \simeq 10^{-5}$ [1] one finds an upper limit on the strength of magnetic field $B \lesssim 3$ nG [4].

In the case of inhomogeneous magnetic fields, there are several models that predict magnetic fields with no homogeneous term or tangled magnetic fields [5]. In this case one assumes that the magnetic field is statistically homogeneous and isotropic with a two point correlation function

$$\langle B_i(\mathbf{k}) B_j^*(\mathbf{q})\rangle = \delta^3(\mathbf{k} - \mathbf{q}) P_{ij}(\mathbf{k}) P_B(k), \tag{3}$$

where P_{ij} is a projection tensor and P_B is the power spectrum of the primordial magnetic field that in general is assumed to be a power law, $P_B = Ck^{n_B}$ with C a constant and n_B the spectral index of the magnetic field. For this type of magnetic field configuration, limits on the magnetic field strength are model dependent. For example from the CMB angular temperature anisotropy, the limit on magnetic field strength at scale $\lambda_B \simeq 1$ Mpc is $B_\lambda \lesssim 3 \times 10^{-9}$ [6]. On the other hand, Faraday rotation of the CMB polarization can be used to constrain the magnetic field strength on a given mode scale λ_B and a spectral index n_B as shown in Fig. 1.

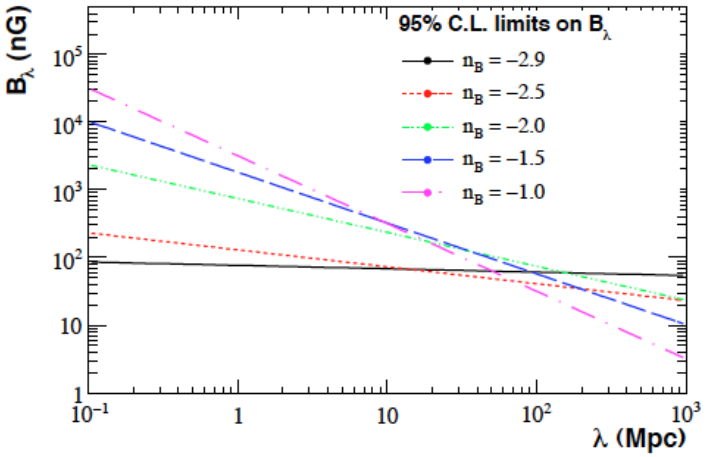

Figure 1: Limits on the magnetic field strength B_λ vs. λ_B from Faraday polarization of CMB as shown in Ref. [7]

.

3 Axion production in cosmological magnetic fields

In Sec. 2 we discussed about the spatial structure and strength of large scale magnetic fields for two different spatial configurations. It is well known that in the presence of a magnetic field photons can mix with axions and eventually oscillate into them in macroscopic B-fields. Therefore a natural question that comes is which is the impact of such mechanism on CMB spectral distortions. This process was studied in Refs. [8, 9] in the case of large scale uniform magnetic fields and tangled magnetic fields. In general to study such a process for the CMB case, it is necessary to take into account coherence breaking in the cosmological plasma. This is done by working with the density matrix ρ of the photo-axion system that obeys the following kinetic equation:

$$\frac{d\rho}{dt} = i[M, \rho] - \{\Gamma, (\rho - \rho_{eq})\}, \tag{4}$$

where M is the mixing matrix between the photon states and the axion and is given by the Raffelt-Stodolsky matrix equation as shown in Ref. [10].

In the case of large scale uniform magnetic fields, new limits on the axion mass and magnetic field strength are found. If we require that the resonant photon-axion mixing occurs during the μ epoch, one finds constraints on the axion mass (see Ref. [8]) in the range

$$2.66 \times 10^{-6}\,\mathrm{eV} \lesssim \bar{m}_a \lesssim 4.88 \times 10^{-5}\,\mathrm{eV}, \tag{5}$$

where $\bar{m}_a$ is the resonant axion mass during the μ epoch. By requiring that CMB μ distortion is totally due to photon-axion mixing one finds a simple relation between the magnetic field strength B_{nG} (in units of nano gauss), the CMB μ parameter and the resonant axion mass $\bar{m}_a$ as follows

$$B_{\mathrm{nG}} = 6.76 \times 10^{-2}\,\frac{\sqrt{\mu}}{\bar{m}_a\, C_{a\gamma}}, \tag{6}$$

where $C_{a\gamma}$ is a constant that essentially depends on the QCD axion model (KSVZ or DFSZ). In Fig. 2 the exclusion plot for COBE and the sensitivity plot for PIXIE/PRISM [11] in the case of KSVZ and DFSZ axions models in the $B - \bar{m}_a$ plane, are shown.

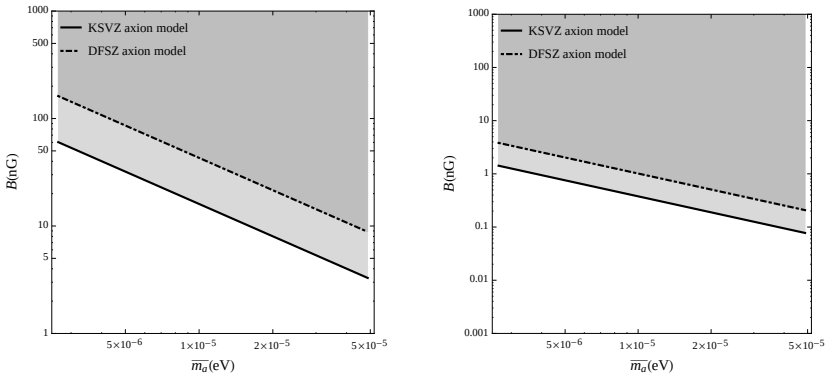

Figure 2: Exclusion plot on the left for the COBE limit on μ distortion and the sensitivity plot on the right for the PIXIE/PRISM sensitivity limit on μ for different axion models as shown as in Ref. [8].

In the case of axion production in tangled magnetic fields the situation slightly changes because in this case the magnetic field itself would produce a CMB μ distortion. As shown in Ref. [9] one needs to modify Eq. (6) in order to include dissipative effects of tangled magnetic fields. In this case Eq. (6) is modified as follows:

$$B_{\rm nG} = \sqrt{\mu}\left(1.6\times 10^3\, C_{n_B}^{-1/2}(\lambda_B/\lambda_D)^{-(\frac{n_B+3}{2})} + 3.38\times 10^{-2}\frac{1}{\bar{m}_a\, C_{a\gamma}}\right), \quad (\lambda_B \ll \lambda_D) \qquad (7)$$

for $\lambda_B \ll \lambda_D$. Here λ_D is the damping scale of the tangled magnetic field, λ_B is its wave-mode and C_{n_B} is a numerical factor. On the other hand for $\lambda_D \ll \lambda_B$ one finds

$$B_{\rm nG} = \sqrt{\mu}\left(1.6\times 10^3\, D_{n_B}^{-1/2}(\lambda_B/\lambda_D) + 3.38\times 10^{-2}\frac{1}{\bar{m}_a\, C_{a\gamma}}\right), \quad (\lambda_D \ll \lambda_B), \qquad (8)$$

where D_{n_B} is a numerical constant. In Fig. 3 the exclusion plot of COBE and the sensitivity plot of PIXIE/PRISM [11] in the case of KSVZ axion model and spectral index $n_B = 3$ for different axion masses are shown.

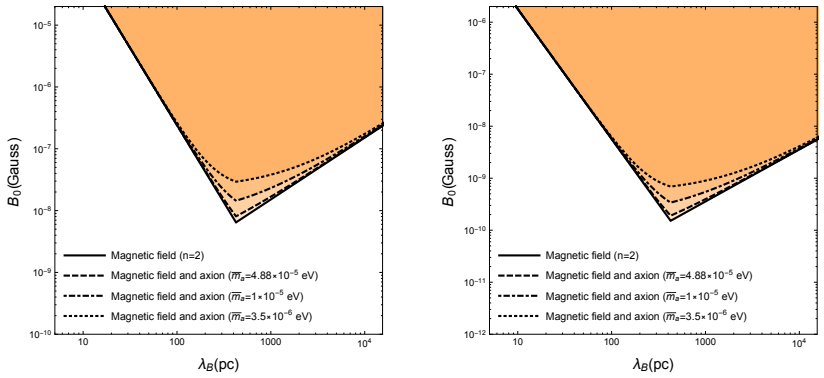

Figure 3: On the left the exclusion plot for the COBE limit on μ, KSVZ axion model and magnetic field spectral index $n_B = 2$. On the right the sensitivity plot of PIXIE/PRISM for the expected limit on μ, KSVZ axion model and $n_B = 2$ is shown.

4 Conclusions

Again the CMB turns out to be one of the most important ways that we have to test fundamental physics in different ways. It can couple to the large scale magnetic fields present in the early Universe and mix with low mass bosons such as axions, axion like particles, scalar bosons and gravitons. In the case of axions its production probability essentially depends on the coupling constant of axions to two photons $g_{a\gamma}$ or its mass, photon/axion energy ω and magnetic field strength.

Axions are extremely important for the standard model of particle physics since they allow to solve the strong CP problem. However, there is an inconvenient with them because we neither know their mass nor their coupling constant to photons. The only way that we have at

present to study them is by direct experimental searches or looking for their impact indirectly. In the latter case the CMB turns out to be extremely important in this regard.

Here we have shown that the coupling of CMB photons with the cosmological magnetic field can generate CMB μ distortions prior to the recombination epoch. This allows us to speculate on the axion mass and magnetic field strength at present time. In the case of a homogeneous magnetic field, it is found that for the magnetic field upper limit of $B \lesssim 3.2$ nG one would constrain the axion mass to be $m_a \lesssim 4.8 \times 10^{-5}$ eV for the KSVZ axion model, see Fig. 2 left panel. On the other hand, using the value of excluded axion mass $m_a \simeq 3.5 \times 10^{-6}$ eV from the ADMX experiment [12] together with the COBE bound on μ, we find the limit $B \simeq 46$ nG for the KSVZ axion model and $B \simeq 130$ nG for the DFSZ axion model, for a homogeneous magnetic field with coherence length at the present epoch $\lambda_B \simeq 1.3$ Mpc [8].

In the case of tangled magnetic field we find new limits on the magnetic field strength that are in general weaker in comparison with other studies. These limits are obviously model dependent and essentially depend on the magnetic field cut-off scale λ_B [9] and the spectral index n_B. For example by using the COBE upper limit on μ and for the magnetic field scale $\lambda_B \simeq 415$ pc, a weaker limit in comparison with other studies on the magnetic field strength ($B_0 \leq 8.5 \times 10^{-8}$ G) up to a factor 10 for the DFSZ axion model and the axion mass $m_a \geq 2.6 \times 10^{-6}$ eV is found. A forecast for the expected sensitivity of PIXIE/PRISM on μ is also presented. If CMB μ distortion could be detected by the future space missions PIXIE/PRISM and assuming that the strength of the large scale uniform magnetic field is close to its canonical value, $B \simeq 1 - 3$ nG, axions in the mass range $2\,\mu$eV - $3\,\mu$eV would be potential candidates of CMB μ distortion.

Acknowledgments

The author's work is supported by POR fellowship of Laboratori Nazionali del Gran Sasso and by Top 100 program of Novosibirsk State University. The author thanks the PATRAS organizing committee for the warm and scientifically stimulating atmosphere created during the workshop.

References

[1] D. J. Fixsen, E. S. Cheng, J. M. Gales, J. C. Mather, R. A. Shafer and E. L. Wright, Astrophys. J. **473**, 576 (1996).

[2] Y. B. Zeldovich and R. A. Sunyaev, Astrophys. Space Sci. **4**, 301 (1969).
R. A. Sunyaev and Y. B. Zeldovich, Astrophys. Space Sci. **7**, 20 (1970).

[3] W. Hu and J. Silk, Phys. Rev. D **48**, 485 (1993).
J. Chluba and R. A. Sunyaev, Mon. Not. Roy. Astron. Soc. **419**, 1294 (2012).
R. Khatri and R. A. Sunyaev, JCAP **1209**, 016 (2012).

[4] Ya. B. Zel'dovich, JETP **48**, 986 (1965).
K. S. Thorne, ApJ, **148**, 51 (1967).
J. D. Barrow, P. G. Ferreira and J. Silk, Phys. Rev. Lett. **78**, 3610 (1997).

[5] R. Durrer, P. G. Ferreira and T. Kahniashvili, Phys. Rev. D **61**, 043001 (2000).
R. Durrer and C. Caprini, JCAP **0311**, 010 (2003).
R. Durrer and A. Neronov, Astron. Astrophys. Rev. **21**, 62 (2013).

[6] D. Paoletti and F. Finelli, Phys. Lett. B **726**, 45 (2013).

[7] T. Kahniashvili, Y. Maravin and A. Kosowsky, Phys. Rev. D **80**, 023009 (2009).

[8] D. Ejlli, Phys. Rev. D **90**, 123527 (2014).

[9] D. Ejlli, Eur. Phys. J. C **75**, 397 (2015).

[10] G. Raffelt and L. Stodolsky, Phys. Rev. D **37**, 1237 (1988).

[11] A. Kogut, D. J. Fixsen, D. T. Chuss, J. Dotson, E. Dwek, M. Halpern, G. F. Hinshaw and S. M. Meyer *et al.*, JCAP **1107**, 025 (2011).
P. Andre *et al.* [PRISM Collaboration], arXiv:1306.2259 [astro-ph.CO].

[12] S. J. Asztalos *et al.* Phys. Rev. Lett. **104**, 041301 (2010).

Indirect Dark Matter Searches with MAGIC Telescopes

Konstancja Satalecka[1] for the MAGIC Collaboration

[1]Universidad Complutense, Madrid, Spain

DOI: http://dx.doi.org/10.3204/DESY-PROC-2015-02/satalecka_konstancja

In the last few years the indirect dark matter (DM) searches became a hot topic, with several experimental results showing hints of DM signal. The Major Atmospheric Gamma Imaging Cherenkov (MAGIC) telescopes are two 17 m diameter Cherenkov telescopes, located on the Canary island La Palma (Spain). MAGIC carries out a broad DM search program, including observations of dwarf galaxies, galaxy clusters and other DM dominated objects. In these proceedings recent MAGIC results from this field are presented, and discussed in a context of the present and future DM searches with Cherenkov telescopes.

1 MAGIC

MAGIC is a system of two, 17 m diameter Imaging Atmospheric Cherenkov Telescopes (IACTs), located at the Observatory Roque de los Muchachos, in the Canary island of La Palma (28.8 N, 17.8 W, 2200 m a.s.l.). IACTs are instruments optimised for ground-based detection of very high energy (VHE) gamma-rays, i.e. photons with energies between $\sim$50 GeV and 50 TeV. MAGIC-I has been in operation since 2004, and in 2009 it was joined by MAGIC-II. In 2012 a major camera and read-out system upgrade was completed, and currently, at low zenith angles, MAGIC achieves a sensitivity of (0.67+/-0.04)% of Crab Nebula flux, above 290 GeV (for 5σ significance detection in 50 hr) [1]. Due to its large mirror area MAGIC is also one of the best suited instruments to measure very high energy γ-rays below 100 GeV.

The MAGIC telescopes lead an extensive physics program covering γ-ray emission from many types of galactic and extragalactic sources. The collected data is analysed not only in terms of standard astrophysical topics such as the particle acceleration and emission mechanisms from cosmic sources, but also a wide range of fundamental physics studies is performed. These proceedings focus on the latest MAGIC results related to indirect dark matter searches.

2 Indirect dark matter searches

A major open question for modern physics is the nature of dark matter (DM): strong experimental evidence suggests the presence of this elusive component in the energy budget of the Universe (see e.g. [2]), without, however, being able to provide conclusive results about its nature. From the IACT point of view the most interesting are the theories offering DM particle candidates which could annihilate or decay into γ-ray photons, such as Weakly Interacting

Massive Particles (WIMPs) [3].

A γ-ray signal from DM origin would provide one of the clearest and most concluding evidences for DM. Spectral features such as annihilation lines [4] and internal bremssstralhung [5] as well as a characteristic cut-off at the DM particle mass would show up in a measured spectrum, shedding light over the nature of the DM constituent.

The expected DM annihilation flux is essentially proportional to the product of two parameters (see e.g., [6] for details). The first one, which we will label as Φ_{phys}, captures all the particle physics: DM particle mass, cross section, branching ratio, etc. The second one, J_{astro}, accounts for all the astrophysical considerations, such as the DM distribution and the distance to the source. Both of those factors are still poorly constrained and suffer from large uncertainties.

Astrophysical regions where high DM density is predicted are the best candidates to expect γ-ray emission from DM annihilation or decay. Here we describe in more detail MAGIC observations of the Perseus galaxy cluster, dwarf galaxies and Unassociated Fermi Objects.

2.1 Perseus galaxy cluster

Galaxy clusters are the biggest DM dominated objects in the local Universe, as much as 80% of their mass is believed to be constituted of DM. MAGIC observed the Perseus cluster in mono mode in November and December 2008 [7], collecting 24.4 h of high quality data. No significant VHE signal was detected and integral flux upper limit was derived for energies above 100 GeV and spectral index of -1.5: $F_{UL}(\geq 100\,\mathrm{GeV}) = 4.63 \times 10^{12}\,\mathrm{cm}^{-2}\,\mathrm{s}^{-1}$.

In order to estimate the expected DM annihilation flux we assumed an optimistic SUSY scenario [8], in which $\Phi_{phys} = 10^{32}\,\mathrm{GeV}^2\,\mathrm{cm}^3\,\mathrm{s}^{-1}$ above 100 GeV. The Navarro-Frenk-White [9] DM density profile was used to estimate the integrated astrophysical factor: $J_{astro} = 1.4 \times 10^{16}\,\mathrm{GeV}^2\,\mathrm{cm}^{-5}$. Finally we obtained a maximum DM annihilation flux of $1.4 \times 10^{16}\,\mathrm{cm}^{-2}\,\mathrm{s}^{-1}$ for energies above 100 GeV.

It can be seen that we need a boost in flux of the order of 10^4 to reach the predicted DM annihilation flux values. This boost factor could come from different effects, such as the presence of substructures that may enhance the annihilation γ-ray flux notably and that were not taken into account in the above calculation.

We continue observations of Perseus in stereo mode. In the years 2009-2015 MAGIC collected ~ 300 h of data from this target. The preliminary results of the analysis, focusing on the decaying DM models, were presented during the 34^{th} ICRC [10].

2.2 Dwarf galaxies

The dwarf spheroidal galaxies (dSphs) represent the best known targets for indirect DM searches thanks mainly to their very large mass-to-light ratios and low baryonic content. So far, around thirty dSphs have been identified in the MW. MAGIC observed three of them in mono mode: Draco [11], Willman [12] and Segue 1 [13].

Here, we will focus on the most recent Segue 1 observations, performed in stereo mode between January 2011 and February 2013 for a total time of 158 h [14], which makes these observations the longest exposure of any dwarf satellite galaxy by any IACT so far. Segue 1 data were analysed using the full likelihood approach [15], which takes into account the complete spectral information of the recorded events and the potential signal. The sensitivity

improvement of about a factor of 2 was achieved with respect to the conventional method [16], commonly used in IACT data analyses.

No significant gamma-ray excess above the background was found. Consequently, we derived 95% confidence level upper limits on the velocity-averaged annihilation cross section ($\langle\sigma\nu\rangle$), and lower limits on the dark matter particle lifetime, assuming several different annihilation and decay channels. These are the strongest bounds from observations of dSphs by any IACT so far. Additionally, for leptonic annihilation channels we achieved the strongest limits above a few hundreds GeV from any dShp observation till now, including the Fermi-LAT observations of 15 dSphs [17]. For the quark-antiquark channel and higher DM particle masses, the most constraining bounds are derived from the HESS observations of the Galactic Center halo [18, 19].

2.3 Unassociated Fermi Objects as dark matter clump candidates

DM subhalos with masses lower than the dSphs could be too small to have attracted enough baryonic matter to start star-formation and would therefore be invisible to past and present astronomical observations. Since γ-ray emission from DM annihilation is expected to be constant, these clumps would most probably only show up in all-sky monitoring programs at very high energies. This can be best provided by the Fermi satellite telescope[1] as Unassociated Fermi Objects (UFOs) not detected at any other wavelengths. Very likely, the distinct spectral cut-off at the DM particle mass is located at too high an energy (see, e.g. the neutralino mass lower limits in [20]) to be measurable by Fermi within reasonable time and can only be limited by IACTs observations.

We selected the most promising DM subhalo candidates out of the 1FGL [21] and 2FGL [22] catalogs, basing on their spectral characteristics, time variability and potential associations. In order to assess their detection prospects for IACTs for each source we estimated the time needed for detection by MAGIC by extrapolating the spectrum measured by Fermi-LAT. We also counted the number of photons $\geq$10 GeV seen by Fermi coming from their vicinity, to confirm that this extrapolation is sound. Finally, four most optimal candidates were observed in stereo mode and 50 h of good quality data were collected. More details on the selection procedure and the observations can be found in [23, 24].

The analysis did not reveal any significant VHE signal and upper limits for source emission were calculated with a confidence level of 95%, using the conventional method [16]. Assuming $z = 0$ we can exclude the direct extrapolation of Fermi-LAT spectrum for two of the candidates. We cannot neither rule out nor confirm the possibility that the emission in the Fermi-LAT energy range is due to DM, but the recently collected multiwavelength data seem to support the hypothesis that those sources belong rather to the standard AGN class of emitters.

3 Summary and outlook

The modern IACTs lead a wide range of astroparticle physics studies and MAGIC is one of the leading experiments in this field, especially designed to achieve the lowest energy threshold and high sensitivity below 100 GeV. MAGIC continues its wide DM search program with stereo observations of the most promising targets. We plan to operate the telescopes during the next few years, depending on the progress of the Cerenkov Telescope Array (CTA)[2] construction.

[1] http://fermi.gsfc.nasa.gov/
[2] https://www.cta-observatory.org/

CTA will be an open observatory, consisting of more than 100 IACTs located on two sites: one in Chile (CTA South) and one on the Canary island of La Palma (CTA North). In comparison to the present generation of instruments, CTA will have a factor of ten better sensitivity, larger field of view and considerably improved energy and angular resolution. Recent studies show that CTA will be capable of probing the ($\langle\sigma\nu\rangle$) parameter space below the natural cross-section for DM particle masses above a few hundreds of GeV [25].

Acknowledgments

We would like to thank the Instituto de Astrofísica de Canarias for the excellent working conditions at the Observatorio del Roque de los Muchachos in La Palma. The financial support of the German BMBF and MPG, the Italian INFN and INAF, the Swiss National Fund SNF, the ERDF under the Spanish MINECO (FPA2012-39502), and the Japanese JSPS and MEXT is gratefully acknowledged. This work was also supported by the Centro de Excelencia Severo Ochoa SEV-2012-0234, CPAN CSD2007-00042, and MultiDark CSD2009-00064 projects of the Spanish Consolider-Ingenio 2010 programme, by grant 268740 of the Academy of Finland, by the Croatian Science Foundation (HrZZ) Project 09/176 and the University of Rijeka Project 13.12.1.3.02, by the DFG Collaborative Research Centers SFB823/C4 and SFB876/C3, and by the Polish MNiSzW grant 745/N-HESS-MAGIC/2010/0.

References

[1] J. Aleksic et al., Astroparticle Physics **72**, 76 (2016).
[2] P.A.R. Ade, submitted to A&A (2013).
[3] D. Cerdeño, these proceedings.
[4] G. Bertone, et al., Phys. Rev. D **80**, 023512 (2009).
[5] T. Bringmann, et al., JHEP **0801**, 049 (2008).
[6] N. W. Evans, F. Ferrer, S. Sarkar, Phys. Rev. D **69**, 123501 (2004).
[7] J. Aleksić et al., Astrophys. J. **710**, 634 (2010).
[8] M. A. Sánchez-Conde et al., Phys. Rev. D **76**, 123509 (2007).
[9] J. F. Navarro, C. S. Frenk, S. D. M. White, ApJ, **490**, 493 (1997).
[10] J. Palacio et al., Proceedings of the 34$^{\text{th}}$ ICRC, the Hague (2015).
[11] J.Albert et al., Astrophys. J. **679**, 428 (2008).
[12] E. Aliu et al., Astrophys. J. **697**, 1299 (2009).
[13] J. Aleksić, et al., JCAP **1106**, 035 (2011).
[14] J. Aleksić et al., JCAP **02**, 008 (2014).
[15] J. Aleksić, J. Rico and M. Martinez, JCAP **10**, 032 (2012).
[16] W. A. Rolke, A. M. Lopez and J. Conrad, Nucl. Instrum. Meth. A **A551**, 493 (2005).
[17] M. Ackermann et al. Phys. Rev. D **89**, 042001 (2014).
[18] A. Abramowski et al. Phys. Rev. Lett. **106**, 161301 (2011).
[19] V. Lefranc et al., Proceedings of the 34$^{\text{th}}$ ICRC, the Hague (2015).
[20] K. Nakamura, et al. (Particle Data Group), J. Phys. G **37**, 075021 (2010).
[21] A. A. Abdo et. al., ApJS **188**, 405 (2010).
[22] P. L. Nolan, A. A. Abdo, et al., ApJS **199**, 31 (2012).
[23] D. Nieto et al., Proceedings of the 32$^{\text{th}}$ ICRC, Bejing (2013).
[24] K. Satalecka et al., Proceedings of the 34$^{\text{th}}$ ICRC, the Hague (2015).
[25] CTA Consortium, Astroparticle Physics **43**, 189 (2013).

Proposal to Search for a "Dark-Omega" Vector Boson in Direct Electroproduction Processes

Ashot Gasparian

NC A&T State University, Greensboro, NC, USA

DOI: http://dx.doi.org/10.3204/DESY-PROC-2015-02/gasparian_ashot

We propose performing an experiment to search for a new hidden sector vector boson coupled via baryonic current (V_B or "dark omega") in the (140–650) MeV mass range. It will be produced on low-Z fixed targets using high energy intense electron beams. The multi-gamma decay of this particle will be detected by a high resolution and large acceptance crystal calorimeter providing a few MeV level resolutions in $M_{\gamma\gamma\gamma}$, critically important for the signal to background separation. The motivation, feasibility studies of the setup and estimation of the realistic parameter space of the proposed experiment is discussed.

1 Introduction

Over the last several years there has been increased theoretical and experimental activities to search for a hidden sector dark photon or A' particle in the MeV-GeV mass range, weakly coupling to the Standard Model (SM) matter through a kinetic mixing mechanism ([1] and references within). These search experiments mostly rely on an assumption that the new particle is coupling predominantly to the leptonic field. Therefore, in most of cases, they look for the production of A' in the Coulomb field of heavy nucleus and consequently decaying to leptonic pairs (e^+e^- or $\mu^+\mu^-$). On the other hand, several other additional $U(1)'$ gauge symmetries and associated vector gauge bosons were proposed soon after the electroweak $SU(2) \times U(1)_Y$ model that are one of the best motivated extensions of the SM. One successful model, a dark-sector gauge vector boson, coupling to the baryonic matter (quarks), was proposed in 1989 [2] and subsequently discussed extensively in the literature (see references in [3]). S. Tulin in his recent article ([3] by analyzing the properties of the interaction Lagrangian and requiring the low-energy symmetries of QCD, demonstrated that this new particle can be assigned the same quantum numbers as the ω meson, J^{PC}=1^{--} with the leading decay channel $V_B \to \pi^0 + \gamma$ for the $M_\pi \leq M_{V_B} \leq 650$ MeV mass range. It was also suggested to search for these new particles in rare radiative decays of light neutral mesons [3, 9]. Here, we are suggesting an alternative experimental approach to search for this new particle in their direct electro-production channels in fixed-target experiments covering the same mass range.

2 Proposed experiment

We propose searching for V_B in direct electroproduction channels $e + A \to e' + V_B + (X) \to e' + \pi^0\gamma + (X) \to e' + \gamma + \gamma + \gamma + (X)$. These particles will be produced on low-Z fixed targets

in forward directions by a 11.5 GeV electron beam and they will be identified as a "*bump*" on the continuous experimental background of the $M_{\gamma\gamma\gamma}$ distribution. Four electromagnetic particles, e' and three decay photons will be detected in a crystal calorimeter. One of the major advantages of this experiment is that a high vacuum will be provided between the solid production target and the detection system. This will allow a significant minimization of the direct (by the beam) or secondary production of known particles in between the target and the detectors, which is the main source of so called "kinematical reflections", a typical problem for many other search experiments. The scattered electrons, e' will be detected in forward direction ($\sim 0.5^\circ - 5^\circ$) and within an energy range of (0.5–1.5) GeV to select forward and high energy virtual photons in the reaction. That, in turn, will enhance the production of forwardly directed energetic V_B particles to boost the three decay photons to the forward calorimeter acceptance (see Sec. 4.1). We propose to run this experiment in parallel with the neutral pion form factor $F_{\gamma^*\gamma\pi^o}$ measurement at very low Q^2. Therefore, the trigger in the experiment will be formed on two levels: first level, $E_{calor} \geq 8GeV$, and second level, $N_{cluster} \geq 3$.

3 Experimental setup

We propose using the PRad experimental setup currently being developed for the proton charge radius measurement with a sub-percent precision to address the *"proton charge radius puzzle"* in nuclear and atomic physics [4, 5]. This stand-alone setup consists of the following main elements (see Fig. 1): (i) windowless hydrogen gas flow target; (ii) a set of X-, Y-GEM coordinate detectors; (iii) high resolution, large acceptance PrimEx HyCal electromagnetic calorimeter; and (iv) a vacuum box with a single thin window at the calorimeter only, spanning ~ 5 m, with a 1.7 m diameter thin Al window at the front of HyCal. The Al window will have a thickness of 2.5 mm, with a 4 cm diameter and thin-walled cylindrical Al-pipe attached to the central part of the window for the passage of electron beam. This vacuum pipe is also passing through the centers of GEM and HyCal to reduce the beam-related electromagnetic background in the experiment. For this experiment we plan to use the same gas flow target mechanical structure, attaching thin 0.1-0.3% R.L. solid ^{12}C films to the target ladder, which is able to move remotely on both X- and Y-directions perpendicular to the beam. The HyCal calorimeter [6] is a hybrid electromagnetic calorimeter consisting of two different type of shower detectors, 576 Pb-glass modules ($4.0 \times 4.0 \times 45$ cm^3) and 1152 $PbWO_4$ crystal modules ($2.05 \times 2.05 \times 18.0$ cm^3) in the central part of the calorimeter. The central 2×2 $PbWO_4$ modules are removed from the assembly (4.0×4.0 cm^2 hole) providing passage of the incident electron beam through the calorimeter. The calorimeter with its cross sectional area of 118×118 cm^2 will be located in the beam line at a distance of ~ 5 m from the target, providing a large geometrical acceptance in the experiment. The incident electrons with an 11.5 GeV energy will scatter off a ^{12}C target and together with the 3 decay photons from the produced V_B particles will be detected in the HyCal calorimeter. This experimental setup is nearly ready for the PRad experiment.

4 Expected results and uncertainties

In order to investigate the detection efficiency (including the geometrical acceptances), uncertainties in measured quantities and expected results, a full Monte Carlo (MC) simulation code based on GEANT3.21 package has been developed. This program takes into account the realistic geometry of the setup, including all resolutions of the detectors. It generates events based

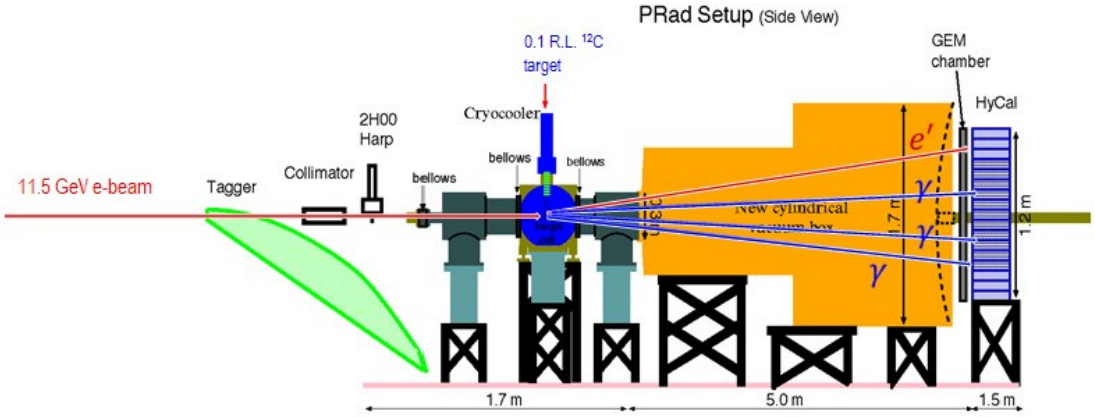

Figure 1: Schematic layout of the PRad experimental setup (not to scale). It will be used for the proposed experiment.

on estimated cross sections which are then traced through the target and detection system. The MC generated events are then analyzed to reconstruct the "measured" experimental quantities.

4.1 Detection efficiency

Four final state particles will be detected in this experiment: the forward scattered electrons and three decay photons from V_B. The scattered electrons within the (0.5–1.5) GeV energy range will be detected in order to select energetic and forwardly directed V_B particles to maximize the detection efficiency in the experiment. The simulated detection efficiency *vs.* target to calorimeter distance are shown in Fig. 2, Left. As it is seen from these simulations, the currently existing $Z = 5$ m distance for the PRad setup, is also well optimized for this proposed experiment, with relatively large (30–60)% detection acceptances for the (140–650) MeV mass range.

4.2 Invariant mass resolution

For the fixed target to calorimeter distance ($Z = 5$ m) the HyCal position and energy resolutions are defining the $M_{\gamma\gamma\gamma}$ invariant mass resolutions. The inner $PbWO_4$ crystal part of the HyCal calorimeter has excellent energy and position resolutions: $\sigma_E/E = 2.6\%/\sqrt{E}$ and $\sigma_{x,y} = 2.5$ mm$/\sqrt{E}$ greatly improving the $M_{\gamma\gamma\gamma}$ resolution. The outer Pb-glass part of HyCal has a factor of 2 less resolution in both energy and position reconstructions. The distribution of simulated invariant masses are shown in Fig. 2, Right, for three typical values of M_{V_B}. The proposed experiment will provide an MeV-level resolutions in reconstructed M_{V_B}, which is critically important for the signal-to-background separation (see Sec. 4.5).

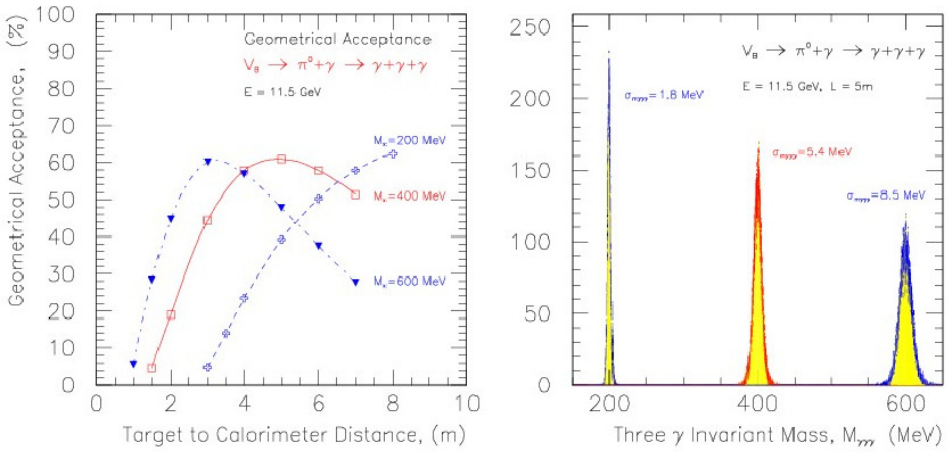

Figure 2: Left: Detection efficiency *vs.* Z for three typical M_{V_B} masses. Right: Distribution of reconstructed invariant mass for three M_{V_B}: 200 MeV, 400 MeV and 600 MeV.

4.3 Displaced vertex resolution

Solid thin-targets offer an additional selection mechanism in search experiments. That requires reconstruction of the decay vertex on event-by-event bases. This usually done by additional set of tracking detectors, in cases when the decay particles are charged [1]. In the proposed experiment the decay particles are three photons, however, there is an interesting way to determine the $V_B \to \pi^0\gamma$ decay vertex by using the $\pi^0 \to \gamma\gamma$ channel, assuming that the M_{π^0} is known. An example of the simulated vertex distribution is shown in Fig. 3, Left for M_{V_B}=400 MeV particles produced in forward direction. Though, our resolutions on this particular selection criterion (cm-level) are not as good as in the case of the charged-particle tracking [1], it can still be used very effectively in search experiments testing different ranges of coupling constants and mass (see Fig. 4).

4.4 Experimental backgrounds

The detection system in this experiment will be able to separate photons from the electromagnetic charge particles in the final states (using GEM and HyCal). Therefore, only events with three energetic photons ($E_\gamma > 0.5$ GeV) in final state will be considered as a background process *vs.* signal events. The potential sources of the background events are: (a) accidental coincidences of events with multi-photon bremsstrahlung processes (beam background); (b) production of particles decaying into three or more energetic photons (physics background). At this stage we have identified and simulated two major physics processes contributing to the physics background: forward electro-production of $2\pi^0$ mesons from the target and second, forward production of ρ mesons with their consequent decay into $\pi^0\gamma$. In both cases the π^0's decay into 2γ. The results of MC simulations for two physics background processes are shown in Fig. 3, Right, for 10 days of beam time (with E_e=11.5 GeV, $I_e = 0.1\mu$A, and 0.1% R.L. ^{12}C target). The beam background was also simulated, it has a typical exponential drop *vs.* $M_{\gamma\gamma\gamma}$

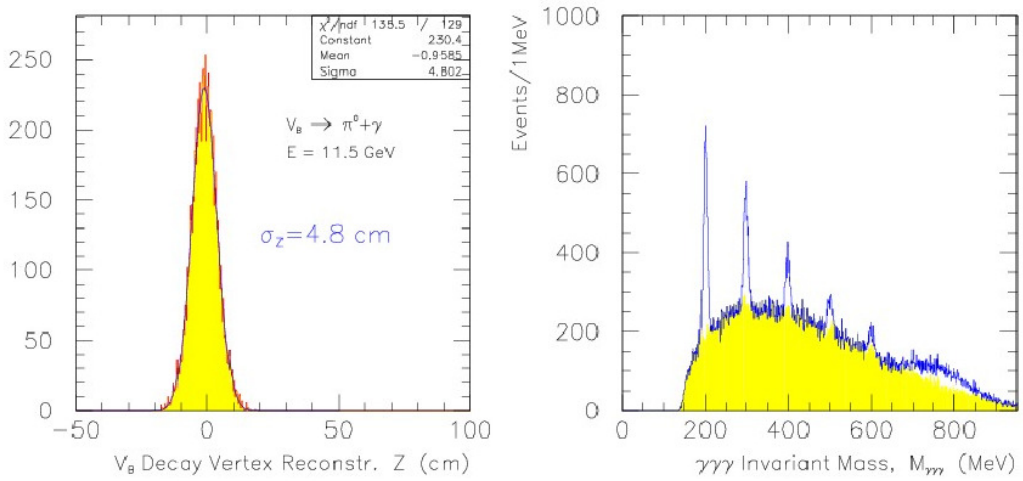

Figure 3: Left: Distribution of reconstructed vertex position. Right: Distribution of total physics background *vs.* $M_{\gamma\gamma\gamma}$. The $2\pi^0$ production process is the dominant background for this experiment (the yellow shaded area), the $\rho \to \pi^0\gamma$ background is the small bump at (650-850) MeV range. The five narrow distributions are the signal events simulated for M_{V_B}= 200, 300, 400, 500 and 600 MeV.

with an order of magnitude smaller than the physics backgrounds (not shown in Fig. 3).

4.5 Sensitivity of the proposed experiment

For the simulation of signal events the V_B production cross sections are required. Currently, theoretical activities are in progress to estimate these cross sections based on realistic models [7]. At this stage, based on general physics considerations, we assumed that these cross sections can be estimated by [8]: $\sigma(\gamma + P \to V_B + X) \sim (\alpha_{em}/\pi)(\alpha_B/\alpha_{em})(M_\omega/M_B)^2\sigma(\gamma + P \to hadrons)$. Then, if we take for $\sigma(\gamma + P \to hadrons) \sim 1\mu$b, we obtain $\sigma(\gamma +^{12} C \to V_B + X) \sim 1$ pb for V_B coupling constant α_B =10^{-8} and mass M_B=200 MeV. The corresponding experimental yields simulated for 10 days of beam time (E_e=11.5 GeV, I_e = 0.1μA, 0.1% R.L. ^{12}C target) are shown in Fig. 3, Right for five different masses of V_B boson. These yields are shown on the top of estimated backgrounds simulated under the same conditions. The sensitivity of this experiment to search for V_B bosons on 5σ level is plotted in Fig. 4 (short-dash red line). This proposed experiment, as it can be seen from the plot, has a good potential to improve the exclusion limits on the coupling constant, α_B for about one order of magnitude *vs.* other experiments/projects (other exclusion limits in Fig. 4 are discussed in [3]).

4.6 Summary

We are proposing a new fixed-target experiment to search for hidden sector leptophobic particles, V_B in the (140-650) MeV mass range. These particles will be produced in a low-Z target by an 11.5 GeV electron beam and detected by their $V_B \to \pi^0\gamma \to \gamma\gamma\gamma$ decay channel. The forward

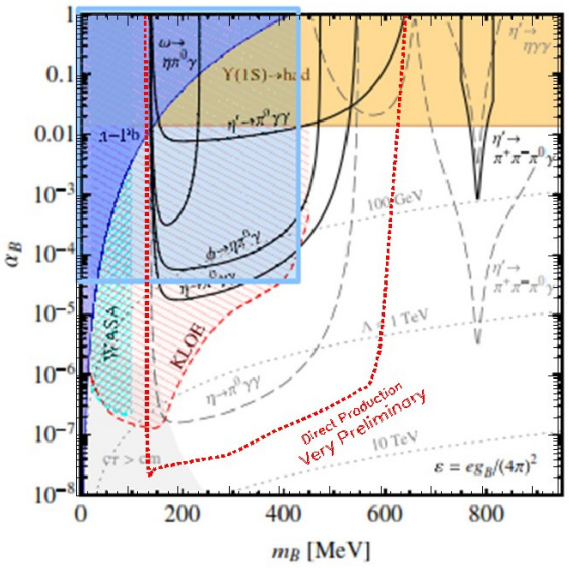

Figure 4: Current exclusion regions on V_B boson coupling *vs.* mass. The sensitivity region of the proposed experiment is shown with short-dash red line. For discussion of other exclusion limits see [3]).

scattered electrons ($\sim$ 1. GeV) and three decay photons will be detected by the high resolution and large acceptance HyCal calorimeter. A narrow resonance ($\sim$ 3 MeV) over the continuum experimental background will signal observation of these particles. The capability of vertex reconstruction (though with a moderate resolutions) will add a new dimension in filtering the background processes. These types of direct production experiments are fully complimentary to already suggested projects to search in rare radiative decays of light mesons [9].

This project is supported in part by the USA NSF awards PHY-1205962 and PHY-1506388.

References

[1] HPS Proposal, `http://www.jlab.org/exp_prog/proposals/11/PR12-11-006.pdf`.

[2] A. E. Nelson and N, Tetradis, Phys. Lett. B **221**, 80 (1989).

[3] S. Tulin, Phys. Rev. D **89**, 114008 (2014).

[4] PRad Proposal, `http://www.jlab.org/exp_prog/proposals/11/PR12-11-106.pdf`.

[5] A. Gasparian, MENU 2013, EPJ Web Conf., **7**3, 07006 (2014).

[6] M. Kubantsev *et al.*, AIP Conf. Proc. **867**, 51 (2006).

[7] S. Tulin, private communication.

[8] M. Pospelov, private communication.

[9] L. Gan, *et al.*, JLab Prop. E12-14-004, `http://www.jlab.org/exp_prog/proposals/14/PR12-14-004.pdf`.

Implications of a Running Dark Photon Coupling

Hooman Davoudiasl

Department of Physics, Brookhaven National Laboratory, Upton, NY 11973, USA

DOI: http://dx.doi.org/10.3204/DESY-PROC-2015-02/davoudiasl_hooman

For an "invisible" dark photon Z_d that dominantly decays into dark states, the running of its fine structure constant α_d with momentum transfer $q > m_{Z_d}$ could be significant. A similar running in the kinetic mixing parameter ε^2 can be induced through its dependence on $\alpha_d(q)$. The running of couplings could potentially be detected in "dark matter beam" experiments, for which theoretical considerations imply $\alpha_d(m_{Z_d}) \lesssim 0.5$.

The following is a summary of a talk - entitled "Running in the Dark Sector" - given by the author at the 11$^{\rm th}$ Patras Workshop on Axions, WIMPs and WISPs, held at the University of Zaragoza, Spain, June 22-26, 2015. The presentation is based on the work in Ref.[1], where a more complete set of references can be found.

The possibility of a dark sector that includes not only dark matter (DM), but also dark forces and other states has attracted a great deal of attention in recent years [2]. In particular, it has been noted that a "dark photon" Z_d of mass $m_{Z_d} \lesssim 1$ GeV, mediating a dark sector $U(1)_d$ force may explain potential astrophysical signals of DM [3]. It is often assumed that the Z_d can couple to the electromagnetic current of the Standard Model (SM) via a small amount of kinetic mixing ε [4] (though it may have other couplings as well [5]) which can be naturally loop induced: $\varepsilon \sim e g_d/(16\pi^2)$ [4] where e and g_d are the electromagnetic and $U(1)_d$ coupling constants, respectively. The $3.5\,\sigma$ muon $g-2$ anomaly [6] may potentially be explained by a light ($m_{Z_d} \lesssim 0.1$ GeV) Z_d with $\varepsilon \sim 10^{-3}$ [7].

If there are dark states, such as DM, that have $U(1)_d$ charge $Q_d \neq 0$ and have a mass $m_d < m_{Z_d}/2$, then they will likely be the dominant decay channels for Z_d, making it basically invisible. This possibility can be employed to form beams of light (sub-GeV) DM that may be detectable in fixed target experiments (whose detection in nuclear recoil experiments would be challenging). The basic idea is that an intense beam of protons or electrons impinging on a target (or beam dump) can lead to production of boosted Z_d particles that decay in flight mostly into light DM states, generating a "DM beam" which can be detected via Z_d-mediated scattering from atoms [8, 9]. See Figure 1 for a schematic illustration of such a setup. The production rate of on-shell dark photons is controlled by $\alpha\varepsilon^2$, while the detection of the DM particles is governed by $\alpha_d\alpha\varepsilon^2$, where $\alpha \equiv e^2/(4\pi)$ and $\alpha_d \equiv g_d^2/(4\pi)$.

If the above light DM particles are thermal relics, one expects [8, 9]

$$\alpha_d \sim 0.02\, w \left(\frac{10^{-3}}{\varepsilon}\right)^2 \left(\frac{m_{Z_d}}{100\ \text{MeV}}\right)^4 \left(\frac{10\ \text{MeV}}{m_d}\right)^2 , \qquad (1)$$

where $w \sim 10$ for a complex scalar [8], and $w \sim 1$ for a fermion [9]. As experiments probe smaller values of ε, one could start probing $\alpha_d \sim 1$, which in the presence of light DM with $Q_d \neq 0$ can lead to significant running of α_d. As the fixed target experiments (Figure 1) probe

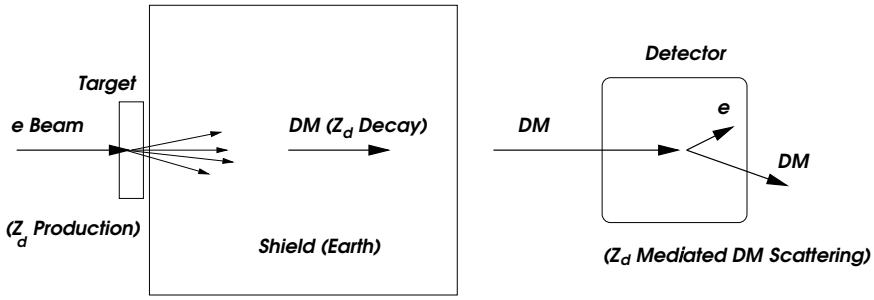

Figure 1: Schematic illustration of a fixed target "Dark Matter beam" experiment, using an electron beam.

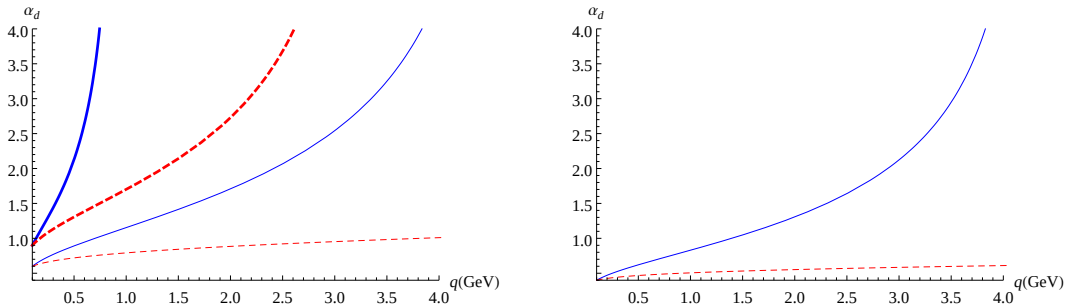

Figure 2: Running of $\alpha_d(q)$, with (a) one DM particle, where the thin (thick) lines correspond to $\alpha_d(q_0) = 0.6$ (0.9), and (b) two DM states with $\alpha_d(q_0) = 0.4$. The solid (dashed) lines correspond to fermion (scalar) DM states. In both cases, the contribution from a dark Higgs particle is included, $q_0 = 0.1$ GeV, and $m_{Z_d} \lesssim q_0$ is assumed.

momentum transfer values in the GeV range, *i.e.* $q^2 \gg m_{Z_d}^2$, the effect of running on the event rate can be significant and it may even lead to unreliable predictions for $\alpha_d(q^2) \gg 1$. To illustrate these points, we will consider n_F fermions and n_S scalars with $|Q_d| = 1$, all below m_{Z_d}. We will assume that the mass of Z_d is generated by a dark Higgs scalar and hence $n_S \geq 1$ in our analysis.

We will employ a 2-loop beta function for $U(1)_d$

$$\beta(\alpha_d) = \frac{\alpha_d^2}{2\pi}\left[\frac{4}{3}\left(n_F + \frac{n_S}{4}\right) + \frac{\alpha_d}{\pi}(n_F + n_S)\right], \tag{2}$$

where $\beta(\alpha_d) \equiv \mu\, d\alpha_d/d\mu$, with μ, the renormalization scale, set by the relevant momentum transfer q. The reference infrared momentum transfer is taken to satisfy $q_0 \gtrsim m_{Z_d}$ and we will ignore the mass of Z_d in what follows. The form of $\beta(\alpha_d)$ in the above suggests that perturbative control is lost when $\alpha_d \gtrsim \pi$.

In Figures 2 (a) and (b), we have presented the effect of running for various values of α_d and one and two DM states, respectively. We see that for values of $\alpha_d \lesssim 1$ the running effect can

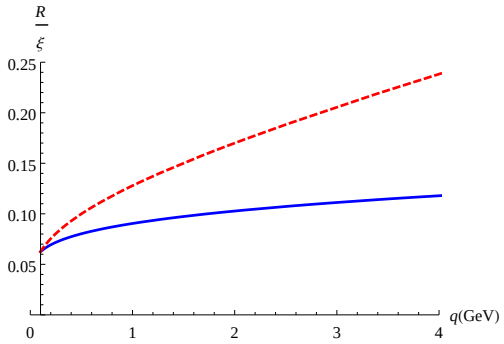

Figure 3: Running of R/ξ with q, assuming one (solid) and two (dashed) dark matter fermions. Here, $\alpha_d(q_0) = 0.25$, $q_0 = 0.1$ GeV, and $m_{Z_d} \lesssim q_0$ are assumed. A dark Higgs boson contributes to the running in both cases.

be significant and may result in loss of perturbative reliability for predictions. The running is more pronounced for light fermion states, but could still be significant for scalars for $\alpha_d \gtrsim 0.4$. These results suggest that one may be able to use the running effect, if measurable, to probe the number and the type (spin) of the low lying states in the dark sector.

An approach to measuring the running of $\alpha_d(q)$ may take advantage of the fact that at $q^2 > m_{Z_d}$ the scattering of DM from the nucleus is similar to electron or muon electromagnetic scattering from the nucleus governed by quantum electrodynamics. One may then normalize the DM scattering cross section $\sigma_{\rm DM}$ to the well-understood lepton scattering cross section $\sigma_{\rm EM} \propto 1/q^2$ which can be well-measured. We then have

$$R \equiv \sigma_{\rm DM}/\sigma_{\rm EM} \simeq \alpha_d\, \varepsilon^2/\alpha \simeq \xi\, \alpha_d^2\,, \tag{3}$$

with ξ approximately constant. In the above, we have used the typical assumption of loop-induced kinetic mixing that implies $\varepsilon^2(q) \propto \alpha_d(q)$. In Figure 3, we have plotted the running of R/ξ for one (solid) and two (dashed) light DM fermions and one dark Higgs boson, assuming $\alpha_d(q_0) = 0.25$, $q_0 = 0.1$ GeV, and $m_{Z_d} \lesssim q_0$. As can be seen, the running is significant for GeV $0.1 \lesssim q \lesssim 4$ GeV, typical of fixed target experiments, and the two cases are quite distinct, suggesting that with sufficient statistics one may uncover the low lying dark sector spectrum.

As α_d increases beyond $\mathcal{O}(1)$ values, the theory will become strongly coupled. However, in a sensible framework, this behavior should be terminated at some scale. A straightforward possibility is for $U(1)_d$ to transition to a non-Abelian gauge interaction that is asymptotically free. If this transition to new physics occurs at $q = q^*$, one expects $\varepsilon(q^*) = 0$, with a non-zero value induced below q^* due to the quantum effects of particles with masses $m < q^*$ that carry hypercharge and have $Q_d \neq 0$. However, such particles cannot be too light, $m \gtrsim 100$ GeV [10], given existing experimental bounds. Thus, on general grounds, we expect q^* to be larger than $\mathcal{O}(100\,\text{GeV})$.

For $\alpha_d(q^*)\ln(q^*/q_0) \gg 1$, we find

$$\alpha_d(q_0) \approx \frac{3\pi}{(2n_F + n_S/2)\ln(q^*/q_0)}\,, \tag{4}$$

where we have used a 1-loop approximation for the running. The above formula then yields the value of $\alpha_d(q_0)$ that would lead to the onset of a Landau pole at $q \sim q^*$. For example, setting

$q_0 = 0.1$ GeV and $q^* = 1$ TeV (a reasonable value given the preceding discussion), the upper bound $\alpha_d(q_0) \lesssim 0.5/(n_F + n_S/4)$ is obtained. Hence, for $m_{Z_d} \lesssim 0.1$ GeV, we may expect the upper bound $\alpha_d(m_{Z_d}) \lesssim 0.5$ as a generic guide for the invisible dark photon scenario, where dark states below m_{Z_d} are assumed.

Acknowledgments

Th author thanks the organizers of Patras 2015 for giving him the opportunity to present the above results and for providing a pleasant venue for stimulating discussions. This article is based on work supported by the US Department of Energy under Grant Contract DE-SC0012704.

References

[1] H. Davoudiasl and W. J. Marciano, Phys. Rev. D **92**, no. 3, 035008 (2015) [arXiv:1502.07383 [hep-ph]].

[2] R. Essig, J. A. Jaros, W. Wester, P. H. Adrian, S. Andreas, T. Averett, O. Baker and B. Batell *et al.*, arXiv:1311.0029 [hep-ph].

[3] N. Arkani-Hamed, D. P. Finkbeiner, T. R. Slatyer and N. Weiner, Phys. Rev. D **79**, 015014 (2009) [arXiv:0810.0713 [hep-ph]].

[4] B. Holdom, Phys. Lett. B **166**, 196 (1986).

[5] H. Davoudiasl, H. S. Lee and W. J. Marciano, Phys. Rev. D **85**, 115019 (2012) [arXiv:1203.2947 [hep-ph]].

[6] G. W. Bennett *et al.* [Muon G-2 Collaboration], Phys. Rev. D **73**, 072003 (2006) [hep-ex/0602035].

[7] M. Pospelov, Phys. Rev. D **80**, 095002 (2009) [arXiv:0811.1030 [hep-ph]].

[8] P. deNiverville, M. Pospelov and A. Ritz, Phys. Rev. D **84**, 075020 (2011) [arXiv:1107.4580 [hep-ph]].

[9] E. Izaguirre, G. Krnjaic, P. Schuster and N. Toro, arXiv:1411.1404 [hep-ph].

[10] H. Davoudiasl, H. S. Lee and W. J. Marciano, Phys. Rev. D **86**, 095009 (2012) [arXiv:1208.2973 [hep-ph]].

Parameters of Astrophysically Motivated Axion-like Particles

Sergey Troitsky

Institute for Nuclear Research of the Russian Academy of Sciences, Moscow, Russia

DOI: http://dx.doi.org/10.3204/DESY-PROC-2015-02/troitsky_sergey

Popular explanations of the anomalous transparency of the Universe for energetic gamma rays include conversion of photons into hypothetical axion-like particles (ALPs) and back in astrophysical magnetic fields. This could either happen in the gamma-ray source and in the Milky Way, or the photon-ALP oscillations could take place in the intergalactic magnetic fields all along the way between the source and the observer. Given recent astrophysical constraints on ALPs and on intergalactic magnetic fields, these two mechanisms imply very different ALP parameters: masses and couplings. Therefore, confirmation of the anomalies and identification of one of the scenarios would mean cornering of ALP parameters to a particular narrow region.

1 Anomalous transparency and ALPs

The modern evidence for the anomalous transparency of the Universe for energetic gamma rays is based on studies of ensembles of distant VHE sources. The observed spectra of these sources have been corrected for pair-production effects ("deabsorbed") within the lowest-absorption models to obtain the intrinsic spectra emitted at the sources. These intrinsic spectra exhibit unphysical redshift dependence which is readily interpreted as an overestimation of the absorption even in the minimal models [1–3].

An ALP mixes with photons in external magnetic fields [4], which may allow to suppress the attenuation due to pair production: gamma-ray photons convert to ALPs, then travel unattenuated and eventually convert back to photons. The photon beam is still attenuated, but the flux suppression becomes less severe. To reduce the opacity of the Universe for TeV gamma rays from blazars, two particular scenarios involving ALPs are important. The purpose of the present study is to emphasise and to explore the difference between the two approaches (see a more detailed discussion in Ref. [5]).

The first scenario implies that the intergalactic magnetic field is strong enough to provide for ALP/photon conversion all along the path between the source and the observer. Originally suggested in Ref. [6] in a different context, this mechanism, known also as the DARMA scenario, was invoked for the TeV blazar spectra in Ref. [7]. If it is at work, then the photon/ALP mixed beam propagates through the Universe and, since the photons are attenuated while ALPs are not, the effective suppression of the flux is smaller compared to the pure-photon case. A detailed recent study of this scenario is given in Ref [3], where the most recent constraints on the relevant ALP parameters are derived. In what follows, we will refer to this mechanism as the "intergalactic conversion" and use the parameter constraints [3] for this scenario.

The second approach assumes that there are quite strong magnetic fields inside or around the source, as well as around the observer, while for the most part of the distance the beam travels in weak magnetic fields, insufficient for ALP/photon mixing. The conversion may happen either in the blazar itself and in the Milky Way [8] or in the galaxy cluster or filament [9] (see also a more detailed subsequent study in Ref. [10]) containing the source and the observer, in various combinations. A detailed recent study of this mechanism is presented in Ref. [11], where it is called "the general-source" scenario. In the rest of the paper, we refer to this mechanism as the "galactic conversion" and use parameter constraints derived in Ref. [11] for this case.

Regions of parameters of the ALP, that is of its mass m and its inverse coupling to photons M, required for efficient operation of one or another mechanism, overlap in a large range. However, when the most recent experimental and astrophysical constraints are taken into account, the parameter regions allowed for the two scenarios become disconnected; this means that if we determine that one or another scenario works in Nature, we strongly constrain the ALP mass and coupling! We illustrate this fact in Fig. 1, where shaded blue areas, excluded by constraints from the CERN axion solar telescope (CAST, Ref. [13]), evolution of the horizontal-branch (HB) stars [14], reanalysis of the supernova (SN) 1987A data [15] and HESS constraints from the absence of irregularities in a blazar spectrum [16], indicate the most restrictive relevant limits. The key constraint contributing to the separation of the two regions is that of Ref. [15]. The separation of the two regions, which are often unified in a single large band referred to as the "transparency hint" in relevant plots, is remarkable.

2 Discrimination between galactic and intergalactic scenarios

Anisotropy.- The magnetic field of the Milky Way galaxy has a complicated structure, and the probability of the ALP/photon conversion there, which is required in the galactic scenario, depends strongly on the direction. Evidence for direction dependence in the anomalous transparency of the Universe may therefore be a strong argument in favour of the galactic scenario [8, 9, 17].

In Reference [8], it was pointed out that the positions of a few TeV blazars with redshifts $z > 0.1$ known by that time fit surprisingly well the regions in the sky where the conversion probability, calculated within the model of the Galactic magnetic field (GMF) of Ref. [12], is high. Here, we assume this as a hypothesis and attempt to test it with the new observational data. Clearly, more elaborated approaches should be used in further studies. We consider a sample of blazars with firm detection beyond $\tau = 1$ which consists of 15 objects observed by IACTs and 5 objects observed by FERMI LAT (the sample of Ref. [2]), supplemented by additional 6 blazars rejected in Ref. [2] because of the insufficient number of data points for fitting spectra with breaks. We drop 4 nearby objects with $z < 0.1$ from the sample, like it was done in Ref. [8]. Figure 2, represents the distribution of these objects in the sky together with the conversion probability for the same GMF model [12]. The objects indeed follow the regions of high conversion probability, qualitatively confirming the trend seen in Ref. [8].

It is not possible, however, to rigorously test the hypothesis quantitatively, because the blazars we discuss do not form a complete isotropic sample. Nevertheless, for illustration, we present here the results of a simple statistical test, keeping in mind its qualitative level. For each of the 22 sources in the sample, we calculate the ALP/photon conversion probability in the GMF of Ref. [12]. The same distributions were calculated and averaged for 100 sets of

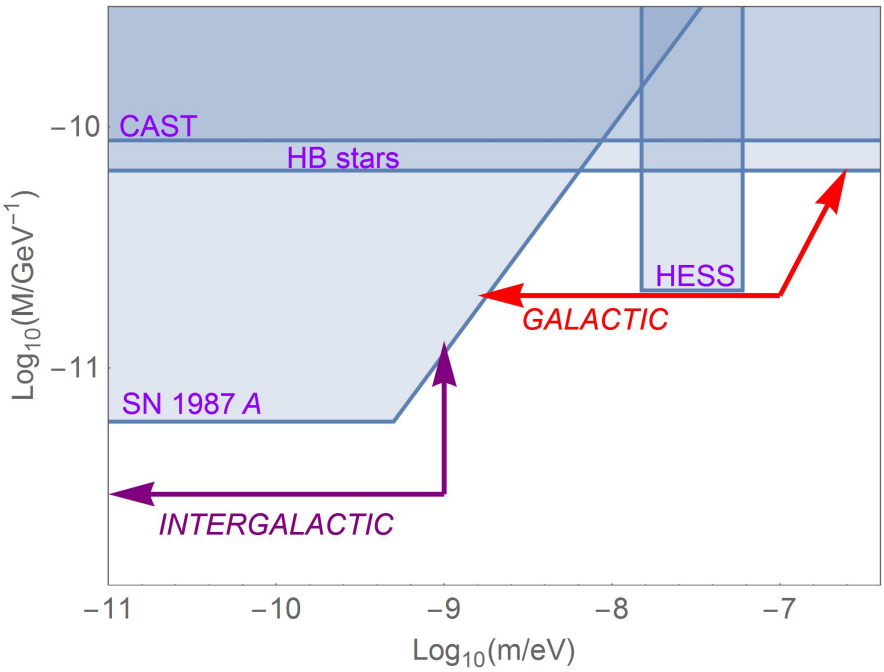

Figure 1: ALP parameter space (ALP-photon inverse coupling M versus ALP mass m) with current constraints (see text). The regions corresponding to the Galactic [3] and intergalactic [11] ALP/photon conversion explanations of the gamma-ray anomalies are indicated; they extend to the forbidden regions as shown by arrows. Given all constraints, the two regions are well separated.

22 objects distributed isotropically in the sky. The Kolmogorov-Smirnov probability that the distribution seen for the real data is a fluctuation of that for simulated directions is 0.02, that is, the entire picture does not contradict the galactic conversion scenario.

Distant objects.- In the ideal case and in the long-distance limit, the effective optical depth $\tau_{\rm ALP}$ behaves differently in the two scenarios: for intergalactic conversion, $\tau_{\rm ALP} \sim (2/3)\tau$ (and therefore grows approximately linearly with distance, like the standard optical depth τ), while for the galactic scenario, assuming maximal mixing, it reaches a constant, distance-independent value corresponding to the flux suppression by a factor of $\sim 2/9$, that is $\tau_{\rm ALP} \sim 1.5$. At a certain redshift $z_{\rm crit}$, the value of which depends on the details of the absorption model and of magnetic fields assumed, the two suppression factors are equal, while beyond $z_{\rm crit}$, the absorption becomes stronger and stronger in the intergalactic scenario, remaining constant in the galactic one. This means that for very high redshifts, the anomalous transparency effect would hardly be seen in observations for the intergalactic scenario, therefore any evidence for the effect for very distant sources [2] speaks in favour of the galactic conversion.

Intergalactic magnetic fields.- The intergalactic scenario requires rather high intergalactic magnetic fields (IGMF), $B \sim (10^{-10}$–$10^{-9})$ G, otherwise the conversion probability would be too low. The suppression of the intergalactic conversion is implied in the galactic scenario, so

we refer to $B \lesssim 10^{-11}$ G in this case. Present-day knowledge does not allow for a firm conclusion about real values of B. A number of constraints are summarized in the review [18]. The most stringent observational limit, based on the redshift independence of the Faraday rotation from distant sources, is $B \leq 1.2 \times 10^{-9}$ G [19].

While all three methods to distinguish between the two scenarios favour weakly the galactic conversion mechanism, it is clear that future tests are required both to confirm the anomalous transparency of the Universe and to single out its explanation. To approach the tests on more solid grounds, future observations are necessary. Of particular importance are spectral and anisotropy studies, for which the following directions are especially important. First, to enlarge the overall statistics of TeV blazars, which is best achieved with the coming CTA. Second, to study absorption effects in the spectra of the most distant blazars, for which one needs high-sensitivity observations at energies $\sim$ (10-100) GeV. The sensitivities of both FERMI LAT and CTA [20] are insufficient in this energy range; the solution may be provided by high-altitude low-threshold Cerenkov detectors [21]. Presently, two projects of this kind are under consideration, the ALEGRO in Atacama, Chile, and EGO at the Mount Elbrus, Russia. Third, to move into the strong-absorption energy range for bright nearby blazars, which would require observations at $\sim$ 100 TeV. The proper instruments for that would be extensive-air-shower detectors, in particular, TAIGA [22] and the upgraded Carpet array in Baksan [23] in the nearest future, as well as LHAASO [24] and HiSCORE [25] several years later.

Additional important contributions to the discussion are expected from observational constraints on the IGMF values and, of course, from laboratory searches for the responsible ALP, with the most sensitive planned instruments being IAXO [26] and ALPS-II [27] .

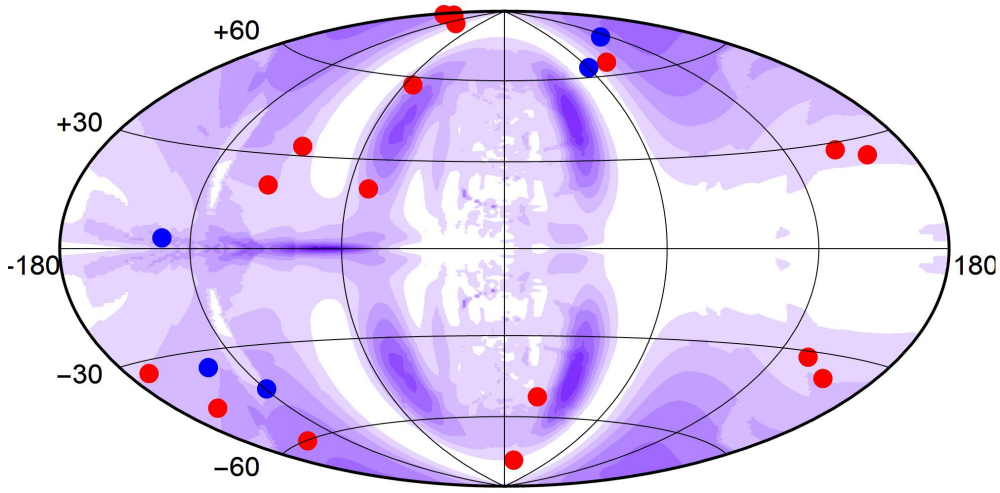

Figure 2: The skymap (Galactic coordinates, Hammer projection) with positions of blazars with detected gamma-ray flux at energies for which $\tau > 1$ (red, $0.1 < z < 1$; blue, $z > 1$), see text. Deeper shading corresponds to higher ALP-photon conversion probability in the Milky Way (the GMF of Ref. [12]).

Acknowledgements

The author is indebted to G. Galanti, M. Meyer, M. Pshirkov, M. Roncadelli and G. Rubtsov for interesting discussions. This work was supported in part by the RFBR grant 13-02-01293.

References

[1] D. Horns and M. Meyer, JCAP **1202**, 033 (2012), arXiv:1201.4711
[2] G. I. Rubtsov and S. V. Troitsky, JETP Lett. **100**, 355 (2014) [Pis'ma ZhETF **100**, 397 (2014)]
[3] G. Galanti *et al.*, arXiv:1503.04436 [astro-ph.HE].
[4] G. Raffelt and L. Stodolsky, Phys. Rev. D **37**, 1237 (1988).
[5] S. Troitsky, arXiv:1507.08640 [astro-ph.HE].
[6] C. Csaki *et al.*, JCAP **0305**, 005 (2003), hep-ph/0302030
[7] A. De Angelis, M. Roncadelli and O. Mansutti, Phys. Rev. D **76**, 121301 (2007), arXiv:0707.4312
[8] M. Simet, D. Hooper and P. D. Serpico, Phys. Rev. D **77**, 063001 (2008), arXiv:0712.2825
[9] M. Fairbairn, T. Rashba and S. V. Troitsky, Phys. Rev. D **84**, 125019 (2011), arXiv:0901.4085
[10] D. Horns *et al.*, Phys. Rev. D **86**, 075024 (2012), arXiv:1207.0776
[11] M. Meyer, D. Horns and M. Raue, Phys. Rev. D **87**, no 3, 035027 (2013), arXiv:1302.1208
[12] D. Harari, S. Mollerach and E. Roulet, JHEP **9908**, 022 (1999), astro-ph/9906309
[13] S. Andriamonje *et al.* [CAST Collaboration], JCAP **0704**, 010 (2007), hep-ex/0702006
[14] A. Ayala *et al.*, Phys. Rev. Lett. **113**, n 19, 191302 (2014), arXiv:1406.6053
[15] A. Payez *et al.*, JCAP **1502**, 02, 006 (2015), arXiv:1410.3747
[16] A. Abramowski *et al.* [HESS Collaboration], Phys. Rev. D **88**, n 10, 102003 (2013)
[17] D. Wouters and P. Brun, JCAP **1401**, 016 (2014), arXiv:1309.6752
[18] R. Durrer and A. Neronov, Astron. Astrophys. Rev. **21**, 62 (2013), arXiv:1303.7121
[19] M. S. Pshirkov, P. G. Tinyakov and F. R. Urban, arXiv:1504.06546
[20] M. Actis *et al.* [CTA Consortium Collaboration], Exper. Astron. **32**, 193 (2011), arXiv:1008.3703.
[21] J. Albert i Fort *et al.*, Astropart. Phys. **23**, 493 (2005).
[22] N. M. Budnev *et al.* [TAIGA Collaboration], JINST **9**, C09021 (2014).
[23] J. Szabelski et al. [Carpet-3 Collaboration], Nucl. Phys. Proc. Suppl. **196**, 371 (2009), arXiv:0902.0252
[24] S. Cui *et al.* [LHAASO Collaboration], Astropart. Phys. **54**, 86 (2014)
[25] M. Tluczykont *et al.*, Adv. Space Res. **48**, 1935 (2011), arXiv:1108.5880.
[26] I. G. Irastorza *et al.*, JCAP **1106**, 013 (2011) arXiv:1103.5334
[27] R. Bahre *et al.*, JINST **8**, T09001 (2013), arXiv:1302.5647

Axion-Photon Coupling: Astrophysical Constraints

Oscar Straniero[1], *Adrián Ayala*[2,3], *Maurizio Giannotti*[4], *Alessandro Mirizzi*[5], *Inma Domínguez*[2]

[1]INAF-Osservatorio di Teramo, Teramo, Italy
[2]University of Granada, Granada, Spain
[3]University of Tor Vergata, Roma, Italy
[4]Barry University, Miami, USA
[5]University of Bari and INFN Bari, Bari, Italy

DOI: http://dx.doi.org/10.3204/DESY-PROC-2015-02/straniero_oscar

We revise the astrophysical bound to the axion-photon coupling, as obtained by comparing $R = N_{HB}/N_{RGB}$, the ratio of the numbers of stars observed in the Horizontal Branch (HB) and in the Red Giant Branch (RGB) of 39 Galactic Globular Clusters with up-to-date theoretical predictions. First results have already been published in a PRL paper in 2014. Here we present a new and more accurate method to calculate the theoretical R, which makes use of synthetic Color-Magnitude diagrams to be directly compared to the observed (real) diagrams. Preliminary results of our analysis are discussed.

1 Introduction

Globular Clusters (GC) are building blocks of any kind of galaxy. They are found in spirals (such as the Milky Way or M31), ellipticals (M87), as well as in Dwarfs Spheroidals or irregular galaxies (e.g. the Magellanic Clouds). Our Galaxy hosts hundreds of GCs. They are preferentially located in the Halo and in the Bulge. A typical GC contains between 10^5 and 10^7 almost coeval stars, as old as 13 Gyr, all linked together by reciprocal gravitational interactions. There exists a growing amount of observational evidences showing that GCs host multiple stellar populations, characterized by diverse chemical compositions.

In a color-magnitude diagram (CM diagram), stars belonging to the same cluster are grouped in distinct sequences (or branches), representing different evolutionary phases. For instance, in the Red Giant Branch (RGB) we find stars that are approching the He-burning phase: a He-rich and H-depleted core develops, rather high densities are attained, so that free electrons become highly degenerate. After the He ignition, these stars will move to the so-called Horizontal Branch (HB), the CM diagram location of core-He-burning stars. HB stars present an extended convective core, powered by the central He burning, surroundend by a semiconvective layer. A shell-H burning is always active in both RGB and HB stars. The number of stars observed in a given portion of the CM diagram is proportional to the time spent by a star in this region, e.g., $N_{RGB} \propto t_{RGB}$, where t_{RGB} is the RGB lifetime of a typical stars presently found in the RGB phase of a Galactic GC. Therefore, the ratio of the numbers of stars observed in the HB and in the RGB portion brighter than the zero-age HB[1], the so-called R parameter, represents

[1]It corresponds to the luminosity of the faintest HB stars.

the ratio of the respective stellar lifetimes:

$$R = \frac{N_{HB}}{N_{RGB}} = \frac{t_{HB}}{t_{RGB}} \tag{1}$$

R does not depend on metallicity and age of the cluster; however, R increases linearly with the He mass fraction (Y). For this reason, measurements of R in GCs have been largely used to estimate the pristine He content of our Galaxy. However, this method requires a detailed knowledge of the stellar lifetimes, usually obtained by means of stellar models. In practice, it relies on our knowledge of all the physical processes that produce or dissipate energy in stellar interiors, such as, for instance, the nuclear reactions or the thermal neutrino energy loss. On the other hand, if the GC He content is known, the R parameter measurements may be used to constrain these physical processes. On this basis, Ref. [4] investigated the axion production by the Primakov process, possibly occurring in the hot stellar interior. By comparing the t_{HB}/t_{RGB} derived from up-to-date stellar models of RGB and HB stars with the average R parameter of a sample of 39 galactic GCs with metallicity [Fe/H]< -1.1 ($R = 1.39 \pm 0.03$), we were able to put a rather strong upper bound for the axion-photon coupling, namely $g_{a\gamma} < 0.66 \times 10^{-10}$ GeV^{-1} (95% C.L.).

2 A step forward

More recently we have developed a new tool to generate *synthetic* CM diagrams. It is based on a more extended set of stellar models and allows us to plot perfect theoretical counterparts of real CM diagrams. For instance, stochastic variations of the position of the points representing stars, such as those due to the mass loss or to the photometric errors, are easily accounted for.

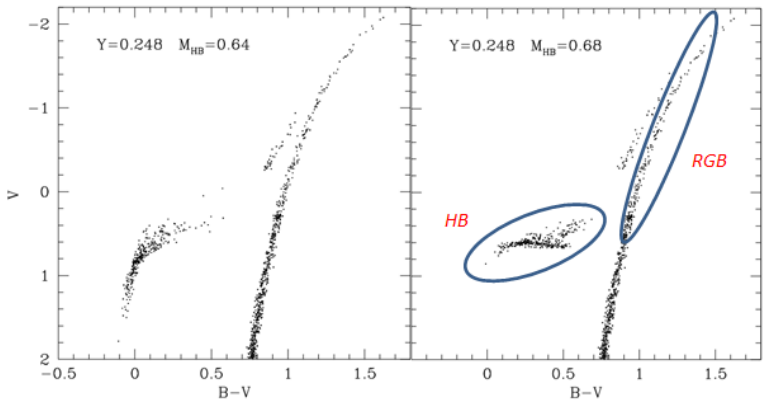

Figure 1: Example of synthetic CM diagrams. The diagram in the left panel has been obtained by assuming a stronger average mass loss rate during the RGB. As a result, the mean mass of HB stars (M_{HB}) is lower than that of the diagram in the right panel. The HB and the RGB portions used in the calculation of the R parameter are surrounded by ellipses.

In this way, we may calculate the *theoretical* R parameter by counting the stars (or their models) found in different branches of the synthetic CM diagram, precisely as we do for real

Parameter	error	Reference
$^{14}\mathrm{N}(p,\gamma)^{15}\mathrm{O}$	7%	[1]
$^{4}\mathrm{He}(2\alpha,\gamma)^{12}\mathrm{C}$	10%	[2]
$^{12}\mathrm{C}(\alpha,\gamma)^{16}\mathrm{O}$	20%	[6]
R	1.39 ± 0.03	[4]
Y	0.255 ± 0.002	[5],[3]

Table 1: List of the 5 parameters varied in the Monte Carlo analysis described in section 3. The first three rows refer to the rates of the 3 more relevant nuclear reactions that directly affect the lifetimes of HB and RGB stellar models. The fourth and the fifth rows contain the average R parameter of the 39 Cluster sample and the initial He mass fraction, respectively. The adopted 1σ errors and the sources of the measurements are listed in columns 2 and 3, respectively.

GCs. A first advantage of this method is that it allows us to reduce or eliminate some systematic uncertainties, such as those due to the determination of the zero-age HB. In addition, we may also estimate the uncertainty due to statistical fluctuations of the photometric sample. At the same time, we may also estimate the influence on the calculated R parameter of all the uncertainties of the stellar models. In particular, we have investigated the uncertainties due to nuclear reaction rates (RGB and HB models), convection (HB models), rate of energy-loss by plasma neutrino (RGB models) and some others. Examples of synthetic CM diagrams are shown in Figure 1.

3 Results

Although our analysis is still in progress, in this section we present some preliminary results. To combine all the uncertainties and obtain the propagation of their errors into the estimated upper bound for the axion-photon coupling, we have used a Monte Carlo method (MC): a sequence of synthetic CM diagrams are generated, each time with a different set of values for the parameters affected by the major uncertainties. The MC generates each set of parameters according to their errors. As an example, here we have considered variations of 5 parameters, namely, the 3 more relevant nuclear reaction rates, the He mass fraction (Y) and the measured R. The assumed values of these 5 parameters and the respective references are reported in Table 1.

Figure 2 illustrates the result of the MC. The axion-photon coupling ($g_{a\gamma}$) depends on the difference between the theoretical R_{th} (computed without axion energy loss) and the measured R_{GCs}: $\theta = R_{th} - R_{GCs}$. Note that R_{th} depends on Y and the 3 relevant reaction rates (see Table 1). In practice, we find that: $g_{a\gamma} = \alpha\theta^2 + \beta\theta$.

4 Conclusions

By means of synthetic CM diagrams, we have calculated the relation between $g_{a\gamma}$ and 5 parameters, namely Y, R, and the 3 more relevant nuclear rates affecting the HB and the RGB lifetimes. By combining the uncertainties on this 5 parameters we find $g_{10} = 0.29 \pm 0.18$, where

$g_{10} = g_{a\gamma}/10^{-10}\mathrm{GeV}^{-1}$, corresponding to an axion-photon upper bound (95% C.L.):

$$g_{10} < 0.65 \tag{2}$$

which confirms our previous finding [4].

The main source of uncertainty of the model is the $^{12}\mathrm{C}(\alpha,\gamma)^{16}\mathrm{O}$ reaction rate. This uncertainty is due to the possible interference between two subthreshold resonances in the $^{16}\mathrm{O}$ ($j^\pi = 1^-,\ 2^+$). Presently available measurements seem to exclude a constructive interference (enhanced rate). However, a destructive interference cannot be excluded yet. It this case, the reaction rate would be reduced down to the 50% of the most probable value. It would imply a systematic decrease of the theoretical R, thus reducing or even cancelling the apparent need of an additional cooling process. New low-energy measurements are required for this important nuclear process. A second issue concerns the adopted He mass fraction. Direct measurements of He abundances are very difficult for Globular Cluster stars, because their atmospheres are too cool to excite He atoms. Alternatively, we have used precise measurements of He abundances in extragalactic HII molecular regions (see Table 1) whose metallicity is in the same range of the galactic GCs. In general, it is expected that these environments experienced a limited chemical evolution (as the low metallicity testifies), so that their Y should be close to the primordial one. Note that the value of Y obtained from low-Z HII clouds is in tension with the standard prediction of primordial nucleosynthesis calculations and with results of the latest CMB analysis from the PLANCK collaboration. Note that with a lower Y, the need of an additional energy sink in HB stars disappears.

Summarizing, while the upper bound for the axion-photon coupling, as derived from the analysis of the R parameters of galactic GCs, is a firm result, the occurrence of a measured R lower than that predicted by stellar models (without axion energy loss) cannot be considered a proof of the existence of these particles.

References

[1] Adelberger, E. G., García, A., Robertson, R. G. H. et al., Reviews of Modern Physics **83**, 195 (2011).

[2] Angulo, C. et al., Nuclear Physics A **3**, 656 (1999).

[3] Aver, E., Olive, K. A., & Skillman, E. D., JCAP **7**, 011 (2015).

[4] Ayala A., Domínguez I., Giannotti M., Mirizzi A. & Straniero O., Phys. Rev. Lett. **113**, 191302 (2014).

[5] Izotov, Y. I., Thuan, T. X., & Guseva, N. G., MNRAS, **445** 778 (2014).

[6] Schürmann, D., Gialanella, L., Kunz, R. & Strieder, F., Physics Letters B, **35** 711 (2012).

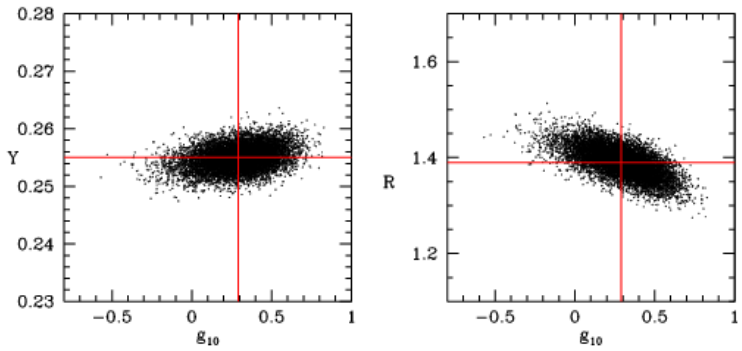

Figure 2: Monte Carlo results. These plots show the values of g_{10} as obtained by varying the 5 parameters listed in Table 1 as a function of two of them, i.e. the Globular Cluster R parameter (right panel) and the He mass fraction (Y, left panel). R and Y are varied according to a normal error function with the 1σ errors reported in column 2 of Table 1. Similar plots may be obtained for the 3 most relevant nuclear reaction rates.

ALPs Explain the Observed Redshift-Dependence of Blazar Spectra

Marco Roncadelli[1], *Giorgio Galanti*[2], *Alessandro De Angelis*[3], *Giovanni F. Bignami*[4]

[1]INFN Pavia, Pavia, Italy,
[2]Dipartimento di Fisica, Universitá dell'Insubria, Como, Italy
[3]INFN Padova, Padova, Italy
[4]INAF Roma, Roma, Italy

DOI: http://dx.doi.org/10.3204/DESY-PROC-2015-02/roncadelli_marco

We considered a complete sample of blazars observed with the Imaging Atmospheric Cherenkov Telescopes above $E \geq 80\,\mathrm{GeV}$, out to $z = 0.54$ and described by standard photon emission models which predict simple power-law spectra to a good approximation. We first show that the best-fit regression line of the emitted slope distribution $\{\Gamma_{\rm em}(z)\}$ decreases with z, in disagreement with physical intuition. Next, we demonstrate that, by allowing for photon-ALP oscillations in intergalactic space, for a realistic values of the parameters the best-fit regression line becomes exactly horizontal in the $\Gamma_{\rm em} - z$ plane. This result is amazing, because it is the only possibility in agreement with physical expectation, and so it can be regarded as a strong hint of the existence of an ALP.

1 Introduction and background

Thanks to the observations carried out with the Imaging Atmospheric Cherenkov Telescopes (IACTs) like H.E.S.S., MAGIC and VERITAS, according to the Tevcat catalog 43 blazars with known redshift have been detected in the VHE range. We stress that 40 of them are in a flaring state, whose typical lifetime ranges from a few hours to a few days. As far as the present analysis is concerned, 3 of them 1ES 0229+200, PKS 1441+25 and S3 0218+35 will be discarded for reasons to be explained below. All observed spectra of the considered VHE blazars are well fitted by a single power-law, and so they have the form $\Phi_{\rm obs}(E_0, z) = K_{\rm obs}(z)\, E_0^{-\Gamma_{\rm obs}(z)}$, where E_0 is the observed energy, while $K_{\rm obs}(z)$ and $\Gamma_{\rm obs}(z)$ denote the observed normalization constant and the slope, respectively, for a source at redshift z. So, we will be dealing with a sample of 40 blazars, whose $\Gamma_{\rm obs}$ values are plotted versus z in Fig. 1 with their error bars.

Unfortunately, the observational results do not provide any *direct* information about the intrinsic properties of the sources, since the VHE gamma-ray data strongly depend on the nature of photon propagation. Indeed, according to conventional physics the blazar spectra in the VHE range are strongly affected by the presence of the Extragalactic Background Light (EBL), namely the infrared/optical/ultraviolet background photons produced by stars throughout the history of the Universe [1]. This effect has been quantified in [2]. VHE photons with energy E emitted by a blazar at z get depleted by scattering off EBL photons of energy ϵ through the

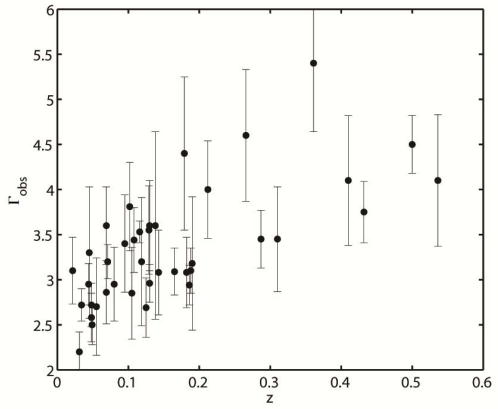

Figure 1: The values of the slope $\Gamma_{\rm obs}$ are plotted versus the source redshift z for all considered blazars.

process $\gamma_{\rm VHE} + \gamma_{\rm EBL} \to e^+ + e^-$ whose Breit-Wheeler cross-section gets maximized when

$$\epsilon(E) \simeq \left(\frac{900\,{\rm GeV}}{E}\right)\,{\rm eV}\ . \tag{1}$$

So, for $100\,{\rm GeV} < E < 100\,{\rm TeV}$ $\sigma(\gamma\gamma \to e^+e^-)$ is maximal for $9 \cdot 10^{-3}\,{\rm eV} < E < 9\,{\rm eV}$, indeed in the EBL band. After a long period of uncertainty, today the spectral energy distribution (SED) of the EBL is well determined, and for definiteness we use the model of Franceschini, Rodighiero and Vaccari (FRV) which provides the optical depth $\tau_\gamma(E_0, z)$ [3].

As a rule, the blazar SED of the non-thermal radiation shows two broad humps, the first one peaking at low frequency – from IR to soft-X rays, depending on the specific source – while the second one in the gamma-ray band, often reaching multi-TeV energies. We restrict our discussion to the two standard competing models for the VHE photon emission by blazars, namely the Synchrotron-Self-Compton (SSC) mechanism and the Hadronic Pion Production (HPP) in proton-proton scattering. Both mechanisms predict emitted spectra which, to a good approximation, have a single power-law behavior $\Phi_{\rm em}(E) = K_{\rm em}(z)\,E^{-\Gamma_{\rm em}}$ for all observed VHE blazars, where $E = (1+z)E_0$ is the emitted energy, whereas $K_{\rm em}(z)$ and $\Gamma_{\rm em}$ are the emitted normalization constant and slope, respectively.

The relation between $\Phi_{\rm obs}(E_0, z)$ and $\Phi_{\rm em}(E)$ can be expressed in general terms as

$$\Phi_{\rm obs}(E_0, z) = P_{\gamma\to\gamma}(E_0, z)\,\Phi_{\rm em}\big(E_0(1+z)\big)\ , \tag{2}$$

where $P_{\gamma\to\gamma}(E_0, z)$ is the photon survival probability from the source to us, and in conventional physics it is written in terms of the optical depth $\tau_\gamma(E_0, z)$ as

$$P_{\gamma\to\gamma}(E_0, z) = e^{-\tau_\gamma(E_0, z)}\ . \tag{3}$$

We should also mention that a radically different mechanism has been put forward. Basically, the idea is that *protons* are accelerated inside blazars up to energies of order $10^{11}\,{\rm GeV}$, while VHE emitted photons are neglected altogether. When the proton distance from the Galaxy is

in the range $10 - 100\,\mathrm{Mpc}$, they scatter off EBL photons through the process $p + \gamma \to p + \pi^0$, so that the immediate decays $\pi^0 \to \gamma + \gamma$ produce an electromagnetic shower of secondary photons: it is *these photons* that replace the emitted photons in such a scenario [4]. Such a mechanism can apply only to the 3 sources detected so far which have a constant VHE luminosity [5, 6]. Actually, an analysis of the properties of the blazar 1ES 0229+200 has shown that it hardly fits within the photon emission models, and since its VHE luminosity is constant, this source is more likely explained by the proton emission model [7]. For this reason, we discard it from our discussion.

We also discard PKS 1441+25 and S3 0218+35 because they have $z \simeq 0.94$, since we want to consider only a relatively local sample with extend up to $z \simeq 0.54$ (3C 279).

Finally, we are in position to state the main goal of the work reported in this talk, namely to investigate a possible correlation between the distribution of VHE blazar *emitted spectra* and the *redshift*.

Superficially, the reader might well wonder about such a question. Why should a correlation of this kind be expected? Cosmological evolutionary effects are certainly harmless out to redshift $z \simeq 0.5$, and when observational selection biases are properly taken into account no such a correlation should show up.

As we shall see, this is *not the case*. Indeed, a statistical analysis of the $\{\Gamma_{\rm em}(z)\}$ distribution performed within conventional physics implies that the resulting best-fit regression line *decreases with increasing redshift*. So, how can the source distribution get to know the redshifts in such a way to adjust their individual $\Gamma_{\rm em}(z)$ values so as to reproduce such a statistical correlation? In particular, it implies that blazars with harder spectra are found *only* at larger redshift. While this trend might be interpreted as an observational selection effect, a deeper scrutiny based on observational information shows that this is by no means the case. Thus, we are led to the conclusion that such a behavior is at odd with physical intuition, which would instead demand the best-fit regression line to be redshift-independent.

As an attempt to achieve a physically satisfactory scenario, we put Axion-Like Particles (ALP) into the game [8]. They are spin-zero, neutral and extremely light pseudo-scalar bosons predicted by several extensions of the Standard Model of particle physics, and especially by those based on superstring theories. They are supposed to interact only with two photons. Depending on their mass and two-photon coupling, they can be quite good candidates for cold dark matter and give rise to very interesting astrophysical effects, so that nowadays ALPs are attracting growing interest. Specifically, we suppose that photon-ALP oscillations take place in extragalactic magnetic fields of strength about $0.1\,\mathrm{nG}$ – in agreement with the predictions of the galactic outflows models [9, 10] – as first proposed in [11]. Amazingly, for and ALP mass $m < 10^{-9}\,\mathrm{eV}$ and a two-photon coupling consistent with the CAST bound now the best-fit regression line of the $\{\Gamma_{\rm em}(z)\}$ distribution becomes exactly horizontal in the $\Gamma_{\rm em} - z$ plane, namely redshift-independent. This fact leads in turn to a very simple new picture of VHE blazars.

A much more thorough discussion of these matters along with a complete list of references can be found in our original paper [12].

2 Conventional propagation in extragalactic space

We start by deriving the emitted spectrum of every source, starting from the observed ones.

As a first step, we rewrite Eq. (2) as

$$\Phi_{\rm em}\big(E_0(1+z)\big) = e^{\tau_\gamma(E_0,z)}\, K_{\rm obs}(z)\, E_0^{-\Gamma_{\rm obs}(z)} \ . \tag{4}$$

Next, we best-fit $\Phi_{\rm em}\big(E_0(1+z)\big)$ to a single power-law with slope $\Gamma^{\rm CP}_{\rm em}(z)$ – namely to $K^{\rm CP}_{\rm em}(z)\,\big[(1+z)E_0\big]^{-\Gamma^{\rm CP}_{\rm em}(z)}$ – over the energy range ΔE_0 where the source is observed. Finally, we plot the values of $\Gamma^{\rm CP}_{\rm em}$ versus z in the left panel of Fig. 2

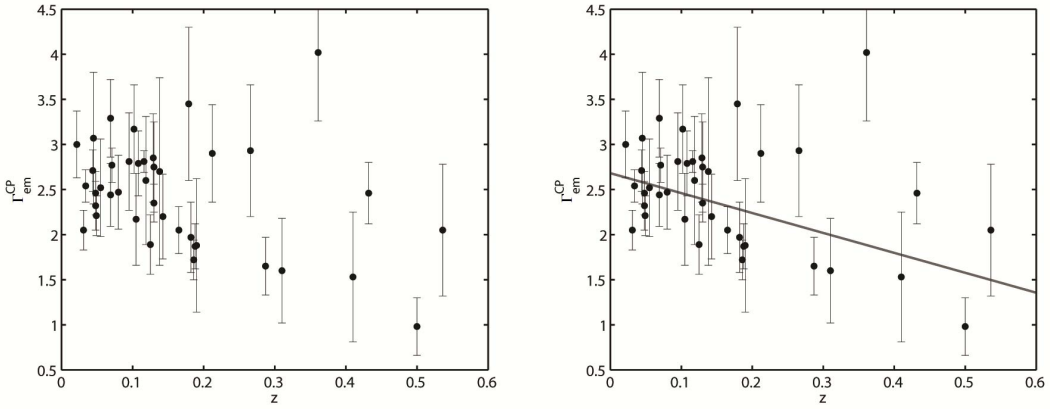

Figure 2: *Left panel:* The values of the slope $\Gamma^{\rm CP}_{\rm em}$ are plotted versus the source redshift z for all considered blazars. *Right panel:* Same as the left panel but with superimposed the best-fit straight regression line.

We proceed by performing a statistical analysis of all values of $\Gamma^{\rm CP}_{\rm em}(z)$ as a function of z. We use the least square method and try to fit the data with one parameter (horizontal straight line), two parameters (first-order polynomial), and three parameters (second-order polynomial). In order to test the statistical significance of the fits we compute the corresponding $\chi^2_{\rm red}$. The values of the $\chi^2_{\rm red}$ obtained for the three fits are 2.35, 1.83 and 1.87, respectively. Thus, data appear to be best-fitted by the first-order polynomial $\Gamma^{\rm CP}_{\rm em}(z) = 2.68 - 2.21\, z$. The distribution of $\Gamma^{\rm CP}_{\rm em}(z)$ as a function of z – with superimposed the best-fit straight regression line as defined by the last equation – is plotted in the right panel of Fig. 2

Manifestly, the $\{\Gamma^{\rm CP}_{\rm em}\}$ distribution shows a nontrivial redshift-dependence. What is the *physical meaning* of this fact? Note that it implies a large variation of the the emitted flux with redshift, since we have

$$\Phi^{\rm CP}_{\rm em}(E,0) \propto E^{-2.68} \ , \qquad\qquad \Phi^{\rm CP}_{\rm em}(E,0.6) \propto E^{-1.35} \ . \tag{5}$$

Because we are dealing with a relatively local sample of blazars, cosmological evolutionary effects are totally irrelevant. Moreover, we have checked that that all possible selection biases play no role. Thus, it looks mysterious how the source distribution can get to know the redshifts in such a way to adjust their individual $\Gamma_{\rm em}(z)$ values so as to reproduce such a bets-fit straight regression line.

3 Photon-ALP oscillations in extragalactic space

Let us now turn our attention to an extension of the Standar Model containing ALPs – to be denoted by a – which are supposed to interact only with two photons through a term $g_{a\gamma\gamma}\mathbf{E}\cdot\mathbf{B}$ in the Lagrangian. We take the ALP mass $m < 10^{-9}\,\mathrm{eV}$ and $g_{a\gamma\gamma} < 0.88\cdot 10^{-10}\,\mathrm{GeV}^{-1}$ in order to be consistent with the very robust CAST bound. Here $\mathbf{E}$ is the electric field of a propagating VHE photon while $\mathbf{B}$ denotes the extragalactic magnetic fields of strength about $0.1\,\mathrm{nG}$ – in agreement with the predictions of the galactic outflows models [9, 10] – as first proposed in [11]. Moreover, $\mathbf{B}$ is supposed to have a domain-like structure with coherence length $L_{\rm dom}$ in the range $1-10\,\mathrm{Mpc}$, with a direction randomly changing from one domain to the next keeping however the same strength. In such a situation energy-conserving and mass-independent photon-ALP oscillations take place in extragalactic space. As a consequence, photons acquire a split personality, traveling for some time as real photons – which suffer EBL absorption – and for some time as ALPs, which are unaffected by the EBL. Therefore, $\tau_\gamma(E_0,z)$ gets replaced by the effective optical depth $\tau_\gamma^{\rm eff}(E_0,z)$, which is manifestly *smaller* than $\tau_\gamma(E_0,z)$ and is a monotonically increasing function of E_0 and z. The crux of the argument is that since the photon survival probability is now $P^{\rm ALP}_{\gamma\to\gamma}(E_0,z)=e^{-\tau_\gamma^{\rm eff}(E_0,z)}$, even a *small* decrease of $\tau_\gamma^{\rm eff}(E_0,z)$ with respect to $\tau_\gamma(E_0,z)$ gives rise to a *large* increase of the photon survival probability, as compared to the case of conventional physics. Hence, the main consequence of photon-ALP oscillations is to *substantially attenuate* the EBL absorption and consequently to considerably enlarging the conventional γ-ray horizon [2].

Needless to say, $P^{\rm ALP}_{\gamma\to\gamma}(E_0,z)$ can be computed exactly in term of two parameters $\xi\propto g_{a\gamma\gamma}\,B$ and $L_{\rm dom}$. Realistic values of these parameters are $\xi=0.1,0.5,1,5$ and $L_{\rm dom}=4\,\mathrm{Mpc},10\,\mathrm{Mpc}$, which will be regarded as our benchmark values.

Henceforth, we proceed in parallel with the discussion in Section 2. Hence, we start by rewriting Eq. (2) as

$$\Phi^{\rm ALP}_{\rm em}\big(E_0(1+z)\big)=\Big(P^{\rm ALP}_{\gamma\to\gamma}(E_0,z)\Big)^{-1}\,K_{\rm obs}(z)\,E_0^{-\Gamma_{\rm obs}(z)}\ . \tag{6}$$

Next, we best-fit $\Phi_{\rm em}\big(E_0(1+z)\big)$ to a single power-law with spectral index $\Gamma^{\rm ALP}_{\rm em}(z)$ – namely to $K^{\rm ALP}_{\rm em}(z)\,\big[(1+z)E_0\big]^{-\Gamma^{\rm ALP}_{\rm em}(z)}$ – over the energy range ΔE_0 where the source is observed. This procedure is performed for each benchmark value of ξ and $L_{\rm dom}$. Finally, we carry out a statistical analysis of all values of $\Gamma^{\rm ALP}_{\rm em}(z)$ as a function of z – again for all benchmark values of ξ and $L_{\rm dom}$ – along the same lines of Section 2. The best-fitting procedure selects out the two following preferred cases: $L_{\rm dom}=4\,\mathrm{Mpc}$, $\xi=0.5$, $\Gamma^{\rm ALP}_{\rm em}=2.52$ and $\chi^2_{\rm red}=1.43$ and $L_{\rm dom}=10\,\mathrm{Mpc}$, $\xi=0.5$, $\Gamma^{\rm ALP}_{\rm em}=2.58$ and $\chi^2_{\rm red}=1.39$. Manifestly, in either case the best fit straight regression line in redshift independent, in perfect agreement with physical intuition. Both situations are plotted in Fig.3.

4 Conclusions

An ALP with $m<10^{-9}\,\mathrm{eV}$ and $g_{a\gamma\gamma}\sim 10^{-11}\,\mathrm{GeV}^{-1}$ remarkably achieves three important results. First, it explains the *pair-production anomaly* [13, 14]. Second, it allows flat spectrum radio quasars to emit in the VHE band [15]. Third, it provides a new view of VHE blazars, in which 95 % of them have a small spread in the values of $\Gamma^{\rm ALP}_{\rm em}(z)$ (they lie in the grey band of

Fig. 3) which gets amplified in the values of $\Gamma_{\rm obs}$ due to the last scatter in their redshift. All this taken together provides a preliminary evidence for the existence of an ALP.

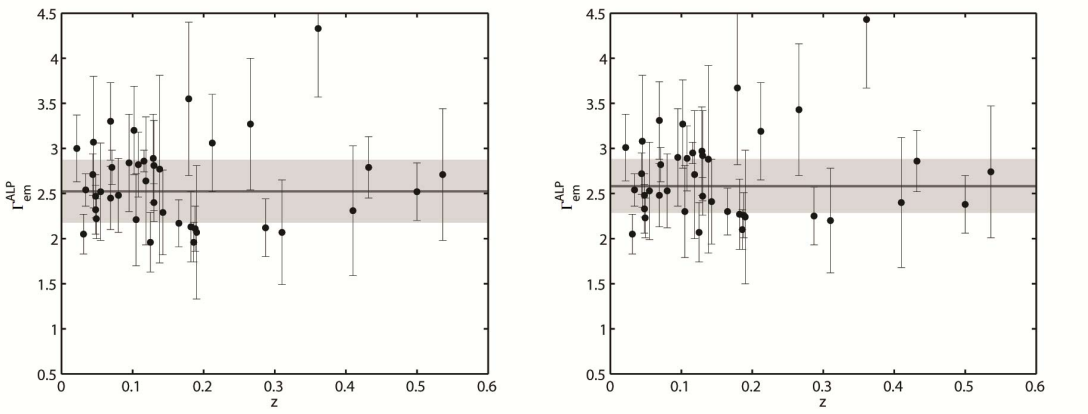

Figure 3: *Left panel:* The values of the slope $\Gamma_{\rm em}^{\rm ALP}$ are plotted versus the source redshift z for all considered blazars in the case $L_{\rm dom} = 4\,{\rm Mpc}$. Superimposed are the horizontal best-fit straight regression line and a grey band encompassing 95 % of the considered sources. *Right panel:* Same as left panel but for the case $L_{\rm dom} = 10\,{\rm Mpc}$.

References

[1] E. Dwek, F. Krennrich, Astroparticle Phys. **43**, 112 (2013).

[2] A. De Angelis, G. Galanti and M. Roncadelli, Mon. Not. R. Astron. Soc. **432**, 3245 (2013).

[3] A. Franceschini, G. Rodighiero, E. Vaccari, Astron. Astrophys. **487**, 837 (2008).

[4] W. Essey and A. Kusenko, Astroparticle Physics **33**, 81 (2010).

[5] A. Prosekin, W. Essey, A. Kusendo and F. Aharonian, Astrophys. J. **757**, 183 (2012).

[6] K. Murase, C. D. Dermer, H. Takami and G. Migliori, Astrophys. J. **749**, 63 (2012).

[7] G. Bonnoli, F. Tavecchio, G. Ghisellini and T. Sbarrato, arxiv:1501.01974.

[8] J. Jaeckel and A Ringwald, Ann. Rev. Nucl. Part. Sci. **60**, 405 (2010).

[9] S. R. Furlanetto and A. Loeb, Astrophys. J. **556**, 619 (2001).

[10] S. Bertone, C. Vogt and T. Ensslin, Mon. Not. R. Astron. Soc. **370**, 319 (2006).

[11] A. De Angelis, M. Roncadelli, O. Mansutti, Phys. Rev. D **76**, 121301 (2007).

[12] G. Galanti, M. Roncadelli, A. De Angelis and G. F. Bignami, arxiv:1503.04436.

[13] D. Horns and M. Meyer, JCAP **02**, 033 (2012).

[14] M. Meyer, D. Horns and M. Raue, Phys. Rev. D **87**, 035027 (2013).

[15] F. Tavecchio, M. Roncadelli, G. Galanti and G. Bonnoli, Phys. Rev. D **86**, 085036 (2012).

Status of the ANAIS Dark Matter Project at the Canfranc Underground Laboratory

J. Amaré, S. Cebrián, C. Cuesta, E. García, M. Martínez,† M. A. Oliván,‡ Y. Ortigoza, A. Ortiz de Solórzano, C. Pobes,§ J. Puimedón, M.L. Sarsa, J.A. Villar, P. Villar*

Laboratorio de Física Nuclear y Astropartículas, Universidad de Zaragoza, Zaragoza, Spain and Laboratorio Subterráneo de Canfranc, Canfranc Estación, Huesca, Spain

DOI: http://dx.doi.org/10.3204/DESY-PROC-2015-02/olivan_miguel_talk

The ANAIS experiment aims at the confirmation of the DAMA/LIBRA signal. A detailed analysis of two NaI(Tl) crystals of 12.5 kg each grown by Alpha Spectra will be shown: effective threshold at 1 keVee is at reach thanks to outstanding light collection and robust PMT noise filtering protocols and the measured background is well understood down to 3 keVee, having quantified K, U and Th content and cosmogenic activation in the crystals. A new detector was installed in Canfranc in March 2015 together with the two previous modules and preliminary characterization results will be presented. Finally, the status and expected sensitivity of the full experiment with 112 kg will be reviewed.

1 The ANAIS experiment

The ANAIS (Annual modulation with NaI Scintillators) project is intended to search for dark matter annual modulation with ultrapure NaI(Tl) scintillators at the Canfranc Underground Laboratory (LSC) in Spain, in order to provide a model-independent confirmation of the signal reported by the DAMA/LIBRA collaboration [1] using the same target and technique. Similar performance to DAMA/LIBRA detectors in terms of threshold and background are consequently mandatory. The total active mass will be divided into modules, each consisting of a 12.5 kg NaI(Tl) crystal encapsulated in copper and optically coupled to two photomultipliers (PMTs) working in coincidence. Nine modules in a 3×3 matrix are expected to be set-up at LSC along 2016. The shielding for the experiment consists of 10 cm of archaeological lead, 20 cm of low activity lead, 40 cm of neutron moderator, an anti-radon box, and an active muon veto system made up of plastic scintillators covering the top and sides of the whole set-up. The experiment hut at the hall B of LSC (under 2450 m.w.e.) is already operative and shielding materials, selected Hamamatsu R12669SEL2 PMTs and electronic chain components are ready. The main challenge of the project has been the achievement of the required crystal radiopurity. A 9.6 kg NaI(Tl) crystal made by Saint-Gobain was first operated [2–5] but disregarded due

*Present address: Department of Physics, Center for Experimental Nuclear Physics and Astrophysics, University of Washington, Seattle, WA, USA

†Present address: Università di Roma La Sapienza, Roma, Italy

‡Attending author

§Present address: Instituto de Ciencia de Materiales de Aragón, Universidad de Zaragoza-CSIC, Zaragoza, Spain

^{40}K (mBq/kg)	^{238}U (mBq/kg)	^{210}Pb (mBq/kg)	^{232}Th (mBq/kg)
1.25 ± 0.11 (41 ppb K)	0.010 ± 0.002	3.15	0.0020 ± 0.0008

Table 1: Internal activity measured in the ANAIS-25 detectors.

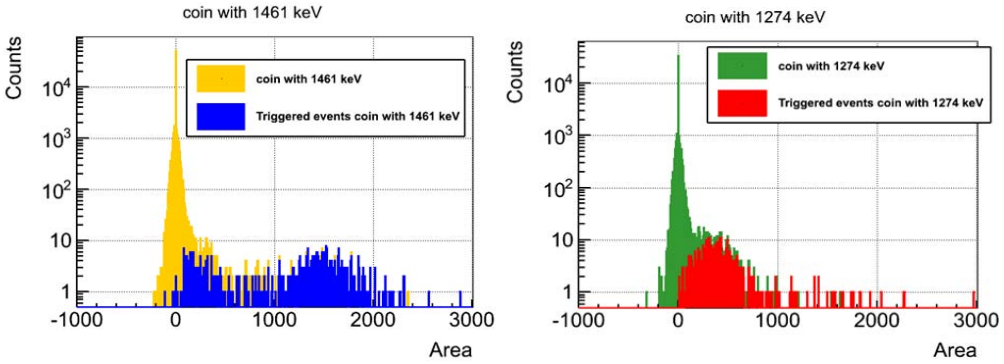

Figure 1: ANAIS-25 D0 coincident events at low energy for ^{40}K (left) and for ^{22}Na (right).

to an unacceptable K content. Two prototypes of 12.5 kg mass, made by Alpha Spectra, Inc. Colorado with ultrapure NaI powder, took data at the LSC since December 2012 (ANAIS-25 set-up) and a new module also built by Alpha Spectra using improved protocols for detector production was added in March 2015 (ANAIS-37 set-up).

2 The ANAIS-25 and ANAIS-37 set-ups

The main goals for the ANAIS-25 set-up [6] were to measure the crystal contamination, evaluate light collection, fine-tune the data acquisition and test the filtering and analysis protocols. The two modules (named D0 and D1) are cylindrical, 4.75" in diameter and 11.75" in length, with quartz windows for PMTs coupling. A Mylar window in the lateral face allows for low energy calibration. After testing other PMT models, Hamamatsu R12669SEL2 units were used for both detectors. The modules were shielded by 10 cm of archaeological plus 20 cm of low activity lead at LSC. An impressive light collection at the level of ∼15 phe/keV has been measured for these detectors [7]. Background contributions have been thoroughly analyzed and Table 1 shows the results of the activities determined for the main crystal contaminations: ^{40}K content has been measured performing coincidence analysis between 1461 keV and 3.2 keV energy depositions in different detectors [4] and the activities from ^{210}Pb and ^{232}Th and ^{238}U chains have been deduced by quantifying Bi/Po sequences and the total alpha rate determined through pulse shape analysis. The content of ^{40}K, above the initial goal of ANAIS (20 ppb of K), is acceptable, ^{232}Th and ^{238}U activities are low enough but an out-of-equilibrium activity of ^{210}Pb at the mBq/kg level was observed, precluding the background goals of the experiment. Cosmogenic radionuclide production in NaI(Tl) was also quantified [8] and ^{22}Na and ^{3}H were found to be very relevant in the region of interest. A complete background model of ANAIS-25 data has been developed [9] and the measured background is well understood down to 3 keVee.

The low energy events populations from internal ^{40}K and ^{22}Na have been studied. The K-shell electron binding energy following electron capture in ^{40}K (3.2 keV) and ^{22}Na (0.9 keV) can be tagged by the coincidence with a high energy γ-ray in a second detector (1461 keV

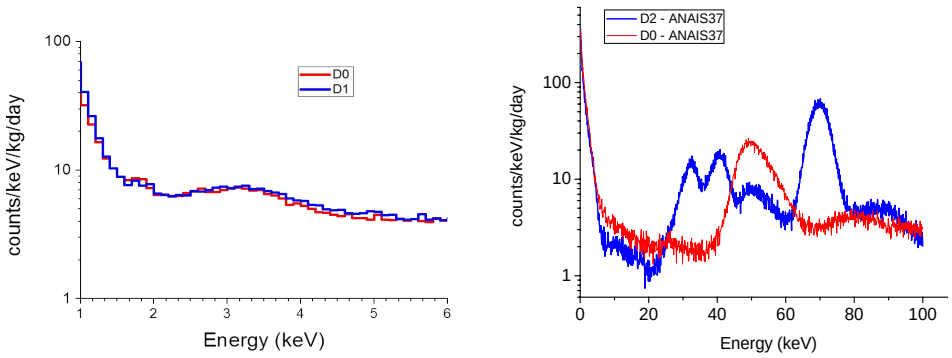

Figure 2: Left: Preliminary filtered background spectra corrected by triggering and filtering efficiencies for ANAIS-25 detectors D0 and D1 (filtering procedures still being optimized). Right: Raw background spectra of D0 and D2 detectors measured at the ANAIS-37 set-up.

and 1274 keV respectively). In Figure 1 both populations are shown, together with the events effectively triggering our acquisition. It can be concluded that triggering at 1 keVee is clearly achieved in ANAIS-25 and therefore an energy threshold of the order of 1 keVee is at reach. To remove the PMT origin events, dominating the background below 10 keVee, and then reach the 1 keVee threshold, specific filtering protocols for ANAIS-25 detectors have been designed following [2]. A preliminary spectrum, after filtering and correcting for the efficiencies of the cuts, determined with low energy events from a ^{109}Cd calibration, is shown in Fig. 2 (left).

The origin of the large ^{210}Pb contamination found in ANAIS-25 crystals was identified and addressed by Alpha Spectra in the construction of the new module (named D2) integrated in the ANAIS-37 set-up. Very preliminary results corresponding to 50 days of live-time are presented here for D2. A total alpha rate of 0.58 ± 0.01 mBq/kg has been obtained, which is a factor 5 lower than in D0 and D1, concluding that effective reduction of Rn entrance in the growing and/or purification at Alpha Spectra has been achieved. A K content of 44 ± 4 ppb compatible with that of D0 and D1 (see Table 1) has been measured using the same technique applied to previous prototypes. The measured light collection of D2 is compatible with that of ANAIS-25 detectors too [7] and the measured background of the new module is well described by the expected components [9]. Figure 2 (right) compares the raw background spectra of D0 and D2 in the ANAIS-37 setup; in spite of the presence of cosmogenic activation in D2 (still decaying) there is a very promising reduction of the background level below 20 keVee.

3 Sensitivity

Figure 3 (left) shows the design for the full ANAIS experiment considering a 3×3 crystal configuration. Prospects of the sensitivity to the annual modulation in the WIMP mass–cross-section parameter space are shown in Fig. 3, right for a 100 kg configuration and 5 years of data taking. The analysis window considered is from 1 to 6 keVee. The background assumed is the one measured in ANAIS-25 (shown in Fig. 2), but with the ^{210}Pb activity measured in the new module D2, i.e. the contribution of 2.57 mBq/kg of ^{210}Pb has been subtracted to the background measured at ANAIS-25. Further reduction from anticoincidence measurements, dependent on the detector matrix assumed, is expected. A conservative approach to derive these

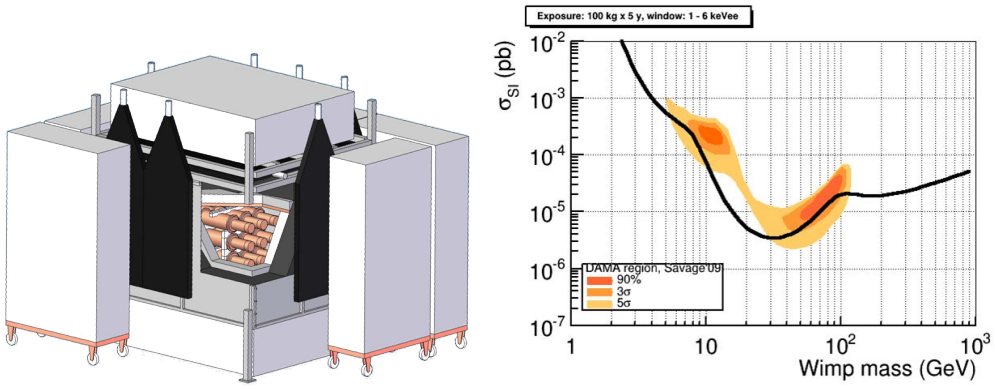

Figure 3: Left: Design of the ANAIS experiment for a 3×3 crystal matrix with a total mass of 112 kg. Right: Prospects of ANAIS annual modulation sensitivity for 100 kg total detection mass, presently achieved background without profiting from anticoincidence rejection, five years of data taking and an energy window from 1 to 6 keVee. These prospects correspond to a detection limit at 90% CL with a critical limit at 90% CL, following [10].

prospects has been followed, but even in this case, there is a considerable discovery potential of dark matter particles as responsible of the DAMA/LIBRA signal.

Acknowledgments

This work was supported by the Spanish Ministerio de Economía y Competitividad and the European Regional Development Fund (MINECO-FEDER) (FPA2011-23749, FPA2014-55986-P), the Consolider-Ingenio 2010 Programme under grants MULTIDARK CSD2009-00064 and CPAN CSD2007-00042, and the Gobierno de Aragón (Group in Nuclear and Astroparticle Physics, ARAID Foundation). P. Villar is supported by the MINECO Subprograma de Formación de Personal Investigador. We also acknowledge LSC and GIFNA staff for their support.

References

[1] R. Bernabei *et al.*, Eur. Phys. J. C **73**, 2648 (2013).

[2] C. Cuesta *et al.*, Eur. Phys. J. C **74**, 3150 (2014).

[3] S. Cebrián *et al.*, Astropart. Phys. **37**, 60 (2012).

[4] C. Cuesta *et al.*, Int. J. of Mod. Phys. A. **29**, 1443010 (2014).

[5] C. Cuesta *et al.*, Opt. Mat. **36**, 316 (2013).

[6] J. Amaré *et al.*, Nucl. Instrum. Meth. A **742**, 197 (2014).

[7] J. Amaré *et al.*, "Light collection in the prototypes of the ANAIS dark matter project", in these proceedings.

[8] J. Amaré *et al.*, JCAP **02**, 046 (2015).

[9] J. Amaré *et al.*, "Background model of NaI(Tl) detectors for the ANAIS dark matter project", in these proceedings.

[10] S. Cebrián *et al.*, Astropart. Phys. **14**, 339350 (2001).

New Axion and Hidden Photon Constraints from a Solar Data Global Fit

Núria Vinyoles[1], *Aldo Serenelli*[1], *Francesco Villante*[2], *Sarbani Basu*[3], *Javier Redondo*[4], *Jordi Isern*[1]

[1]Institute of Space Sciences (CSIC-IEEC), Campus UAB, 08193 Cerdanyola del Vallès, Spain
[2]Dipartimento di Scienze Fisiche e Chimiche, Università dell'Aquila, I-67100 L'Aquila, Italy
[3]Department of Astronomy, Yale University, PO Box 208101, New Haven, CT 06520, USA
[4]Departamento de Física Teórica, Universidad de Zaragoza, 50009 Zaragoza, Spain

DOI: http://dx.doi.org/10.3204/DESY-PROC-2015-02/vinyoles_nuria

We present a new statistical analysis that combines helioseismology and solar neutrino observations to place upper limits to the properties of non standard weakly interacting particles. We present two applications to test the method: the well studied case of axions and the more novel case of low mass hidden photons. For axions we obtain an upper limit at 3σ for the axion-photon coupling constant of $g_{a\gamma} < 4.1 \cdot 10^{-10}\mathrm{GeV}^{-1}$. For hidden photons we obtain the most restrictive upper limit available accross a wide range of masses for the product of the kinetic mixing and mass of $\chi m < 1.8 \cdot 10^{-12}\mathrm{eV}$ at 3σ. Both cases improve the previous solar constraints based on the Standard Solar Models.

1 Introduction

Many studies have focused on using the Sun for setting limits on the properties of different types of exotic particles. The Sun is by far the best-known star. The solar structure, revealed by helioseismology and solar neutrinos, is well determined, and accurate solar models give us information about the past, present and the future of the Sun [1]. While in some cases (e.g. axions) the most restrictive limits are not inferred from solar studies, the Sun remains the most useful benchmark for testing and validating both stellar models and different statistical approaches to constrain particle properties. Also, it is important to keep in mind that CAST [2] and the forthcoming IAXO [3, 4] are experiments specifically designed to detect exotic particles directly from the Sun, so having predictions of upper limits for expected solar fluxes for exotic particles remains an important aspect to be considered.

Solar constraints on particle properties have been generally derived from applying limits to variations of either neutrino fluxes [5, 6] or the sound speed profile derived from helioseismology [5]. However, a systematic approach aimed at combining different sources of data accounting in detail for the observational and theoretical errors is badly missing in literature.

The goal of this work is to extend the general statistical approach presented in [7] to constrain properties of particles (e.g. mass, coupling constant) making the best possible use of all the available information of the Sun, both observational and theoretical. For this purpose, we use the helioseismic data combined with the neutrino fluxes in a statistical approach that includes the theoretical and observational uncertainties and takes into account possible tensions among

data and solar model input parameters. We then derive solar limits for the well-studied hadronic axions –to gauge the performance of our statistical approach– and for the more novel case of hidden photons for which the Sun sets the most restrictive limits on the kinetic mixing parameter for small hidden photon masses, $m \lesssim$eV.

2 Standard Solar Models

In this work we use standard solar models (SSMs) as reference models. SSMs have been computed using GARSTEC [8] and are calibrated to match the present-day solar radius $R_\odot = 6.9598 \cdot 10^{10}$ cm, luminosity $L_\odot = 3.8418 \cdot 10^{33}$ erg s^{-1} and surface metal-to-hydrogen ratio $(Z/X)_\odot$. The choice of this last constraint is critical because it essentially determines the distribution of metals in the entire solar structure and it has been the subject of much discussion over recent years in the context of the *solar abundance problem* [9, 10, 11, 12].

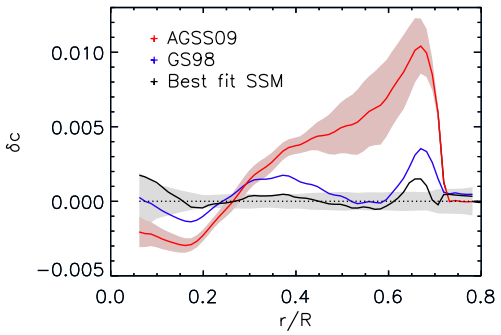

Figure 1: Comparison of sound speed profiles of SSMs. Red and blue lines are SSMs with AGSS09 and GS98 reference compositions and all input SSM parameters fixed to their central values. The black line shows results for the best SSM [7] resulting from finding the SSM with free composition.

To avoid that the results depend on the solar abundance problem we use an SSM that best reproduces the thermal stratification of the Sun and the solar neutrino data. This model is calculated following the method used in [7] that lets the solar composition free and adjusts the input parameters in SSMs within their experimental uncertainties (nuclear cross sections, microsocopic diffusion rate, etc.). In Fig. 1 we have plotted the SSM using different solar composition (GS98 [13] and AGSS09 [14]) and the best fit resulting from letting the composition free, showing that this last model matches the thermal stratification of the Sun, and thus, is a good model to be used as reference model.

2.1 SSMs with axions and hidden photons

We have calculated different SSM adding an extra energy-loss rate in the GARSTEC code resulting from the presence of axions or hidden photons. The dominant production of axions in the Sun comes from the Primakoff processes (conversion of a photon to an axions in presence of electro-magnetic fields) and the energy-loss rate used is the one in [5]. For axions, we aim to constrain the axion-photon coupling constant ($g_{a\gamma}$). For hidden photons, we have only considered in this paper the longitudinal component. Hidden photons are produced by the conversion of a photon to a hidden photon, whose probability depends on the hidden photon mass (m) and the kinetic mixing constant (χ). The product χm is the parameter that can be constrained. The limits derived from the Sun will be valid for the mass range $m_{HP} < 0.3\,$keV because for the longitudinal hidden photons, the resonance emission will occur when its mass is equal or smaller than the plasma frequency of the Sun (ω_P) as it is explained in [15]. The energy-loss rate used is taken from [15]. In Fig. 2 we show some of the results for SSM with

axions and hidden photons before marginalizing over the composition in order to understand how the energy loss affects the structure and evolution of the Sun.

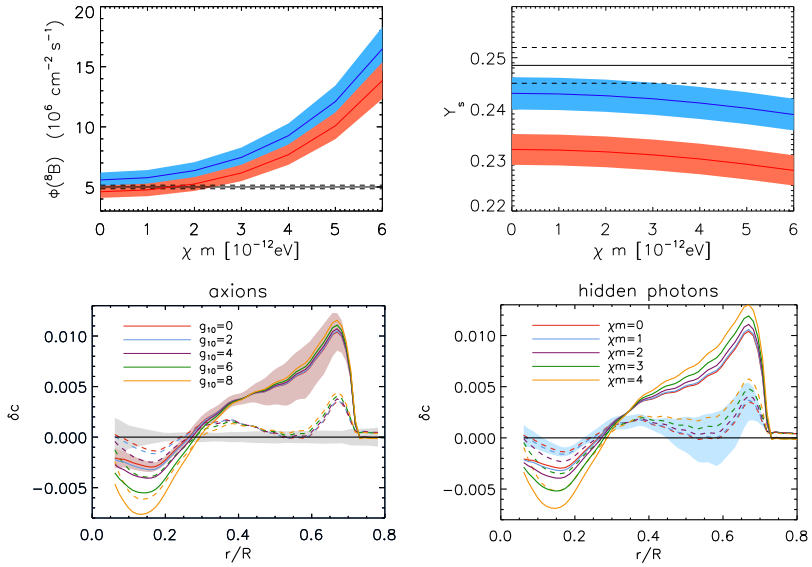

Figure 2: Upper panel: ^{8}B and Y_s as a function of χm for hidden photons. Blue lines correspond to the GS98 composition and red ones to the red ones to AGSS09. Shaded lines show the model error and black lines the observational value and their errors. Lower pannel: Sound speed profile for hidden photons and axions for different values of g_{10} and χm. Solid lines correspond to models with AGSS09 composition and dashed ones to GS98. Red and blue shaded zones correspond to the model errors and the grey one to the observational ones.

3 Method and statistical procedure

The statistical approach is based on the procedure presented in [7] that constructs a χ^2 function that uses a figure-of-merit for the quality of different solar models in reproducing the observables. We build this function by considering 34 different observable quantities: the neutrino fluxes $\Phi(^8\mathrm{B})$ and $\Phi(^7\mathrm{Be})$; the convective envelope properties $\mathrm{Y_S}$ and $\mathrm{R_{CZ}}$ and the sound speed determinations $\mathrm{c}_i \equiv c(r_i)$ for 30 different value of $r/\mathrm{R}_\odot$ where $r/\mathrm{R}_\odot < 0.80$.

The bounds on axions and hidden photons are obtained by marginalizing with respect to the surface composition (best fit model), i.e. for each assumed value of g_{10} and χm we rescale the surface abundances of volatile and refractory elements by the factors $(1 + \delta z_{\mathrm{vol}})$ and $(1 + \delta z_{\mathrm{met}})$ in order to achieve the best possible agreement with observational data (best fit model). Then, the results have a very minimal dependence on the reference solar composition used. For simplicity, we show here the results obtained by using the AGSS09 as reference composition (i.e. as pivot point for expansion in δz_{ref} and δz_{vol}). Identical results are obtained if GS98 composition is instead used.

4 Results

In Fig. 3, we show the χ^2 function after marginalizing for the composition as function of g_{10} and χm. This function has been calculated using: 1) all the observables combined, 2) only the sound speed profile, and 3) the neutrino fluxes combined with the surface helium and the convective radius. This way is useful to understand how much of each piece of experimental information contributes to the bounds. The sound speed profile gives the most restrictive limit, however, the neutrino fluxes and the convective parameters also have a noticeable contribution to the global bound. By setting a limit at $\Delta\chi^2 = 9$ we derive the upper bound $g_{10} < 4.1$ at a 3-σ CL for axions, almost a factor of 2 lower than previous solar limits, and the upper bound $\chi m = 1.8 \cdot 10^{-12}$ eV at a 3-σ CL.

For a longer discussion and more details on the method and the results, see [16].

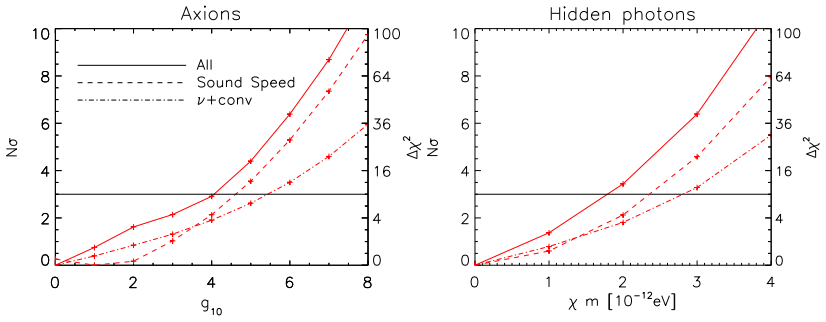

Figure 3: Values of $N\sigma$ and $\Delta\chi^2$ for models with axions and hidden photons. Solid line: using all observables $\Phi(^7\mathrm{Be})$, $\Phi(^8\mathrm{B})$, $\mathrm{Y_s}$, $\mathrm{R_{CZ}}$ and 30 points of the sound speed profile. Dashed line: using the sound speed. Dotted-dashed line: using the neutrinos and convective envelope properties.

References

[1] A.M. Serenelli, W.C. Haxton and C. Peña-Garay, ApJ **743**, 24 (2011) [arXiv:1104.1639].

[2] K. Zioutas *et al.*, Physics Research A **425**, 480 (2010) [astro-ph/9801176].

[3] I. collaboration, *IAXO - The International Axion Observatory*, `http://iaxo.web.cern.ch`.

[4] **IAXO** Collaboration, E. Armengaud *et al.*, JINST **9**, 5002 (2014) [arXiv:1401.3233].

[5] H. Schlattl, A. Weiss, and G. Raffelt, Astropart. Phys. **10**, 353 (1999) [hep-ph/98].

[6] P. Gondolo and G.G. Raffelt, Phys. Rev. D **79**, 107301 (2009) [arXiv:0807.2926].

[7] F. L. Villante, A. M. Serenelli, F. Delahaye, and M. H. Pinsonneault, ApJ **787**, 13 (2014) [arXiv:1312.3885].

[8] A. Weiss and H. Schattl, Ap&SS **316**, 99 (2008).

[9] S. Basu and H. M. Antia, ApJL **606**, L85 (2004) [astro-ph/0403485].

[10] J. N. Bahcall, A. M. Serenelli, and S. Basu, ApJL **621**, L85 (2005) [astro-ph/0412440].

[11] A. M. Serenelli, S. Basu, J. W. Ferguson, and M. Asplund, ApJL **705**, L123 (2009) [arXiv:0909.2668].

[12] J. A. Guzik and K. Mussack, ApJ **713**, 1108 (2010) [arXiv:1001.0648].

[13] N. Grevesse and A.J Sauval, Space Sci. Rev. **85**, 161 (1998).

[14] M. Asplund, N.Grevesse, A.J. Sauval and P. Scott, ARA&A **47**, 481 (2009) [arXiv:0909.0948].

[15] J. Redondo and G. Raffelt, JCAP **8**, 34 (2013) [arXiv:1305.2920].

[16] N. Vinyoles, A. Serenelli, F.L. Villante, S. Basu, J. Redondo and J. Isern, arXiv:1501.01639.

Exploring Dark Matter with AMS-02 through Electroweak Corrections

Leila Ali Cavasonza, Michael Krämer, Mathieu Pellen

Institute for Theoretical Particle Physics and Cosmology, RWTH Aachen University, D-52056 Aachen, Germany

DOI: http://dx.doi.org/10.3204/DESY-PROC-2015-02/pellen_mathieu

The AMS-02 experiment is now measuring charged cosmic rays fluxes with an unprecedented precision. It is thus necessary to provide appropriate and complementary predictions for dark matter signals. To that end, computing electroweak corrections to the dark matter annihilation is an important task. It is particularly relevant for leptophilic models where anti-protons can be produced through the decay of massive gauge bosons. From the lack of particular spectral features in the AMS positron flux, we derive new model independent upper limits on the annihilation cross section. In particular we use a newly introduced background function that allows to set limits using all the energy spectrum probed by AMS-02. This is particularly interesting as important phenomena such as solar modulation take place at low energy. Using a new calculation of electroweak radiation for vector dark matter annihilation, we can predict the maximum flux of anti-protons in such leptophilic scenarios, to be compared with future AMS measurments.

1 Introduction

The Alpha Magnetic Spectrometer (AMS-02) experiment located on the International Space Station (ISS) measures charged cosmic rays fluxes and composition with unprecedented accuracy. The anomaly in the positron fraction measured by AMS-02 [1] could be either caused by poorly understood astrophysical background effects, originate from astrophysical phenomena such as nearby astrophysical source like pulsars or supernovae, or be due to dark matter annihilation in the halo. Advocating a pure dark matter origin for the AMS-02 signal requires rather contrived scenarios. In the following, we assume that the AMS-02 positron excess is mainly due to astrophysical sources and that the contribution due to dark matter annihilation in the Galaxy is sub-dominant.

To accommodate the presence of an excess in the positron fraction and the absence of such an excess in the antiproton fluxes, leptophilic dark matter models have been proposed, where dark matter annihilates directly only into leptons. This makes electroweak corrections relevant for dark matter annihilation [2, 3], as all stable standard model particles (including antiprotons) can be produced through the radiation of electroweak gauge bosons that subsequently decay. It is also worth noticing that electroweak corrections induce correlations between different fluxes. This opens great possibilities to explore complementary measurements.

In this work [4], we derive new model independent upper limits on the dark matter annihi-

lation cross section for generic models annihilating into an electron/positron pair. We use the most recent data from the AMS-02 collaboration [1]. Finally, we use a newly introduced background function. This allows us to set upper limits over the whole energy range measured by the AMS-02 collaboration. In particular, we put particular effort into describing the low energy part of the spectrum where astrophysical effects such as solar modulation can be important and where most of a dark matter signal would concentrate. This constitutes an improvement over previous work [5] and allows for a more extensive use of the AMS-02 data. After this we compute all massive gauge boson radiations for a generic leptophilic dark matter model annihilating into electron/positron pairs. As we do not assume any particular model and do not invoke boost factors, we can simply assume in an agnostic way that a dark matter signal is lying at the exclusion limits. We then use this to make predictions for the maximum flux of antiproton thanks to the correlation between different fluxes through electroweak emission. This shows promising complementarity between the electron/positron flux and the antiproton flux searches.

2 Upper limits

Up to now, the fluxes measured by the AMS collaboration have been described by a very simple phenomenological model, where the fluxes are given by the sum of an individual diffuse power laws and a single common source. For our analysis, we use the improved background model:

$$\Phi_{e+} = \frac{E^2}{\widehat{E}^2}\left[C_{e+}\widehat{E}^{-\gamma_{e+}} + C_S\widehat{E}^{-\gamma_S}\exp\left(-\widehat{E}/E_S\right)\right], \tag{1}$$

and

$$\Phi_{e-} = \frac{E^2}{\widehat{E}^2}\left[C_{e-}\widehat{E}^{-\gamma_{e-}} + C_S\widehat{E}^{-\gamma_S}\exp\left(-\widehat{E}/E_S\right)\right]. \tag{2}$$

The modified energy $\widehat{E}$ is defined as $\widehat{E} = E + \Psi_\pm$, where $\Psi_\pm$ are effective parameters, intro-

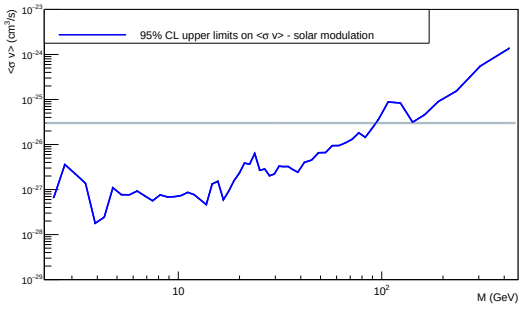

Figure 1: Model independent upper limits on the $2 \to 2$ dark matter annihilation cross section.

duced to take into account low energy effects, like solar modulation. Note that the parameter C_{e-} is energy dependant in order to also account for low energy effects. In the flux, λ quantifies the smoothness of the transition from a spectral index γ_{e-} below E_b to a spectral index

$\gamma_{e-} + \Delta\gamma_{e-}$ above E_b. The reason to use such a background function is that the simple phenomenological model is not reproducing properly the low energy part of the spectrum, where not well understood astrophysical phenomena, for instance solar modulation, play a significant role. Moreover, since a significant part of particles due to dark matter annihilation after propagating through the Galaxy would concentrate in the low energy region, it is necessary to have an appropriate description of the background also in the low energy part of the spectrum. The results of our upper-limit procedure to exclude any signal at 95% confidence level are shown in Fig. 1.

2.1 Anti-protons prediction

Even if electroweak corrections have only a relative impact on upper limits, they are nonetheless extremely important. Indeed they induce a correlation with the antiprotons flux. Assuming that a dark matter signal is just lying at the 95 % confidence level limit of the electron/positron data, one can then make predictions for the maximum flux of antiprotons. These predictions for the antiprotons/protons ratio can be compared to the measurements done by the PAMELA [6] and AMS-02 collaboration. They are shown in Fig. 2 for representative masses. There we consider the measurement made by the PAMELA and AMS-02 collaboration to be the astrophysical background. To this we add the dark matter signals that we have computed.

It shows that for dark matter masses of the order of 400 GeV or higher, the expected flux at high energy is increasing in magnitude. This is extremely interesting as it means that there could be a dark matter signal hiding in the electron/positron fluxes but appearing in the anti-proton. In particular, the signal that one expects from a dark matter source, would intriguingly accommodate the measurement and could still be consistent with the electrons/positrons measurements.

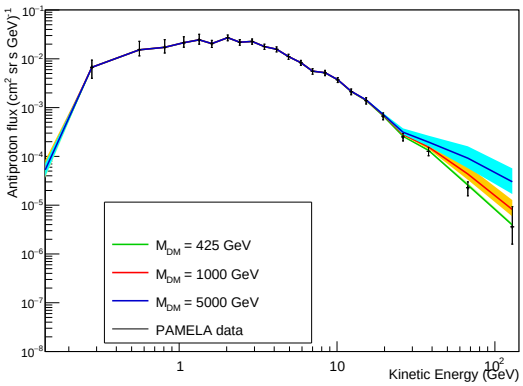

Figure 2: Prediction for maximum dark matter signal for the antiproton flux for $M_{\rm DM} = 425, 750, 1000, 3000, 5000$ GeV.

3 Conclusion

Electroweak corrections are small but important. For leptophilic dark matter models, they are of prime importance as they are the only way to obtain antiprotons. Moreover electroweak emissions introduce a correlation between different fluxes of particles. We have derived new upper limits using the last available data. To do that we have used a new background function that allow us to fit the whole energy spectrum of the electron/positron measurements. In particular this opens up the possibility to properly describe the low energy part of the spectrum. This is crucial as in this energy range, most of the dark matter signal would concentrate and interesting astrophysical phenomena such as solar modulation take place. By assuming that a dark matter signal is just about to be detected, we can predict the corresponding maximum antiprotons flux. The comparison of the expected fluxes with the existing data is very promising as the high energy part of the spectrum seems to be extremely sensitive. This demonstrates the extraordinary possibilities of complementary measurements linked by electroweak effects.

Acknowledgments

We would like to thank Henning Gast, Fabrizio Parodi and Stefan Schael for useful discussions. LAC and MP are grateful to the Mainz Institute of Theoretical Physics (MITP) for its hospitality and its partial support during the completion of this work. This work was supported by the Deutsche Forschungsgemeinschaft DFG through the research training group "Particle and Astroparticle Physics in the Light of the LHC" and by the Helmholtz Alliance for Astroparticle Physics (HAP).

References

[1] AMS Collaboration, M. Aguilar, *et al.*, "Electron and Positron Fluxes in Primary Cosmic Rays Measured with the Alpha Magnetic Spectrometer on the International Space Station," Phys. Rev. Lett. **113**, 121102 (2014).

[2] P. Ciafaloni, D. Comelli, A. Riotto, F. Sala, A. Strumia, *et al.*, "Weak Corrections are Relevant for dark matter Indirect Detection," JCAP **03**, 019 (2011) [arXiv:1009.0224 [hep-ph]].

[3] L. Ali Cavasonza, M. Krämer, M. Pellen, "Electroweak fragmentation functions for dark matter annihilation," JCAP **02**, 021 (2015) [arXiv:1409.8226 [hep-ph]].

[4] L. Ali Cavasonza, M. Krämer, M. Pellen, "Model-independent limits on dark matter annihilation from AMS-02 electron and positron fluxes," to be published.

[5] L. Bergstrom, T. Bringmann, I. Cholis, D. Hooper, C. Weniger, "New limits on dark matter annihilation from AMS cosmic ray positron data," Phys. Rev. Lett. **111**, 171101 (2013) [arXiv:1306.3983 [astro-ph.HE]].

[6] PAMELA Collaboration, O. Adriani, *et al.*, "PAMELA results on the cosmic-ray antiproton flux from 60 MeV to 180 GeV in kinetic energy," [arXiv:1007.0821 [astro-ph.HE]].

Commissioning of TREX-DM, a Low Background Micromegas-based Time Projection Chamber for Low Mass WIMP Detection

F. J. Iguaz[*], *J. García Garza, F. Aznar*[†], *J. F. Castel, S. Cebrián, T. Dafni, J. A. García, I. G. Irastorza, A. Lagraba, G. Luzón, A. Peiró*

Laboratorio de Física Nuclear y Astropartículas, Universidad de Zaragoza, Spain

DOI: http://dx.doi.org/10.3204/DESY-PROC-2015-02/iguaz_francisco

Dark Matter experiments are recently focusing their detection techniques in low-mass WIMPs, something which requires the use of light elements and low energy threshold. In this context, we describe the TREX-DM experiment, a low background Micromegas-based Time Projection Chamber for low-mass WIMP detection. Its main goal is the operation of an active detection mass ∼0.3 kg, with an energy threshold below 0.4 keVee and fully built with previously selected radiopure materials. This work focuses on the commissioning of the actual setup situated in a laboratory on surface. A preliminary background model of the experiment is also presented, based on Geant4 simulations and two discrimination methods: a conservative muon/electron and one based on a ^{252}Cf source. Based on this model, TREX-DM could be competitive in the search for low mass WIMPs and, in particular, it could be sensitive to the WIMP interpretation of the DAMA/LIBRA hint.

1 Motivation

The main strategy of Dark Matter experiments [1] is based on accumulating large target masses of heavy nuclei (like Xenon), keeping low background levels by a systematic radiopurity control of all components and an enhancement of the electron/neutron discrimination methods. However, some recent positive hints, which may be interpreted in terms of low mass WIMPs, have changed the detection strategy to sub-keV energies and light gases. This research line could be led in future experiments by Time Projection Chambers (TPCs), as they can reach energy thresholds ∼ 100 eV and have access to richer topological information. In contrast to current gaseous-based experiments, focused on directional Dark Matter detection [2], the TREX-DM experiment proposes a strategy based on high gas pressures, even if neutron/electron discrimination could be less effective, but keeping a low energy threshold. TREX-DM is a low background Micromegas-based TPC for low-mass WIMP detection and will profit from all developments made in Micromegas technology [3, 4], as well as in the selection of radiopure materials [5, 6], specially in CAST [7] and NEXT-MM [8] projects. Its main goal is the operation of an active detection mass ∼0.3 kg with an energy threshold below 0.4 keVee (as already observed in [7]).

[*]Corresponding author (iguaz@unizar.es)

[†]Present address: Centro Universitario de la Defensa, Universidad de Zaragoza, Spain.

2 Description and commissioning

The actual setup (Fig. 1) is composed of a copper vessel, with an inner diameter of 0.5 m, a length of 0.5 m and a wall thickness of 6 cm. The vessel contains two active volumes (*a* in the design), separated by a central copper cathode (*b*). At each side there is a field cage (*d*) that makes uniform the drift field along the 19 cm between the cathode and the detector. Each bulk Micromegas detector (*e*) [9] is screwed to a copper base, which is then attached to the vessel's inner walls by means of four columns. The gas enters the vessel by a feedthrough at the bottom part (*h*) and comes out by another one at the top part (*i*). The calibration system consists of a plastic tube entering in the bottom part (*h*), which allows to calibrate each side at four different points (*c*) with a ^{109}Cd source, emitting X-rays of 22.1 (K_α) and 24.9 keV (K_β).

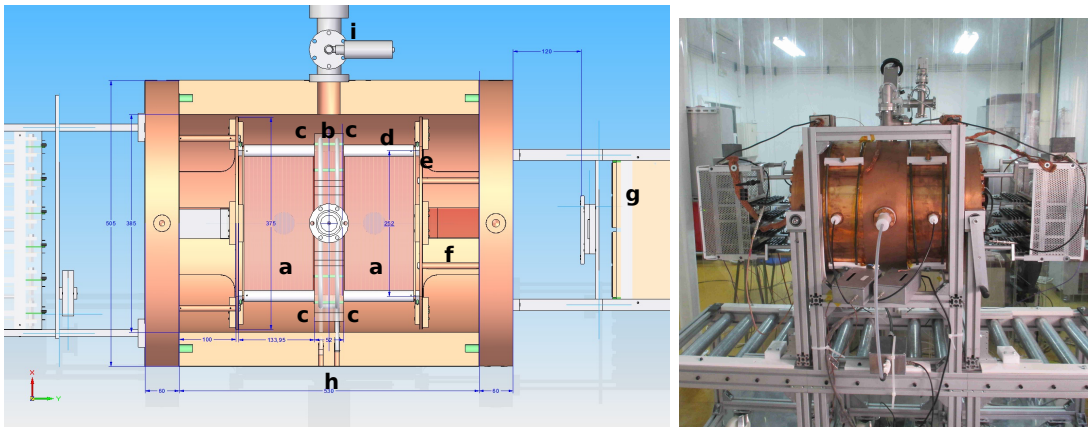

Figure 1: Left: Design of the TREX-DM detector. Its different parts are described in detail in the text: active volumes (a), central cathode (b), calibration points (c), field cage (d), Micromegas detector and support base (e), flat cables (f), AFTER-based electronics (g), gas system (h) and pumping system (i). Right: A view of the experiment during the comissioning.

The TREX-DM prototype is part of the wider scope ERC-funded project called TREX (TPCs for Rare Events eXperiments), that since 2009 is devoted to R&D on low background TPCs and their potential applications in axion, double beta decay and dark matter experiments. Work on the TREX-DM prototype started in 2012 with the first designs and it is now being commissioned at the TREX lab at Zaragoza. Most of the components have been validated: the leak-tightness of all feedthroughs has been verified for pressures up to 10 bar, the drift cage has been tested at high voltage, and all experimental parameters like the pressure, the temperature and voltages are continuously monitored by a slow control. Moreover, during the first semester of 2015, some issues have been successfully solved: the noise level has been effectively reduced by a new High Voltage filter for the central cathode and a Faraday cage for the interface cards, a new field cage has been installed to reduce border effects, and a new DAQ to read both detectors at a rate of 45 Hz each side has been installed. During the next months, the detector will be characterized in Ar+2%iC_4H_{10} and Ar+5%iC_4H_{10}, with the aim to detect sub-keV energies at high gas pressures. In parallel, the first designs of a fully radiopure setup are being made, which include a lead shielding and the replacement of some dirty components in terms of radiopurity.

3 Background model of TREX-DM

The sensitivity of the experiment has been studied creating a first background model which reproduces the conditions at the Canfranc Underground Laboratory (LSC). We have considered two light gas mixtures at 10 bar: Ar+2%iC$_4$H$_{10}$ and Ne+2%iC$_4$H$_{10}$, with an active mass of 0.3 and 0.16 kg respectively and which are good candidates to detect low mass WIMPs. However, the sensitivity of an argon-based mixture may be limited by one of its isotopes (^{39}Ar), which is β-emitter and has a long life-time. In our model, we have considered the lowest content of this isotope, measured in argon extracted from undeground sources [10]. We have also simulated the main radioactive isotopes of all the inner components using their measured activities [5, 6] and the cosmic muon flux in Canfranc. In some cases like the Micromegas detectors or their connectors, we have considered the activities of their radiopure alternative. The external gamma flux has not been included as its contribution may be supressed by an external shielding.

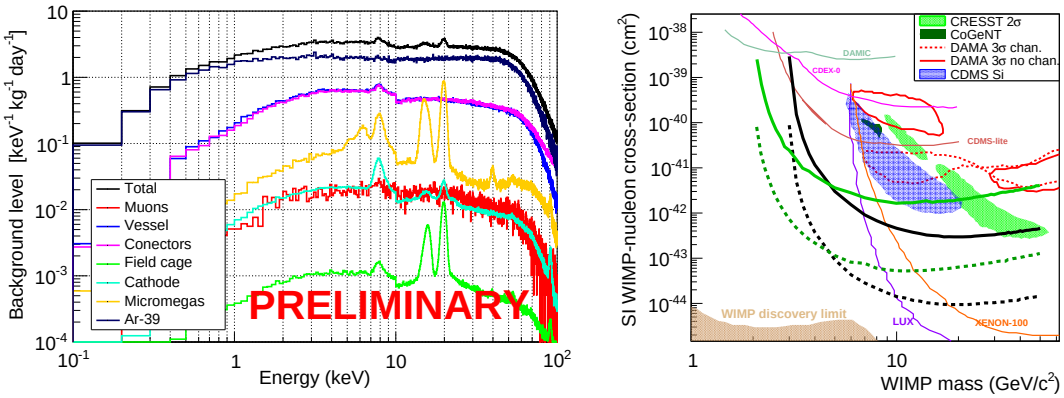

Figure 2: Left: Background spectrum expected in TREX-DM experiment (black line) during a physics run in an underground laboratoy if operated in Ar+2%iC$_4$H$_{10}$ at 10 bar. The contribution of the different simulated components is also plotted: external muon flux (red line), vessel contamination (blue line), connectors (magenta line), field cage (green line), central cathode (brown line), Micromegas detector (purple line) and ^{39}Ar (dark blue line). Right: WIMP parameter space focused on the low-mass range. Filled regions represent the values that may explain the hints of positive signals observed in CoGeNT, CDMS-Si, CRESST and DAMA/LIBRA experiments. The thick lines are the preliminary sensitivity of TREX-DM supposing a 0.4 keVee energy threshold and two different hypothesis on background and exposure: 100 (solid) and 1(dashed) keV^{-1} kg^{-1} day^{-1}, and 1 and 10 kg-year respectively, and for both argon- (black) and neon-based (green) mixtures.

Two analysis have been used in this background model. The first one is a modified version of the CAST one [7], optimized to discriminate low energy X-rays from complex topologies like gammas and cosmic muons. It uses two likelihood functions generated by the X-rays' cluster features of a calibration source. Fixing a total of 80% signal efficiency, the expected background level for an argon- (neon-) based mixture gas at 10 bar is ∼3.1 (∼1.4) keV^{-1} kg^{-1} day^{-1}, dominated by the ^{39}Ar isotope in the case of argon and by the connectors and the vessel in the case of neon. The contribution of each component is shown in Fig. 2 (left) for the argon

case. The second analysis is based on the simulation of a ^{252}Cf neutron source, which reproduces better WIMPs signals. The level obtained in argon is a ∼44% lower, as nuclear recoils show narrower cluster widths. Suposing a 0.4 keVee energy threshold and former background levels, the TREX-DM experiment could be sensitive to a relevant fraction of the low-mass WIMP parameter space (see Fig. 2, right) including the regions invoked in some interpretations of the DAMA/LIBRA results and other hints of positive WIMPs signals, with an exposure of 1 kg-year.

4 Conclusions and prospects

TREX-DM is a low background Micromegas-based TPC for low-mass WIMP detection. Its main goal is the operation of a light gas at high pressure (active mass ∼0.3 kg) with an energy threshold of 0.4 keVee or below and fully built with previously selected radiopure materials. The detector is being comissioned at TREX laboratory and may be installed at the LSC during 2016 for a possible physics run.

Acknowledgments

We acknowledge the Micromegas workshop of IRFU/SEDI and the Servicio General de Apoyo a la Investigación-SAI of the University of Zaragoza. We acknowledge the support from the European Commission under the European Research Council T-REX Starting Grant ref. ERC-2009-StG-240054 of the IDEAS program of the 7th EU Framework Program. We also acknowledge support from the Spanish Ministry MINECO under contracts ref. FPA2008-03456 and FPA2011-24058, as well as under the CPAN project ref. CSD2007-00042 from the Consolider-Ingenio 2010 program. These grants are partially funded by the European Regional Development funded (ERDF/FEDER). F.I. acknowledges the support from the Juan de la Cierva program and T.D. from the Ramón y Cajal program of MICINN.

References

[1] L. Baudis, "Direct dark matter detection: The next decade", Physics of the Dark Universe **1**, 94 (2012).

[2] S. Ahlen et al., "The Case for a Directional Dark Matter Detector and the Status of Current Experimental Efforts", Int. Jour. Mod. Phys. A **25**, 1 (2010).

[3] I. Giomataris et al. "Micromegas in a bulk", Nucl. Instrum. Meth. A **560**, 405 (2006).

[4] S. Andriamonje, D. Attie, E. Berthoumieux, M. Calviani, P. Colas et al., "Development and performance of Microbulk Micromegas detectors", JINST **5**, P02001 (2010).

[5] S. Cebrián et al., "Radiopurity of micromegas readout planes", Astropart. Phys. **34**, 354 (2011).

[6] F. Aznar et al. "Assesment of material radiopurity for Rare Event experiments using Micromegas", JINST **8**, C11012 (2013).

[7] S. Aune, J. Castel, T. Dafni, M. Davenport, G. Fanourakis et al., "Low background x-ray detection with Micromegas for axion search", JINST **9**, P01001 (2014).

[8] V. Alvarez et al. "Description and commissioning of NEXT-MM prototype: first results from operation in a Xenon-Trimethylamine gas mixture", JINST **9**, P03010 (2014).

[9] F.J. Iguaz et al., "Micromegas detector develpments for Dark Matter directional detection with MIMAC", JINST **6**, P07002 (2011).

[10] J. Xu et al., "A study of the trace ^{39}Ar content in argon from deep undergound sources", Astrop. Part. **66**, 53 (2015).

Axion Search and Research with Low Background Micromegas

J. A. García[1], *F. Aznar*[1], *J. Castel*[1], *F. E. Christensen*[2], *T. Dafni*[1], *T. A. Decker*[3], *E. Ferrer-Ribas*[4], *I. Giomataris*[4], *J. G. Gracia*[1], *C. J. Hailey*[5], *R. M. Hill*[3], *F. J. Iguaz*[1], *I. G. Irastorza*[1], *A. C Jakobsen*[2], *G. Luzón*[1], *H. Mirallas*[1], *T. Papaevangelou*[4], *M. J. Pivovaroff*[3], *J. Ruz*[3], *T. Vafeiadis*[6], *J. K. Vogel*[3]

[1]Laboratorio de Física Nuclear y Astropartículas, Universidad de Zaragoza, Zaragoza, Spain
[2]DTU Space, Tech. Univ. of Denmark, Copenhagen, Denmark
[3]Lawrence Livermore National Laboratory, Livermore, CA, USA
[4]Centre d'Études Nucléaires de Saclay (CEA-Saclay), Gif-sur-Yvette, France
[5]Columbia Univ. Astrophysics Laboratory, New York, NY, USA
[6]Aristotle University of Thessaloniki, Thessaloniki, Greece

DOI: http://dx.doi.org/10.3204/DESY-PROC-2015-02/garcia_juanan

Helioscopes are one of the most promising techniques for axion discovery in which low background X-ray detectors are mandatory. We report the latest developments of the Micromegas detectors for the CERN Axion Solar Telescope (CAST). The use of low background techniques has led to background levels below 10^{-6} c keV^{-1} cm^{-2} s^{-1}, more than a factor 100 lower than the first generation of Micromegas detectors at CAST. The helioscope technique can be enhanced by the use of an X-ray focusing device, increasing the signal-to-background ratio. A new dedicated X-ray optic was installed at CAST during 2014 with a low background Micromegas in its focal plane. Apart from increasing CASTs sensitivity, the system has been conceived as a technological pathfinder for the International Axion Observatory IAXO.

1 Introduction

Axions and ALPs are well motivated particles that have been extensively searched since past decades, being the helioscope technique one of the most promising for axion discovery. The helioscope strategy was proposed by Sikivie [1] in 1983. Axions and ALPs could be produced in the Sun via Primakoff conversion. These solar axions could be reconverted into photons inside strong magnetic fields via inverse Primakoff effect. The expected axion signal would be an excess of X-rays in the detectors placed at the magnet bore ends while the magnet is pointing to the Sun and thus, low background X-ray detectors are mandatory.

Different helioscopes have been developed for axion searches, the most sensitive of which is the CERN Axion Solar Telescope (CAST), operating at CERN since 2003. One of the singularities of CAST is the use of X-ray telescopes in order to improve the signal to background ratio. Three of the four detectors currently installed at CAST are of the Micromegas type. Beyond CAST, a new generation helioscope has been proposed: IAXO the International AXion

Observatory [2]. IAXO will exploit the helioscope technique with a dedicated supertoroidal magnet, X-ray optics and ultra-low background detectors, improving CAST sensitivity by more than one order of magnitude.

2 Low background techniques

The Micromegas detectors installed at CAST have experimented a reduction of two order of magnitude in the background level since the beginning of the experiment. Different strategies have been developed in order to reduce the background of the detectors [3]: the intrinsic radiopurity of the Micromegas readout [4], the detector performance (closely related with the improvements on the manufacturing process), the event discrimination of the events (that could be improved by the upgrade of the front end electronics to the AFTER [5] chip) and, finally, the shielding, which is mainly composed by different copper and lead layers and an active muon veto. These techniques have been developed in the context of the TREX project [6] at the University of Zaragoza.

2.1 Test benches and simulations

The main purpose of the test benches and simulations are to determine the different contributions to the background. The measurements performed in special setups were crucial for the upgrade of the Micromegas detectors at CAST. Two different setups have been mounted: one underground at the Laboratorio Subterráneo de Canfranc (LSC) and other at surface level.

The setup at the LSC shows the lowest background level, $\sim 10^{-7}$ c keV^{-1} cm^{-2} s^{-1} [3], in an environment where the muon flux is reduced by a factor 10^4 relative to surface. Different contributions have been measured at Canfranc, like the aluminum cathode and the effect of the airborne ^{222}Rn. On the other hand, the measurements performed at surface level were important in order to determine the contribution the cosmic muons, for this purpose two plastic scintillators were installed as active muon vetoes. The background level after the discrimination of these events diminished to $\sim 10^{-6}$ c keV^{-1} cm^{-2} s^{-1} of which the scintillators account for a 50% of the background events.

In order to understand the experimental results different simulations have been performed, using the RESTSoft tools [7], developed by the group at the University of Zaragoza. The simulations have been extremely important when it came to the shielding upgrade of the Micromegas detectors at CAST. The results of these studies confirmed the importance of the cosmic muons to the contribution of the background level. Following, the lead shieldings were extended along the magnet bore pipes, in an attempt to lower the contribution of the cosmic events.

2.2 Micromegas at CAST: State of art

Following the prescriptions of the low-background studies, the Micromegas detectors at CAST were upgraded. In a first stage a new shielding design for the Micromegas at the sunset side was installed. The different lead and copper layers of the shielding have been increased and two plastic scintillators have been installed in order to minimize the effect of the cosmic muons. Also, the electronics have been upgraded to the AFTER chip. After these upgrades the background level was reduced to $\sim 10^{-6}$ c keV^{-1} cm^{-2} s^{-1} [8], a factor ~ 6 of reduction with respect to the previous set-up.

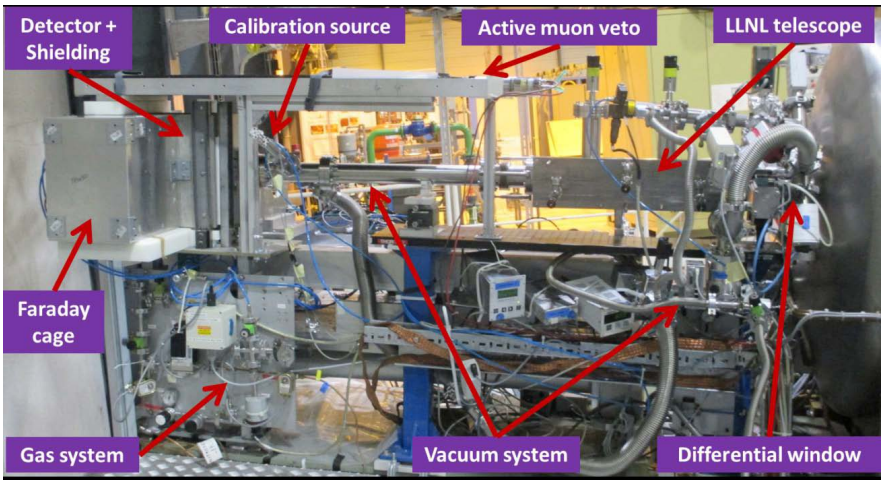

Figure 1: Photo of the new Sunrise Micromegas + X-ray telescope system in the CAST experiment. The different parts of the set-up have been labeled.

During 2014 a new X-ray focusing device was installed in the sunrise side with a Micromegas in its focal plane. It is the first time an X-ray optic is specifically designed and built for axion research. Moreover, the detector has a novel design that summarizes the current state of art on low background techniques developed for the Micromegas detectors.

The X-ray telescope has been manufactured using the same techniques developed for the NASA NuSTAR mission [9]. It consists of segmented glass substrates with 13 W/B_4C nested layers that lead to a focal length of 1.5 m and a focusing spot from 1–5 mm^2. The new X-ray telescope represents a big milestone for CAST, as it is expected to improve the effective background of the Micromegas by a factor ~ 100 and could be considered as a pathfinder for IAXO.

A new Micromegas detector has been designed and built for the sunrise side in which the body and the chamber of the detector is made of 18 mm thick radiopure copper. The materials close to the detector, mainly copper and polytetrafluoroethylene, are intrinsically radiopure and have been carefully cleaned. Also, a field shaper has been installed in order to ensure the uniformity of the drift field. The setup includes all the features of the sunset upgrade, like the shielding design, a plastic scintillator and the AFTER electronics (see Figure 1). In addition, new Micromegas detectors have been manufactured with excellent spatial and energy resolution. After the implementation of these upgrades the background was reduced to 8×10^{-7} c $keV^{-1}cm^{-2}s^{-1}$, the lowest level that have been reached by a detector at CAST.

The X-ray telescope and the Micromegas were installed and aligned in August 2014. The alignment procedure was performed with a laser which was properly aligned with the line and using a transparent chamber replica. The quantum efficiency of the Micromegas has been increased by the use of a new cathode design; now the signal spot is centered in the central circle of the detector avoiding the grid structure.

Due to the reduction of the background of the Micromegas and the new X-ray telescope, CAST will improve its previous limit in a re-scanned vacuum phase to an expected value of $g_{a\gamma} < 6 \times 10^{-11}$ GeV^{-1} as shown in Figure 2.

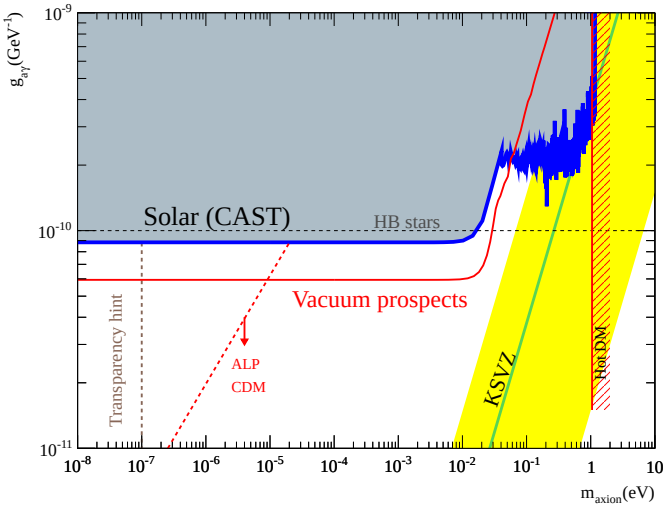

Figure 2: Expected sensitivity of the new vacuum phase in the CAST experiment (red line), in comparison with the current CAST limit (blue line). ALP hints and theoretical limits are also drawn.

3 Future prospects

Although the research in low background techniques in Micromegas detectors has led to an impressive reduction of the background at CAST, an ultra-low background detector is required for IAXO, with a goal of 10^{-7} c keV^{-1} cm^{-2} s^{-1}, down to 10^{-8} if possible. New improvements and research lines have been proposed for IAXO such as: veto coverage, extended scintillator surface area, and the use of new gas mixtures like Xe or depleted Ar in order to remove the ^{39}Ar isotope. Thanks to IAXO, a big part of the parameter space could be explored during the next decade, with a sensitivity that will enter in the most favored regions for axions and ALPs.

IAXO could also be sensitive to non-hadronic Solar axions, with a flux that could be considerably larger than the Primakoff conversion [10]. Also, more exotic particles could be explored at IAXO like chameleons. In both cases the key would be the reduction of the low energy threshold and the increase of the transparency of the detectors to soft X-rays. New research and design lines are being investigated:

- New thin windows: The efficiency of the Micromegas at low energies is limited by the X-ray transparency of the cathode window. Different materials are being investigated.

- AGET front-end electronics: The novel AGET [11] electronics keep the main features of the AFTER but with auto-trigger functionality. So a lower energy threshold could be archieved.

- Resistive Micromegas: The use of this type of detectors will allow to work at higher gain.

4 Conclusions

Axions and ALPs are well motivated particles that appear as a solution of the strong CP problem, being attractive candidates to form part of the dark matter. The CAST experiment has been looking for solar axions since 2003 being the most sensitive helioscope so far. The helioscope technique could be enhanced, among other things, by reducing the background of the detectors, with this purpose different strategies have been developed and have led to a background reduction of a factor ~ 100 at CAST.

The new X-ray telescope and the low background Micromegas system at CAST will improve the sensitivity of the experiment and could be considered as a pathfinder of the new generation axion helioscope IAXO. New research lines have been proposed in order to reduce the background level of the Micromegas that are required for IAXO. On the other hand, the reduction of the low energy threshold in the Micromegas will open new physics for IAXO.

Acknowledgments

We thank our CAST colleagues for their excellent work during many years of collaboration and R. de Oliveira and his team at CERN for their effort manufacturing the microbulk detectors. We acknowledge the support from the European Commission under the European Research Council T-REX Starting Grant ref. ERC-2009-StG-240054 of the IDEAS program of the 7th EU Framework Program. We also acknowledge support from the Spanish Ministry MINECO under contracts ref. FPA2008-03456 and FPA2011-24058, as well as under the CPAN project ref. CSD2007-00042 from the Consolider-Ingenio 2010 program. These grants are partially funded by the European Regional Development funded (ERDF/FEDER). F.I. acknowledges the support from the Juan de la Cierva program and T.D. from the Ramón y Cajal program of MICINN.

References

[1] P. Sikivie, Phys. Rev. Lett. **51**, 1415 (1983) [Phys. Rev. Lett. **52**, 695 (1984)].

[2] E. Armengaud *et al.*, JINST **9**, T05002 (2014) [arXiv:1401.3233 [physics.ins-det]].

[3] S. Aune *et al.*, JINST **9**, no. 01, P01001 (2014) [arXiv:1310.3391 [physics.ins-det]].

[4] S. Cebrian *et al.*, Astropart. Phys. **34**, 354 (2011) [arXiv:1005.2022 [physics.ins-det]].

[5] P. Baron *et al.*, IEEE Trans. Nucl. Sci. **55**, 1744 (2008).

[6] I. G. Irastorza *et al.*, EAS Publ. Ser. **53**, 147 (2012) [arXiv:1109.4021 [physics.ins-det]].

[7] A. Tomas, CERN-THESIS-2013-062.

[8] S. Aune *et al.*, JINST **8**, C12042 (2013) [arXiv:1312.4282 [physics.ins-det]].

[9] J. E. Koglin *et al.*, SPIE 7437, 10 (2009).

[10] J. Redondo, JCAP **1312**, 008 (2013) [arXiv:1310.0823 [hep-ph]].

[11] P. Baron *et al.*, Nuclear Science Symposium and Medical Imaging Conference (NSS/MIC), IEEE 754 (2011).

Unconventional Ideas for Axion and Dark Matter Experiments

Fritz Caspers
CERN, Geneva, Switzerland

DOI: http://dx.doi.org/10.3204/DESY-PROC-2015-02/caspers_fritz

In this contribution an entirely different way compared to conventional approaches for axion, hidden photon and dark matter (DM) detection is proposed for discussion. The idea is to use living plants which are known to be very sensitive to all kind of environmental parameters, as detectors. A possible observable in such living plants could be the natural bio-photon level, a kind of metabolism related chemoluminescence. Another observable might be morphological changes or systematic leave movements. However a big problem for such kind of experiment would be the availability of a known, controllable and calibrated DM source. The objective of this small paper is primarily to trigger a debate and not so much to present a well-defined and clearly structured proposal.

1 Introduction

There appears to be growing evidence that very faint photon emissions in living biologic systems (bio-photons) could play an important role in intracellular communication and control of the growth. Those photon emissions are powered by the metabolism and can be considered as a kind of bio-luminescence. Dead plants or other dead organic materials do *not* emit bio-photons. This kind of "living cell radiation" has been first postulated by A. Gurwitsch nearly 100 years ago [1] and he conducted probably the first near UV light shining through the wall experiment on onion roots. Of course everybody was laughing at him at this time. Around 1970 this kind of very faint radiation (range from 200 to 800 nm) on living plants was measured for the first time by F.A. Popp [2] in Marburg (Germany) with highly sensitive photodetectors. Popp proposed that this radiation might be both semi-periodic and coherent. However this view is not generally accepted. If confirmed true, those biological systems (plants, cell cultures, etc.) can react on very faint photon signals in a measurable way. We have two possible observables: observation of structure changes under the influence of some DM or axion flux (do we know it and are we able to control it?) and / or observation of changes of the bio-photon activity. With modern highly sensitive photon detectors and cameras the observation of those bio-photon activity is real fun and rather easy and one can see very nicely when e.g., some leaf of a plant is killed by injecting some toxic substance, how the bio-photon activity first strongly increases and then a few seconds to minutes later stops entirely (cry before death). But why should we consider to use plants or cell cultures and not observe such axion and DM related photons directly? Plants and cell cultures are full of cellular membranes (dielectric double layers and cell membranes with strong internal electric fields) where axions and other DM might convert into mm wave or probably optical photons which then could have an impact on the biological

activity. Living systems are not in thermo-dynamical equilibrium (otherwise they would be dead) and thus may have a rather low effective "noise temperature" (some people claim effects like stochastic resonance there). It should be noted that an electronic amplifier may exhibit a noise temperature of say 30 K when operating at ambient (a typical satellite antenna pre-amplifier for 10 GHz). The electronic amplifier is also not in thermo-dynamical equilibrium since it is connected to a power source. Perhaps such kind of bio-detectors are much more broadband that our presently used or discussed structures and they can be operated also in a strong magnetic field but of course not at cryo. There exist interesting theories by Fröhlich [3, 4] on biological very low level coherent mm waves in biological systems.

2 Designing an experiment

Now regarding a practical proposal for such kind of test, I would propose to copy-paste one of the many plants experiments on temporal variation of the tidal force. The results are very convincing and also well accepted by the biologists community [5, 6]. Observables are, amongst other parameters, leaf movements and morphological changes in the roots. Unfortunately we cannot just look for other, probably DM related periodicities in the observables since the known or anticipated variation of the DM flux (diurnal period) are extremely small. Lacking a controllable calibrated axion/hidden photon DM source we should maybe consider placing such an experiment in the vicinity of a nuclear reactor or beyond the (ionizing radiation) shielding of a beam dump/target which is frequently used, in some accelerator. It is clear that this experiment would NOT try to compete with biological experiments which are looking for ionizing radiation related changes e.g., on DNS strings or cell cultures. Such experiments have been carried out also in underground areas, but with negative results. Here the idea is rather to focus on observable "behavioural" or "state" changes e.g., leave movements and variations of the biophoton level. In any case the DM will not be seen (if any) directly by the plant but only via some real photons (mm wave range?) created by some conversion mechanism when e.g., hidden photons pass through cell membranes.

Acknowledgements

The author would like to thank K. Zioutas, M. Schumann, E. Wagner, P. W. Barlow and L. Beloussov for stimulating and challenging discussions as well as M. Betz for help in editing the manuscript.

References

[1] A. Gurwitsch, "Die Mitogenetische Strahlung. Monographien aus dem Gesamtgebiet der Physiologie der Pflanzen und der Tiere", J. Springer, Bd. 25, Berlin (1932).

[2] F. A. Popp, "Properties of biophotons and their theoretical implications", Indian Journal of Experimental Biology, **41**, 391, (2003).

[3] H. Fröhlich, IEEE Transactions on Microwave Theory and Techniques, VOL. MIT-26, NO. 8, (1978).

[4] S. N. Mayburov, arXiv:1205.4134, Quantum Information conference, Torino, (2012).

[5] P. W. Barlow *et al.*, "Arabidopsis thaliana root elongation growth is sensitive to lunisolar tidal acceleration and may also be weakly correlated with geomagnetic variations", Annals of Botany **111**, 859, (2013).

[6] J. Normann *et al.*, "Rhythms in Plants", Springer, ISBN 978-3-319-20516-8, pp. 35-55, (2015).

Status of the CRESST-II Experiment for Direct Dark Matter Search

Andrea Münster for the CRESST collaboration

Physik-Department and Excellence Cluster Universe, Technische Universität München, Garching, Germany

DOI: http://dx.doi.org/10.3204/DESY-PROC-2015-02/muenster_andrea

The CRESST-II (Cryogenic Rare Event Search with Superconducting Thermometers) experiment aims for the direct detection of dark matter in form of WIMPs. Scintillating $CaWO_4$ single crystals are used as target material. We present the results of a low-threshold analysis of one single detector module employing a crystal (m $\sim$ 250 g) grown at the Technische Universität München with an improved radiopurity and excellent properties of the phonon detector. With an exposure of 29 kg days new parameter space could be explored for WIMP masses below 3 GeV/c^2. In addition, the high potential of CRESST in the low WIMP-mass regime will be shown in a projection employing detectors that are further improved in performance and radiopurity.

1 Introduction

CRESST-II (Cryogenic Rare Event Search with Superconducting Thermometers) is an experiment for the direct search of dark matter in form of Weakly Interacting Massive Particles (WIMPs). A particle interaction in one of the scintillating $CaWO_4$ single crystals used as target produces heat (phonon signal) and scintillation light (light signal). Both signals are recorded simultaneously by two separate detectors (forming a detector module) operated at mK temperatures. The phonon signal consisting of the main part of the energy deposited enables a precise energy measurement. The light signal depends on the kind of interacting particle. The parameter *light yield* defined as the fraction of light energy to phonon energy is, therefore, used for particle discrimination on an event-by-event basis: electron recoils are normalized to a light yield of 1 (at 122 keV). α-particles and nuclear recoils, due to light quenching, are found at lower light yields of $\sim$ 0.22 and $\sim$ 0.02–0.11 (depending on the nucleus), respectively [1]. For WIMPs, nuclear recoils at energies smaller than 40 keV are expected.

2 CRESST-II Phase 2

CRESST-II Phase 2 collected two years of data between summer 2013 and summer 2015. The main goal was to clarify the origin of an excess signal observed in CRESST-II Phase 1 [2]. In the present work we concentrate on the results of only one $CaWO_4$ crystal (TUM40) equipped with an upgraded crystal holding scheme. By holding the block-shaped crystal (m $\sim$ 250 g) with scintillating $CaWO_4$ sticks, background events related to the decays of ^{210}Po nuclei on non-

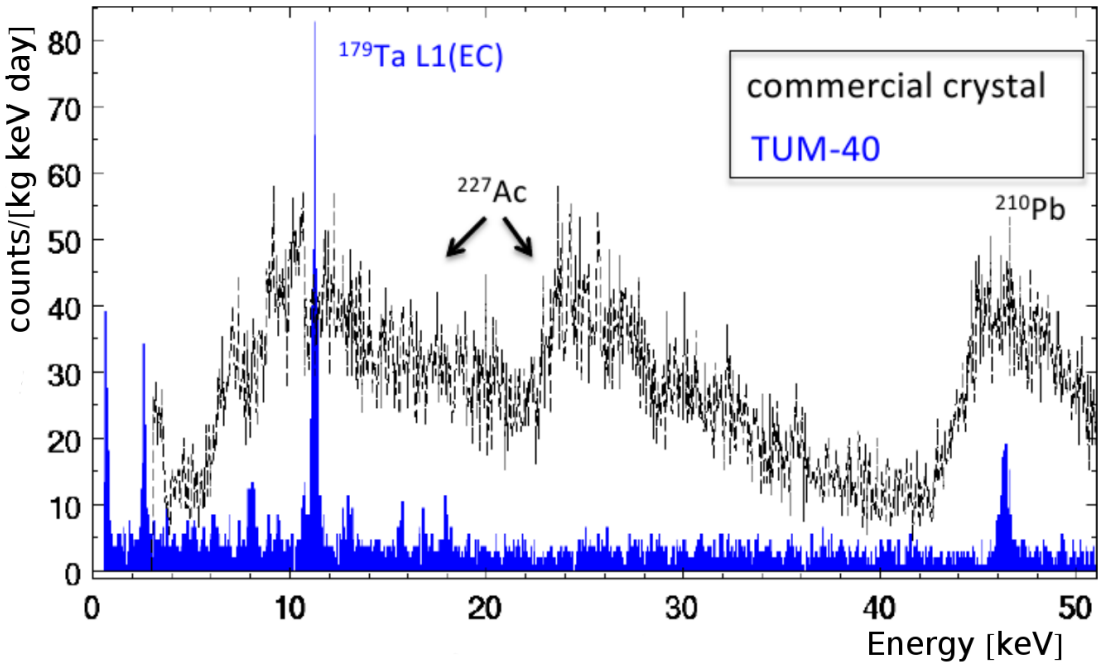

Figure 1: Low-energy spectrum of TUM40 (blue) compared to a typical commercial crystal (black). The commercial crystal is dominated by the decays of ^{227}Ac and ^{210}Pb from the natural decay chains. Due to the improved radiopurity of TUM40, lines originating from cosmogenic activation of ^{182}W become visible in its spectrum.

scintillating clamps, as observed in CRESST-II Phase 1 [2], are efficiently vetoed. The single crystal mounted in this stick-design module was directly grown at the Technische Universität München (TUM) via the Czochralski method.

It is crucial for CRESST detectors to have a radiopurity as good as possible. The radiopurity of TUM40 in comparison to $CaWO_4$ crystals obtained from commercial suppliers was quantified in [3, 4] by determining total α-activities between 1.5 MeV and 7 MeV. The total α-activity of TUM40 was found to be 3.07 ± 0.11 mBq/kg which is comparable to the radiopurest commercial crystals with activities ranging between $\sim$ 3 mBq/kg and 107 mBq/kg [3]. As can be seen in Figure 1, this result is confirmed by the investigation of background events at low energies: in the energy range (1–40) keV, 3.51 counts/(kg keV day) were detected for TUM40, whereas commercial crystals are worse by a factor of 2–10 (6–30 counts/(kg keV day)) [4]. The γ-lines visible in the spectrum of TUM40 in Figure 1 mainly originate from the cosmogenic activation reaction ^{182}W(p, α)^{179}Ta.

In addition to this significant improvement in radiopurity, TUM40 shows an excellent performance of the phonon detector, in particular, a low trigger threshold of 603 eV and an outstanding baseline resolution of $\sim$ 90 eV [5]. A non-blind low-threshold analysis applied to the first 29 kg days of data results in the exclusion limit (solid red line) shown in Figure 2 [6]. Part of the signal region seen in CRESST-II Phase 1 can already be excluded by this analysis. Additionally, new parameter space could be explored for WIMP masses below 3 GeV/c^2. A

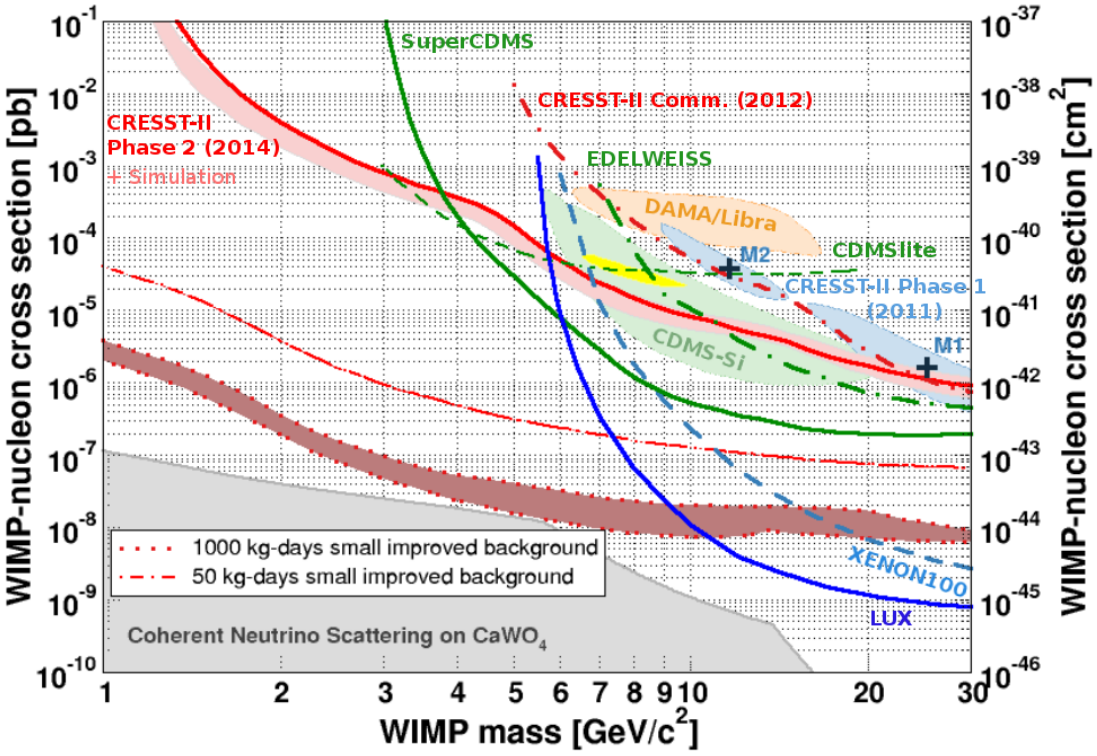

Figure 2: Spin-independent WIMP-nucleon cross section plotted against the WIMP mass including the results of selected direct dark matter search experiments [2, 7, 8, 9, 10, 11, 12, 13, 14, 15]. The solid red line shows the exclusion limit obtained from a low-threshold analysis of the CRESST-II Phase 2 detector TUM40 (29 kg days) [6]. A simulation of the expected sensitivity based on an empirical e^-/γ-background-only model is included (light red band). In addition, the sensitivity (1σ C.L.) expected for the operation of small (24 g) $CaWO_4$ crystals with a radiopurity improved by a factor of 100 is plotted for two different exposures [16].

simulation of the sensitivity expected from an empirical e^-/γ-background-only model is included (1σ borders as light-red shaded area in Figure 2) and shows no hint for any additional background not considered.

3 CRESST-III

In the upcoming CRESST-III the low WIMP-mass region will be further investigated which requires more improvements in the performance of the detectors. Smaller crystals with a mass of only 24 g are expected to lower the threshold of the phonon detector to less than 100 eV. Furthermore, the smaller size allows more light to escape the crystal resulting in a higher amount of light detected. For the second phase of CRESST-III we aim to improve the radiopurity of the $CaWO_4$ crystals by a factor of 100 to $\sim 10^{-2}$ counts/(kg keV day). This improvement is feasible as all the crystal production steps take place at the TUM (see Figure 3): starting

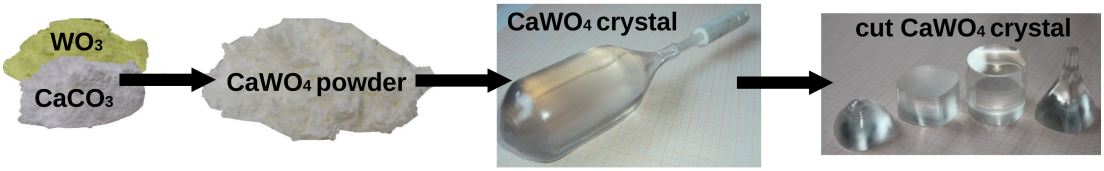

Figure 3: Production of $CaWO_4$ detector crystals starting from the two raw materials $CaCO_3$ and WO_3. As all production steps including the powder processing, the crystal growth, the aftergrowth treatment and further processing of the crystals take place at the TUM [17], further improvements in radiopurity can be achieved.

from the high-purity raw materials $CaCO_3$ and WO_3, $CaWO_4$ powder can be synthesized via a solid-state reaction. This $CaWO_4$ powder is the base material for the growth of $CaWO_4$ single crystals via the Czochralski method [17]. The grown crystals are then further processed to CRESST detectors. There are, in particular, two ways to achieve the required improvement in radiopurity: a) In a chemical purification, contaminations can be extracted from the raw materials, b) recrystallization of an already grown crystal uses the fact that crystal growth itself is a cleaning process.
Figure 2 shows the sensitivity (1σ C.L.) expected for the operation of 24 g crystals with this improved radiopurity for an exposure of 50 kg days (dash-dotted red line) as well as for an exposure of 1000 kg days (dotted red line) [16].

4 Conclusion and outlook

In this work we present the results of a low-threshold analysis of the CRESST-II Phase 2 detector TUM40. New parameter space could be explored for WIMP masses below 3 GeV/c^2. A further improvement of the limit in the low WIMP-mass region could be achieved with the detector module Lise [18]. Additionally, the combined exposure of several detectors operated will clarify the origin of the signal observed in CRESST-II Phase 1.

It was shown, that a suitable technology for the development of an experiment with a high target mass is available. However, the highest potential of CRESST lies in the investigation of the low WIMP-mass region. In two phases, CRESST-III will be able to explore new parameter space with a changed detector design using small $CaWO_4$ crystals. Additionally, in the second phase it is aimed for an increased exposure and a radiopurity improved by a factor of 100. It is demonstrated in a projection that the resulting sensitivity will be close to the region where coherent neutrino nucleus scattering becomes an irreducible background for dark matter search with $CaWO_4$ crystals [19].

Acknowledgments

This research was supported by the DFG cluster of excellence: Origin and Structure of the Universe, the Helmholtz Alliance for Astroparticle Physics, the Maier-Leibnitz-Laboratorium (Garching), the Science & Technology Facilities Council (UK) and by the BMBF: Project 05A11WOC EURECA-XENON. We are grateful to Michael Stanger from the crystal laboratory (TUM) and to LNGS, in particular to Marco Guetti, for the constant support of CRESST.

References

[1] R. Strauss *et al.*, EPJ C **74**, 7 (2014), [arXiv:1401.3332 [astro-ph.IM]].

[2] G. Angloher *et al.*, EPJ C **72**, 4 (2012), [arXiv:1109.0702 [astro-ph.CO]].

[3] A. Münster *et al.*, JCAP **2014 05**, 018 (2014), [arXiv:1403.5114 [astro-ph.IM]].

[4] R. Strauss *et al.*, JCAP **2015 06**, 030 (2015), [arXiv:1410.4188 [physics.ins-det]].

[5] R. Strauss *et al.*, EPJ C **75**, 8 (2015), [arXiv:1410.1753 [physics.ins-det]].

[6] G. Angloher *et al.*, EPJ C **74**, 12 (2014), [arXiv:1407.3146 [astro-ph.CO]].

[7] A. Brown *et al.*, Phys. Rev. D **85**, 021301 (2012), [arXiv:1109.2589 [astro-ph.CO]].

[8] R. Agnese *et al.*, Phys. Rev. Lett. **112**, 241302 (2014), [arXiv:1402.7137 [hep-ex]].

[9] R. Agnese *et al.*, Phys. Rev. Lett. **112**, 041302 (2014), [arXiv:1309.3259 [physics.ins-det]].

[10] R. Agnese *et al.*, Phys. Rev. Lett. **111**, 251301 (2013), [arXiv:1304.4279 [hep-ex]].

[11] E. Aprile *et al.*, Phys. Rev. Lett. **109**, 181301 (2012), [arXiv:1207.5988 [astro-ph.CO]].

[12] D. S. Akerib *et al.*, Phys. Rev. Lett. **112**, 091303 (2014), [arXiv:1310.8214 [astro-ph.CO]].

[13] C. Savage *et al.*, JCAP **2009 04**, 010 (2009), [arXiv:0808.3607 [astro-ph]].

[14] E. Armengaud *et al.*, Phys. Rev. D **86**, 051701 (2012), [arXiv:1207.1815 [astro-ph.CO]].

[15] C. E. Aalseth *et al.*, Phys. Rev. D **88**, 012002 (2013), [arXiv:1208.5737 [astro-ph.CO]].

[16] G. Angloher *et al.*, arXiv:1503.08065 [astro-ph.IM].

[17] A. Erb and J.-C. Lanfranchi, CrystEngComm **15**, 2301-2304 (2013).

[18] G. Angloher *et al.*, to be published (2015)

[19] A. Gütlein *et al.*, Astroparticle Physics **69**, 44 - 49 (2015), [arXiv:1408.2357 [hep-ph]].

The Coldest Axion Experiment at CAPP/IBS/KAIST in Korea

Woohyun Chung

Center for Axion and Precision Physics Research, IBS, Korea

DOI: http://dx.doi.org/10.3204/DESY-PROC-2015-02/woohyun_chung

The axion, a hypothetical elementary particle arising from Peccei-Quinn solution to the strong-CP problem, is a well-motivated dark matter candidate. The IBS Center for Axion and Precision Physics Research (CAPP) in Korea will explore the dark matter axion using a method suggested by P. Sikivie, converting the axions into microwave photons in a resonant cavity permeated by a strong magnetic field. CAPP's first microwave axion experiment in an ultra-low temperature setup is being launched at KAIST (Korea Advanced Institute of Science and Technology) campus this summer, utilizing top of the line equipment and technology. I will discuss the progress and future plans of the axion experiment.

1 Axion research at CAPP

The Center for Axion and Precision Physics Research (CAPP) of the Institute for Basic Science (IBS) was founded to launch a state-of-the-art axion dark matter experiment in Korea. CAPP's design of the axion experiment is based on P. Sikivie's haloscope scheme [1] which employs high Q-factor tunable microwave cavity submerged in a very high magnetic field. The signal from the cavity is amplified through the SQUID amplifier and transmitted to the room temperature RF receiver unit to be processed further. The physical temperature of the cavity should be maintained extremely low in order to reduce the noise from the black body radiation, and eventually to improve the signal-to-noise ratio and speed up the experiment. The RF receiver unit to amplify and process the radio frequency signal from the resonant cavity could be considered to be the most sensitive radio on earth. CAPP's plan, as a late starter, is to acquire experience through the collaboration with existing experiments and to build a competitive, qualitatively and quantitatively, axion experiment in Korea through local resources. It requires the powerful 25 T magnet delivery from BNL (Brookhaven National Laboratory), the next generation SQUID development from KRISS (Korea Research Institute for Standards and Science) and the superconducting high frequency cavity through the col-

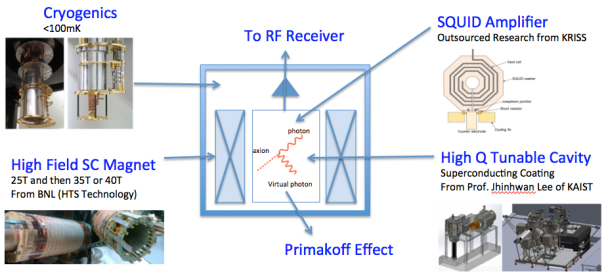

Figure 1: CAPP's plan for axion search

laboration with KAIST (Figure 1). The ultra high field magnet being developed by BNL has exceptionally big 10 cm bore and is based on a new technology called HTS (High Temperature Superconductor). The compact (outer diameter of only 30 cm) design of the magnet was intended to produce even higher field of 35 T or 40 T magnet by adding another layer of magnet outside in the future. If successful, this magnet will be the highest-field superconducting magnet in the world with HTS technology. Another innovative feature of the design of the magnet is the use of stainless steel as an insulator in superconducting tapes. It will reduce the chance of failure (quench) and minimize the damage that failure could cause. The experience we gain and the success of those outsourced projects would be crucial to building CAPP's own axion experiment and provide very competitive edge over the existing experiments.

2 CAPP's Ultra Low Temperature Axion Search in Korea (CULTASK)

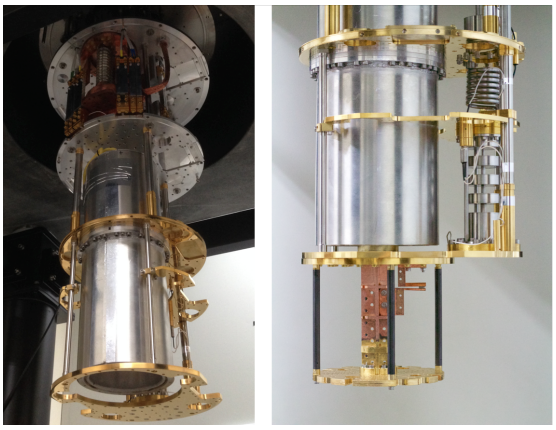

Figure 2: BlueFors LD400 Dilution Refrigerator at KAIST

CAPP's new laboratory located at KAIST Munji Campus will be ready for the first axion experiment in Korea by the end of this year or early next year. The architect's design of the space for 7 dedicated dilution refrigerators with low vibration facility is completed and the construction will begin some time in late summer. While waiting for the building ready, CAPP decided to prepare our axion experiment, taking advantage of the downtime (4 months) of Prof. Hyoungsoon Choi's (KAIST) dilution refrigerator. The refrigerator (BlueFors LD400) happens to be exactly the same model that will be used for our axion experiment and has preinstalled 8 T superconducting magnet (inner bore size: 6 cm) in it. The SQUID amplifiers and the superconducting cavities might not be ready soon enough to be used in this setup, but it is a great opportunity as an engineering run to build an infrastructure and prepare ourselves for the upcoming axion experiment. Figure 2 shows Prof. Choi's dilution refrigerator with superconducting magnet.

2.1 High Q-factor cavity development

2.1.1 Fabricated Cavities

We have several prototype cavities fabricated so far. A couple of cavities were made with conventional electroplating (inner surface), with and without annealing. The local machining company made a couple of stainless steel (2 mm thick) cavities back in April and one of them was coated with electroplating and the second one was sent to the coating lab of the Technical University of Munich for 50 micron thick sputtering coating of 6N pure copper. They would also

test the possibility of sputtering pure 6N Al inside the stainless steel cavity. One last cavity we outsourced for research and expected to be completed in summer is from STC (Seoul Teracom) of Seoul National University's Prof. Gunsik Park. These cavities will have pure copper sheet (1 mm thick) brazed inside the stainless steel cavity instead of coating. They will be delivered with complete test results.

2.1.2 RRR and RF Q-factor

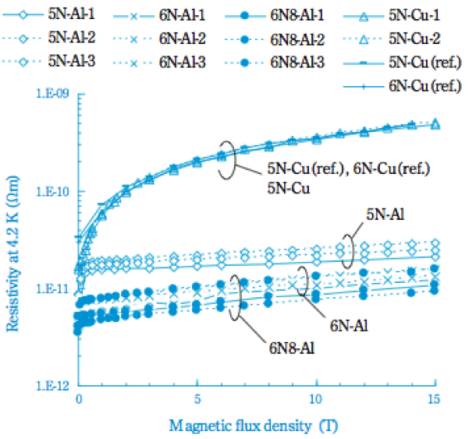

Fig. 11 Transverse magnetoresistance at 4.2 K of 0.5-mm-diameter-specimens. Dashed lines show the results obtained using the delta mode method, while solid lines show the results obtained from the use of a DC current source. The literature data are also plotted for comparison as 5N-Cu (ref.) and 6N-Cu (ref.).[12)]

Figure 3: Magnetoresistance: Pure Al vs. Cu from Sumitomo Chemical [2]

The RRR (residual resistivity ratio= resistivity@296K / resistivity@4K) of ultra pure copper and aluminum is, in some sense a measure of purity, and could go up to 50000 if annealed properly. The measured Q-factor of the RF cavity is expected to be proportional to the square root of the resistivity assuming that the condition of the surface is perfect and there is no contact problem. However, there is magnetoresistance effect which degrades RRR, tens, even hundreds times when magnetic field is applied. The natural choice of coating on the inner surface is copper, but recent development in material purification shows that high purity aluminum (99.9999%) exhibits exceptional RRR of 50000 when annealed properly and the degradation of RRR in high magnetic field (1-10 T) is much smaller than that of copper (Figure 3) [2]. The coating with pure Al was one of the recently added research projects. We have already started joint efforts with KAIST to measure RRR of various samples (4N, 5N, and 6N Cu and Al) with and without annealing. Also we are planning to make test cavities with ultra pure Cu and Al and perform a quick Q-factor measurement (dunk test) with a large neck (5.5 cm diameter) Helium dewar, which can be done in parallel with our engineering run.

2.1.3 Support structure

The thermal simulation study for the support structure with COMSOL Multiphysics package is planned. In case we have trouble lowering the temperature of the cavity, other choice of the support structure could be the copy of Prof. Choi's support structure which he routinely use for reaching 6 mK. Our setup with the cavity has more materials and several heat sources, but should be able to go under 100 mK according to Prof. Choi (simulation should verify too).

2.1.4 Tuning system

The actuator with the controller for tuning system will go through precision test in coming weeks. The step size for the frequency scan in 5 GHz resonant frequency should be around 10 kHz, which corresponds to a thousandth of a degree of the actuator rotation per operation.

2.2 RF electronics and DAQ

2.2.1 Cryo-RF

The cryogenic circulators (isolators) and amplifiers (HEMT) have been received and tested at KRISS by Dr. Yonuk Chong using his dilution refrigerator. He will give us a report of the test and has plans to have a another test with a simple cavity (OFHC mock-up, delivered) with circulators and amplifiers using Cryo-Cooler, whose fabrication is going to be completed in September. The integration of cryo-RF parts into Prof. Choi's dilution refrigerator will be done as soon as we are confident about the performance of our cavity and associated tuning system.

2.2.2 RT-RF Receiver

Both the design and the fabrication of room temperature RF signal processing receiver chain are complete. The initial tests have been done by Dr. Young-Im Kim. The signal digitization or recording of the data has been tested by Dr. Myungjae Lee. The next step is to wait for the healthy signal coming (from the cavity) through cryogenic RF signal processing, which includes cryogenic circulators and amplifiers (HEMT).

3 Conclusion

Our preparation for the engineering run of CULTASK is rather complete at this stage and ready to go. However, we plan to go step by step, placing one thing at a time into the dilution refrigerator and make sure everything works as expected. Along with the engineering run, we will also measure RRR of our pure Cu and Al samples and quick Q-factor measurement with Helium dewar. Our goal is to build a complete axion experiment (minus SQUID) that works before this year is over. We are scheduled to have two dilution refrigerators (BlueFors LD400) and a superconducting magnet installed in Munji Campus in the last week of Jan. next year. What we learn from this engineering run will be crucial to the success of the upcoming axion experiment.

References

[1] P. Sikivie, Phys. Rev. Lett. 41 (1983) 1415

[2] Sumitomo Chemical Co., Ltd. R&D Report, "SUMITOMO KAGAKU", vol. 2013

Searching for Axion Dark Matter in Atoms: Oscillating Electric Dipole Moments and Spin-Precession Effects

Benjamin M. Roberts[1], *Yevgeny V. Stadnik*[1], *Victor V. Flambaum*[1,2], *Vladimir A. Dzuba*[1]

[1] School of Physics, University of New South Wales, Sydney, Australia
[2] Mainz Institute for Theoretical Physics, Johannes Gutenberg University, Mainz, Germany

DOI: http://dx.doi.org/10.3204/DESY-PROC-2015-02/roberts_benjamin_axions

We propose to search for axion dark matter via the oscillating electric dipole moments that axions induce in atoms and molecules. These moments are produced through the intrinsic oscillating electric dipole moments of nucleons and through the P,T-violating nucleon-nucleon interaction mediated by pion exchange, both of which arise due to the axion-gluon coupling, and also directly through the axion-electron interaction. Axion dark matter may also be sought for through the spin-precession effects that axions produce by directly coupling to fermion spins.

1 Introduction

Astrophysical observations indicate that the matter content of the Universe is overwhelmingly dominated by dark matter (DM), the energy density of which exceeds that of ordinary matter by a factor of five. In order to explain the observed abundance of DM, it is reasonable to expect that DM interacts non-gravitationally with ordinary matter. Searches for weakly interacting massive particle (WIMP) DM, which look for the scattering of WIMPs off nuclei, have not yet produced a strong positive result. Further progress with these traditional searches is hindered by the observation that the sought effects are fourth-power in the underlying interaction strength between DM and Standard Model (SM) matter, which is known to be extremely small.

We propose to search for other well-motivated DM candidates that include the axion, which may also resolve the strong CP problem of Quantum Chromodynamics (QCD), by exploiting effects that are first-power in the interaction strength between the axion and SM matter (by contrast, haloscope [1] and helioscope [2] methods look for second-power effects, while light-shining-through-wall methods [3] look for fourth-power effects). We focus on the oscillating electric dipole moments (EDMs) and spin-precession effects that axions induce in atoms and molecules. There is strong motivation to search for axions in atomic and related systems via such signatures — to date, static EDM measurements in atoms, molecules and ultracold neutrons have served as sensitive probes of new physics beyond the Standard Model (see e.g. the reviews [4, 5, 6]), while searches for sidereal spin-precession effects with atoms and ultracold neutrons have placed stringent limits on CPT- and Lorentz-invariance-violating models (see e.g. Ref. [7] for an overview).

2 Axion dark matter

Axions produced by the vacuum misalignment mechanism are very cold with no pressure. Furthermore, if axions are sufficiently light and weakly interacting, then they may survive until the present day and reside in the observed galactic DM haloes (where they have become virialised over time with $v_{\rm virial} \sim 10^{-3}$). The number density of ultralight (sub-eV) axions per de Broglie wavelength readily exceeds unity, $n_a/\lambda_{\rm dB}^3 \gg 1$, meaning that axions behave as a coherently oscillating classical field, $a(t) \simeq a_0 \cos(m_a t - \boldsymbol{p}_a \cdot \boldsymbol{r})$ on time scales less than $\tau_{\rm coh} \sim 2\pi/m_a v_{\rm virial}^2$ and length scales less than $l_{\rm coh} \sim 2\pi/m_a v_{\rm virial}$. Thus the couplings of an oscillating galactic axion field to SM particles produce a number of oscillating signatures which can be sought for experimentally. As we will see below, the particularly interesting signatures are those where the observables scale as $\mathcal{O} \propto 1/f_a$ with the axion decay constant f_a.

The axion couplings to SM particles that are of most interest are the following:

$$\mathcal{L}_{\rm int} = \frac{a}{f_a}\frac{g^2}{32\pi^2} G\tilde{G} \; - \sum_{f=e,n,p} \frac{C_f}{2f_a} \partial_\mu a \; \bar{f}\gamma^\mu\gamma^5 f, \tag{1}$$

where the first term represents the coupling of the axion field to the gluonic field tensor G and its dual $\tilde{G}$, and the second term represents the coupling of the derivative of the axion field to the fermion axial-vector currents. C_f are dimensionless model-dependent coefficients. Typically, $|C_n| \sim |C_p| \sim 1$ in models of the QCD axion [8]. Within the DFSZ model, where the tree level coupling of the axion to the electron is non-vanishing, $|C_e| \sim 1$ [8]. However, within the KSVZ model, $|C_e| \sim 10^{-3}$, since the tree level coupling vanishes and the dominant effect arises at the 1-loop level [8]. For more generic axion-like pseudoscalar particles, the coefficients C_f are essentially free parameters, and the coupling to gluons is generally presumed absent.

Oscillating P,T-violating nuclear electromagnetic moments — The coupling of an oscillating axion field to the gluon fields, which is described by the first term in Eq. (1), induces an oscillating EDM of the neutron [9, 10],

$$d_n(t) \simeq 1.2 \times 10^{-16} \; \frac{a_0}{f_a} \cos(m_a t) \; e \cdot \text{cm}, \tag{2}$$

which in turn induces oscillating P,T-violating nuclear electromagnetic moments. In nuclei, a second and more efficient mechanism exists for the induction of oscillating electromagnetic moments by axions — namely, the P,T-violating nucleon-nucleon interaction that is mediated by pion exchange, with the axion field supplying the oscillating source of P and T violation at one of the πNN vertices [10] (Fig. 1).

Oscillating atomic and molecular electric dipole moments — Axion-induced oscillating P,T-odd nuclear electromagnetic moments can in turn induce oscillating EDMs in atoms and molecules. In diamagnetic species ($J = 0$), only oscillating nuclear Schiff moments (which require $I \geq 1/2$) produce an oscillating atomic/molecular EDM (oscillating nuclear EDMs are effectively screened for typical axion masses, as a consequence of Schiff's theorem [11]). Two atoms that are of particular experimental interest are ^{199}Hg and ^{225}Ra, for which the axion induces the following oscillating EDMs [10]:

$$d(^{199}\text{Hg}) = -1.8 \times 10^{-19} \; \frac{a_0}{f_a} \cos(m_a t) \; e \cdot \text{cm}, \tag{3}$$

$$d(^{225}\text{Ra}) = 9.3 \times 10^{-17} \; \frac{a_0}{f_a} \cos(m_a t) \; e \cdot \text{cm}, \tag{4}$$

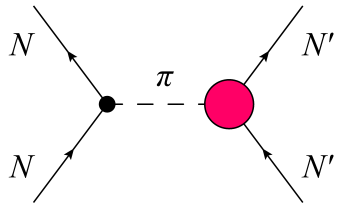

Figure 1: Main process responsible for the induction of oscillating P,T-odd nuclear electromagnetic moments by an oscillating axion field. The black vertex on the left is due to the usual strong P,T-conserving πNN coupling ($g_{\pi NN} = 13.5$), while the magenta vertex on the right is due to the axion-induced P,T-violating πNN coupling ($\bar{g}_{\pi NN} \simeq 0.027 \cos(m_a t)\ a_0/f_a$) [10].

with the large enhancement in ^{225}Ra compared with ^{199}Hg due to both collective effects and small energy separation between members of the relevant parity doublet, which occurs in nuclei with octupolar deformation and results in a significant enhancement of the nuclear Schiff moment [12, 13]. A possible platform to search for the oscillating EDMs of diamagnetic atoms in ferroelectric solid-state media has been proposed in Ref. [14].

Paramagnetic species ($J \geq 1/2$) offer more rich possibilities. Firstly, axion-induced oscillating nuclear magnetic quadrupole moments (which require $I \geq 1$) also produce an oscillating atomic/molecular EDM [15], which is typically larger than that due to an oscillating nuclear Schiff moment (since magnetic quadrupole moments are not subject to screening of the applied electric field by atomic/molecular electrons). Secondly, an entirely different mechanism exists for the induction of oscillating EDMs in paramagnetic species, through the direct interaction of the axion field with atomic/molecular electrons via the second term in Eq. (1). The $\mu = 0$ component of this second term mixes atomic/molecular states of opposite parity (with both imaginary and real coefficients of admixture), generating the following oscillating atomic EDM (due to the real coefficients of admixture) in the non-relativistic approximation for an $S_{1/2}$ state [10],

$$d_a(t) \sim -\frac{C_e a_0 m_a^2 \alpha_s}{f_a \alpha} e \sin(m_a t), \tag{5}$$

where α_s is the static scalar polarisability. Fully relativistic Hartree-Fock atomic calculations are in excellent agreement with the scaling $d_a \propto \alpha_s$ in Eq. (5) [15, 16]. The imaginary coefficients of admixture in the perturbed atomic wavefunction produce P-violating, T-conserving effects in atoms, while the analogous imaginary coefficients of admixture in the perturbed nuclear wavefunction (due to the axion-nucleon interaction via the $\mu = 0$ component of the second term in Eq. (1)) produce P-violating, T-conserving nuclear anapole moments [10, 15, 16].

Oscillating spin-precession effects — The coupling of an oscillating axion field to the fermion axial-vector currents produces the following time-dependent non-relativistic potential for a spin-polarised source, via the $\mu = 1, 2, 3$ components of the second term in Eq. (1)

$$H_{\rm int}(t) = \sum_{f=e,n,p} \frac{C_f a_0}{2 f_a} \sin(m_a t)\ \boldsymbol{\sigma}_f \cdot \boldsymbol{p}_a, \tag{6}$$

which gives rise to spin-precession effects [10, 17, 18]. Deformation of the axion field by the gravitational field of a massive body also produces a time-dependent potential of the form

$H'_{\rm int}(t) \propto (C_f a_0/f_a)\sin(m_a t)\ \boldsymbol{\sigma}_f \cdot \hat{\boldsymbol{r}}$, which is directed towards the centre of the gravitating body [10]. These spin-precession effects can be sought for using a wide range of spin-polarised systems, including atomic co-magnetometers, ultracold neutrons and torsion pendula. The nucleon spin contents for nuclei of experimental interest have been performed in Ref. [19] for the accurate interpretation of laboratory measurements.

Acknowledgments

This work was supported by the Australian Research Council. B. M. R. and V. V. F. are grateful to the Mainz Institute for Theoretical Physics (MITP) for its hospitality and support.

References

[1] S. J. Asztalos *et al.* (ADMX Collaboration), "SQUID-Based Microwave Cavity Search for Dark-Matter Axions," Phys. Rev. Lett. **104**, 041301 (2010).

[2] E. Armengaud *et al.* (IAXO Collaboration), "Conceptual Design of the International Axion Observatory (IAXO)," JINST **9**, T05002 (2014).

[3] R. Bahre *et al.* (ALPS-II Collaboration), "Any light particle search II – Technical Design Report," J. Instr. **8**, T09001 (2013).

[4] J. S. M. Ginges, V. V. Flambaum, "Violations of fundamental symmetries in atoms and tests of unification theories of elementary particles," Phys. Rep. **397**, 63 (2004).

[5] M. Pospelov, A. Ritz, "Electric dipole moments as probes of new physics," Ann. Phys. **318**, 119 (2005).

[6] B. M. Roberts, V. A. Dzuba, V. V. Flambaum, "Parity and Time-Reversal Violation in Atomic Systems," Annu. Rev. Nucl. Part. Sci. **65**, 63 (2015).

[7] V. A. Kostelecky, N. Russell, "Data tables for Lorentz and CPT violation," Rev. Mod. Phys **83**, 11 (2011).

[8] M. Srednicki, "Axion couplings to matter: (I). CP-conserving parts," Nucl. Phys. B **260**, 689 (1985).

[9] P. W. Graham, S. Rajendran, "Axion dark matter detection with cold molecules," Phys. Rev. D **84**, 055013 (2011).

[10] Y. V. Stadnik, V. V. Flambaum, "Axion-induced effects in atoms, molecules, and nuclei: Parity nonconservation, anapole moments, electric dipole moments, and spin-gravity and spin-axion momentum couplings," Phys. Rev. D **89**, 043522 (2014).

[11] L. I. Schiff, "Measurability of Nuclear Electric Dipole Moments," Phys. Rev. **132**, 2194 (1963).

[12] N. Auerbach, V. V. Flambaum, V. Spevak, "Collective T- and P-Odd Electromagnetic Moments in Nuclei with Octupole Deformations," Phys. Rev. Lett. **76**, 4316 (1996).

[13] V. Spevak, N. Auerbach, V. V. Flambaum, "Enhanced T-odd, P-odd electromagnetic moments in reflection asymmetric nuclei," Phys. Rev. C **56**, 1357 (1997).

[14] D. Budker, P. W. Graham, M. Ledbetter, S. Rajendran, A. O. Sushkov, "Proposal for a Cosmic Axion Spin Precession Experiment (CASPEr)," Phys. Rev. X **4**, 021030 (2014).

[15] B. M. Roberts, Y. V. Stadnik, V. A. Dzuba, V. V. Flambaum, N. Leefer, D. Budker, "Parity-violating interactions of cosmic fields with atoms, molecules, and nuclei: Concepts and calculations for laboratory searches and extracting limits," Phys. Rev. D **90**, 096005 (2014).

[16] B. M. Roberts, Y. V. Stadnik, V. A. Dzuba, V. V. Flambaum, N. Leefer, D. Budker, "Limiting P-Odd Interactions of Cosmic Fields with Electrons, Protons, and Neutrons," Phys. Rev. Lett. **113**, 081601 (2014).

[17] V. V. Flambaum, in Proceeding of the 9th Patras Workshop on Axions, WIMPs and WISPs, Schloss Waldthausen, Mainz, Germany, 2013, http://axion-wimp2013.desy.de/e201031.

[18] P. W. Graham and S. Rajendran, "New observables for direct detection of axion dark matter," Phys. Rev. D **88**, 035023 (2013).

[19] Y. V. Stadnik, V. V. Flambaum, " Nuclear spin-dependent interactions: searches for WIMP, axion and topological defect dark matter, and tests of fundamental symmetries," Eur. Phys. J. C **75**, 110 (2015).

Gravity Resonance Spectroscopy and Einstein-Cartan Gravity

Hartmut Abele[1], *Andrei Ivanov*[1], *Tobias Jenke*[1], *Mario Pitschmann*[1], *Peter Geltenbort*[2]

[1]Atominstitut, Technische Universität Wien, Wien, Austria
[2]Institut Laue Langevin, Grenoble, France

DOI: http://dx.doi.org/10.3204/DESY-PROC-2015-02/abele_hartmut

The *q*BOUNCE experiment offers a new way of looking at gravitation based on quantum interference. An ultracold neutron is reflected in well-defined quantum states in the gravity potential of the Earth by a mirror, which allows to apply the concept of gravity resonance spectroscopy (GRS). This experiment with neutrons gives access to all gravity parameters as the dependences on distance, mass, curvature, energy-momentum as well as on torsion. Here, we concentrate on torsion.

1 Introduction

In the past few years, the *q*BOUNCE collaboration has developed a new quantum-technique based on ultra-cold neutrons. Due to their quantum nature, neutrons can be manipulated in novel ways for gravity research. For that purpose a gravitational resonance spectroscopy (GRS) technique has been implemented to measure the discrete energy eigenstates of ultra-cold neutrons in the gravity potential of the Earth, see Fig. 1. The energy levels are probed, using neutrons bouncing off a horizontal mirror with increasing accuracy. In 2011 [1], we demonstrated that such a resonance spectroscopy can be realized by a coupling to an external resonator, i.e., a vibrating mirror. In 2014, the first precision measurements of gravitational quantum states with this method were presented. The energy differences between eigenstates shown in Fig. 1 are probed with an energy resolution of 10^{-14} eV. At this level of precision, we are able to provide constraints on any possible gravity-like interaction. Then, we determined experimental limits, first, for a prominent quintessence theory (chameleon fields) and, second, for axions at short distances [2]. Detailed information on an experimental realization of the quantum bouncing ball by measuring the neutron density distribution given by the wave function can be found in [3, 4]. The demonstration of the neutron's quantum states in the gravity potential of the Earth has been published in [5, 6].

It is planned to extend the sensitivity of this method to an energy resolution of 10^{-17}eV, and in the long run to 10^{-21}eV. The resonance spectroscopy method will be therefore extended to a Ramsey-like spectroscopy technique [7].

At this level of sensitivity, the experiment addresses some important problems of particle, nuclear and astrophysics: three of the most important current theoretical and experimental problems of cosmology and particle physics are i) the current phase (late-time) acceleration of the expansion of the Universe [8–10], ii) the nature of dark energy, which accounts for about

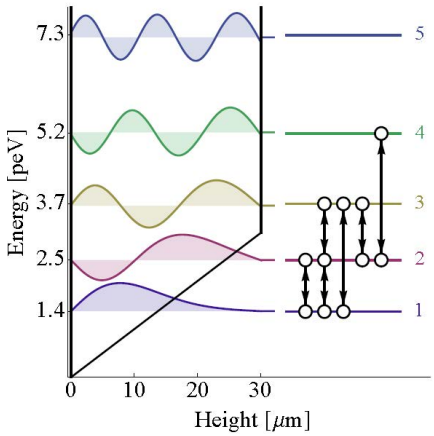

Figure 1: Pico-eV energy eigenstates E_1 to E_5 and Airy-function solutions of the Schrödinger equation for bound ultra-cold neutrons in the linear gravity potential of the Earth. The energy eigenstates are used for gravity resonance spectroscopy and the observed transitions between energy eigenstates are indicated by black arrows.

69 % of the density in the Universe, i.e., $\Omega_\Lambda \approx 0.69$ [11, 12], and iii) the possible existence and nature of torsion, providing a basis for, e.g., Einstein-Cartan gravity [13–17]. One of the simplest explanations for the acceleration of the expansion of the Universe and dark energy is the introduction of the cosmological constant [12], which was introduced for the first time in 1917 by Einstein in his paper *Cosmological Considerations in the General Theory of Relativity* [18]. Einstein's original motivation, outdated by Hubble's discovery of the expansion of the Universe soon afterwards, was to obtain a static solution for the Universe. However, modern quantum field theories naturally connect the cosmological constant with the vacuum-energy of quantum fields. To account for the experimentally observed expansion of the Universe consistent with theories of the history of the Universe, the so-called chameleon scalar fields have been introduced. To avoid any conflict with observations at terrestrial and solar system scales, the properties of these new chameleon fields have to depend on the environmental density. Specially, the effective mass of the chameleon field, and therefore the effective range of its interaction, depend on the density of the environment [19, 20]. The chameleon field is a specific realization of *quintessence* [21]. The chameleon field as a source of dark energy has been discussed in [22].

2 Einstein-Cartan Gravity

In 1922 - 1925 Cartan proposed a theory [13, 14], which is an important generalization of Einstein's general theory of relativity [15]. In contrast to general relativity, Einstein-Cartan theory allows space-time to have torsion in addition to curvature, which may in principle couple to a particle spin. For a long time Einstein-Cartan theory was unfamiliar to physicists and did not attract any attention. In the beginning of the '60s of the last century the theory of gravitation with torsion and spin was rediscovered by Kibble [16] and Sciama [17]. From the 1970s on, Einstein-Cartan theory has been intensively investigated [23–28]. Recently, it has been shown [29] that in the non-relativistic approximation of the Dirac equation in the effective gravitational potential of the Earth, a torsion–matter interaction naturally appears after taking into account also chameleon fields. Such a result demonstrates that chameleon fields can also serve as an origin of space-time torsion. Gravity with torsion, caused by a scalar field, was discussed in detail by Hammond in the review paper [25].

In Einstein-Cartan gravity torsion appears as the antisymmetric part of the affine connection [23]. Thus, torsion is an additional natural geometrical quantity characterizing space-time geometry through spin–matter interactions [23–28]. It allows to probe the rotational degrees of freedom of space-time in terrestrial laboratories. Torsion may be described by a third rank tensor $\mathcal{T}_{\alpha\mu\nu}$, which is antisymmetric with respect to last two indices ($\mathcal{T}_{\alpha\mu\nu} = -\mathcal{T}_{\alpha\nu\mu}$). It can be represented in the following general form [26]: $\mathcal{T}_{\alpha\mu\nu} = \frac{1}{2}(g_{\alpha\mu}\mathcal{T}_\nu - g_{\alpha\nu}\mathcal{T}_\mu) - \frac{1}{6}\,\varepsilon_{\alpha\mu\nu\beta}\mathcal{A}^\beta + \mathcal{M}_{\alpha\mu\nu}$, where $g_{\alpha\sigma}$ and $\varepsilon_{\alpha\mu\nu\beta}$ are the metric and the Levi-Civita tensor, respectively. It possesses 24 independent degrees of freedom, which are related to a 4-vector $\mathcal{T}_\mu$, a 4-axial-vector $\mathcal{A}_\mu$ and a 16-tensor $\mathcal{M}_{\alpha\mu\nu}$. The tensor degrees of freedom $\mathcal{M}_{\alpha\mu\nu}$ obey the constraints $g^{\alpha\mu}\mathcal{M}_{\alpha\mu\nu} = \varepsilon^{\sigma\alpha\mu\nu}\mathcal{M}_{\alpha\mu\nu} = 0$. A minimal inclusion of torsion in terms of the affine connection leads to torsion–matter interactions, caused by the 4-axial degrees of freedom only. As it has been shown in [24, 26, 27], the effects of the torsion axial-vector degrees of freedom are extremely small. An upper bound of order (10^{-22}–10^{-18}) eV has been obtained from the null results on measurements of Lorentz invariance violation. Recent measurements of neutron spin rotation in liquid ^{4}He, carried out by Lehnert *et al.* [30], have lead to the upper bound $|\zeta| < 5.4 \times 10^{-5}$ eV on a parity violating linear combination of the time-components of the vector $\mathcal{T}_\mu$ and the axial-vector $\mathcal{A}_\mu$. Since the order of the time-component of the torsion axial-vector is about 10^{-18} eV [26], an enhancement of the torsion-spin-neutron parity violating interaction can be attributed to a contribution of the time-component of the torsion vector $\mathcal{T}_\mu$. Unfortunately, interactions of both the torsion vector $\mathcal{T}_\mu$ and the torsion tensor $\mathcal{M}_{\alpha\mu\nu}$ can be introduced only phenomenologically in a non-minimal way [26]. This diminishes a little bit the predicting power of the experimental data [30], since the experimental quantity ζ depends on some set of phenomenological parameters multiplied by the time-components of the torsion vector, $\mathcal{T}_0$, and axial-vector, $\mathcal{A}_0$. Nevertheless, the experimental upper bound by Lehnert *et al.* [30] can be accepted as a hint on a possible dominance of the torsion vector degrees of freedom, $\mathcal{T}_\mu$, over the torsion axial-vector ones, $\mathcal{A}_\mu$.

3 The *q*Bounce Experiment

Concerning chameleon fields, the corresponding solutions of the non-linear equations of motion confined between two mirrors have been obtained in [31] and used in [2] in the extraction of the contribution to the transition frequencies of quantum gravitational states of ultra-cold neutrons (UCNs).

Furthermore, the development of a version of Einstein-Cartan gravity with the torsion vector $\mathcal{T}_\mu$ degrees of freedom introduced in a minimal way becomes meaningful and challenging. Clearly, such an extension of general relativity must not contradict well-known data on the late-time acceleration of the expansion of the Universe and dark energy dynamics. A possible route is using our results [29] and taking the torsion vector components $\mathcal{T}_\mu$ as the gradient of the chameleon field. Such a version of a torsion gravity theory allows to retain all properties of the chameleon field, which are necessary for the explanation of the late-time acceleration of the Universe expansion, dark energy dynamics and the equivalence principle [32] (see also [19, 20]) and to extend them by chameleon–photon and chameleon–electroweak boson interactions, introduced in a minimal way.

For the experimental analysis of these chameleon induced torsion - matter interactions very sensitive experiments are needed, which need to overcome the barrier of extremely small magnitudes of the torsion degrees of freedom. As has been pointed out in [31, 35] and proved experimentally in [2], UCNs, bouncing in the gravitational field of the Earth above a mirror

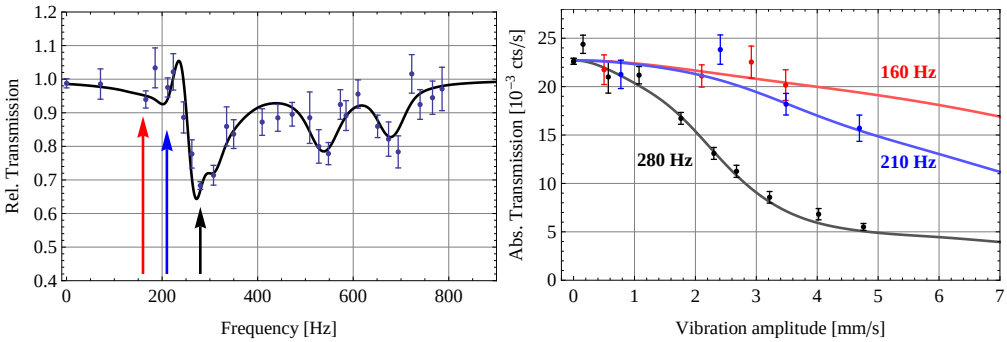

Figure 2: Results for the employed GRS. Left: The transmission curve determined from the neutron count rate behind the mirrors as a function of oscillation frequency showing dips corresponding to the transitions shown in Fig. 1. Right: Upon resonance at 280 Hz, the transmission decreases with the oscillation amplitude in contrast to the detuned 160 Hz. Because of the damping, no revival occurs. A detailed description of the experiment can be found in [2].

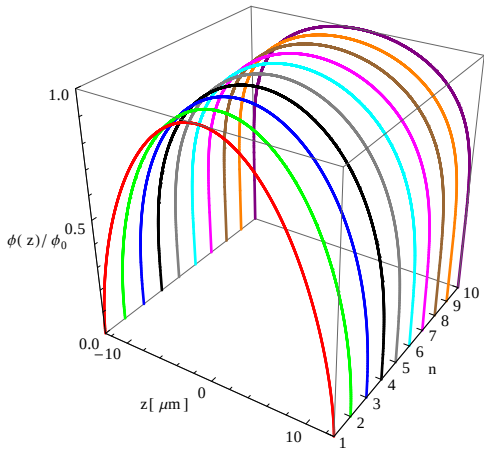

Figure 3: The profiles of the chameleon field, calculated in the strong coupling limit $\beta > 10^5$ in the spatial region $z^2 \leq d^2/4$ for $d = 30.1\,\mu$m and $n \in [1, 10]$ in [31] and used for the extraction of the upper bound of the coupling constant β, i.e. $\beta < 5.8 \times 10^8$ [2].

and between two mirrors can be a good laboratory for testing chameleon–matter field interactions. The quantum energy scale of UCNs is $\varepsilon = mg\ell_0 = 0.602\,\text{peV}$, where m, g and ℓ_0 are the neutron mass, the Newtonian gravitational acceleration [11] and the quantum spatial scale of UCNs such as $\ell_0 = (2mg^2)^{-1/3} = 5.87\,\mu\text{m} = 29.75\,\text{eV}^{-1}$ [2, 7]. In Figure 2 we plot the transmission curves of the transitions between the quantum states shown in Fig. 1. The extraction of the upper bound of β, i.e. $\beta < 5.8 \times 10^8$, has been performed within chameleon field theory using the Ratra-Peebles potential for the chameleon self-interaction [19, 20, 31, 35]. The profiles of the chameleon field, confined between two mirrors and separated by a distance $d = 30.1\,\mu$m have been calculated in [31] and are shown in Fig. 3. A precision analysis of the chameleon–matter coupling constant β can be performed by neutron interferometry as proposed by Brax *et al.* [36, 37] and has been realized by Lemmel *et al.* [33]. Best limits on β have been

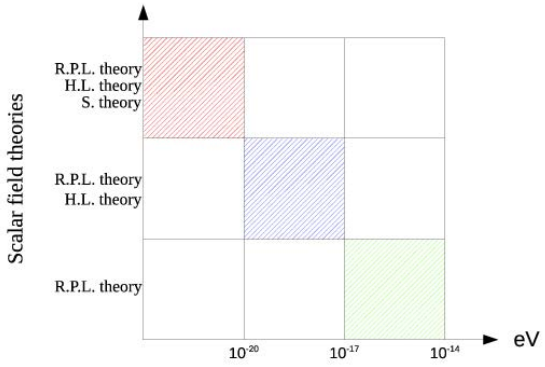

Figure 4: The dependence of the observation of the potential of the self-interaction of scalar (chameleon) field theory on the sensitivity of the experimental data on the transition frequencies of quantum gravitational states of UCNs, measured in qBOUNCE experiments.

achieved by atom interferometry in [34].

As it is well known, the Ratra-Peebles potential is just one possible potential for the self-interaction of scalar fields ϕ. The potential can also be taken in the Higgs-like form [38] (see also [39]) and in the symmetric form [40, 41], respectively. The scalar field with a self-interaction potential, which is symmetric with respect to a transformation $\phi \to -\phi$, is called *symmetron*. As it has been shown in [31], the qBOUNCE experiments with UCNs are able to distinguish the shape of the self-interaction potential of the scalar field. In Figure 4 we show the dependence of the shape of the self-interaction potential of the scalar field on the sensitivity of the experimental data of the qBOUNCE experiments. One may see that the region of accuracies $\Delta E = (10^{-17}\text{–}10^{-14})\,\text{eV}$ is sensitive to the Ratra-Peebles potential only. In turn, the regions of accuracies $\Delta E = (10^{-20}\text{–}10^{-17})\,\text{eV}$ and $\Delta E < 10^{-20}\,\text{eV}$ are sensitive to the scalar field theories with the Higgs-like potential and the symmetron, respectively. A sensitivity of about $\Delta E \approx 10^{-21}\,\text{eV}$ is feasible in the qBOUNCE experiments [7]. Hence, qBOUNCE experiments can be a good tool for measurements of the effective low-energy torsion–spin–matter (neutron) interactions, which can be derived from those obtained in [28]. The use of the qBOUNCE experiments for measurements of torsion–spin–matter (neutron) interactions should be helpful to overcome the barrier of extremely small magnitudes of torsion.

The new method profits from small systematic effects in such systems, mainly due to the fact that in contrast to atoms, the electric polarisability of the neutron is extremely low. Neutrons are also not disturbed by short range electric forces such as van der Waals or Coulomb forces and other polarisability effects such as the Casimir-Polder interaction of UCNs with reflecting mirrors. Together with the neutron neutrality, this provides the key to a sensitivity of several orders of magnitude below the strength of electromagnetism. A search for a non-vanishing charge of the neutron is also possible.

Hence, experimental measurements of the transition frequencies of quantum gravitational states of UCNs in the qBOUNCE experiments [1, 2, 7] and the quantum free fall of UCNs together with the experimental investigations of the phase shifts of the wave functions of slow neutrons in neutron interferometry [33] are very important tools for probing dark energy and theories of torsion gravity [28, 29].

References

[1] T. Jenke, P. Geltenbort, H. Lemmel, and H. Abele, Nature Phys. **7**, 468 (2011).

[2] T. Jenke, G. Cronenberg, J. Burgdorfer, L. A. Chizhova, P. Geltenbort, A. N. Ivanov, T. Lauer, T. Lins, S. Rotter, H. Saul, Phys. Rev. Lett. **112**, 151105 (2014).

[3] H. Abele *et al.*, Nuclear Physics A **827**, 593c (2009) .

[4] T. Jenke et al.: Nucl. Instr. and Meth. A **611**, 318 (2009).

[5] A. Westphal, H. Abele, S. Baessler, V.V. Nesvizhevsky, A.K. Petukhov, K.V. Protasov and A.Yu. Voronin, Eur. Phys. J. C **51**, 367 (2007).

[6] V. V. Nesvizhevsky, H. G. Boerner, A. K. Petukhov, H. Abele, Nature **415**, 297 (2002).

[7] H. Abele, T. Jenke, H. Leeb, and J. Schmiedmayer, Phys. Rev. D **81**, 065019 (2010).

[8] S. Perlmutter *et al.*, Bull. Am. Astron. Soc. **29**, 1351 (1997).

[9] A. G. Riess *et al.*, Astron. J. **116**, 1009 (1998).

[10] S. Perlmutter *et al.*, Astron. J. **517**, 565 (1999).

[11] K. A. Olive *et al.* (Particle Data Group), Chin. Phys. A **38**, 090001 (2014).

[12] E. J. Copeland, M. Sai, and S. Tsujikawa, Int. J. Mod. Phys. D **15**, 1753 (2006).

[13] É. Cartan, C. R. Acad. Sci. (Paris) **174**, 593 (1922).

[14] E. Cartan, Ann. Ec. Norm. **40**, 325 (1923); Ann. Ec. Norm. **41**, 1 (1924); Ann. Ec. Norm. **42**, 17 (1925).

[15] E. Cartan and A. Einstein, "Letters of Absolute Parallelism," Princeton University Press, Princeton, 1975.

[16] T. W. B. Kibble, J. Math. Phys. **2**, 212 (1961).

[17] D. W. Sciama, in "Recent Developments in General Relativity," p. 415, Oxford, Pergamon Press and Warszawa, 1962; Rev. Mod. Phys. **36**, 463 (1964).

[18] A. Einstein, Sitzungsber. Preuss. Akad. Wiss. Berlin (Math. Phys.) **1917**, 142 (1917).

[19] J. Khoury and A. Weltman, Phys. Rev. Lett. **93**, 171104 (2004); Phys. Rev. D **69**, 044026 (2004).

[20] D. F. Mota and D. J. Shaw, Phys. Rev. D **75**, 063501 (2007); Phys. Rev. Lett. **97**, 151102 (2007).

[21] Sh. Tsujikawa, Class. Quantum Grav. **30**, 214003 (2013).

[22] Bh. Jain *et al.*, arXiv:1309.5389 [astro-ph.CO].

[23] F. W. Hehl, J. D. McRea, E. W. Mielke, and Y. Ne'eman, Phys. Rep. **258**, 1 (1995) and references therein.

[24] C. Lämmerzahl, Phys. Lett. A **228**, 223 (1997).

[25] R. T. Hammond, Rep. Prog. Phys. **65**, 599 (2002) and references therein.

[26] V. A. Kostelecky, N. Russell, and J. D. Tasson, Phys. Rev. Lett. **100**, 111102 (2008).

[27] Yu. N. Obukhov, A. J. Silenko, and O. V. Teryaev, Phys. Rev. D **90**, 124068 (2014).

[28] A. N. Ivanov and M. Wellenzohn, Phys. Rev. D **91**, 085025 (2015) and references therein.

[29] A. N. Ivanov and M. Pitschmann, Phys. Rev. D **90**, 045040 (2014).

[30] R. Lehnert, W. M. Snow, and H. Yan, Phys. Lett. B **730**, 353(2014).

[31] A. N. Ivanov, R. Höllwieser, T. Jenke, M. Wellenzohn, and H. Abele, Phys. Rev. D **87**, 105013 (2013).

[32] Cl. M. Will, in "Theory and experiment in gravitational physics," Cambridge University Press, Cambridge 1993.

[33] H. Lemmel, Ph. Brax, A. N. Ivanov, T. Jenke, G. Pignol, M. Pitschmann, T. Potocar, M. Wellenzohn, M. Zawisky, and H. Abele, Phys. Lett. B **743**, 310 (2015).

[34] P. Hamilton, M. Jaffe, P. Haslinger, Q. Simmons, H. Mller, and J. Khoury Science **21**, 849 (2015).

[35] Ph. Brax and G. Pignol, Phys. Rev. Lett. **107**, 111301 (2011).

[36] Ph. Brax, G. Pignol, and D. Roulier, Phys. Rev. D **88**, 083004 (2013).

[37] Ph. Brax, Physics Procedia **51**, 73 (2014).

[38] A. Upadhye, S. S. Gubser, and J. Khoury, Phys. Rev. D **74**, 104024 (2006).

[39] E. G. Adelberger, B. Heckel, S. Hoedl, C. Hoyle, D. Kapner, and A. Upadhye, Phys. rev. Lett. **98**, 131104 (2007).

[40] K. Hinterbichler and J. Khoury, Phys. Rev. Lett. **104**, 231301 (2010).

[41] A. Upadhye, Phys. Rev. Lett. **110**, 031301 (2013).

Dark Matter at the LHC and IceCube – a Simplified Models Interpretation

Jan Heisig, Mathieu Pellen

Institute for Theoretical Particle Physics and Cosmology, RWTH Aachen U., Aachen, Germany

DOI: http://dx.doi.org/10.3204/DESY-PROC-2015-02/heisig_jan

We present an interpretation of searches for Dark Matter in a simplified model approach. Considering Majorana fermion Dark Matter and a neutral vector mediator with axial-vector interactions we explore mono-jet searches at the LHC and searches for neutrinos from Dark Matter annihilation in the Sun at IceCube and place new limits on model parameter space. Further, we compare the simplified model with its effective field theory approximation and discuss the validity of the latter one.

1 Introduction

Weakly interacting massive particles (WIMPs) are popular candidates to account for Dark Matter (DM) in the universe. In the absence of a complete theory of new physics – like supersymmetry – there are basically two ways of describing the phenomenology of a WIMP DM scenario. One is the use of effective operators describing the interactions between the standard model (SM) and the WIMP in the framework of effective field theory (EFT). Another approach is to use simplified models. Here a limited set of new particles is introduced that allows to describe the phenomenology via renormalizable interactions. A simplified model can either be seen as self-consistent extension to the SM or a parametrization of a particular corner in the parameter space of a more complete theory.

Although the EFT framework has been successfully used for the description of DM interactions at rather low scales, it has been pointed out that the use of EFT for the derivation of LHC limits could be problematic [1–3]. In this article we consider a model that extends the SM by a Majorana fermion DM and a vector mediator which couples to the DM and the SM quarks with axial-vector interactions, with couplings g_χ and g_q, respectively. For such a model, LHC searches are expected to be more sensitive than direct detection experiments as the model does not provide any contribution to spin-independent WIMP-nucleon scattering.

In this article we present LHC limits on the parameters space of this model and compare them to the respective limits obtained in the EFT approximation. For realistic values of the couplings, $g_\chi, g_q \lesssim 1$, the LHC provides limits on the messenger mass in the ballpark of 100 GeV to 1 TeV. As these are accessible energies at LHC collisions, contributions from on-shell messenger production can be large. Hence, limits from the simplified model and the EFT can differ significantly as we will discuss in section 2.

As a complementary constraint on the parameter space we consider limits on the spin-dependent WIMP-nucleon scattering from Dark Matter annihilation in the Sun provided by

the IceCube collaboration [4]. These limits are particularly constraining for large DM masses where the LHC looses its sensitivity. We discuss them in section 3.

2 LHC mono-jet constraints

In this work we interpret two searches for mono-jet plus missing transverse momentum signatures performed by ATLAS [5] and CMS [6] at the 8 TeV LHC. To this end we performed a Monte Carlo simulation of the signal and imposed the search cuts detailed in [5, 6]. Based on the background analysis provided in these references we are thus able to set 95% C.L. exclusion limits on the parameters of the model. For details we refer to [7].

The considered model has four independent parameters. The DM mass, m_χ, the mediator mass, M_V, and the couplings of the mediator to the DM, g_χ, and the SM quarks g_q. We assume universal couplings to all SM quarks and neglect couplings to leptons. We show our results for various slices of the parameter space where we fix the product of the couplings, $g_\chi g_q$ and the mediator width, Γ_V. We choose this parametrization as the cross section for DM production directly depends on these parameters. However, not all values of Γ_V and g_χ, g_q are actually consistent within this model as we will show below. In the EFT approximation we integrate out the messenger and obtain a 4-fermion contact interaction with an effective coupling $d = g_\chi g_q / M_V^2$. Hence, the parameter space reduces to two parameters, m_χ and d.

In Figure 1 we show the exclusion limits for the EFT (dashed lines) and the simplified model (solid lines) for four slices of the considered parameter space. Whilst the EFT limit extents to very high DM masses, above a TeV the limit from simplified models goes down very drastically for $M_V \lesssim 2m_\chi$. In this region the EFT approximation is not valid. However, also for $M_V \gg m_\chi$ we find significant deviations in the resulting limit on M_V. This is due to the fact that the limit on M_V placed for $\sqrt{g_\chi g_q} \leq 1$ lies in the region of reachable LHC energies. Hence, the contribution from on-shell mediator production enhances the cross section. This is the dominant effect for the parameter slices with $\Gamma_V = 0.01 M_V$ (left panels of Fig. 1). The effect becomes more pronounced for the smaller coupling, $\sqrt{g_\chi g_q} = 0.2$, (see lower panels) as the limits are placed at lower M_V where the contribution from on-shell mediator production is larger.

For the slices with the larger width $\Gamma_V = 0.5 M_V$ (see right panels of Fig. 1) the limits from simplified models and the EFT are more similar for $M_V \gg m_\chi$. Note that for very small M_V the EFT overestimates the limit. This can be seen in the case $\sqrt{g_\chi g_q} = 0.2$, $\Gamma_V = 0.5 M_V$ (lower right panel) where the CMS limit for the simplified model completely vanishes whilst the EFT would exclude $M_V \gtrsim 200\,\text{GeV}$.

As mentioned above not all combinations of m_χ, M_V, $\sqrt{g_\chi g_q}$ and Γ_V are consistent within the model. In Figure 1 we marked in blue the regions where no such solution exist. Note that the region $M_V > 2m_\chi$ —the region where the EFT shows its best agreement— is strongly constrained and almost excluded for a reasonably small width of $\Gamma_V = 0.01 M_V$.

3 Constraints from DM annihilation in the Sun

If WIMPs scatter in heavy objects such as the Sun, they can loose enough energy to become gravitationally trapped and accumulate inside the Sun. This leads to a locally enhanced WIMP density providing significant DM annihilation. Neutrinos that are produced as primary or secondary products of such annihilations can escape the Sun and be detected on Earth. On

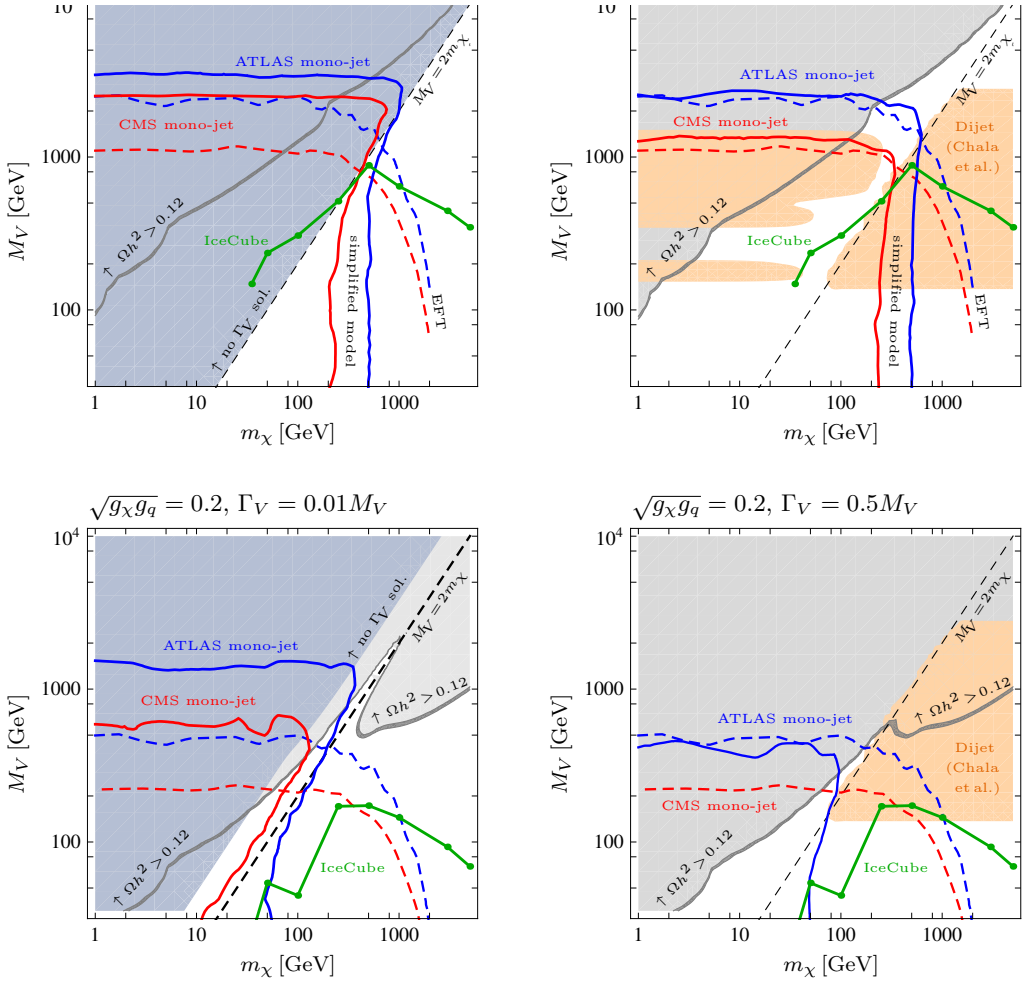

Figure 1: Exclusion limits in the m_χ-M_V plane in four slices of the considered parameter space regarding $\sqrt{g_\chi g_q}$ and Γ_V. The 95% CL exclusion limits from mono-jet searches at ATLAS (blue lines) and CMS (red lines) are shown for the simplified model (solid lines) and the EFT approximation (dashed lines). Further, we show 90% CL exclusion limits from the IceCube Neutrino Observatory (green lines). The dark grey shaded band denotes the region where the relic density matches the dark matter density within ±10%. In the light-grey shaded region above it, the Dark Matter is over-produced. The blue shaded region in the left panels do not allow for a consistent solution for the mediator width as a function of $M_V, m_\chi, \sqrt{g_\chi g_q}$ within the model. The orange shaded regions are exculded from searches for resonances in di-jet signatures taken from Ref. [8].

large time-scales, an equilibrium between the capturing and annihilation can be reached. In this case, a limit on the neutrino flux can be translated into a limit on the scattering cross section of WIMPs inside the Sun. As the Sun contains large amounts of hydrogen, it provides sensitivity to spin-dependent WIMP-proton scattering.

We use data from the IceCube Neutrino Observatory, which are interpreted in two benchmark scenarios according to dark matter annihilation into $b\bar{b}$ or WW only. In most of the parameter space of our model, annihilations into $b\bar{b}$ or $t\bar{t}$ dominate. Therefore we reinterpret the limits from Ref. [4] in order to estimate a limit for annihilation into $t\bar{t}$ by applying conversion factors for $t\bar{t}$ [9] to the WW-channel. We then conservatively apply the limit from the dominant contribution to annihilation (among $b\bar{b}$ and $t\bar{t}$) for each point in parameter space. The resulting limits are shown in Fig. 1 (green lines). In the region of large m_χ where LHC searches loose sensitivity, the limits from IceCube are able to exclude mediator masses up to $M_V \simeq 200\,\text{GeV}$ (1 TeV) for $\sqrt{g_\chi g_q} = 0.2$ (1).

4 Conclusion

We have considered a model with a vanishing spin-independent WIMP-nucleon cross section and set new limits on the model parameter space from LHC mono-jet searches as well as IceCube. From the LHC, for $\sqrt{g_\chi g_q} = 1$ we can exclude mediator masses up to around 3 TeV for $m_\chi \lesssim 1\,\text{TeV}$ while for $\sqrt{g_\chi g_q} = 0.2$ we exclude M_V in the range of 500 GeV to 1.5 TeV with a strong dependence on the mediator width. We compared these limits to the ones obtained in the EFT and found that these are neither entirely conservative nor optimistic in the whole considered parameter space. Limits from IceCube are complementary probing particularly large m_χ where the LHC is not sensitive at all reaching up to $M_V \simeq 1\,\text{TeV}$ for $\sqrt{g_\chi g_q} = 1$.

References

[1] O. Buchmueller, M.J. Dolan, C. McCabe, "Beyond Effective Field Theory for Dark Matter Searches at the LHC," JHEP **1401**, 025 (2014) [arXiv:1308.6799 [hep-ph]].

[2] G. Busoni, A. De Simone, J. Gramling, E. Morgante, A. Riotto, "On the Validity of the Effective Field Theory for Dark Matter Searches at the LHC, Part II: Complete Analysis for the s-channel," JCAP **1406**, 060 (2014) [arXiv:1402.1275 [hep-ph]].

[3] O. Buchmueller, M.J. Dolan, S.A. Malik, C. McCabe, "Characterising dark matter searches at colliders and direct detection experiments: Vector mediators," JHEP **1501**, 037 (2015) [arXiv:1407.8257 [hep-ph]].

[4] IceCube Collaboration, M. Aartsen, *et al.*, "Search for dark matter annihilations in the Sun with the 79-string IceCube detector," Phys.Rev.Lett. **110**, no. 13, 131302 (2013) [arXiv:1212.4097 [astro-ph.HE]].

[5] G. Aad *et al.* [ATLAS Collaboration], "Search for new phenomena in final states with an energetic jet and large missing transverse momentum in pp collisions at $\sqrt{s}$ =8 TeV with the ATLAS detector," Eur. Phys. J. C **75**, no. 7, 299 (2015) [Eur. Phys. J. C **75**, no. 9, 408 (2015)] [arXiv:1502.01518 [hep-ex]].

[6] V. Khachatryan *et al.* [CMS Collaboration], "Search for dark matter, extra dimensions, and unparticles in monojet events in proton?proton collisions at $\sqrt{s}$ = 8 TeV," Eur. Phys. J. C **75**, no. 5, 235 (2015) [arXiv:1408.3583 [hep-ex]].

[7] J. Heisig, M. Kraemer, M. Pellen, C. Wiebusch, "Constraints on Majorana Dark Matter from the LHC and IceCube", *in preparation.*

[8] M. Chala, F. Kahlhoefer, M. McCullough, G. Nardini and K. Schmidt-Hoberg, "Constraining Dark Sectors with Monojets and Dijets," JHEP **1507**, 089 (2015) [arXiv:1503.05916 [hep-ph]].

[9] G. Wikstrom and J. Edsjo, "Limits on the WIMP-nucleon scattering cross-section from neutrino telescopes," JCAP **0904**, 009 (2009) [arXiv:0903.2986 [astro-ph.CO]].

The Rethermalizing Bose-Einstein Condensate of Dark Matter Axions

Nilanjan Banik, Adam Christopherson, Pierre Sikivie, Elisa Maria Todarello

University of Florida, Gainesville, FL 32611, USA

DOI: http://dx.doi.org/10.3204/DESY-PROC-2015-02/sikivie_pierre

The axions produced during the QCD phase transition by vacuum realignment, string decay and domain wall decay thermalize as a result of their gravitational self-interactions when the photon temperature is approximately 500 eV. They then form a Bose-Einstein condensate (BEC). Because the axion BEC rethermalizes on time scales shorter than the age of the universe, it has properties that distinguish it from other forms of cold dark matter. The observational evidence for caustic rings of dark matter in galactic halos is explained if the dark matter is axions, at least in part, but not if the dark matter is entirely WIMPs or sterile neutrinos.

1 Axion dark matter

The story we tell applies to any scalar or pseudo-scalar dark matter produced in the early universe by vacuum realignment and/or the related processes of string and domain wall decay. However, the best motivated particle with those properties is the QCD axion since it is not only a cold dark matter candidate but also solves the strong CP problem of the standard model of elementary particles [1, 2]. So, for the sake of definiteness, we discuss the specific case of the QCD axion.

The Lagrangian density for the axion field $\phi(x)$ may be written as

$$\mathcal{L}_a = \frac{1}{2}\partial_\mu\phi\partial^\mu\phi - \frac{1}{2}m^2\phi^2 + \frac{\lambda}{4!}\phi^4 + ... \tag{1}$$

where the dots represent interactions of the axion with the known particles. The properties of the axion are mainly determined by one parameter f with dimension of energy, called the 'axion decay constant'. In particular the axion mass is

$$m \simeq \frac{f_\pi m_\pi}{f}\frac{\sqrt{m_u m_d}}{m_u + m_d} \simeq 6 \cdot 10^{-6}\text{eV}\ \frac{10^{12}\ \text{GeV}}{f} \tag{2}$$

in terms of the pion decay constant f_π, the pion mass m_π and the masses m_u and m_d of the up and down quarks, and the axion self-coupling is

$$\lambda \simeq \frac{m^2}{f^2}\frac{m_d^3 + m_u^3}{(m_u + m_d)^3} \simeq 0.35\frac{m^2}{f^2} \quad . \tag{3}$$

All couplings of the axion are inversely proportional to f. When the axion was first proposed, f was thought to be of order the electroweak scale, but its value is in fact arbitrary [3]. However

the combined limits from unsuccessful searches for the axion in particle and nuclear physics experiments and from stellar evolution imply $f \gtrsim 3 \cdot 10^9$ GeV [4].

An upper limit $f \lesssim 10^{12}$ GeV is obtained from the requirement that axions are not overproduced in the early universe by the vacuum realignment mechanism [5], which may be briefly described as follows. The non-perturbative QCD effects that give the axion its mass turn on at a temperature of order 1 GeV. The critical time, defined by $m(t_1)t_1 = 1$, is $t_1 \simeq 2 \cdot 10^{-7}\ \mathrm{sec}(f/10^{12}\ \mathrm{GeV})^{\frac{1}{3}}$. Before t_1, the axion field ϕ has magnitude of order f. After t_1, ϕ oscillates with decreasing amplitude, consistent with axion number conservation. The number density of axions produced by vacuum realignment is

$$n(t) \sim \frac{f^2}{t_1}\left(\frac{a(t_1)}{a(t)}\right)^3 = \frac{4 \cdot 10^{47}}{\mathrm{cm}^3}\left(\frac{f}{10^{12}\ \mathrm{GeV}}\right)^{\frac{5}{3}}\left(\frac{a(t_1)}{a(t)}\right)^3 \quad , \tag{4}$$

where $a(t)$ is the cosmological scale factor. Their contribution to the energy density today equals the observed density of cold dark matter when the axion mass is of order 10^{-5} eV, with large uncertainties. The axions produced by vacuum realignment are a form of cold dark matter because they are non-relativistic soon after their production at time t_1. Indeed their typical momenta at time t_1 are of order $1/t_1$, and vary as $1/a(t)$, so that their velocity dispersion is

$$\delta v(t) \sim \frac{1}{mt_1}\frac{a(t_1)}{a(t)} \quad . \tag{5}$$

The average quantum state occupation number of the cold axions is therefore

$$\mathcal{N} \sim \frac{(2\pi)^3\ n(t)}{\frac{4\pi}{3}(m\delta v(t))^3} \sim 10^{61}\left(\frac{f}{10^{12}\ \mathrm{GeV}}\right)^{\frac{8}{3}} \quad . \tag{6}$$

$\mathcal{N}$ is time-independent, in agreement with Liouville's theorem. Considering that the axions are highly degenerate, it is natural to ask whether they form a Bose-Einstein condensate [6, 7]. We discuss the process of Bose-Einstein condensation and its implications in the next section.

The thermalization and Bose-Einstein condensation of cold dark matter axions is also discussed in Refs. [8, 9, 10, 11] with conclusions that do not necessarily coincide with ours in all respects.

2 Bose-Einstein condensation

Bose-Einstein condensation occurs in a fluid made up of a huge number of particles if four conditions are satisfied: 1) the particles are identical bosons, 2) their number is conserved, 3) they are highly degenerate, i.e. $\mathcal{N}$ is much larger than one, and 4) they are in thermal equilibrium. Axion number is effectively conserved because all axion number changing processes, such as axion decay to two photons, occur on time scales vastly longer than the age of the universe. So the axions produced by vacuum realignment clearly satisfy the first three conditions. The fourth condition is not obviously satisfied since the axion is very weakly coupled. In contrast, for Bose-Einstein condensation in atoms, the fourth condition is readily satisfied whereas the third is hard to achieve. The fourth condition is a matter of time scales. Consider a fluid that satisfies the first three conditions and has a finite, albeit perhaps very long, thermal relaxation time scale τ. Then, on time scales short compared to τ and length scales large compared to a

certain Jeans' length (see below) the fluid behaves like cold dark matter (CDM), but on time scales large compared to τ, the fluid behaves differently from CDM.

Indeed, on time scales short compared to τ, the fluid behaves as a classical scalar field since it is highly degenerate. In the non-relativistic limit, appropriate for axions, a classical scalar field is mapped onto a wavefunction ψ by

$$\phi(\vec{r},t) = \sqrt{2} Re[e^{-imt}\psi(\vec{r},t)] \quad . \tag{7}$$

The field equation for $\phi(x)$ implies the Schrödinger-Gross-Pitaevskii equation for ψ

$$i\partial_t \psi = -\frac{1}{2m}\nabla^2\psi + V(\vec{r},t)\psi \quad , \tag{8}$$

where the potential energy is determined by the fluid itself:

$$V(\vec{r},t) = m\Phi(\vec{r},t) - \frac{\lambda}{8m^2}|\psi(\vec{r},t)|^2 \quad . \tag{9}$$

The first term is due to the fluid's gravitational self-interactions. The gravitational potential $\Phi(\vec{r},t)$ solves the Poisson equation:

$$\nabla^2\Phi = 4\pi G m n \quad , \tag{10}$$

where $n = |\psi|^2$. The fluid described by ψ has density n and velocity $\vec{v} = \frac{1}{m}\vec{\nabla}\arg(\psi)$. Eq. (8) implies that n and $\vec{v}$ satisfy the continuity equation and the Euler-like equation

$$\partial_t \vec{v} + (\vec{v}\cdot\vec{\nabla})\vec{v} = -\frac{1}{m}\vec{\nabla}V - \vec{\nabla}q \quad , \tag{11}$$

where

$$q = -\frac{1}{2m^2}\frac{\nabla^2\sqrt{n}}{\sqrt{n}} \quad . \tag{12}$$

q is commonly referred to as 'quantum pressure'. The $\vec{\nabla}q$ term in Eq. (11) is a consequence of the Heisenberg uncertainty principle and accounts, for example, for the intrinsic tendency of a wavepacket to spread. It implies a Jeans length [12]

$$\ell_J = (16\pi G\rho m^2)^{\frac{-1}{4}} = 1.01\cdot 10^{14}\ \text{cm}\left(\frac{10^{-5}\ \text{eV}}{m}\right)^{\frac{1}{2}}\left(\frac{10^{-29}\ \text{gr/cm}^3}{\rho}\right)^{\frac{1}{4}} \quad . \tag{13}$$

where $\rho = nm$ is the energy density. On distance scales large compared to ℓ_J, quantum pressure is negligible. CDM satisfies the continuity equation, the Poisson equation, and Eq. (11) without the quantum pressure term. So, on distance scales large compared to ℓ_J and time scales short compared to τ, a degenerate non-relativistic fluid of bosons satisfies the same equations as CDM and hence behaves as CDM. The wavefunction describing density perturbations in the linear regime is given in Ref. [13].

On time scales large compared to τ, the fluid of degenerate bosons does not behave like CDM since it thermalizes and forms a BEC. Most of the particles go to the lowest energy state available to them through their thermalizing interactions. This behavior is not described by classical field theory and is different from that of CDM. When thermalizing, classical fields

suffer from an ultraviolet catastrophe because the state of highest entropy is one in which each field mode has average energy $k_B T$, where T is temperature. In contrast, for the quantum field, the average energy of each mode is given by the Bose-Einstein distribution, and the ultraviolet catastrophe is removed. To see whether Bose-Einstein condensation is relevant to axions one must estimate the relaxation rate $\Gamma \equiv \frac{1}{\tau}$ of the axion fluid. We do this in the next section.

When the mass is of order 10^{-21} eV or smaller, the Jeans length is long enough to affect structure formation in an observable way [14]. Because we are focussed on the properties of QCD axions, we do not consider this interesting possibility here.

3 Thermalization rate

It is convenient to introduce a cubic box of size L with periodic boundary conditions. In the non-relativistic limit, the Hamiltonian for the axion fluid in such a box has the form

$$H = \sum_j \omega_j a_j^\dagger a_j + \sum_{j,k,l,m} \frac{1}{4} \Lambda_{jk}^{lm} a_j^\dagger a_k^\dagger a_l a_m \quad . \tag{14}$$

with the oscillator label j being the allowed particle momenta in the box $\vec{p} = \frac{2\pi}{L}(n_x, n_y, n_z)$, with n_x, n_y and n_z integers, and the Λ_{jk}^{lm} given by [7]

$$\Lambda_{\vec{p}_1,\vec{p}_2}^{\vec{p}_3,\vec{p}_4} = \Lambda_s{}_{\vec{p}_1,\vec{p}_2}^{\vec{p}_3,\vec{p}_4} \quad + \quad \Lambda_g{}_{\vec{p}_1,\vec{p}_2}^{\vec{p}_3,\vec{p}_4} \quad . \tag{15}$$

where the first term

$$\Lambda_s{}_{\vec{p}_1,\vec{p}_2}^{\vec{p}_3,\vec{p}_4} = -\frac{\lambda}{4m^2 L^3}\, \delta_{\vec{p}_1+\vec{p}_2,\vec{p}_3+\vec{p}_4} \tag{16}$$

is due to the $\lambda\phi^4$ self-interactions, and the second term

$$\Lambda_g{}_{\vec{p}_1,\vec{p}_2}^{\vec{p}_3,\vec{p}_4} = -\frac{4\pi G m^2}{L^3} \delta_{\vec{p}_1+\vec{p}_2,\vec{p}_3+\vec{p}_4} \left(\frac{1}{|\vec{p}_1 - \vec{p}_3|^2} + \frac{1}{|\vec{p}_1 - \vec{p}_4|^2} \right) \tag{17}$$

is due to the gravitational self-interactions.

In the particle kinetic regime, defined by the condition that the relaxation rate $\Gamma \equiv \frac{1}{\tau}$ is small compared to the energy dispersion $\delta\omega$ of the oscillators, the Hamiltonian of Eq. (14) implies the evolution equation

$$\dot{\mathcal{N}}_l = \sum_{k,i,j=1} \frac{1}{2} |\Lambda_{ij}^{kl}|^2 \left[\mathcal{N}_i \mathcal{N}_j (\mathcal{N}_l + 1)(\mathcal{N}_k + 1) - \mathcal{N}_l \mathcal{N}_k (\mathcal{N}_i + 1)(\mathcal{N}_j + 1) \right] 2\pi\delta(\omega_i + \omega_j - \omega_k - \omega_l) \tag{18}$$

for the quantum state occupation number operators $\mathcal{N}_l(t) \equiv a_l^\dagger(t) a_l(t)$. The thermalization rate in the particle kinetic regime is obtained by carrying out the sums in Eq. (18) and estimating the time scale τ over which the $\mathcal{N}_j$ change completely. This yields [6, 7]

$$\Gamma \sim n\, \sigma\, \delta v\, \mathcal{N} \quad . \tag{19}$$

where σ is the scattering cross-section associated with the interaction, and $\mathcal{N}$ is the average state occupation number of those states that are highly occupied. The cross-section for scattering by $\lambda\phi^4$ self-interactions is $\sigma_\lambda = \frac{\lambda^2}{64\pi m^2}$. For gravitational self-interactions, one must take the

cross-section for large angle scattering only, $\sigma_g \sim \frac{4G^2m^2}{(\delta v)^4}$, since forward scattering does not change the momentum distribution.

However, the axion fluid does not thermalize in the particle kinetic regime. It thermalizes in the opposite "condensed regime" defined by $\Gamma >> \delta\omega$. In the condensed regime, the relaxation rate due to $\lambda\phi^4$ self-interactions is [6, 7]

$$\Gamma_\lambda \sim \frac{n\lambda}{4m^2} \tag{20}$$

and that due to gravitational self-interactions is

$$\Gamma_g \sim 4\pi G n m^2 \ell^2 \tag{21}$$

where $\ell = \frac{1}{m\delta v}$ is, as before, the correlation length of the particles. One can show that the expressions for the relaxation rates in the condensed regime agree with those in the particle kinetic regime at the boundary $\delta\omega = \Gamma$.

We apply Eqs. (20) and (21) to the fluid of cold dark matter axions described at the end of Section 1. One finds that $\Gamma_\lambda(t)$ becomes of order the Hubble rate, and therefore the axions briefly thermalize as a result of their $\lambda\phi^4$ interactions, immediately after they are produced during the QCD phase transition. This brief period of thermalization has no known implications for observation. However, the axion fluid thermalizes again due to its gravitational self-interactions when the photon temperature is approximately [6, 7]

$$T_{\rm BEC} \sim 500 \text{ eV} \left(\frac{f}{10^{12} \text{ GeV}}\right)^{\frac{1}{2}} \quad . \tag{22}$$

The axion fluid forms a BEC then. After BEC formation, the correlation length ℓ increases till it is of order the horizon and thermalization occurs on ever shorter time scales relative to the age of the universe.

4 Observational consequences

As was emphasized in Section 3, the axion fluid behaves differently from CDM when it thermalizes. Indeed when all four conditions for Bose-Einstein condensation are fulfilled, almost all the axions go to their lowest energy available state. CDM does not do that. One can readily show that, in first order of perturbation theory and within the horizon, the axion fluid does not rethermalize and hence behaves like CDM. This is important because the cosmic microwave background observations provide very strong constraints in this arena and they are consistent with CDM. In second order of perturbation theory and higher, axions generally behave differently from CDM. The rethermalization of the axion BEC is sufficiently fast that axions that are about to fall into a galactic gravitational potential well go to their lowest energy state consistent with the total angular momentum they acquired from nearby protogalaxies through tidal torquing [7]. That state is a state of net overall rotation. In contrast, CDM falls into galactic gravitational potential wells with an irrotational velocity field. The inner caustics are different in the two cases. In the case of net overall rotation, the inner caustics are rings [15] whose cross-section is a section of the elliptic umbilic D_{-4} catastrophe [16], called caustic rings for short. If the velocity field of the infalling particles is irrotational, the inner caustics have a 'tent-like' structure which is described in detail in Ref. [17] and which is quite distinct from

caustic rings. There is observational evidence for caustic rings [18]. It was shown [19] that the assumption that the dark matter is axions explains not only the existence of caustic rings but also their detailed properties, in particular the pattern of caustic ring radii and their overall size. Furthermore, it was shown [20] that axion BEC solves the galactic angular momentum problem, the tendency of CDM to produce halos that are too concentrated at the center compared to observations.

In a recent paper [21], J. Dumas et al. compare the predictions of the caustic ring model with the rotation curve of the Milky Way and the observations of the Sagittarius sattelite's tidal disruption.

Acknowledgments

We would like to thank Joerg Jaeckel, Alan Guth, Mark Hertzberg and Chanda Prescod-Weinstein for stimulating discussions. This work was supported in part by the US Department of Energy under grant DE-FG02-97ER41209.

References

[1] R.D. Peccei and H. Quinn, Phys. Rev. Lett. **38** 1440 (1977) and Phys. Rev. **D16** 1791 (1977).

[2] S. Weinberg, Phys. Rev. Lett. **40** 223 (1978); F. Wilczek, Phys. Rev. Lett. **40** 279 (1978).

[3] J. Kim, Phys. Rev. Lett. **43** 103 (1979) ; M. A. Shifman, A. I. Vainshtein and V. I. Zakharov, Nucl. Phys. **B166** 493 (1980); A. P. Zhitnitskii, Sov. J. Nucl. 31 **260** (1980); M. Dine, W. Fischler and M. Srednicki, Phys. Lett. B104 **199** (1981).

[4] J.E. Kim and G. Carosi, Rev. Mod. Phys. **82** 557 (2010), and references therein.

[5] J. Preskill, M. Wise and F. Wilczek, Phys. Lett. **B120** 127 (1983) ; L. Abbott and P. Sikivie, Phys. Lett. **B120** 133 (1983) ; M. Dine and W. Fischler, Phys. Lett. **B120** 137 (1983).

[6] P. Sikivie and Q. Yang, Phys. Rev. Lett. **103** 111301 (2009).

[7] O. Erken, P. Sikivie, H. Tam and Q. Yang, Phys. Rev. **D85** 063520 (2012).

[8] S. Davidson and M. Elmer, JCAP **1312** 034 (2013).

[9] K. Saikawa and M. Yamaguchi, Phys. Rev. **D87** 085010 (2013).

[10] J. Berges amd J. Jaeckel, Phys. Rev. **D91** 025020 (2015).

[11] A.H. Guth, M.P. Hertzberg, C. Prescod-Weinstein, arXiv:1412.5930. See the talk by C. Prescod-Weinstein at this workshop.

[12] M.Y. Khlopov, B.A. Malomed and Y.B. Zeldovich, MNRAS **215** 575 (1985).

[13] N. Banik, A. Christopherson, P. Sikivie and E. Todarello, Phys. Rev. **D91** 123540 (2015).

[14] S.-J. Sin, Phys. Rev. **D50** 3650 (1994); J. Goodman, New Astronomy Reviews **5** 103 (2000); W. Hu, R. Barkana and A. Gruzinov, Phys. Rev. Lett. **85** 1158 (2000); H.-Y. Schive et al., arXiv:1508.04621, and references therein. See the talk by D. Grin at this workshop.

[15] P. Sikivie, Phys. Lett. **B432** 139 (1998).

[16] P. Sikivie, Phys. Rev. **D60** 063501 (1999).

[17] A. Natarajan and P. Sikivie, Phys. Rev. **D73** 023510 (2006).

[18] L. Duffy and P. Sikivie, Phys. Rev. **D78** 063508 (2008).

[19] P. Sikivie, Phys. Lett. **B695** 22 (2011).

[20] N. Banik and P. Sikivie, Phys. Rev. **D88** 123517 (2013).

[21] J. Dumas et al., arXiv:1508.04494.

Laboratory Search for New Spin-dependent Interaction at CAPP, IBS

Yunchang Shin[1], *Dong-Ok Kim*[2], *Yannis K. Semertzidis*[1,2]

[1]Center for Axion and Precision Physics Research, IBS, Daejeon, South Korea
[2]Department of Physics, KAIST, Daejeon, South Korea

DOI: http://dx.doi.org/10.3204/DESY-PROC-2015-02/shin_yunchang

Axions are light pseudo-scalar particles originally proposed to explain the strong CP problem in Standard Model. Axions could also be a possible component of Dark Matter. Direct search of axions is the current experiment at Center for Axion and Precision Physics Research (CAPP). In addition, axions would mediate spin-dependent interactions in macroscopic scale. A precision experiment that detects spin-dependent interactions in long range has been recently proposed. The experiment includes polarized ^{3}He gas and a unpolarized mass to induce a monopole-dipole interaction. The experiment can look into axion mass range between 10^{-6} eV to 10^{-3} eV. We describe the experimental plan at CAPP.

1 Introduction

Axions are pseudo-scalar particles that were originally introduced to solve the so-called strong CP problem. Axions are also excellent candidates for Dark Matter if their mass is lighter than $\sim 10^{-5}$ eV. The existence of a new spin-dependent long-range interaction may be a signature of axion because theoretically such spin-dependent interaction could be mediated by light, pseudo-scalar bosons like axions [1]. This paper describes a table-top experiment to detect such interactions between matter objects. The concept of the propose experiment is based on

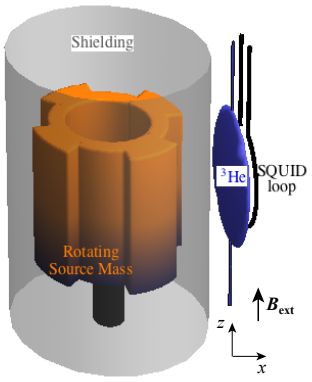

Figure 1: Schematic of experimental search for spin-dependent interaction.

the the resonant coupling between the rotational frequency of a source mass and an ensemble of polarized ^{3}He as nuclear magnetic resonance (NMR) sample with a matching spin precession frequency. In the presence of an anomalous CP-violating interaction with the source mass, the spins in the NMR material will resonantly precess off the axis of polarization. This can be measured with a superconducting quantum interference device (SQUID). There have been many experiments employing precision magnetometer technique to seek such spin-dependent long range interactions [2], [3], [4]. But this experiment is different from previous ones since the resonant effect enhances the signal to detect. With NMR technique, this experiment can look for axion mediated CP-violating forces between masses with a range between $\sim 100\,\mu$m and $\sim 10\,$cm or axion masses between $\sim 10^{-6}\,$eV and $\sim 10^{-3}\,$eV.

2 Concept of the proposed experiment

The general form of the potential caused by the exchange of axion between polarized and unpolarized matters is given as [1]:

$$U_{sp}(r) = g_s^1 g_p^2 \frac{(\hbar c)^2}{8\pi m_2 c^2} (\hat{\sigma_2} \cdot \hat{r}) \left(\frac{1}{r\lambda_a} + \frac{1}{r^2} \right) \exp(-r/\lambda_a), \tag{1}$$

where g_s^1 and g_p^2 are the relevant coupling coefficient of first object (scalar) and the second one (pseudoscalar), respectively. Their product gives the strength of the potential. m_2 and σ_2 are the mass and spin of the polarized particle, r is the distance between the particles, and $\lambda_a = \hbar/m_a c$ is the range of the interaction. The proposed experiment involves a segmented rotating cylinder mass made with high density material such as tungsten to source the axion field, and laser-polarized ^{3}He nuclei that interact with the axion field. The segment in the cylinder generates a time-varying potential at the nuclear spin precession frequency. A conceptual drawing of the experimental setup is shown in Figure 1. In the presence of an axion-mediated interaction, the nuclear spins in the hyper-polarized sample will cause a resonant precession of the axis of the polarization. This change in the magnetization can be detected by a superconducting quantum interference device (SQUID). The key advantage of this experiment is that by rotating the mass so that the segments pass by the medium at the resonant frequency, the sensitivity is enhanced by the quality factor $Q = \omega T_2$ which can be quite large. The interaction potential in Eq.1 can be expressed with axion potential $V_a(r)$ as

$$U_{sp}(r) = -\vec{\nabla} V_a(r) \cdot \hat{\sigma}_2, \tag{2}$$

where $V_a(r) = \frac{\hbar^2 g_s^1 g_p^2}{8\pi m_p} \frac{e^{-\frac{r}{\lambda_a}}}{r}$ is an axion generated potential, which acts on a nearby fermion just like an effective magnetic field of size and direction given by $\vec{B}_{\text{eff}} = \frac{\vec{\nabla} V_a(r)}{\hbar \gamma_f}$, where γ_f is the fermion gyromagnetic ratio. This effective magnetic field is, however, different from an ordinary magnetic field because it does not couple to electric charges or angular momentum. Therefore, a superconducting shielding can be placed between the source mass and detector to screen background electromagnetic field.

3 The Future Plan at CAPP

This experiment requires minimizing all environmental noise that may swamp the effective magnetic field. In this section, a couple of design features to reduce magnetic and vibrational noise and the integration of the setup at CAPP will be presented.

3.1 Anti-vibration Platform

In the proposed experiment, the reduction of vibrational noise plays an important role to make high precision measurement possible. The constant environmental vibration from cars or trains passing near by the building where the measurement takes place has been increased as urban city has evolved. This means that the transmission of vibration from outside become significant source of noise in the precision measurement. The objective of using insulating mechanisms for experimental setup is to reduce repetitive, or sinusoidal vibrations. The task is to keep the motion of the flexibly mounted machine within permissible limits for operation. The vibration insulators selected must have sufficient dampening capacity. Anti-vibration platforms with vibration isolators will be installed in CREATION HALL at KAIST Munji campus. Seven platforms will be installed in total and one of the platforms will be designated for the experimental search of axion with spin-dependent interaction. Figure 2 shows the conceptual design of anti-vibration platform. Expected isolation efficiency of the platform that will be installed is listed in Table 1.

Frequency (Hz)	Efficiency (dB)	Ratio (%)
10	-15	75
20	-25	93
30∼100	-35	97

Table 1: The frequency dependent isolation efficiency of the anti-vibration platform.

3.2 Magnetic Shielding Room (MSR)

This experiment measuring spin-dependent interaction with high precision NMR employs the use of incredibly sensitive magnetometers, such as SQUID to pick up on low level fields induced by the precession within the ^{3}He cell. This signal, however, may be swamped by background fields unless they are properly suppressed. Therefore, the experiment requires shielding from electromagnetic fields with a magnetically shielded room (MSR). The concept for the magnetic shield of the MSR is based on conventional shielding with highly optimized material processing, design and demagnetization, characterization and passive and active compensation of fields. For the proposed experiment, CAPP will have a MSR at CREATION HALL with an extraordinary performance. This MSR will be designed to have residual field at 2 nT with field gradient at 0.5 nT. The shielded room with inside dimensions of 2.8 m×2.5 m×2.5 m cube consists of two layers of μ-metal and an electrically shielding layer of aluminum. The MSR will be eventually installed on the anti-vibration platform to maximize the shielding performance. The frequency-dependent damping factor is tabulated in Table 2.

Frequency	Shielding performance
0.01 Hz	200 times or more
0.1 Hz	300 times or more
1 Hz above	2000 times or more
10 Hz $\sim$ 400 MHz	more than 10,000 times
400 MHz $\sim$ 1000 MHz	more than 1,000 times

Table 2: The shielding performance of the proposed magnetic shielding room.

3.3 Compact ^{3}He Polarization Unit

The ^{3}He polarizing unit is specially designed to fulfill the needs of the experiment at CAPP. The unit will deliver at least 1 atm$\cdot$ liter of spin-polarized ^{3}He gas in the measurement cell every measurement cycle. ^{3}He from a reservoir is fed into the polarizing cell. Metastability Exchange Optical Pumping (MEOP) method will be employed to produce polarized ^{3}He gas with pressure at $\sim$mbar in the cell [6]. To avoid complication in the transport of the polarized ^{3}He, the magnetic field from the optical pumping unit to the measurement cell will be aligned in same direction. The pressure inside the system will be controlled by mass flow controller. The gas will be purified by means of a getter-based purifier. After the purification, the ^{3}He gas is fed into the optical pumping cells. The optical pumping cells will consists of two quartz glass tube with $\sim$ 1 m length and $\sim$ 50 mm diameter. After the optical pumping, the polarized ^{3}He gas will be compressed in a compression unit made with non-magnetic piston and will be stored in a storage volume at 1 atm pressure. All unit will be installed on three different faces of vertical triangular post [7]. Six sets of coils will be installed around the posts to provide uniform magnetic field while ^{3}He gas is polarized and transported. The integration of our compact ^{3}He polarization unit into the anti-vibration platform and MSR is shown in Figure 2. The polarization unit will be mounted at the central region of the anti-vibration platform. The ^{3}He gas will be polarized and transported directly from the polarization unit to the experimental setup. With this configuration, the polarized ^{3}He will undergo the same direction of magnetic guiding field while they are transported and one can avoid the complication of magnetic guiding field.

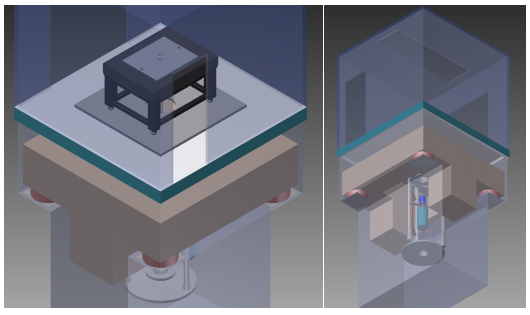

Figure 2: 3D design of the experimental platform with the polarization unit and MSR.

4 Summary

We presented a new concept in experimental search for axions from a spin-dependent interaction. The proposed experiment will be complementary to our CAPP's flagship experiment of axion search with a resonant cavity. In addition, the experimental scheme presented here, in particular, may improve the experimental constraints in respective characteristic energy ranges of axions. Most of these experimental concepts including anti-vibration platform and compact polarization unit are expected to be installed at CAPP in near future for the experimental search of axions from spin-dependent interaction.

Acknowledgement

This work was supported by the Institute for Basic Science under grant no. IBS-R017-D1-2015-a00.

References

[1] J. E. Moody and F. Wilczek, "New macroscopic forces?", Phys. Rev. D, **30**, 130 (1984).

[2] W. Zheng, *et al.*, "Search for spin-dependent short-range force between nucleons using optically polarized He3 gas", Phys. Rev. D, **85**, 031505 (2012).

[3] M. Bulatowicz, *et al.*, "Laboratory Search for a Long-Range T-Odd, P-Odd Interaction from Axionlike Particles Using Dual-Species Nuclear Magnetic Resonance with Polarized Xe129 and Xe131 Gas", Phys. Rev. Lett., **111**,102001 (2013).

[4] P. H. Chu, *et al.*, "Laboratory search for spin-dependent short-range force from axionlike particles using optically polarized He3 gas", Phys. Rev. D, **87**, 011105 (2013).

[5] A. Arvanitaki and A. A. Geraci, "Resonantly Detecting Axion-Mediated Forces with Nuclear Magnetic Resonance", Phys. Rev. Lett., **113**, 161801 (2014).

[6] G. Collier. "Metastability Exchange Optical Pumping (MEOP) of 3He in situ", PhD thesis, Jagiellonian University (2011).

[7] A. Kraft, *et al.*, "Development of a 3He magnetometer for a neutron electric dipole moment experiment", EPJ Tech., **1**, 8 (2014).

Hidden Photon CDM Search at Tokyo

Jun'ya Suzuki, Yoshizumi Inoue, Tomoki Horie, Makoto Minowa

The University of Tokyo, Japan

DOI: http://dx.doi.org/10.3204/DESY-PROC-2015-02/junya_suzuki

We report on a search for hidden photon cold dark matter (HP CDM) using a novel technique with a dish antenna. We constructed two independent apparatuses: one is aiming at the detection of the HP with a mass of $\sim$ eV which employs optical instruments, and the other is for a mass of $\sim 5 \times 10^{-5}$ eV utilizing a commercially available parabolic antenna facing on a plane reflector. From the result of the measurements, we found no evidence for the existence of HP CDM and set upper limits on the photon-HP mixing parameter χ.

1 Introduction

Astronomical observations of the past decades reveal that there exists invisible non-baryonic matter (dark matter, DM) in the universe. Exploring the nature of DM is one of the most important issues in astrophysics and cosmology today, and a variety of experiments have been carried out to directly detect DM particles.

The most prominent candidate for DM is the Weakly Interacting Massive Particle (WIMP), and most of the current experiments aim at the detection of WIMPs. However, there are alternative candidates to account for the features of DM, and Weakly Interacting Slim Particles (WISP), e.g. axion-like particles (ALP) or hidden-sector photons (HP), can be the main component of DM [1].

Hidden photon cold dark matter (CDM) can be experimentally investigated via kinetic mixing $(\chi/2)F_{\mu\nu}\tilde{X}^{\mu\nu}$ between photons and hidden photons. For example, the Axion Dark Matter eXperiment (ADMX) [2], which employs a resonant cavity and magnetic field to search for axion dark matter, also has sensitivity to hidden photon CDM, and its non-detection of the signal [3, 4, 5, 6, 7] was translated to the upper limit for the kinetic mixing parameter χ [1].

Additionally, a novel method with a spherical mirror to search for HP CDM was recently proposed [8], with which wider mass-range can be probed without rearranging the setup. In this method, ordinary photons of energy $\omega \simeq m_{\gamma'}$ induced by HP CDM via kinetic mixing are emitted in the direction perpendicular to the surface of the mirror, resulting in concentration of the power to the center of the mirror sphere.

This method using a spherical reflector is extremely simple, and can be implemented relatively easily. To confirm its feasibility in real situations, we planned and carried out two experiments to search for HP CDM in two different mass regions: one is for $m_{\gamma'} \sim$ eV using optical equipments and the other for $m_{\gamma'} \sim 50\,\mu$eV employing RF instruments. Here we report on the preparations and the results of those searches for HP CDM using the dish method.

2 Optical search

For the search in $m_{\gamma'} \sim$ eV, we need a spherical mirror and a photodetector. Non-relativistic HPs near the surface of a reflector induce emission of photons in the direction perpendicular to the surface. A photodetector is placed at the point of convergence and detects emitted photons.

We used a parabolic mirror as a 'dish'. The parabolic mirror is 500 mm in diameter, 1007 mm focal length and the focal spot diameter is 1.5 mm. We used a parabolic surface instead of a spherical surface originally proposed in Ref. [8] to reuse the mirror which had been employed in the solar HP helioscope [9]. From the diameter and the focal length of the parabolic mirror, photons emitted perpendicularly to the surface are calculated to concentrate to a small area of 4 mm in diameter at twice the focal length of the mirror, which is small enough compared to the effective area of the photodetector.

Figure 1: The setup for the optical search. After installing optical equipments, this frame was wrapped with black polyethylene sheets to block ambient light.

A photomultiplier tube (PMT) was employed as the detector of emitted photons. We selected Hamamatsu Photonics R3550P because of its low dark count rate of $\sim$ 5Hz. We used a motorized stage to shift the position of the PMT, which enabled us to measure background noise.

The mirror and the detector were mounted on a steel frame, which rigidly holds the arrangement (Fig. 1). After installing the optical equipments, this frame was wrapped with black polyethylene sheets to shield from ambient light. Additionally, the whole setup was installed in a light-tight box of 1m $\times$ 1m $\times$ 3m to attain higher light-tightness.

With this setup, we carried out the experimental search for HP CDM in the eV mass range [10]. The overall duration of the measurement was 8.3×10^5 s for each configuration: with the PMT at the position of convergence of the HP CDM signal (signal, S) and at the position displaced by 25 mm from position S (background, B). We found no excess in count rate measured at position S compared to at position B. We translated this non-detection result to the limit for the mixing parameter χ (Fig. 2).

3 RF search

We also targeted detection in K_u band ($\sim$ 12 GHz) for the feasibility test of the 'dish' method. We can use commercially available dish antennas for this frequency region, though they usually have parabolic shape, which cannot be approximated as spherical shape because of their short focal lengths compared to their diameters. In order to overcome this problem, we let our dish face a plane reflector, from which plane radio waves of HP CDM origin would be emitted perpendicularly to the surface. Because parabolic dishes concentrate plane waves to their focal point, the amplification of HP CDM signal properly works. We used an Anstellar SXT-220 as a dish, which is 2.2 m in diameter and designed for CS broadcast reception. A huge plane reflector was constructed by combining four alminum plates on a rigid frame.

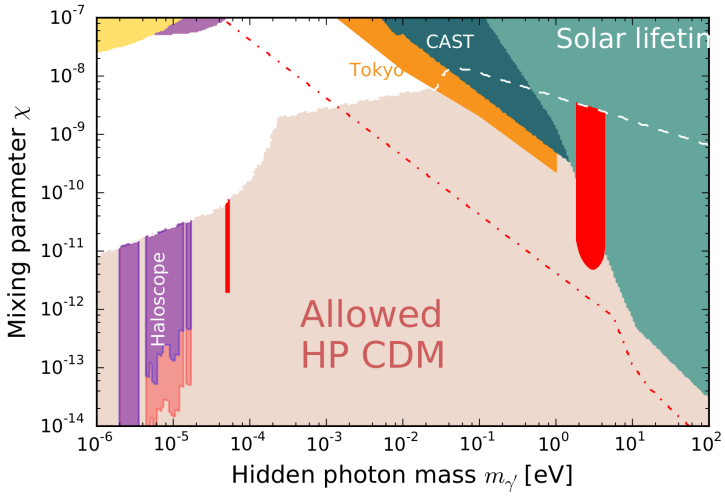

Figure 2: Preliminary results of the experimental searches for HP CDM. The vertical axis shows the mixing parameter χ, and the horizontal axis shows the mass of hidden-photon $m_{\gamma'}$. The red colored regions are excluded by our results for two experimental setups. With the optical setup, we excluded the area around $m_{\gamma'} \sim$ eV. The search in K_u band excluded the region around $m_{\gamma'} \sim 50\,\mu$eV. For a descriptions of the other colored areas, see Ref. [10].

For the converter, we selected Norsat 4506B, which down-converts the signal with the local frequency of 11 GHz. The output of the converter was connected to the Fast Fourier Transform (FFT) analyzer, Rohde & Schwarz FSV-4. The signal of the existence of HP CDM would be seen as a spectral line with a broadening of $\Delta f/f \sim 10^{-6}$ due to the velocity dispersion of DM.

After the calibration, the setup for the experimetal search was constructed by setting the dish in front of the plane reflector (Fig. 3).

Using this setup, we actually carried out the experimental search for four days. We observed no signal-like excess in the power spectrum and set an upper limit for the parameter χ (Fig. 2). Although the limit is narrow in the sensitive mass region, we can expand it only by replacing the converter for one which is capable of handling wider frequency range.

Figure 3: The setup for the search in K_u band. The parabolic dish designed for CS broadcast reception faces on the plane reflector made up of four alminum plates.

4 Conclusion

We constructed two apparatuses utilizing a novel method using a dish antenna. One uses an optical mirror for the survey in $m_{\gamma'} \sim$ eV, and the other uses a dish antenna for CS broadcast reception to search HPs with $m_{\gamma'} \sim 50\,\mu$eV. We actually carried out the experimetal search, and found no evidence for the existence of HP CDM. From the result, we set upper limits on the photon-HP mixing parameter χ in two different mass regions (Fig. 2).

Acknowledgments

T. Horie acknowledges support by Advanced Leading Graduate Course for Photon Science (ALPS) at the University of Tokyo. This reaserch is supported by the Grant-in-Aid for challenging Exploratory Research by MEXT, Japan, and also by the Research Center for the Early Universe, School of Science, the University of Tokyo.

References

[1] P. Arias, D. Cadamuro, M. Goodsell, J. Jaeckel, J. Redondo *et al.*, JCAP **06** 013 (2012).

[2] H. Peng, S.Asztalos, E. Daw, N. A. Golubev, C. Hagmann *et al.*, Nucl. Instr. Meth. A **444** 569 (1999).

[3] S. DePanfilis, A. C. Melissinos, B. E. Moskowitz, J. T. Rogers, Y. K. Semertzidis *et al.*, Phys. Rev. Lett. **59** 839 (1987).

[4] W. U. Wuensch, S. De Panfilis-Wuensch, Y. K. Semertzidis, J. T. Rogers, A. C. Melissinos *et al.*, Phys. Rev. D **40** 3153 (1989).

[5] C. Hagmann, P. Sikivie, N. S. Sullivan, and D. B. Tanner, Phys. Rev. D **42** 1297(R) (1990).

[6] S. Asztalos, E. Daw, H. Peng, L. J Rosenberg, C. Hagmann *et al.*, Phys. Rev. D **64** 092003 (2001).

[7] S. J. Asztalos, G. Carosi, C. Hagmann, D. Kinion, K. van Bibber *et al.*, Phys. Rev. Lett. **104** 041301 (2010).

[8] D. Horns, J. Jaeckel, A. Lindner, A. Lobanov, J. Redondo, and A. Ringwald, JCAP **04** 016 (2013).

[9] T. Mizumoto *et al.*, JCAP **07** 013 (2013) [arXiv:1302.1000 [hep-ex]].

[10] J. Suzuki, T. Horie, Y. Inoue, and M. Minowa, arXiv:1504.00118 [hep-ex]. Accepted for publication in JCAP.

AMELIE: An Axion Modulation hELIoscope Experiment

Javier Galan

University of Zaragoza, Zaragoza, Spain

DOI: http://dx.doi.org/10.3204/DESY-PROC-2015-02/galan_javier

In this work, I present an innovative idea to search for solar axions using a large volume low background Time Projection Chamber (TPC) immersed in a magnetic field. This technique will be sensitive to axion masses above few hundreds of meV in the theoretically favored QCD-axion parameter space. The detector geometry will be such that will allow to monitor the solar axion flux during the whole day. A stationary detector would produce a daily and annual modulation signal pattern given by the angle of the incident axion flux and the TPC magnetic field which is driven by the earth rotation. Recent progress on large volume low background TPC's for rare event searches motivates the development of such helioscope technique. The principle of detection and prospects on the sensitivity of such an experiment will be shown.

1 Introduction

The axion is a hypothetical neutral pseudoscalar particle which was already predicted in 1977 [1]. This weakly interacting particle came out as a simple solution to the CP problem of strong interactions in Quantum Chromodynamics (QCD) [2]. The particular properties of the axion can be restricted by the actual observational consequences that its existence would imply in astrophysics and cosmology [3, 4]. Their detection principle is based on the Primakoff effect using the interaction of the axion with two photons [5]. Experiments searching for axions use an intense magnetic field that provides one of the photons involved in the interaction, aiming to detect the second photon that, for maximum conversion probability, carries the total energy of the axion. The idea here presented belongs to the axion helioscope searches. If axions exist, they should be produced in the inner core of the Sun. The energy spectrum of these axions is related to the core temperature of the Sun, and thus its energy is in the 1-10 keV region. Axion helioscopes aim to detect the solar axion flux on the earth.

The first solar axion searches provided axion-photon coupling sensitivities for a wide axion mass region (see [6] for a detailed review). The CERN Axion Solar Telescope (CAST) provides today the best sensitivity to the axion-photon coupling for solar axions, being the first helioscope exploring a theoretically favored axion region for axion masses $\lesssim$ eV [7]. CAST uses a 9.6 m-long dipole magnet with an intense magnetic field of 8.9 T, capable to track the Sun 3 hours per day. The International AXion Observatory (IAXO) collaboration is developing the future generation helioscope magnet [8]. IAXO will built a dedicated 8-bore large-aperture superconducting magnet 20 m long, reaching an average field intensity of 2.5 T. Each of the 8 (60 cm diameter) magnet bores will be equipped with x-ray focussing devices that will allow to

focus the large aperture area in a spot of just $0.2\,\mathrm{cm}^2$ increasing significatively the signal-to-background ratio. A dedicated tracking system will facilitate taking data during 12 h per day. All these enhancements will allow IAXO to improve by 4-5 orders of magnitude the sensitivity of CAST in terms of signal-to-noise, reaching sensitivities of a few $\times 10^{-12}\mathrm{GeV}^{-1}$.

2 A new helioscope detection technique

We present a new helioscope detection concept that was never before exploited for axion searches, and that could allow to improve actual sensitivities, especially for the $m_a \gtrsim$ eV. To access the higher axion mass region ($\sim$eV) helioscopes use a buffer gas that allows to recover axion-photon conversion probability. The axion field propagates through a long magnetic bore which is filled with helium to minimize the photon re-absorption. The converted photons are transmitted to the end of the bore and detected by low background X-ray detectors. In contrast, the idea proposed here uses a higher-Z (i.e. xenon) buffer gas, allowing to absorb the converted photons directly in the buffer gas. A TPC design immersed in a magnetic field would allow their detection (see Figure 1). Further details for the new helioscope concept presented here can be found at [9].

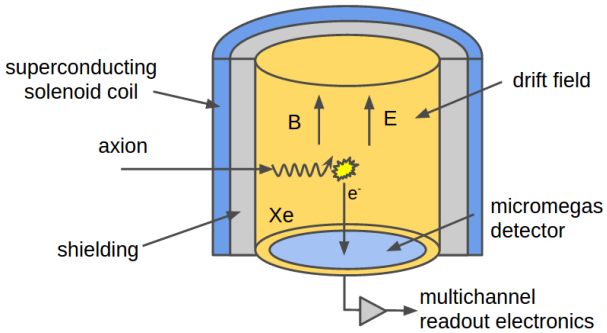

Figure 1: A conceptual drawing showing the TPC drift volume. The axion would convert to a photon inside the TPC, interacting in the gas and producing electrons drifting towards a micropatterned readout, allowing to measure time and spatial event topology. A proper shielding against external radiation should be placed in order to minimize the background level of the detector.

This setup is inspired by an original idea developed in 1989 [10]; the main difference with this work resides on the introduction of a higher-Z buffer gas for axion conversion. The use of higher-Z gases would be possible in this setup thanks to the fact that the buffer gas defining the sensitivity at a given axion mass range and the gas detection volume of the TPC would be the same. Thus, we are interested in using higher-Z gases to maximize the detection efficiency.

The use of a long pipe by actual helioscopes, detecting the transmitted photon component, is justified for the enhancement of the final axion-photon conversion probability that is proportional to B^2L^2 [11], where B the magnetic field and L its length. In the case of a helioscope which aims to detect the absorbed photon component, the conversion probability will be just proportional to B^2L (or to the volume of the TPC, B^2V). This efficiency loss in conversion

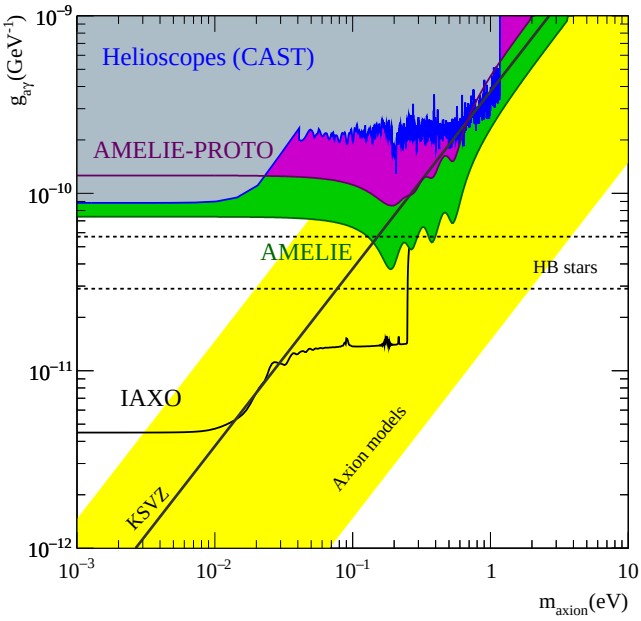

Figure 2: Axion-photon coupling as a function of the axion mass excluded by tracking helioscopes (CAST). The future IAXO sensitivity prospects are also shown. We plot the prospects for a small prototype (AMELIE-PROTO) and a 1 m^3 scale detector (AMELIE). The yellow band represents the favored axion theoretical region.

probability is counter-balanced by using a larger conversion volume, allowing to re-enhance the quantity B^2V, and the longer exposure capability of this type of helioscope.

An obvious implementation maximizing the volume would be a cylindrical shaped TPC. The magnetic field orientation with respect to the incident axion flux would provide a daily modulation pattern due to the change on the effective magnetic field transversal component. The daily average transversal component, B^2, would be about 75% of the absolute field intensity, allowing to track the Sun during 24 hours at the given efficiency. The flexibility of operation of a gaseous TPC at different gas pressures, ranging between few mbar to several bar, would allow to setup the detector to enhance its sensitivity for different axion mass regions, from few hundreds of meV to few eV.

3 Prospects for an AMELIE search

The sensitivity achievable with this type of helioscope will be mainly driven by the quantity B^2V and the background level achievable by a large volume TPC. Recent progress on low background large volume TPCs motivates partially the development of this helioscope technique. Prospects on those TPC developments [12, 13, 14] set the background reachable to be between 0.1-10 keV^{-1} day^{-1} m^{-3}. To reach these levels the detector should be installed at an underground

laboratory, certainly possible using this technique since no tracking alignment is required.

We have calculated the axion-photon coupling sensitivity using an Axion Modulation hELIoscope Experiment (AMELIE). Here, we present two different scenarios, a small size prototype of about 21 dm^3 reaching a background level of 1 day^{-1} m^{-3} keV^{-1}, and a larger TPC of about 0.75 m^3 reaching an improved background level of 0.1 day^{-1} m^{-3} keV^{-1}. Both scenarios have been calculated for an absolute magnetic field of 5 T, and *four* pressure settings at 20, 40, 80 and 160 mbar. For this calculation the total exposure used at the first pressure setting is 5 years, at the second pressure setting is 2.5 years, and the *two* remaining pressure settings is 1.25 years. The resulting sensitivity is shown in Figure 2.

The expected sensitivity shown with this technique would allow to explore a region of the axion-photon coupling and axion mass parameter space not previously accessible, and to probe QCD-axions for masses above $\gtrsim$100 meV. The main challenges to reach such sensitivity would be the development of a TPC-magnet design that allows to keep the background level of the detector below the mentioned levels. Another interesting feature of this type of helioscope resides on the wide field of view allowing to scan an extense region of the space. The wider resonance given by the higher-Z gas used would allow to do measurements at a fixed pressure during long data taking periods, still covering an extense region of the axion mass.

References

[1] Steven Weinberg, "A New Light Boson?," Phys. Rev. Lett. **40** 223-226 (1978).

[2] R. D. Peccei and H. R. Quinn, "Constraints imposed by CP conservation in the presence of pseudoparticles," Phys. Rev. D **16** 1791-1797 (1977).

[3] G. G. Raffelt, "Astrophysical axion bounds," Lect. Notes Phys. **741** 51-71 (2008).

[4] P. Sikivie, "Axion cosmology," Lect.Notes Phys. **741** 19-50 (2008).

[5] P. Sikivie, "Experimental Tests of the "Invisible" Axion," Phys. Rev. Lett. **51** 1415 (1983).

[6] K. Baker, "The quest for axions and other new light particles," Ann. Phys. (Berlin) **525**, No. 6, A93-A99 (2013).

[7] CAST Collaboration, M. Arik *et al.*, "Solar axion search with ^{3}He buffer gas: Closing the hot dark matter gap," Phys. Rev. Lett. **112** 091302 (2014).

[8] E. Armengaud *et al.*, "Conceptual design of the International Axion Observatory (IAXO)," JINST **9** T05002 (2014).

[9] J. Galan *et al.*, "Exploring 0.1-10eV axions with a new helioscope concept," submitted to JCAP (2015) [arXiv:1508.03006].

[10] K. van Bibber *et al.*, "Design for a practical laboratory detector for solar axions," Phys. Lett. D **39** 2089-2099 (1989).

[11] G. G. Raffelt and L. Stodolsky, "Mixing of the photon with low-mass particles," Phys. Rev. D **37** 1237-1249 (1988).

[12] A. Dastgheibi-Fard *et al.*, "Background optimization for a new spherical gas detector for very light WIMP detection," Proceedings of Technology and Instrumentation in Particle Physics (2014).

[13] F.J. Iguaz *et al.* "TREX-DM: a low background Micromegas-based TPC for low mass WIMP detection," Proceedings of the 7th Symposium on Large TPCs for low-energy Rare Events Detection (2015).

[14] S. Aune *et al.*, "Low background x-ray detection with Micromegas for axion search," JINST **9** P01001 (2014).

Recent Progress with the KWISP Force Sensor

G. Cantatore[1,2], *A. Gardikiotis*[3], *D.H.H. Hoffmann*[4], *M. Karuza*[5,2], *Y. K. Semertzidis*[6], *K. Zioutas*[3,7]

[1]Universitá di Trieste, Trieste, Italy
[2]INFN Sez. di Trieste, Trieste, Italy
[3]University of Patras, Patras, Greece
[4]Institut fr Kernphysik, TU-Darmstadt, Darmstadt, Germany
[5]Phys. Dept. and CMNST, University of Rijeka, Rijeka, Croatia
[6]Department of Physics, KAIST, Daejeon, Republic of Korea
[7]European Organization for Nuclear Research (CERN), Géneve, Switzerland

DOI: http://dx.doi.org/10.3204/DESY-PROC-2015-02/cantatore_giovanni

The KWISP opto-mechanical force sensor has been built and calibrated in the INFN Trieste optics laboratory and is now under off-beam commissioning at CAST. It is designed to detect the pressure exerted by a flux of solar Chameleons on a thin (100 nm) Si_3N_4 micromembrane thanks to their direct coupling to matter. A thermally-limited force sensitivity of $1.5 \cdot 10^{-14}$ N/$\sqrt{\text{Hz}}$, corresponding to $7.5 \cdot 10^{-16}$ m/$\sqrt{\text{Hz}}$ in terms of displacement, has been obtained. An originally developed prototype chameleon chopper has been used in combination with the KWISP force sensor to conduct preliminary searches for solar chamaleons.

1 Introduction

The KWISP (Kinetic WISP detection) force-sensor consists of a thin (100 nm) dielectric membrane suspended inside a resonant optical Fabry-Perot cavity [1, 2, 3]. The collective force exerted by solar Chameleons bouncing off the membrane surface [4, 5] will cause a displacement from its equilibrium position which can be sensed by monitoring the cavity resonant frequency. Since, in addition, the membrane is a mechanical resonator, the displacement sensitivity is enhanced by the mechanical quality factor of the membrane. For a detailed description of the KWISP force sensor see [6]. An absolute calibration of the KWISP sensor in terms of force has been obtained in the INFN Trieste optics laboratory by applying a known external force supplied by the radiation pressure of a laser beam (*pump beam technique*). This external force is modulated at a given frequency allowing one to explore the frequency region near the mechanical resonance of the membrane. Here we obtain a force sensitivity already at the 300 K thermal limit [7]. In order to effectively use the KWISP sensor for chameleon detection it is necessary to find a means of modulating the amplitude of the expected chameleon beam. By exploiting the ability of chameleons to reflect off any material surface when impinging at grazing incidence, and to correspondingly traverse it when at normal incidence [4], we have originally devised and built a *chameleon chopper* prototype. The chopper allows one to shift the expected chameleon signal away from the noisy region near zero frequency, eventually reaching, with a suitable high frequency chopper, frequencies near resonance. We have used the prototype

chopper, working at frequencies below 200 Hz, for preliminary solar chameleon search runs, also taking advantage of the fact that the KWISP membrane orientation in space is such, that a hypothetical chameleon beam from the sun will reflect off it at grazing angles between 0 and 20 degrees for about 1.5 hours each day. In the following we will briefly describe the sensor setup, the results from absolute calibration measurements, the chameleon chopper prototype and its use in preliminary solar runs.

2 The KWISP force sensor

The main element of the KWISP force sensor is a vacuum chamber containing an 85 mm-long Fabry-Perot cavity made with two 1-inch diameter, 100 cm curvature radius, high-reflectivity, multilayer dielectric mirrors. A Si_3N_4, 5x5 mm^2, 100 nm thick membrane is inserted inside the cavity and it is initially placed approximately midway between the two cavity mirrors (*membrane-in-the-middle* configuration). The Fabry-Perot cavity is excited using a CW 1064 nm laser beam emitted by a Nd:YAG laser. A second, frequency-doubled, CW beam at 532 nm emitted by the same laser is used as an auxiliary beam (*pump beam*) for alignment and for exerting a known external force on the membrane. When the sensor is in detection mode the Fabry-Perot cavity is frequency-locked to the laser using an electro-optic feedback loop [1]. The error signal generated by this loop is proportional to the instantaneous frequency difference between laser and cavity and its power spectrum contains the information on membrane displacements. The pump beam, amplitude-modulated at a given frequency, is then injected into the cavity and it exerts a known force on the membrane by reflecting off it. The intensity of the pump beam corresponds in our case to a net force of $7.9 \cdot 10^{-14}$ N. The presence of this force is detected as a peak in the measured spectrum of the error signal. The membrane behaves as a mechanical oscillator and its fundamental resonant frequency and quality factor can be directly measured with the pump beam technique. Figure 1 shows a plot of several power spectra of the feedback loop error signal. The peaks indicate the presence of the calibration force, while different peaks correspond to different excitation frequencies. The peak with the largest amplitude occurs when the pump beam modulation frequency matches the membrane mechanical resonance freqeuncy. The background level in Figure 1 gives a force sensitivity of $1.5 \cdot 10^{-14}$ N/$\sqrt{\text{Hz}}$, corresponding to $7.5 \cdot 10^{-16}$ m/$\sqrt{\text{Hz}}$ in terms of displacement. These values correspond to the thermal limit at 300 K [7].

3 Preliminary solar runs with the chameleon chopper

To investigate the possible presence of a signal from a beam of chameleons emitted by the sun, it is necessary to impress a time modulation on it. This can be done by exploiting the general chameleon property of traversing any material when impinging on it at right angles, and of reflecting off it when arriving at grazing incidence (see [4] for details). We have designed and built a prototype chameleon chopper (see Figure 2) exploiting this property.

The chopper was placed in the proper position in order to intercept a hypothetical solar chameleon beam hitting the membrane at grazing incidence angles between 0 and 20 degrees, depending on the time of day. Data were then acquired by recording 40 s-long power spectra of the feedback loop error signal. A partial preliminary analysis of the solar data was conducted by computing for each spectrum the Signal-to-Noise Ratio (SNR) and by plotting the SNR as a function of time. A sample plot of this type is shown in Figure 3.

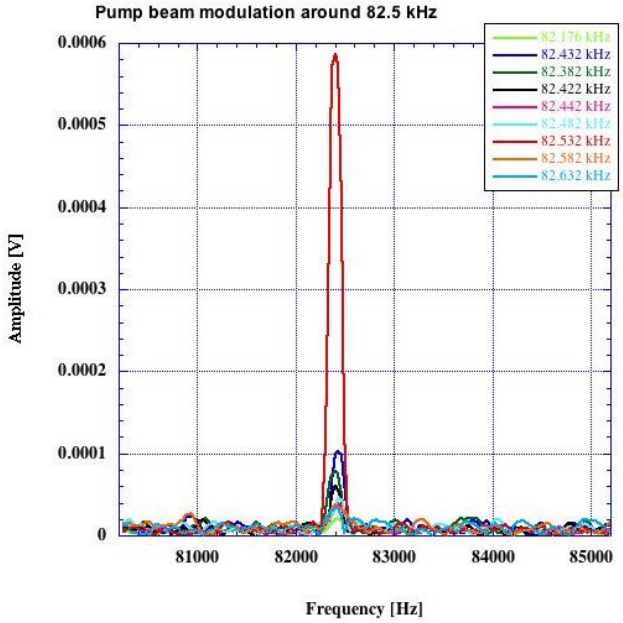

Figure 1: Plot of several power spectra of the error signal from the Fabry-Perot frequency-locking feedback loop. Each spectrum (identified by a unique color) has been taken with the pump beam exciting the membrane at a given frequency near the 82.5 kHz membrane resonance frequency (see legend in the figure). Note how the signal amplitude increases when approaching the resonance frequency. From these data one can estimate a mechanical quality factor of ≈ 3000.

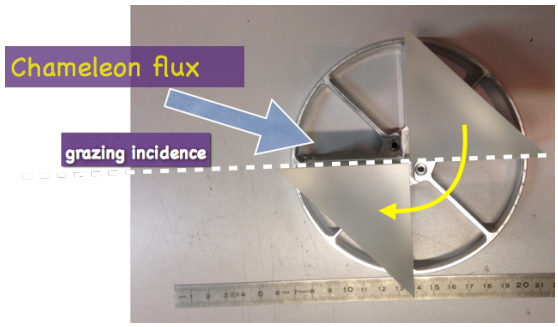

Figure 2: Prototype chameleon chopper and its working principle. The photograph shows a top view of the chameleon chopper prototype consisting of two optical prisms glued to a holding tray capable of rotating along its cylindrical symmetry axis. As the chopper rotates, it presents to the chameleon beam grazing-incidence and normal-incidence surfaces alternatively. The latter transmit chameleons, while the former reflect them, causing the required amplitude modulation. The prototype shown here can rotate at up to ≈ 50 Hz, corresponding to a chopping frequency of ≈ 200 Hz, as a grazing incidence surface is presented to the incoming beam 4 times each turn.

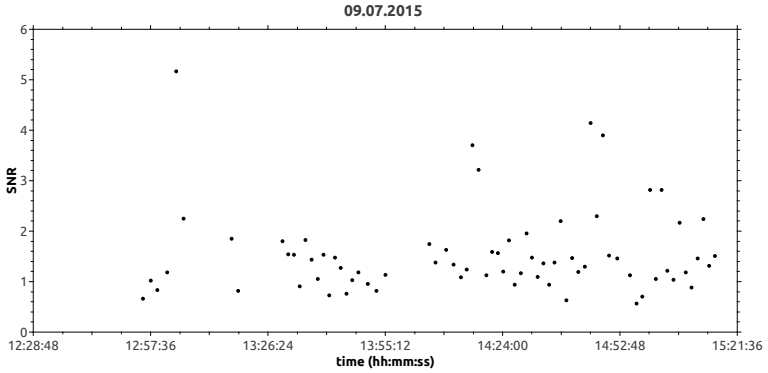

Figure 3: Data from a sample solar run. The graph shows a plot of the Signal-to-Noise ratio (SNR) near the chopper frequency (17 Hz in this case), measured in the power spectrum of the feedback error signal, as a function of time. Data were taken while the sun scanned through grazing incidence angles between 0 and 20 degrees. Notice that the dispersion of the data points indicates the absence of a clear signal.

4 Conclusions

The KWISP force sensor now running in the INFN Trieste optics laboratory has been calibrated in absolute terms using a known force exerted by an auxiliary pump beam. The measured sensitivity of $1.5 \cdot 10^{-14}$ N/$\sqrt{\text{Hz}}$, corresponding to $7.5 \cdot 10^{-16}$ m/$\sqrt{\text{Hz}}$ in terms of displacement, is already at the 300 K thermal limit. The *chameleon chopper* concept has been implemented in a working prototype [8]. This was used in combination with the force-sensor to conduct preliminary runs for the detection of a hypothetical chameleon beam emitted from the sun. Analysis of the data from these runs is in progress [9]. The KWISP force sensor, once coupled to the X-Ray Telescope at CAST, has the potential to access unexplored regions in the Chameleon parameter space, possibly allowing a first glimpse at the nature of Dark Energy [5].

References

[1] G. Cantatore, F. Della Valle, E. Milotti, P. Pace, E. Zavattini, E. Polacco, F. Perrone, C. Rizzo, G. Zavattini, G. Ruoso, Rev. of Sc. Instr. **66(4)**, 27852787 (1999).

[2] M. Karuza, C. Molinelli, M. Galassi, C. Biancofiore, R. Natali, P. Tombesi, G. Di Giuseppe, D. Vitali, New J. of Phys., **14(9)** (2012).

[3] M. Karuza, M. Galassi, C. Biancofiore, C. Molinelli, R. Natali, P. Tombesi, G. Di Giuseppe, D. Vitali, J. of Optics, **15(2)**, 025704 (2013).

[4] O.K. Baker, A. Lindner, Y. K. Semertzidis, A. Upadhye, K. Zioutas, arXiv:1201.0079 (2012).

[5] S. Baum, G. Cantatore, D.H.H. Hoffmann, M. Karuza, Y.K. Semertzidis, A. Upadhye, K. Zioutas, Physics Letters B **739**, 167173 (2014).

[6] M. Karuza, G. Cantatore, A. Gardikiotis, D.H.H. Hoffmann, Y.K. Semertzidis, K. Zioutas, arXiv:1509.04499 (2015).

[7] S. Lamoreaux, arXiv:0808.4000 (2008).

[8] K. Zioutas, G. Cantatore, M. Karuza, in preparation.

[9] G. Cantatore, M. Karuza, K. Zioutas, in preparation.

Status of the ADMX-HF Experiment

Maria Simanovskaia, Karl van Bibber
University of California, Berkeley, USA

DOI: http://dx.doi.org/10.3204/DESY-PROC-2015-02/simanovskaia_maria

The Axion Dark Matter eXperiment - High Frequency (ADMX-HF) was designed to address the specific challenges of the microwave cavity search at higher frequencies in an operating environment. The platform is intended to serve both as a *pathfinder* for data in the frequency range > 5 GHz, as well as an *innovation test-bed* for new cavity and amplifier technologies. ADMX-HF has recently begun operation with a 9 T magnet, a dilution refrigerator, Josephson Parametric Amplifiers, and copper cavities. It will eventually test new concepts such as squeezed-state receivers and single-quantum detectors to evade the quantum limit, and thin-film superconducting cavities to increase conversion power.

1 Introduction

Axions constituting the dark matter of our Milky Way halo may be resonantly converted to a weak RF signal in a tunable high-Q microwave cavity permeated by a strong magnetic field, under the condition that the cavity frequency equals the mass of the axion, i.e. $h\nu = mc^2$ [1] ; see Figure 1. The conversion power is given by

$$P \sim g_{a\gamma\gamma}^2 \, (\rho_a/m_a) \, B^2 \, Q_C \, V C_{nml},$$

where $g_{a\gamma\gamma}^2$ is the axion-photon coupling, m_a and ρ_a the mass of the axion and its local halo density, B the magnetic field strength, and V, Q_C and C_{nml} the volume, quality factor and form factor of the microwave cavity. While the expected signal power is exceedingly small for all experiments to date, being measured in yoctowatts (10^{-24} W), the critical factor for detection is the signal-to-noise ratio,

$$SNR = \frac{P}{k\,T_S}\sqrt{\frac{t}{\Delta\nu_a}}$$

which depends not only upon the signal power, but also on the bandwidth of the signal line ($\Delta\nu_a/\nu_a \sim 10^{-6}$ for virialized axions), the integration time t , and most importantly the system noise temperature T_S. The system noise temperature is the sum of the thermal and the noise equivalent temperature contributions from the amplifier,

$$k\,T_S = h\nu\left(\frac{1}{e^{h\nu/kT}-1}+\frac{1}{2}\right)+k\,T_A$$

which for $kT \gg h\nu$, reduces to $T_S \approx T + T_A$. Linear amplifiers are subject to an irreducible noise temperature, called the Standard Quantum Limit (SQL), $kT_{SQL} = h\nu$, but there are strategies to evade this limit, which will be explored in ADMX-HF.

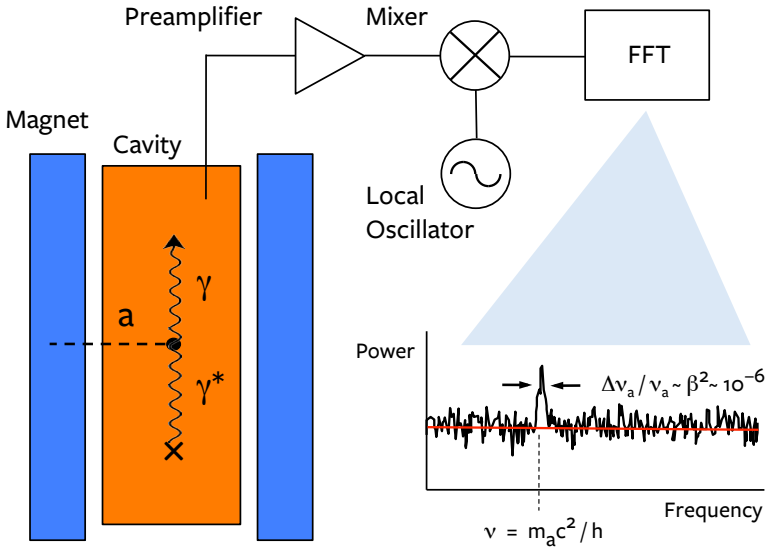

Figure 1: Schematic of the microwave cavity experiment.

Figure 2 displays the excluded range of mass and coupling (m_a, $g_{a\gamma\gamma}$) for the microwave cavity search to date, including the original Rochester-Brookhaven-Fermilab (RBF) [2, 3] and University of Florida (UF) experiments [4], along with the results from the Axion Dark Matter eXperiment (ADMX) [5]. Since 1995, approximately an octave of mass range has been covered by ADMX in the few μeV range within the band of plausible models; ultimately the microwave cavity search or other techniques must cover up to the $\sim$ 10 meV range with a sensitivity to find or exclude axions of the most pessimistic photon coupling, ideally even if they do not saturate the halo dark matter density.

2 ADMX-HF

2.1 Technical description

The Axion Dark Matter eXperiment - High Frequency (ADMX-HF) was proposed to address the challenges of extending the microwave cavity experiment to the next higher decade in mass, i.e. $5 - 25$ GHz ($\sim 20 - 100$ μeV). The collaboration includes Yale University, where the experiment is sited, the University of Colorado, the University of California Berkeley and Lawrence Livermore National Laboratory. ADMX-HF serves both as a *pathfinder* for first data at higher masses, and as an *innovation test-bed* for R&D on new higher frequency cavity and amplifier concepts, to be validated in an operational environment.

The experimental gantry is suspended from a dilution refrigerator (VeriCold) with a base

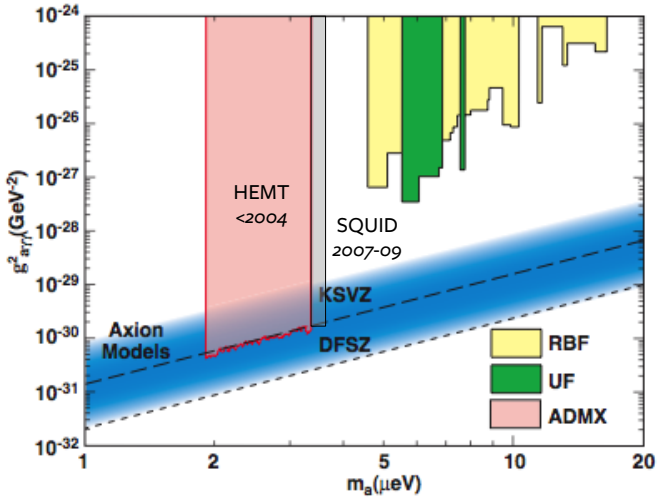

Figure 2: Exclusion region for the microwave cavity experiment.

temperature of 25 mK, and top-loaded into a 9 T superconducting solenoid (Cryomagnetics Inc.), 40 cm long x 17.5 cm diameter. The magnet was designed to provide an exceptional field uniformity ($B_r < 50$ G), anticipating the exploration of thin-film superconducting multilayers on the cylindrical surfaces of the cavity to boost the quality factor Q.

The microwave cavity for initial operation however is normal conducting, consisting of a cylindrical volume (25.4 cm long x 10.2 cm diam.), and tuned by the radial displacement of a metallic rod (5.1 cm diam.). The cavity and tuning rod are made of stainless steel, electroplated with OFHC copper and annealed. The TM_{010} is the mode of choice for the microwave cavity experiment, as its form factor is the largest by far, and can be tuned from $3.6 - 5.8$ GHz here. Berkeley and LLNL share responsibility for all cavity R&D and fabrication.

ADMX-HF represents the inaugural use of Josephson Parametric Amplifiers (JPA) for the microwave cavity axion search. JPAs are a natural technology in the $5 - 10$ GHz range, as they are intrinsically quantum-limited and broadly tunable. They require a magnetically field-free environment to operate however, requiring a "defense in depth" approach to shield out the fringe field from the main magnet. A field compensation coil was designed in the magnet cryostat to cancel out most of the fringe field; this was supplemented with 4 persistent coil packages to further reduce the fringe field and, more importantly, its gradient. Within the coils and $\sim$ 50 cm above the cavity, it is the JPA canister, consisting of two layers of CryoPerm, and lined inside with thin lead sheets, superconducting for $T < 7.2$ K. This design has proven completely successful, and the remnant field at the JPA has been demonstrated to increase by $< 1\%$ of a flux quantum at the JPA when the field is ramped from 0 - 9 T. Figure 3 shows the experiment in various stages of assembly; a more complete description of ADMX-HF is found

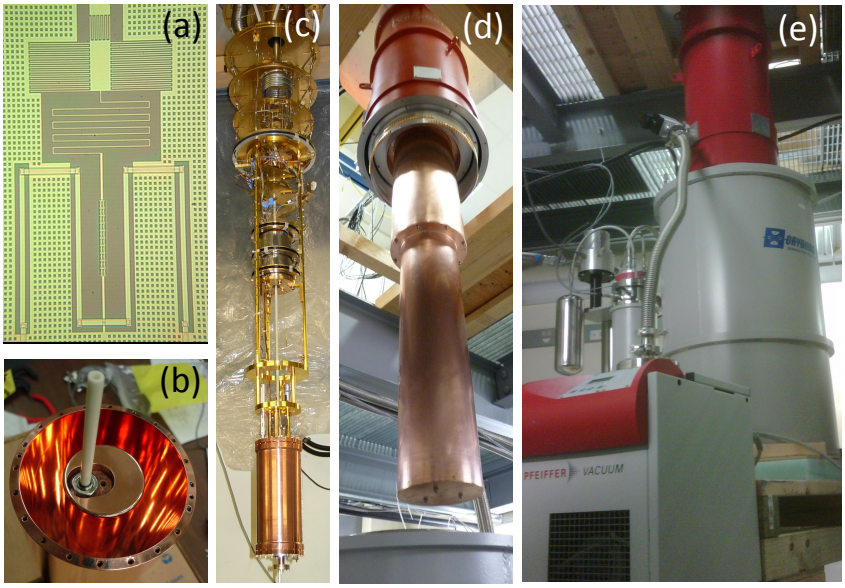

Figure 3: (a) Microphotograph of the JPA. (b) Microwave cavity. (c) Gantry. Dilution refrigerator (top); JPA canister (middle); cavity (bottom). (d) Gantry with thermal shields installed being lowered into the magnet. (e) Fully assembled experiment. Magnet cryostat (gray); dilution refrigerator (red). Floor level for the DAQ and computer is at the top of the photo.

in Reference [6].

2.2 Status

The experiment was completed and commissioned in mid-2015, and has undergone its first short data-taking runs. The system noise temperature was measured to be $kT_{SYS} \approx 800$ mK, about 2.9 times the Standard Quantum Limit. The additional noise source was imputed to the thermal contribution of the tuning rod, which is connected to the rest of the experiment only by a thin ceramic axle. A long data run is planned is planned once an improved thermal link between the rod and the cavity is implemented, and final data acquisition software written.

3 Future developments

ADMX-HF has already proven its utility identifying and addressing the mundane 'low-tech' issues that can impede the experiment from operating in a robust, high duty factor manner at higher frequencies. These include e.g. the proportionately more stringent specifications on

machining and alignment tolerances for the cavity, and minimizing the rod-endcap gap (even $< 250\,\mu m$) to avoid mode-localization and thus keeping the form factor C_{010} as high as possible.

That being said, ADMX-HF was primarily conceived as a test-bed for beyond-state-of-art innovations in both cavities and amplifiers, or photon detection schemes more generally, that could radically advance the sensitivity and mass reach of the experiment. Below we briefly summarize near-term plans in both areas.

3.1 Microwave cavity R&D

Currently, the quality factor of the ADMX-HF cavity critically coupled is $Q_C \sim 20,000$. Compared with the intrinsic line width of the axion signal, $Q_a \sim 10^6$, it is seen that there is a potentially factor of 50 in signal power to be gained, that could improve both the sensitivity and speed up the search rate of the experiment. There is a further imperative to seek an improvement in Q, as on basic scaling grounds, Q will deteriorate as $\nu^{-2/3}$, largely as a consequence of the increasing surface to volume ratio for higher frequency structures.

Recently, Xi et al. have demonstrated that very thin films ($\sim$ 10 nm) of the Type-II superconductor $Nb_xTi_{1-x}N$ exhibits a lossless microwave response, to $>$ 100 GHz, in a high magnetic field oriented perfectly parallel to the surface, $B_{\|} = 10$ T [7]. This suggests the possibility of improving the Q of the cavity by an order of magnitude, by deposition of a multilayer thin superconducting film on all cylindrical surfaces of the cavity and tuning rods. A multilayer will be required, as the required thinness of an individual layer to ensure flux vortices are expelled from the film, $\sim$ 10 nm, is still much less than the penetration depth, of order 100 nm; calculations are underway to determine the optimal design of such a multilayer.

A R&D program is underway at Berkeley, LLNL and Yale to fabricate and characterize NbTiN thin films made by RF plasma deposition; see Figure 4. Films exhibiting DC superconductivity with high critical temperatures ($T_C \sim 14\,\mathrm{K}$) were readily produced, so long as care was taken to prevent oxidation during the plasma deposition process. Film thickness and stoichiometry have been measured by Rutherford Backscattering, and more recently by X-Ray Fluorescence. The next phase of the R&D program will involve measuring the RF performance of the films in small 10 GHz cavity prototypes, along with their magnetic field dependence. Finally, multilayer structures will be modeled, fabricated and characterized; pursuant to successful prototype tests, a full-scale hybrid cavity will be produced, tested and used in ADMX-HF operational conditions.

Other cavity innovations that will be investigated within the next year will be the applicability of Photonic Band Gap structures, i.e. a lattice array of metallic posts but without the boundary condition imposed by an external cylindrical conducting surface [8]. With one or more of the posts removed in the center of the array, a judicious choice of geometry can result in the desired TM_{010} mode being trapped, but the myriad of confounding TE and TEM modes being propagated away. Eliminating the forest of mode crossings would greatly simplify and accelerate covering the mass range in an unbroken manner, by obviating the need for difficult and time-consuming procedures for shifting mode crossings away from an obscured notch in frequency and rescanning.

3.2 Amplifier and single-quantum detector R&D

The other major frontier will be a further reduction in total system noise temperature, circumventing the irreducible noise temperature of linear amplifiers set by quantum mechanics. Two

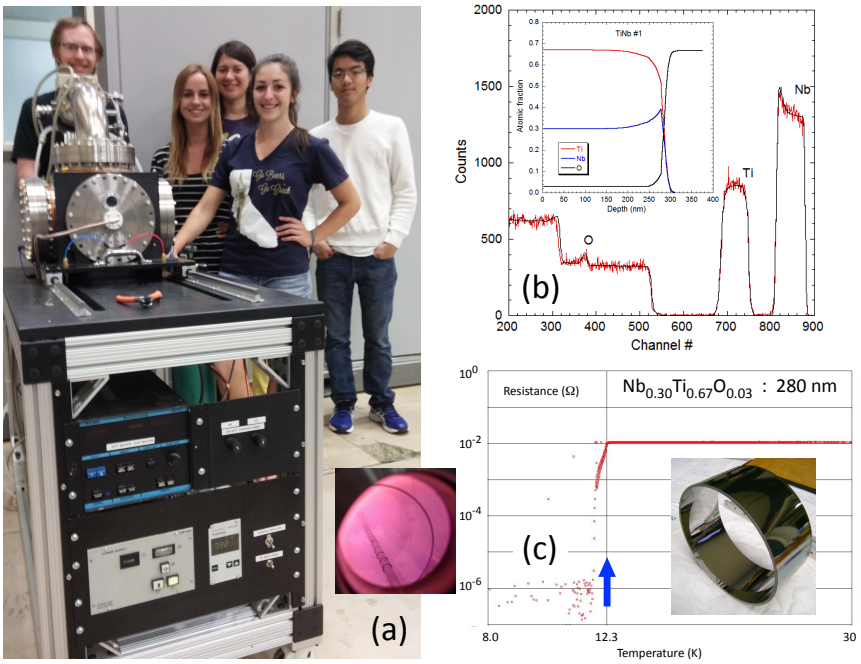

Figure 4: (a) RF plasma deposition unit at UC Berkeley. Inset: RF antenna (NbTi tube) in the plasma during deposition. (b) Rutherford Backscattering profile of a test sample. (c) Test of a planar sample, exhibiting DC superconductivity at $T_C = 12.3$ K. Inset: NbTiN coating on the inside of a 10 cm diameter quartz tube.

strategies will be pursued. In the near term, the JILA/Colorado group will deploy a receiver based on squeezed-vacuum states, by which one JPA prepares and injects a squeezed state into the cavity, and a second one measures the output of the cavity. Noise reduction below T_{SQL} by a factor of 4 has already been demonstrated on the bench by this group; successful deployment in ADMX-HF will however require proper care to eliminate all sources of signal loss (e.g. eliminating couplers, replacing coaxial cables with rigid waveguides, etc.).

Second, the Colorado group is investigating the applicability of single-quantum detection schemes (qubits, etc.) for the axion experiment as well [10, 11, 12], for which there is a significant experience base in the quantum information world to build on.

Acknowledgments

This work was supported under the auspices of the National Science Foundation, under grants PHY-1067242, and PHY-1306729, and the auspices of the U.S. Department of Energy by Lawrence Livermore National Security, LLC, Lawrence Livermore National Laboratory under Contract DE-AC52-07NA27344. We also gratefully acknowledge support from the Heising-

Simons Foundation.

References

[1] P. Sikivie, "Experimental tests of the 'invisible' axion," Phys. Rev. Lett. **51**, 1415 (1983); "Detection rates for 'invisible' axion searches," Phys. Rev. D **32**, 2988 (1985).

[2] S. DePanfilis, A. C. Melissinos, B. E. Moskowitz, J. T. Rogers, Y. K. Semertzidis, W. U. Wuensch, H. J. Halama, A. G. Prodell, W. B. Fowler, and F. A. Nezrick, "Limits on the Abundance and Coupling of Cosmic Axions at $4.5 < m_a < 5.0$ μeV," Phys. Rev. Lett. **59**, 839 (1987).

[3] W. U. Wuensch, S. De Panfilis-Wuensch, Y. K. Semertzidis, J. T. Rogers, A. C. Melissinos, H. J. Halama, B. E. Moskowitz, A. G. Prodell, W. B. Fowler, and F. A. Nezrick, "Results of a Laboratory Search for Cosmic Axions and Other Weakly Coupled Light Particles," Phys. Rev. D **40**, 3153 (1989).

[4] C. Hagmann, P. Sikivie, N. S. Sullivan, and D. B. Tanner, "Results from a Search for Cosmic Axions," Phys. Rev. D **42**, 1297 (1990).

[5] S. J. Asztalos, G. Carosi, C. Hagmann, D. Kinion, K. van Bibber, M. Hotz, L. J. Rosenberg, G. Rybka, J. Hoskins, J. Hwang, P. Sikivie, D. B. Tanner, R. Bradley, and J. Clarke, "A SQUID-based Microwave Cavity Search for Dark Matter Axions," Phys. Rev. Lett. **104**, 041301 (2010).

[6] T. M. Shokair, J. Root, K. A. van Bibber, B. Brubaker, Y. V. Gurevich, S. B. Cahn, S. K. Lamoreaux, M. A. Anil, K. W. Lehnert, B. W. Mitchell, A. Reed, G. Carosi, "Future Directions in the Microwave Cavity Search for Dark Matter Axions," International Journal of Modern Physics A **29**, No. 19 (2014).

[7] Xiaoxiang Xi, J. Hwang, C. Martin, D. B. Tanner, G. L. Carr, "Far-Infrared Conductivity Measurements of Pair Breaking in Superconducting $Nb_{0.5}Ti_{0.5}N$ Thin Films Induced by an External Magnetic Field," Phys. Rev. Lett. **105**, 257006 (2010).

[8] E. I. Smirnova, C. Chen, M. A. Shapiro, R. J. Temkin, "Simulation of metallic photonic bandgap structures for accelerator applications," Proceedings of the 2001 Particle Accelerator Conference (2001), Part 2, Vol. 2, 933.

[9] F. Mallet, M. A. Castellanos-Beltran, H. S. Ku, S. Glancy, E. Knill, K. D. Irwin, G. C. Hilton, L. R. Vale, and K. W. Lehnert, "Quantum state tomography of an itinerant squeezed microwave field," Phys. Rev. Lett. **106**, 220502 (2011).

[10] D. Ristè, J. G. van Leeuwen, H.-S. Ku, K. W. Lehnert, and L. DiCarlo, "Initialization by Measurement of a Superconducting Quantum Bit Circuit," Phys. Rev. Lett. **109**, 050507 (2012).

[11] D. I. Schuster, A. A. Houck, J. A. Schreier, A. Wallraff, J. M. Gambetta, A. Blais, L. Frunzio, J. Majer, B. Johnson, M. H. Devoret, S. M. Girvin and R. J. Schoelkopf, "Resolving Photon Number States in a Superconducting Circuit," Nature **445**, 515 (2007).

[12] R. Vijay, D. H. Slichter, and I. Siddiqi, "Observation of Quantum Jumps in a Superconducting Artificial Atom," Phys. Rev. Lett. **106**, 110502 (2011).

Haloscope Axion Searches with the CAST Dipole Magnet: The CAST-CAPP/IBS Detector

Lino Miceli

IBS Center for Axion and Precision Physics Research, Korea Advanced Institute of Science and Technology, Daejeon, South Korea

DOI: http://dx.doi.org/10.3204/DESY-PROC-2015-02/miceli_lino

The CAST-CAPP/IBS Detector project will use tunable rectangular cavities inserted in the 43 mm twin-bore, 9T, CAST dipole magnet to search for axion DM, initially in the 21 to 25 μeV mass range. The sensitivity of this haloscope could reach into the QCD axion parameter space in a wider, yet-unexplored, mass region. Preliminary model results guiding the project design are presented.

1 Introduction and Motivation

Axions arise as consequence of the Peccei-Quinn solution to the strong CP problem [1]–[7]. They are natural cold dark matter (DM) candidates [8]–[10] if their mass lies within the range (1–100) μeV. In addition to the explicit axion there is a wide range of so-called axion-like particles (ALPs) having similar couplings, but with an often increased coupling constant. They could also be good dark matter candidates [11]–[12]. Axion searches can therefore shed light on the nature of DM, a major issue of contemporary physics. A convenient search method is based on the coupling of axions to two photons, as expressed by the Lagrangian term

$$\mathcal{L} \approx g_{a\gamma\gamma}\varphi_a \mathbf{E}\cdot\mathbf{B} \tag{1}$$

where $g_{a\gamma\gamma}$ is the (model dependent) coupling constant, and φ_a is the axion field. Haloscopes can detect axions in the μeV mass region [13]. They consist of microwave cavities immersed in a strong magnetic field. Similarly to the Primakoff effect [14], the axion-to-photon conversion rate is enhanced in a region of space where a strong magnetic field $\mathbf{B}$ is present. The conversion probability is further enhanced if the outgoing photon, represented by the electric field $\mathbf{E}$ in the previous equation, is detected in a microwave cavity resonating to the frequency of the axion mass. A number of searches using haloscopes have already been undertaken [15]–[17] with solenoid magnets producing the external field, such as the ADMX experiment [18]–[19]. Leveraging on [20] and adding some new ideas, members of the CAPP/IBS, now part of the CAST collaboration, have recently proposed to exploit the CAST dipole magnet to search for axion DM using rectangular cavities. The CAST collaboration then decided to submit a proposal to CERN, an effort that can probe the $\sim (2\text{–}3)\times 10^{-5}$ eV mass range with a sensitivity that could reach into the QCD axion domain. This region has never been explored before for cold DM searches.

2 Experimental Setup

The field strength (9 T) and geometry (9 m length, 43 mm diameter twin bores) of the CAST superconducting dipole magnet, formerly an LHC prototype, are appropriate for cold DM axion searches with rectangular cavities.

2.1 Rectangular Cavities in Dipole Magnets

The on-resonance axion conversion power in a microwave cavity is proportional to B^2, to the cavity quality factor Q (the ratio of the cavity stored-energy to its losses), to its volume V, and geometry factor C [21]

$$P \approx g_{a\gamma\gamma}^2 \frac{\rho_a}{m_a} B^2 \cdot Q \cdot V \cdot C \tag{2}$$

Here ρ_a is the axion field density and m_a is the axion mass. A suitable experimental setup in a dipole field consists of tunable rectangular cavities introduced into the magnet bore, with the magnetic field parallel to the resonator lateral sides. Equation (1) suggests that the sensitivity would be maximized if TE modes are used. The mode frequency depends on the cavity width (w), height (h), length (L), and mode indexes l, m, n, as

$$f_{lmn} \propto \sqrt{\left(\frac{l}{w}\right)^2 + \left(\frac{m}{h}\right)^2 + \left(\frac{n}{L}\right)^2} \tag{3}$$

Assuming L to be along the z direction, and the external B field along y, it is convenient to choose modes in which $m = 0$ so that the resonant electric field is parallel to B

$$E_y \propto \sin\left(\frac{l\pi}{w}x\right) \sin\left(\frac{n\pi}{L}z\right)$$
$$E_x = E_z \equiv 0 \tag{4}$$

The fundamental TE_{101} is the most favourable, giving a geometry factor of 0.66 for an empty cavity, the highest possible in our case. This mode is sufficiently isolated from other modes if the cavity aspect ratio is not too large ($\lesssim 100$). For our estimates we assumed inner cavity lateral sizes of 25 mm × 24 mm. If the cavity is tuned as described in Sec. 3, the maximum frequency will be 5.8 GHz, corresponding to an axion mass of 24×10^{-6} eV.

2.2 Sensitivity

The cavity on-resonance output power from axion to photon conversion can be estimated as [21] (and also [19])

$$P = 1.6 \times 10^{-23}\,\mathrm{W}\left(g_{a\gamma\gamma} 10^{14}\,\mathrm{GeV}\right)^2 \left(\frac{\rho_a}{300\,\mathrm{MeV/cm^3}}\right)\left(\frac{2.4 \times 10^{-5}\,\mathrm{eV}}{m_a}\right)$$
$$\times \left(\frac{B}{9\,\mathrm{T}}\right)^2 \left(\frac{V}{5\,\mathrm{L}}\right)\left(\frac{Q}{5 \times 10^3}\right)\left(\frac{C}{0.66}\right) \tag{5}$$

The value of 300 Mev/cm^3 in Eq. (5) is a commonly used value for the DM density in the vicinity of the Earth. The quality factor Q is the minimum between the loaded-Q, i.e. when

the cavity is coupled to the rest of the detection system, and the DM Q-factor resulting from the energy spread of the axion, which is in the order of 10^6. Here a rather conservative $Q = 5,000$, with a critically coupled cavity, has been assumed. The volume of 5 L corresponds to filling one of the two magnet bores with multiple cavities, provided they can be phase-matched. Under the above conditions the on-resonance cavity power resulting from an axion signal would be $\sim 10^{-23}$ W, assuming a coupling constant $g_{a\gamma\gamma}$ of $10^{-14}\,\mathrm{GeV}^{-1}$. If we require a signal-to-noise ratio of 4, the time required to measure this power level at a given resonant frequency (axion mass) is, as deduced from the radiometer equation [22], in the order of 10 days, for a system temperature of 3.8 K resulting from adding the magnet operating temperature, 1.8 K, to a commercial amplifier noise temperature of 2 K. The signal bandwidth is taken equivalent to the axion DM velocity spread of 10^{-3} times the speed of light [13]. The assumed quality factor in the previous estimates is rather modest. At the experiment operating temperature, 1.8 K, we should expect a much higher Q. The sensitivity would scale accordingly, further demonstrating the good potential of this setup for axion DM search in a region of the parameter space, $g_{a\gamma\gamma}$ vs. axion mass, where no data currently exist.

3 Cavity Design

Since the experiment sensitivity increases with the resonator volume, it would be desirable to completely fill each of the two magnet bores with a single resonator or with phase-matched multiple cavities. As the aspect ratio L/w of the structure increases, however, the quality factor decreases, the resonant frequencies tend to converge to a single value (Eq. (3)), and mechanical tolerances become more demanding. In addition, since a tunable cavity is desired, a proper tuning mechanism must be included. All these aspects have been considered in a preliminary model of a relatively short cavity, 24 mm × 25 mm × 50 cm, that seems able to offer reliable TE_{101} mode operation, frequency separation, and reasonable sensitivity for a first stage experiment. Although a single such cavity will not be able to reach into the QCD axion parameter space, we should be able to set new limits into a yet unexplored domain of that region. Preliminary model results related to tuning, frequency spacing, and mechanical design tolerances are presented in the reminder of this contribution.

We have studied tuning mechanisms consisting in placing dielectric materials and/or metallic plates inside the cavity. Depending on its volume, position and shape, any material placed inside the cavity will alter the cavity mode structure and resonant frequency and, as a consequence, the cavity quality and geometry factors. A sensible tuning mechanism has been identified consisting in two dielectric bars of permittivity $\epsilon = 9$ and sizes 2.5 mm × 15 mm × 45 cm symmetrically placed parallel to the longitudinal sides, simultaneously moving towards the center, as conceptually depicted in the top-left of Fig. 1. This gives a sizable down-tuning range, from 5.8 to 4.2 GHz, as seen on the top right of the same figure.

The frequency spacing is the distance in frequency to the next higher order mode. If this spacing is small compared to the bandwidth of the cavity the two modes will couple to each other resulting in loss of sensitivity. It would be best to operate in single mode, if not however, the loss in sensitivity at the desired frequency might still be acceptable. An approximate criterion to establish the maximum cavity length for small values of the index n, in TE_{10n}, as given in [20], is confirmed by our preliminary modeling. In our example, mode spacing is not an issue as seen in the bottom left of Fig. 1.

Mechanical tolerances play a crucial role due to mode localization. This means that the

mode field distribution in the resonator space is altered depending on the deviation of the cavity shape from its ideal design, thus causing a decrease in the geometry form factor. To observe mode localization and investigate sensitivity to mechanical tolerances we have modeled a trapezoidal resonator in which the width of the cavity, w, changes from the original 25 mm to 24.5 mm, on one side only, and we tracked the geometry form factor as a function of w, as illustrated in the bottom right Fig. 1. Mechanical tolerances at 50 μm level seem sufficient for our benchmark cavity.

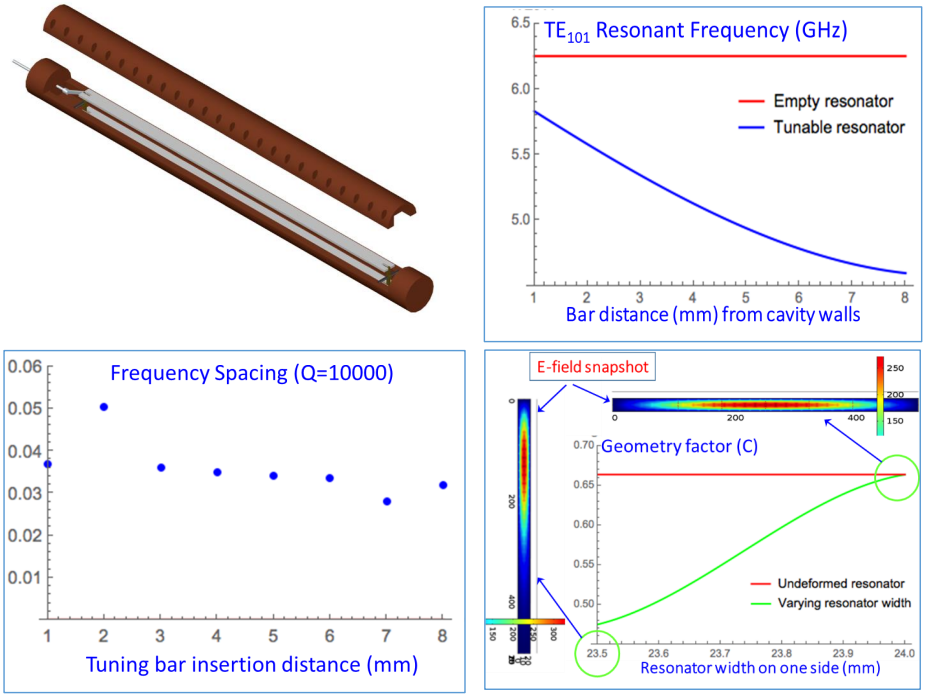

Figure 1: Preliminary modeling results. Top left: Cavity tuning conceptual design. Top right: Tuning range. Bottom left: ratio of resonant bandwidth to frequency spacing. Bottom right: Mode localization from cavity deformation.

4 Conclusion

The CAST-CAPP/IBS Detector project is a haloscope search for axion DM with rectangular cavities inserted in the bores of the CAST dipole magnet. Preliminary cavity engineering models are promising. The haloscope sensitivity may be able to reach into the QCD axion parameter space over the unexplored region of $(2\text{–}3)\times10^{-5}$ eV axion mass range, provided that phase-matching of multiple cavities is possible.

Acknowledgments

Special thanks for their advice and support to Yannis Semertzidis (CAPP/IBS and KAIST), Konstantin Zioutas (CERN), and Fritz Caspers (CERN).

This work is supported by IBS-R017-D1-2015-a00.

References

[1] R. D. Peccei *and* H. R. Quinn, Phys. Rev. Lett. **38**, 1440 (1977).

[2] S. Weinberg, Phys. Rev. Lett. **40**, 223 (1978).

[3] F. Wilczek, Phys. Rev. Lett. **40**, 279 (1978).

[4] J. E. Kim, Phys. Rev. Lett. **43**, 103 (1979).

[5] M. Dine, W. Fischler, and M. Srednicki, Phys. Lett. B **104**, 199 (1981).

[6] M. A. Shifman, A. I. Vainshtein, and V. I. Zakharov, Nucl. Phys. B **166**, 493 (1980).

[7] A. R. Zhitnitsky, Sov. J. Nucl. Phys. **31**, 260 (1980).

[8] J. Preskill, M. B. Wise, and F. Wilczek, Phys. Lett. B **120**, 127 (1983).

[9] L. F. Abbott and P. Sikivie, Phys. Lett. B **120**, 133 (1983).

[10] M. Dine *and* W. Fischler, Phys. Lett. B **120**, 137 (1983).

[11] A. Arvanitaki, S. Dimopoulos, S. Dubovsky, N. Kaloper, and J. March-Russell, Phys. Rev. D **81**, 123530 (2010).

[12] P. Arias, D. Cadamuro, M. Goodsell, J. Jaeckel, J. Redondo, and A. Ringwald, Report No. DESY 11-226; Report No. MPP-2011-140; Report No. CERN-PH-TH/ 2011-323; Report No. IPPP/11/80.

[13] P. Sikivie, Phys. Rev. Lett. **51**, 1415 (1983).

[14] H. Primakoff, Phys. Rev. **81**, 899 (1951).

[15] S. De Panfilis *et al.*, Phys. Rev. Lett. **59**, 839 (1987).

[16] W. Wuensch *et al.*, Phys. Rev. D **40**, 3153 (1989).

[17] C. Hagmann, P. Sikivie, N. S. Sullivan, and D. B. Tanner, Phys. Rev. D **42**, 1297 (1990).

[18] S. J. Asztalos *et al.*, Phys. Rev. D **64**, 092003 (2001).

[19] S. J. Asztalos *et al.* (ADMX Collaboration), Phys. Rev. Lett. **104**, 041301 (2010).

[20] O. Baker *et al.*, Phys. Rev. D **85**, 035018 (2012).

[21] P. Sikivie, Phys. Rev. D **32**, 2988 (1985), **36**, 974 (1987).

[22] R. H. Dicke, Rev. Sci. Inst. **7**, 268 (1946).

Searching for Scalar Dark Matter in Atoms and Astrophysical Phenomena: Variation of Fundamental Constants

Yevgeny V. Stadnik[1], *Benjamin M. Roberts*[1], *Victor V. Flambaum*[1,2], *Vladimir A. Dzuba*[1]

[1] School of Physics, University of New South Wales, Sydney 2052, Australia
[2] Mainz Institute for Theoretical Physics, Johannes Gutenberg University, Mainz, Germany

DOI: http://dx.doi.org/10.3204/DESY-PROC-2015-02/roberts_benjamin

We propose to search for scalar dark matter via its effects on the electromagnetic fine-structure constant and particle masses. Scalar dark matter that forms an oscillating classical field produces 'slow' linear-in-time drifts and oscillating variations of the fundamental constants, while scalar dark matter that forms topological defects produces transient-in-time variations of the constants of Nature. These variations can be sought for with atomic clock, laser interferometer and pulsar timing measurements. Atomic spectroscopy and Big Bang nucleosynthesis measurements already give improved bounds on the quadratic interaction parameters of scalar dark matter with the photon and light quarks by up to 15 orders of magnitude, while Big Bang nucleosynthesis measurements provide the first such constraints on the interaction parameters of scalar dark matter with the massive vector bosons.

1 Introduction

Astrophysical observations indicate that the matter content of the Universe is overwhelmingly dominated by dark matter (DM), the energy density of which exceeds that of ordinary matter by a factor of five. In order to explain the observed abundance of DM, it is reasonable to expect that DM interacts non-gravitationally with ordinary matter. Searches for weakly interacting massive particle (WIMP) DM, which look for the scattering of WIMPs off nuclei, have not yet produced a strong positive result. Further progress with these traditional searches is hindered by the observation that the sought effects are fourth-power in the underlying interaction strength between DM and Standard Model (SM) matter, which is known to be extremely small.

We propose to search for other well-motivated DM candidates that include ultralight (sub-eV) scalar particles, which are closely related to axions (the only difference being the intrinsic parity of the particle, which determines the forms of the interactions with SM particles), by exploiting effects that are first-power in the interaction strength between these scalar particles and SM matter. Ultralight scalar (and axion-like pseudoscalar) DM in the mass range $m_\phi \sim 10^{-24}$–10^{-20} eV has been proposed [1–3] to solve several long-standing astrophysical puzzles, such as the cusp-core, missing satellite, and too-big-to-fail problems [4], due to its effects on structure formation. Scalar DM can produce variations of the fundamental constants of Nature, which leave distinctive signatures in atomic clock, laser interferometer and pulsar tim-

ing observables. The phenomenally high level of precision already attainable in measurements performed with these systems provides strong motivation to utilise them in searches for scalar DM.

2 Scalar dark matter

Scalar (as well as axion-like pseudoscalar) DM may interact quadratically with SM matter as follows:

$$\mathcal{L}_{\rm int} = \frac{\phi^2}{(\Lambda'_\gamma)^2}\frac{F_{\mu\nu}F^{\mu\nu}}{4} - \sum_f \frac{\phi^2}{(\Lambda'_f)^2} m_f \bar{f} f + \sum_V \frac{\phi^2}{(\Lambda'_V)^2}\frac{M_V^2}{2} V_\nu V^\nu, \tag{1}$$

where the first term represents the coupling of the scalar field to the electromagnetic field tensor F, the second term represents the coupling of the scalar field to the fermion bilinears $\bar{f}f$, while the third term represents the coupling of the scalar field to the massive vector boson wavefunctions. The Λ'_X that appear in Eq. (1) are moderately large energy scales that are constrained from stellar energy-loss arguments: $\Lambda'_\gamma \gtrsim 3\times10^3$ GeV, $\Lambda'_p \gtrsim 15\times10^3$ GeV, $\Lambda'_e \gtrsim 3\times10^3$ GeV, which are stronger than bounds from fifth-force searches: $\Lambda'_p \gtrsim 2\times10^3$ GeV (note that a fifth-force due to the quadratic couplings in Eq. (1) arises in the leading order through the exchange of a pair of ϕ-quanta, which generates a less efficient $V(r) \propto 1/(\Lambda'_X)^4 r^3$ attractive potential, instead of the usual Yukawa potential in the case of linear-in-ϕ couplings) [5].

The couplings in Eq. (1) alter the electromagnetic fine-structure constant α and particle masses as follows:

$$\alpha \to \frac{\alpha}{1-\phi^2/(\Lambda'_\gamma)^2} \sim \alpha\left[1+\frac{\phi^2}{(\Lambda'_\gamma)^2}\right],\ \frac{\delta m_f}{m_f} = \frac{\phi^2}{(\Lambda'_f)^2},\ \frac{\delta M_V}{M_V} = \frac{\phi^2}{(\Lambda'_V)^2}. \tag{2}$$

In the simplest case, in which scalar DM is produced non-thermally and forms a coherently oscillating classical field, $\phi(t) \sim \phi_0 \cos(m_\phi t)$, which survives to the present day if the scalar particles are sufficiently light and weakly interacting, scalar DM that interacts with SM matter via Eq. (1) produces both 'slow' linear-in-time drifts and oscillating variations of α and the particle masses [6,7]. Apart from the coherently oscillating classical fields that ultralight scalar DM can form, ultralight scalar DM may also form topological defects (TDs), which arise from the stabilisation of the scalar field under a suitable self-potential [8]. In this case, TDs instead produce transient-in-time variations of α and the particle masses as a defect temporarily passes through some region of space [9,10].

BBN constraints — Astrophysical observations can be used to constrain the interactions of scalar DM with SM matter that appear in Eq. (1). Since the energy density of a non-relativistic oscillating scalar field scales as $\rho_{\rm scalar} \propto (1+z)^3$, the strongest astrophysical constraints on the parameters in Eq. (1) come from the earliest observationally tested epoch of the Universe, namely Big Bang nucleosynthesis (BBN). The interactions between scalar DM and SM matter need to be sufficiently weak (see Fig. 1 for the case of the scalar-photon coupling) to be consistent with the predicted and measured neutron-to-proton ratio at the time of weak interaction freeze-out ($t_{\rm F} \sim 1.1$ s), which determines the primordial ^{4}He abundance [6,7].

Pulsar timing searches — Astrophysical measurements can also be used to directly search for scalar DM. In particular, pulsar timing measurements can be used to search for transient-in-time variations of the neutron mass induced by TDs [10]. A pulsar is a highly magnetised

neutron star, which emits electromagnetic radiation and rotates with (usually a very stable) period ranging from $T \sim 1$ ms to 10 s. Assuming the angular momentum of a pulsar is conserved upon the passage of a defect through a pulsar, then its frequency of rotation would change as follows: $\delta\omega(t)/\omega \sim -\delta m_n(t)/\delta m_n$. For sufficiently non-adiabatic passage of a defect through a pulsar, the defect may potentially trigger a 'pulsar glitch' event (which have already been observed, but the exact origin of which is still disputed [11]) by triggering vortex unpinning or crustal fracture, in which the source of angular momentum required for the glitch event is provided by the pulsar itself [12].

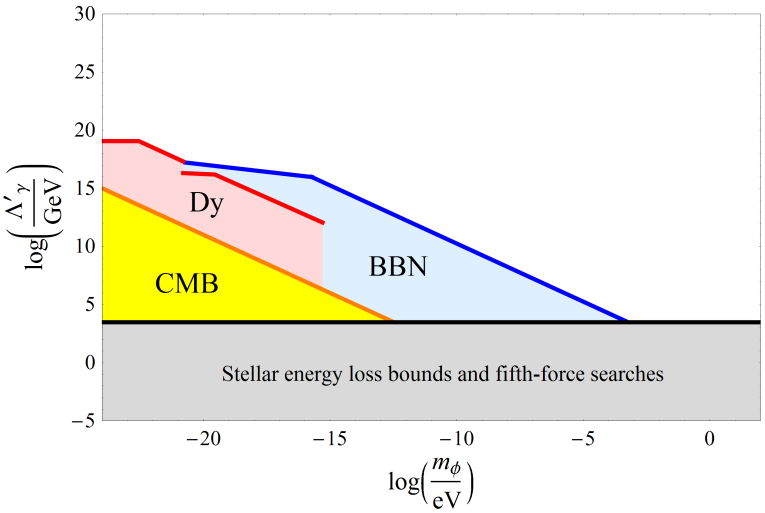

Figure 1: Region of scalar dark matter parameter space ruled out for the quadratic interaction of a scalar field ϕ with the photon. Region below yellow line corresponds to constraints from CMB measurements [6]. Region below blue line corresponds to constraints from comparison of measurements and SM calculations of the ratio $(m_n - m_p)/T_F$ [6, 7]. Region below red line corresponds to constraints from atomic dysprosium spectroscopy measurements [6, 7]. Region below black line corresponds to constraints from stellar energy-loss bounds and fifth-force experimental searches [5].

Laboratory clock searches — Transition frequencies in atomic, molecular and nuclear systems depend on the values of the fundamental constants and particle masses. Thus, comparing the ratio of two different transition frequencies, ω_1/ω_2, in such systems provides a method of searching for the oscillating-in-time and transient-in-time variations of the fundamental constants produced by scalar DM (see the reviews [13, 14] for summaries of the possible systems). The first laboratory search for oscillating-in-time variation of the electromagnetic fine-structure constant has recently been performed in atomic dysprosium [15], and the results have been used to place stringent constraints on the parameter Λ'_γ [6, 7], see Fig. 1.

Laboratory laser interferometry searches — Laser interferometers may also be used to search for the oscillating-in-time and transient-in-time variations of the fundamental constants produced by scalar DM [16]. An atomic transition frequency ω and length of a solid $L = Na_B$, where a_B is the Bohr radius, both depend on the fundamental constants and particle masses. If

the frequency of light inside an interferometer is determined by an atomic transition frequency and the interferometer arm length is allowed to vary freely, the atomic transition wavelength and arm length are compared directly:

$$\Phi = \frac{\omega L}{c} \sim \left(\frac{e^2}{a_{\rm B}\hbar}\right)\left(\frac{N a_{\rm B}}{c}\right) = N\alpha, \tag{3}$$

where the optical atomic transition frequency ω is proportional to the atomic unit of frequency, $e^2/a_{\rm B}\hbar$. Variation of the electromagnetic fine-structure constant thus produces the phase shift $\delta\Phi(t) \sim \Phi\ \delta\alpha(t)/\alpha$.

Acknowledgments

This work was supported by the Australian Research Council. B. M. R. and V. V. F. are grateful to the Mainz Institute for Theoretical Physics (MITP) for its hospitality and support.

References

[1] W. Hu, R. Barkana, A. Gruzinov, "Fuzzy Cold Dark Matter: The Wave Properties of Ultralight Particles"' Phys. Rev. Lett. **85**, 1158 (2000).

[2] D. J. E. Marsh, J. Silk, "A model for halo formation with axion mixed dark matter," Mon. Not. Roy. Astron. Soc. **437**, 2652 (2013).

[3] H.-Y. Schive *et al.*, "Understanding the Core-Halo Relation of Quantum Wave Dark Matter, ψDM, from 3D Simulations," Phys. Rev. Lett. **113**, 261302 (2014).

[4] D. H. Weinberg, J. S. Bullock, F. Governato, R. K. de Naray, A. H. G. Peter, "Cold dark matter: Controversies on small scales,". Proc. Nat. Ac. Sc. (2015), `www.pnas.org/content/early/2015/01/27/1308716112.abstract`

[5] K. A. Olive, M. Pospelov, "Environmental Dependence of Masses and Coupling Constants," Phys. Rev. D **77**, 043524 (2008).

[6] Y. V. Stadnik, V. V. Flambaum, "Can dark matter induce cosmological evolution of the fundamental constants of Nature?" arXiv:1503.08540.

[7] Y. V. Stadnik, V. V. Flambaum, "Constraining scalar dark matter with Big Bang nucleosynthesis and atomic spectroscopy," arXiv:1504.01798.

[8] A. Vilenkin, "Cosmic strings and domain walls," Phys. Rep. **121**, 263 (1985).

[9] A. Derevianko, M. Pospelov, "Hunting for topological dark matter with atomic clocks," Nat. Phys. **10**, 933 (2014).

[10] Y. V. Stadnik, V. V. Flambaum, "Searching for Topological Defect Dark Matter via Nongravitational Signatures," Phys. Rev. Lett. **113**, 151301 (2014).

[11] B. Haskell, A. Melatos, "Models of Pulsar Glitches," Int. J. Mod. Phys. D **24**, 1530008 (2015).

[12] Y. V. Stadnik, V. V. Flambaum, "Reply to comment on 'Searching for Topological Defect Dark Matter via Nongravitational Signatures'," arXiv:1507.01375.

[13] V. V. Flambaum, V. A. Dzuba, "Search for variation of the fundamental constants in atomic, molecular, and nuclear spectra," Can. J. Phys. **87**, 25 (2009).

[14] A. Ong, J. C. Berengut, V. V. Flambaum, "Highly charged ions for atomic clocks and search for variation of the fine structure constant," Springer Tracts Mod. Phys. **256**, 293 (2014).

[15] K. Van Tilburg, N. Leefer, L. Bougas, D. Budker, "Search for ultralight scalar dark matter with atomic spectrosopy", Phys. Rev. Lett. **115**, 011802 (2015).

[16] Y. V. Stadnik, V. V. Flambaum, "Searching for Dark Matter and Variation of Fundamental Constants with Laser and Maser Interferometry," Phys. Rev. Lett. **114**, 161301 (2015).

Phenomenology of Axion Miniclusters

Igor Tkachev

Institute for Nuclear Research of the Russian Academy of Sciences, Moscow 117312, Russia

DOI: http://dx.doi.org/10.3204/DESY-PROC-2015-02/tkachev_igor

I review possible observational phenomena appearing in models leading to dense small-scale substructures in the axionic dark matter. Also, I discuss their imaginable implications for the direct dark matter searches in the laboratory.

1 Introduction

In a wide variety of axion models, the Dark Matter (DM) on smallest scales, $M \sim 10^{-12}\,M_\odot$, is confined in very dense axionic clumps, called miniclusters. Moreover, in every model the DM is clustered on all scales, starting from miniclusters and up to galaxies and clusters of galaxies. In the mass range $10^{-12}\,M_\odot \lesssim M \lesssim 10^{7}\,M_\odot$ the corresponding clusters are called minihalos. Over the lifetime of the Galaxy, these structures may be tidally destroyed forming tidal streams. In this talk I review and discuss possible phenomenological consequences of these structures, both for indirect and direct DM searches.

2 Axion Miniclusters

Let us specify the density of a dark-matter fluctuation prior to matter-radiation equality as $\delta\rho_a/\rho_a \equiv \Phi$. In situation when $\Phi \sim 1$ (which would correspond to non-interacting axion field $a \equiv f_a\theta$ with random initial conditions), these clumps separate from cosmological expansion and form gravitationally bound objects already at $T = T_{\rm eq}$, where $T_{\rm eq}$ is the temperature of equal matter and radiation energy densities. However, at the time when axion oscillations commence, in many regions $\theta \sim 1$, and self-interaction is important, $V(\theta) = m_a^2 f_a^2[1-\cos(\theta)]$. Numerical investigation of the dynamics of the axion field around the QCD epoch [1, 2, 3, 4] had shown that the non-linear effects lead to "fluctuations" with Φ much larger than unity, possibly as large as several hundred. In such situation a clump separates from cosmological expansion at $T \simeq (1+\Phi)T_{\rm eq}$ resulting in a final minicluster density today given by

$$\rho_{\rm mc} \simeq 7\times 10^6\,\Phi^3(1+\Phi)\,{\rm GeV/cm^3}. \tag{1}$$

This should be compared to mean DM density in the Solar neighborhood in the Galaxy, $\bar\rho \approx 0.3\ {\rm GeV/cm^3}$.

The scale of minicluster masses is set by the total mass in axions within the Hubble radius at a temperature around $T \approx$1 GeV when axion oscillations commence, which is about

$$M_{\rm mc} \sim 10^{-12} M_\odot. \tag{2}$$

Masses of miniclusters are relatively insensitive to the particular value of Φ associated with the minicluster. The corresponding minicluster radius as a function of M and Φ is:

$$R_{\rm mc} \approx \frac{3\times 10^7}{\Phi\,(1+\Phi)^{1/3}} \left(\frac{M}{10^{-12}M_\odot}\right)^{1/3} {\rm km}\,. \tag{3}$$

According to Ref. [4], more than 13% of all axionic dark matter are in miniclusters with $\Phi \gtrsim 10$, more than about 20% are in miniclusters with $\Phi \gtrsim 5$ and 70% are in miniclusters ($\Phi > 1$). Roughly half of all axions reside in miniclusters.

2.1 Bose-condensation

It is remarkable that in spite of the apparent smallness of axion quartic self-coupling, $|\lambda_a| \approx (f_\pi/f_a)^4 \sim 10^{-53}(10^{12}\ {\rm GeV/f_a})^{-4}$, the subsequent relaxation in an axion minicluster due to $2a \to 2a$ scattering can be significant as a consequence of the huge mean phase-space density of axions [5]. Then, instead of the classical expression, $t_R^{-1} \sim \sigma\rho_a v_e m_a^{-1}$, where σ is the corresponding cross section and v_e typical velocity in the gravitational well, one gets [5] for the relaxation time $t_R^{-1} \sim \lambda_a^2\rho_a^2 v_e^{-2} m_a^{-7}$. The relaxation time is smaller than the present age of the Universe for miniclusters with $\Phi \gtrsim 30$ [1] which leads to a possibility of Bose-star formation inside such miniclusters. Characteristic sizes and limiting masses of resulting objects can be estimated as follows (if self coupling is negligible, otherwise see [6])

$$R \approx \frac{1}{m_a v_e} \approx 300\,\frac{10^{-12}M_\odot}{M_{BS}} \left(\frac{10\,\mu{\rm eV}}{m_a}\right)^2 {\rm km}. \tag{4}$$

The maximum possible mass of a stable Bose-star corresponds to $v_e \sim 1$ or $M_{\rm max}(\lambda = 0) \approx M_{\rm Pl}^2/m_a$. For non-interacting axions this would be in the range of $\sim 10^{-5}M_\odot$.

However, regardless of its smallness, the axion self-coupling cannot be neglected in the discussion of Bose-star stability as well [7]. The self-coupling of axions is negative and their interaction is attractive. Consequently, instability develops when $M_{\rm max}(\lambda < 0) = f_a\,M_{\rm Pl}/m_a \sim 10^{-12}M_\odot\,(10\,\mu{\rm eV}/m_a)^2$. Overall, with time the mass of the Bose-condensed core, M_{BS}, in the minicluster grows, while its radius shrinks. When the mass of M_{BS} approaches $M_{\rm max}(\lambda < 0)$, the core collapses. At this moment its radius is equal to [7]

$$R_{\rm min} \sim M_{\rm Pl}/f_a m_a \approx 200\ {\rm km}, \tag{5}$$

regardless of m_a. Note that the maximum mass for a stable axion Bose-star at $m_a = 10\,\mu{\rm eV}$ is of the order of the typical mass of the axion minicluster.

2.2 Fast Radio Bursts and Axion Bose-stars

The existence of axion Bose-stars and their explosions into electromagnetic radiation may explain recently discovered phenomena of Fast radio bursts (FRB). Potentially, there are two processes of explosive axion conversion into photons in astrophysical environment. The first process is coherent (parametric resonance) conversion, $a \to 2\gamma$, in a sufficiently dense axionic medium [6]. Second is $a \to \gamma$ in a strong magnetic field of a neutron star (magnetar) [8, 7]. The feasibility and relevance of both processes has to be studied yet in detail. Here we just stress

the similarity of observed characteristics of FRBs to the explosions of axion Bose stars, if the latter do occur.

FRBs exhibit a frequency-dependent time delay, which obeys a quadratic form so strictly, that the only remaining explanation is signal dispersion in cosmic plasma during propagation, for the review see Ref. [9]. The magnitude of this delay is so large that the cosmological distances are inferred for the FRB sources, $z \sim 1$.

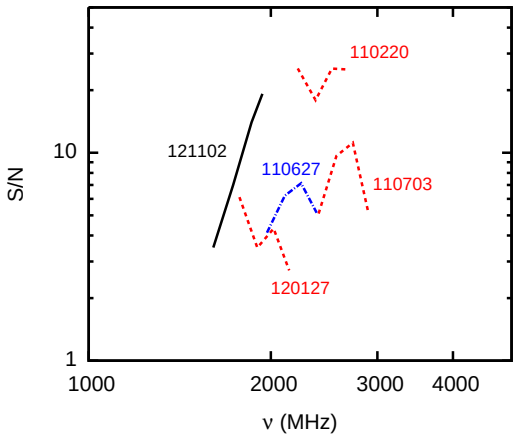

Figure 1: Fast Radio Burst (FRB) spectra shifted to their rest frame [7].

Now, we can compare parameters of FRBs and axion Bose-star explosions.

• Observed fluxes imply that the total energy radiated in the band of observation was in the range $10^{38} - 10^{40}$ ergs, assuming isotropy and quoted redshifts. Now, the typical axion minicuster mass is $10^{-12} M_\odot = 2 \times 10^{42}$ ergs, see Eq.(2). Therefore, the overall energy budget is appropriate and less then 1% conversion efficiency of a minicluster mass into γ radiation is sufficient to explain FRBs.

• Fast radio bursts occur on a very short time scale of millisecond. This implies that the size of the emitting region is small, less then 300 km. This should be compared to the radius of axion Bose-star, Eqs (4) and (5).

• Bursts are frequent, they occur at a high rate, $\sim 10^4$ events/day for the whole sky. This can also be matched (though the issue requires further study), given that the total number of miniclusters in the Galaxy is large, $N \sim 10^{24}$.

• If sources of FRBs are at Gpc distances, their brightness temperature would be $T_B \sim 10^{36}$ K, leading to the conclusion that the radiation from FRB sources should be coherent. Now, both processes of axion to photon conversion mentioned above would lead to a coherent radiation. Moreover, the spectrum will be strongly peaked at the (half) axion mass. This should be compared to FRB spectra shifted to their rest frame, see Fig. 1, which is consistent with spectra being peaked at one and the same frequency, taking into account uncertainties in FRBs redshifts. Such spectra would be unusual for pure astrophysical phenomena.

3 Miniclusters, minihalos and direct DM searches

Axion miniclusters originate from specific density perturbations with $\Phi \gtrsim 1$ which are consequence of non-linear axion dynamics around QCD epoch. Most abundant are miniclusters with $\Phi \approx 1$. There are 10^{24} of such miniclusters in the Galaxy and their density in the Solar neighborhood is 10^{10} pc^{-3}. Today minicluster with $\Phi \approx 1$ will have radius $\sim 10^7$ km. Therefore, during direct encounter of the laboratory with minicluster the local DM density increases by a factor 10^8 for about a day. That would create terrific signal in the detectors. However direct encounter with the Earth would occur less than once in 10^5 years [3].

In any axion model, as in any other cold dark matter model, structures form also on all scales, from galaxies to scales which are much smaller then a dwarf satellite galaxy. This is one and the

same mechanism which leads to a galaxy formation from primordial density perturbations, i.e. corresponds to $\Phi \ll 1$. For WIMPs this process continues down to clumps with $M \sim 10^{-6} M_\odot$, which corresponds to the cut-off scale due to free streaming in a typical WIMP model. For axion DM such minihalos will form down to even smaller scales, down to $M \sim 10^{-12} M_\odot$, which is typical minicluster mass and it corresponds to the mass of all axions in the horizon volume at the epoch when axion oscillations commence. This process has been numerically modeled both for WIMPs and axions in Ref. [10] in the mass range $10^{-6}\, M_\odot \lesssim M \lesssim 10^{-4}\, M_\odot$. For a minihalo with $M \sim 10^{-6} M_\odot$ (which corresponds in our notations to $\Phi = 0.016$) one concludes that the density of such DM haloes in the Solar neighborhood is ~ 500 pc^{-3}, direct encounter with the Earth occurs once in 10^4 years, and during encounter DM density increases by a factor of 100 for about 50 years. That would also create very interesting signal in the detectors, but all those minihalos are tidally destroyed actually, producing an uninteresting density field. The situation is different for axion miniclusters though.

4 Axion streams

4.1 Tidal disruption of miniclusters

The problem of tidal stripping of satellites has a long history. With time they are tidally disrupted and form streams. A collection of these streams would resemble spaghetti of large length L and cross-section radius comparable to the initial clump radius. Recently this process was modeled for minihalos with $M \sim 10^{-6} M_\odot$, see e.g. Ref. [11]. It was found that narrow long streams are formed out of them, with a length which increases in time. For example, in 5 Gyr the length of a stream will be 10^4 of the initial minihalo radius. Therefore, we may conclude that such a stream contributes 10^{-2} of the local DM density and streams originating from tidal disruption of minihalos are not interesting phenomenologically from the point of view of direct DM detection. The situation may be different for miniclusters with $\Phi \gtrsim 1$, let us consider it now.

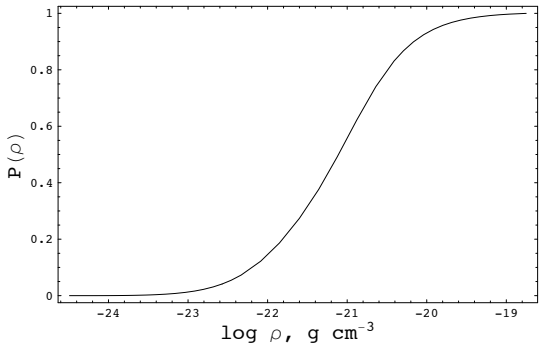

Figure 2: Survival probability for a clump in the Galaxy as a function of its density, from Ref. [13].

For a review of tidal disruption of dense DM clumps in a vide variety of models see Ref. [12]. The averaged survival probability for clumps (with trajectories such that they cross Solar neighborhood in the Galaxy) as a function of a clump density is shown in Fig. 2, see Ref. [13]. In our notations $\rho = 10^{-20}$ g/cm^{-3} corresponds to clumps with $\Phi \approx 0.1$. We see that 5% of clumps with such density is destroyed and their debris form tidal streams with potentially important phenomenological implications since the initial density in minicluster is much larger comparing to mini halo.

4.2 Implications for direct DM searches

An object with relative velocity $v \approx 10^{-3}$ crosses a stream during a time interval $\tau = 2R_{\rm mc}/v \approx 55\,{\rm hr}/\Phi\,(1+\Phi)^{1/3}$. This time interval corresponds to a period of high signal in the detector. The mean time between stream crossings can be found in the following way. The probability for a randomly chosen star to be found inside a stream is given by $P_{in} = \bar{\rho}/\rho_s$, where $\bar{\rho}$ and ρ_s are the mean density and the typical density of DM inside a stream correspondingly. Therefore, the time interval between successive stream crossings is $T = \tau/P_{in}$. This would be correct, however, if all miniclusters would be destroyed. If only a fraction of them is destroyed, T should be multiplied by $F \equiv (1-P_s)^{-1}$, where P_s the survival probability shown in Fig. 2.

Making the simplifying assumption that the resulting tidal stream increases in length with a rate equal to the escape velocity from the clump, and that its width does not change significantly, we find the resulting density inside a stream as well as other parameters relevant for direct DM detection. These parameters are listed in Table 1. We see, that the local DM density increase which occurs when we cross tidal streams from most abundant miniclusters with Φ from 0.1 to 1 might be interesting for the direct DM searches. To specify the situation precisely, one needs to know F as a distribution (indeed, the fate of a minicluster depends on many parameters, so it is not a unique function of Φ) and better knowledge of density evolution inside a stream is required. This study is in progress [14].

	$\Phi \approx 0.1$	$\Phi \approx 1$
Linear increase in 5 Gyr	2×10^4	10^6
Local $\rho/\bar{\rho}_{DM}$	3	100
Signal duration τ	20 days	1 day
Repeats in T	2 years	1 day $\times$ 100 $\times$ F

Table 1: Parameters of tidal streams from miniclusters.

Acknowledgments

I am grateful to V. Dokuchaev, P. Tinyakov and K. Zioutas for useful and stimulating discussions. This work was supported by the Russian Science Foundation grant 14-22-00161.

References

[1] E. W. Kolb and I. I. Tkachev, Phys. Rev. Lett. **71** 3051 (1993) [hep-ph/9303313].

[2] E. W. Kolb and I. I. Tkachev, Phys. Rev. D **49** 5040 (1994) [astro-ph/9311037].

[3] E. W. Kolb and I. I. Tkachev, Phys. Rev. D **50** 769 (1994) [astro-ph/9403011].

[4] E. W. Kolb and I. I. Tkachev, Astrophys. J. **460** L25 (1996) [astro-ph/9510043].

[5] I. I. Tkachev, Phys. Lett. B **261** 289 (1991).

[6] I. I. Tkachev, Sov. Astron. Lett. **12** 305 (1986) [Pisma Astron. Zh. **12** 726 (1986)].

[7] I. I. Tkachev, JETP Lett. **101** 1, 1 (2015) [arXiv:1411.3900 [astro-ph.HE]].

[8] A. Iwazaki, Phys. Rev. D **91** 2, 023008 (2015) [arXiv:1410.4323 [hep-ph]].

[9] S. R. Kulkarni, E. O. Ofek, J. D. Neill, Z. Zheng and M. Juric, arXiv:1402.4766 [astro-ph.HE].

[10] J. Diemand, B. Moore and J. Stadel, Nature **433** 389 (2005) [astro-ph/0501589].

[11] G. W. Angus and H. Zhao, Mon. Not. Roy. Astron. Soc. **375** 1146 (2007) [astro-ph/0608580].

[12] V. S. Berezinsky, V. I. Dokuchaev and Y. N. Eroshenko, Phys. Usp. **57** 1 (2014) [Usp. Fiz. Nauk **184** 3 (2014)] [arXiv:1405.2204 [astro-ph.HE]].

[13] V. Berezinsky, V. Dokuchaev, Y. Eroshenko, M. Kachelriess and M. A. Solberg, Phys. Rev. D **81** 103529 (2010) [arXiv:1002.3444 [astro-ph.CO]].

[14] P. Tinyakov, I. Tkachev, K. Zioutas, in preparation.

Preliminary Results of the CASCADE Hidden Sector Photon Search

N. Woollett[1,2], *I. Bailey*[1,2], *G. Burt*[1,2], *S. Chattopadhyay*[6,7], *J. Dainton*[2,5], *A. Dexter*[1,2], *P. Goudket*[2,3], *M. Jenkins*[1,2], *M. Kalliokoski*[4], *A. Moss*[2,3], *S. Pattalwar*[2,3], *T. Thakker*[2,3], *P. Williams*[2,3]

[1]Lancaster University, Lancaster, United Kingdom
[2]The Cockcroft Institute of Accelerator Science and Technology, Warrington, United Kingdom
[3]STFC ASTEC, Sci-Tech Daresbury, Warrington, United Kingdom
[4]CERN, Geneva, Switzerland
[5]University of Liverpool, Liverpool, United Kingdom
[6]Northern Illinois University, Illinois, United States of America
[7]Fermilab, Illinois, United States of America

DOI: http://dx.doi.org/10.3204/DESY-PROC-2015-02/woollet_nathan

Light shining through a wall experiments can be used to make measurements of photon-WISP couplings. The first stage of the CASCADE experiment at the Cockcroft Institute of Accelerator Science and Technology is intended to be a proof-of-principle experiment utilising standard microwave technologies to make a modular, cryogenic HSP detector to take advantage of future high-power superconducting cavity tests. In these proceedings we will be presenting the preliminary results of the CASCADE LSW experiment showing a peak expected exclusion of 1.10×10^{-8} in the mass range from $1.96\,\mu$eV to $5.38\,\mu$eV, exceeding current limits.

1 Introduction

CASCADE (CAvity Search for Coupling of A Dark sEctor) is an experiment which utilises microwave cavities and amplifiers to search for energy transmission between the cavities beyond that which would be expected through Standard Model processes. This approach is sensitive to hidden sector photons (HSPs) through their kinetic mixing with the photon as described by the Lagrangian,

$$\mathcal{L} = -\frac{1}{4}F^{\mu\nu}F_{\mu\nu} - \frac{1}{4}B^{\mu\nu}B_{\mu\nu} - \frac{1}{2}\chi F^{\mu\nu}B_{\mu\nu} - \frac{1}{2}m_{\gamma'}^2 B_\mu B^\mu, \tag{1}$$

where χ is the coupling factor, F is the standard model electromagnetic field and B is the HSP field.

The method being used is known as a *light shining through a wall*, LSW, experiment. In this design a cavity is powered from an external RF source and a second cavity is shielded from the powered cavity and used as a detector for transmission between the cavities. The cavities are nominally identical and operate at the same resonant frequency. This enables us to look

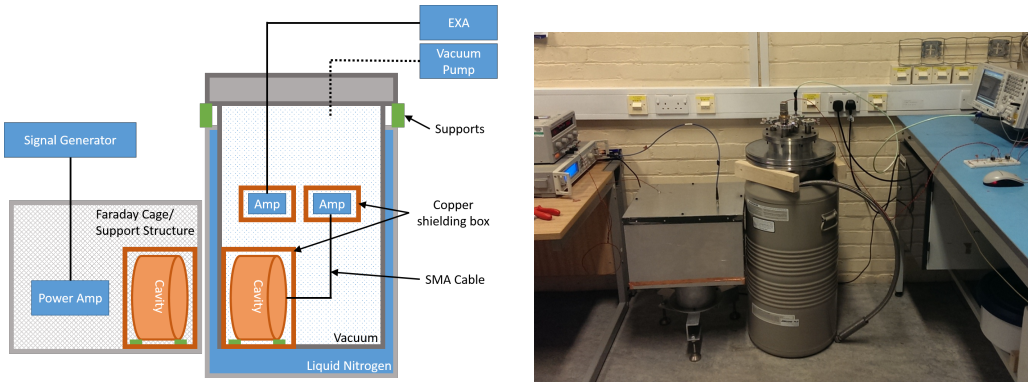

Figure 1: *Left:* A schematic of the CASCADE experiment. On the left hand side is the emitter chain and on the right is the detector chain. Spatial positioning is representative of the final set-up but not to scale. *Right:* A photograph of the final CASCADE set-up that was used to make a measurement. The photograph is taken from the same perspective as the schematic for easy comparison.

for an excess of power in the detector and if the corresponding frequency matches that of our source, we can conclude that the excess may originate from photon-HSP oscillations. A more detailed description of the technique is given in [1].

2 Measurement Set-up

The CASCADE experiment employs two cavities and uses amplifiers to maximise the observable power. To minimise any transmission between the emitter and the detection system, care is taken to separate the two systems. A schematic of the set-up is shown in Fig. 1.

The emitter system consists of a signal generator, a power amplifier and a copper cavity. There are two layers of shielding within this chain, a copper box containing the cavity and an aluminium box around the cavity and power amplifier. By having a shielding box around the amplifier the RF power in the cables between the signal generator and the shielding box is kept at -4 dBm rather than the 28 dBm that was provided to the emitter cavity. The signal generator shares a common 10 MHz reference signal with the detector chain to ensure frequency lock between the two systems.

The detector chain consists of an Agilent Technologies EXA Signal Analyser, two Miteq ASF3 Cryogrenic Amplifiers and a copper cavity. There are two layers of shielding around the cavity with a copper box around the cavity and a stainless steel vacuum box forming a second box which also contains the amplifiers. It was found that if the amplifiers were themselves unshielded anomalous signals would be produced by cross talk between the amplifiers so individual copper boxes are used to shield them from one another.

The cavities were designed to operate in the first transverse magnetic mode (TM010) at 1.3 GHz. The quality(Q) factor was estimated to be up to 22000 at room temperature using simulations in CST Microwave Studio, however, as the copper used is not oxygen free, the Q factor is limited to approximately 10500.

The amplifiers were chosen for their low noise characteristics with a noise figure of 0.6 dB at

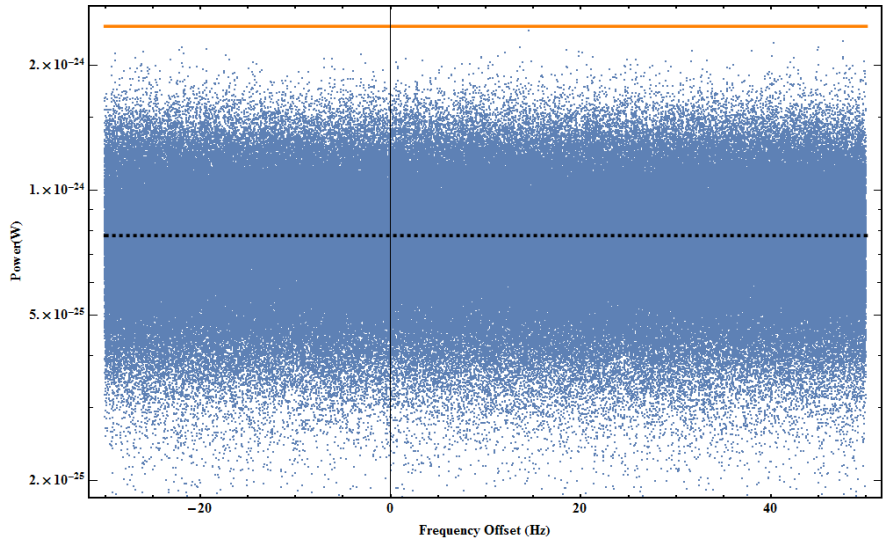

Figure 2: The signal recorded during a CASCADE run. The dashed line indicates the mean noise power and the solid orange line indicates 5 standard deviations. It can be seen that there are no points in excess of this level which indicates a null observation.

room temperature and as low as 0.2 dB at cryogenic temperatures [2]. The frequency region of interest is of the order of 100 MHz, limited by the cavity tuning, and the observation window is only 80 Hz, required to achieve the desired frequency resolution. The change in amplification with frequency for the amplifiers was found to be negligible over this range. Another important feature is their gain of 38 dB, this was tested by recording the observed power as a function of input power. A small increase in amplification was observed with reducing input power but, as the exact cause of the increase was unknown, the minimum observed value of 38 dB per amplifier was used in the calculating limits. By having two amplifiers in series we can amplify the thermal noise floor which is estimated to be -230 dBm above the internal noise of the signal analyser which is approximately -160 dBm.

3 Results

To make an exclusion we need to estimate the smallest signal we would be sensitive to. Since we are using a light shining through a wall experiment the signal frequency is known to be 1.293539940 GHz meaning we can use the side bands in the measurement to estimate the noise level in the signal region. The recorded data was over-sampled giving 524288 points each sensitive to a bandwidth of 0.5 mHz. A 5 sigma confidence level was used as this gives a less than 0.3% probability of having an excess within 1 Hz of the signal frequency assuming a flat noise distribution. No excess of power was recorded as can be seen in Fig. 2 where the 5 sigma power level is indicated by the solid orange line.

The cavities used in CASCADE are aligned coaxially. This enables us to take advantage of the longitudinal polarisation mode of the HSP. For the longitudinal mode the sensitivity is proportional to $(m_{\mathrm{HSP}}/\omega)^2$, rather than $(m_{\mathrm{HSP}}/\omega)^4$ as for the transverse mode where m_{HSP}

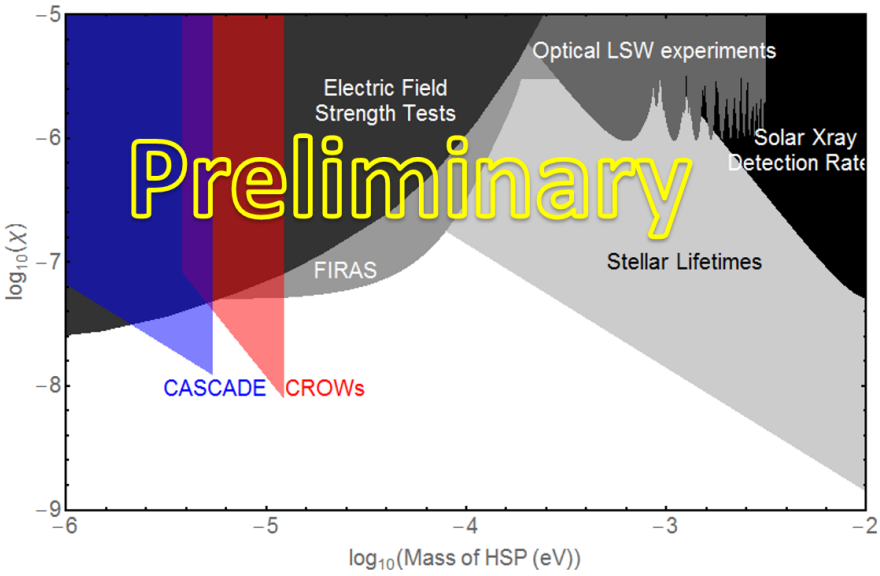

Figure 3: The expected exclusion of the CASCADE experiment based on the far field approximation of cavities coupled through the longitudinal polarisation of the HSP. The CROWs experiment has been highlighted for comparison as it employs the same experimental technique.

is the mass energy of the HSP and ω is the energy of the photons within the source [3]. This enables the search to cover lower masses leading to the mass range where the new parameter space is covered to increase from 1.1 μeV to 3.4 μeV. The preliminary exclusion based on the far field approximation of HSP coupling is shown in Fig. 3 presenting a peak exclusion down to a mixing factor, χ, of 1.10×10^{-8} and the strongest exclusion from 1.96 μeV to 5.38 μeV. However the cavity separation was on the order of the cavity height which is closer than appropriate for the far-field approximation so the final result will be based on a full near-field calculation.

Acknowledgments

This research was funded in part through the STFC Cockcroft Institute Core grant no. ST/G008248/1.

References

[1] J. Jaeckel and A. Ringwald, Phys. Lett. B **659**, 509 (2008) [arXiv:0707.2063 [hep-ph]].

[2] `https://miteq.com/docs/MITEQ-AFS_CR.PDF`

[3] P. W. Graham, J. Mardon, S. Rajendran and Y. Zhao, Phys. Rev. D **90**, no. 7, 075017 (2014) [arXiv:1407.4806 [hep-ph]].

Search for a Leptophobic B-Boson via η Decay at Jlab

Liping Gan

University of North Carolina Wilmington, Wilmington, NC, USA

DOI: http://dx.doi.org/10.3204/DESY-PROC-2015-02/gan_liping

A leptophobic B-boson couples predominantly to quarks and arises from a new $U(1)_B$ baryon number gauge symmetry. Its leading decay is $B \to \pi^0\gamma$ for the mass range of 140–620 MeV [1]. This offers a great experimental opportunity to search for such weakly-coupled gauge bosons in the sub-GeV mass range through the doubly-radiative decay $\eta \to B\gamma \to \pi^0\gamma\gamma$. The Jlab Eta Factory (JEF) experiment has been recently developed to search for B through this decay channel, with sensitivity to the baryonic fine structure constant as low as 10^{-7}. This sensitivity indirectly constrains the existence of anomaly cancelling fermions at the TeV-scale. The proposed search for B in the three-photon final state ($B \to \pi^0\gamma \to 3\gamma$) is complementary to a world-wide effort searching for a dark heavy photon A' at the high-intensity frontier.

1 Introduction

Dark Matter (DM) dominates the matter density in our universe, but very little is known about its nature. The existence and stability of DM provide a strong hint that there may be a dark sector consisting of rich symmetry structure with new forces and new particles that do not interact with the known strong, weak, and electromagnetic forces, except gravity. Discovery of any of these particles, new forces, and associated symmetries would redefine our worldview and have a profound impact. Additional $U(1)'$ gauge symmetries and associated vector gauge bosons are one of the best motivated extensions of the Standard Model (SM) [2]. A conserved charge can explain the stability of dark matter [3]-[7]. In addition, the conserved vector currents are uniquely positioned to avoid the violation of the Glashow-Iliopoulos-Maiani (GIM) mechanism for suppression of Flavor Changing Neutral Currents (FCNC) [8].

One model in the "Vector" portal from the SM sector into the dark sector that has been widely considered is a new force mediated by an abelian $U(1)'$ gauge boson A' (dark photon) that couples very weakly to electrically charged particles through "kinetic mixing" with the photon [9]. The mixing angle ϵ controls the coupling of the DM sector to the SM sector. Searching for a sub-GeV A' has drawn world-wide attention in recent years and has inspired broad experimental programs in different high-intensity frontier centers [10]. Most of experimental searches for the A' are through its decays to e^+e^- or $\mu^+\mu^-$, which rely on the leptonic coupling of this new force.

Another equally compelling model in the "Vector" portal not covered by the dark photon searches is a new force mediated by a leptophobic gauge B-boson that couples predominantly to quarks and arises from a new $U(1)_B$ baryon number gauge symmetry [1, 8]. The $U(1)_B$

symmetry was initially proposed by Lee and Yang back in 1955 [11] and subsequently discussed extensively in the literature [1, 7, 8, 12, 13]. Since quarks experience all known interactions, it is fitting to ask whether additional interactions of quarks exist [14]. A new $U(1)_B$ gauge symmetry provides a natural framework for the Peccei-Quinn mechanism in the quark sector for solving a long standing "strong CP problem" [12]. This model has also been motivated in part by the similar cosmological abundances of dark matter and baryonic matter in the Universe, which may point toward a unified baryogenesis mechanism for both types of matter [15]. Since $U(1)_B$ is spontaneously broken by a new Higgs field, the B-boson is massive. In addition, new baryonic fermions with electroweak quantum numbers are required to cancel the $SU(2)_L^2 \times U(1)_B$ and $U(1)_Y^2 \times U(1)_B$ anomalies. The new fermions acquire masses (Λ) via a $U(1)_B$-breaking Higgs field, with $m_B/\Lambda \geq g_B/(4\pi)$ [16], where m_B is the mass of B-boson and g_B is the $U(1)_B$ gauge coupling. As a result, a positive signal for sub-GeV B with a gauge coupling smaller than 10^{-3} will imply new fermions at the TeV-scale.

Experimental searches for leptophobic bosons at hadron colliders over the last few decades have set upper limits on their couplings for masses in the 50 GeV to 3 TeV range [14, 17, 18]. Masses smaller than the pion mass also have very strong constraints from searches for long-range nuclear forces [19]. However, masses around the QCD scale have been nearly "untouched" due to large SM backgrounds [14]. Nelson and Tetradis first proposed to search for a sub-GeV B-boson through the η decay in 1989 [8]. However, they assumed that $B \to \pi^+\pi^-$ would dominate for $m_B > 2m_\pi$. In that case, the signal of B would be mostly hidden under the ρ meson decay. Tulin demonstrated in his recent article [1] that $B \to \pi^+\pi^-$ is suppressed due to G parity conservation and the leading decay channel is $B \to \pi^0 + \gamma$ for $m_\pi \leq m_B \leq 620$ MeV. This offers a great experimental opportunity to search for B in this mass range through the doubly-radiative decay $\eta \to \pi^0\gamma\gamma$. The new physics decay $\eta \to B\gamma \to \pi^0\gamma\gamma$ would produce a resonance peak at m_B in the $\pi^0\gamma$ invariant mass distribution, while the SM-allowed $\eta \to \pi^0\gamma\gamma$ decay with a suppressed branching ratio of $\sim 2.7 \times 10^{-4}$ [17] would be present as the irreducible background in the signal window.

2 Jlab Eta Factory (JEF) Experiment

The Jlab Eta Factory (JEF) Experiment has been recently developed at Jefferson Lab (Jlab) using the newly developed GlueX apparatus in Hall D to measure η decays with emphasis on rare neutral modes [20]. One of the main physics goals for this experiment is to provide a stringent constraint on a leptophobic gauge boson (B) in the mass region 0.14–0.54 GeV through $\eta \to B\gamma \to \pi^0\gamma\gamma$. A 9.0–11.7 GeV tagged photon beam will be used to produce η mesons at small angles via the $\gamma + p \to \eta + p$ reaction. The majority of decay photons from the η's will be detected in an upgraded Forward Calorimeter (referred to as FCAL-II) in which the central lead glass blocks of the existing calorimeter will be replaced with smaller size, higher resolution $PbWO_4$ crystals. For not-too-small η production angles, the low energy recoil protons will be detected by the start counter and central drift chamber of the GlueX solenoid detector to help suppress backgrounds.

The measurement of rare η decay to 4γ final states has historically been limited by the background from $\eta \to 3\pi^0 \to 6\gamma$ (BR = 32.6%) with missing or merged photons. This problem is addressed in the JEF experiment by the fact that η's are significantly boosted so that the detector thresholds are low relative to the photon energies to reduce missing photons, the kinematics are over-determined (with recoil proton detection), and the decay photons are mea-

sured in an upgraded forward calorimeter (FCAL-II) with a central region of high-granularity, high-resolution lead tungstate crystals with flash ADC readout, to suppress merged photons. The Monte Carlo simulations demonstrate that the backgrounds can be reduced by about two orders of magnitude compared to the existing experiments and to experiments planned at other facilities, while maintaining a healthy η production rate.

3 Experimental Reach for B-Boson

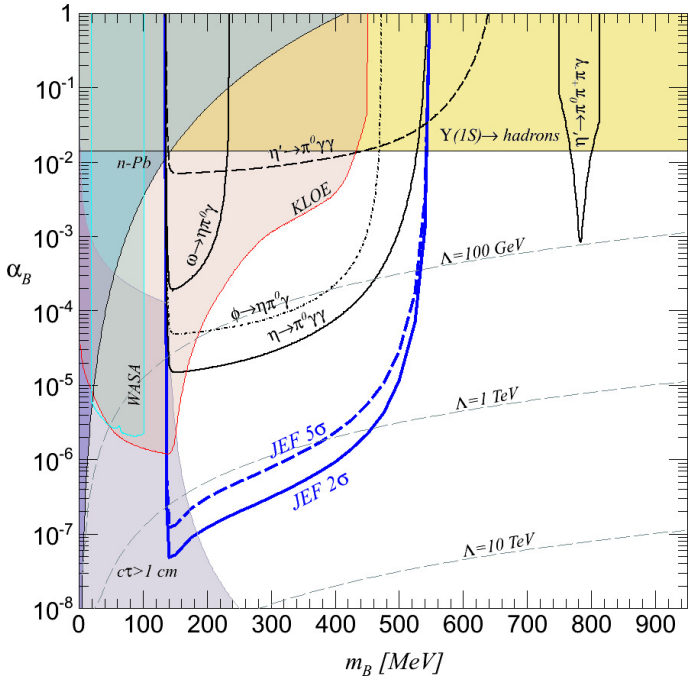

Figure 1: Current exclusion regions for a leptophobic gauge B-boson [1], with the projected JEF search region for the baryonic fine structure constant versus mass plane. Shaded regions are exclusion limits from hadronic $\Upsilon(1S)$ decay [18] and low energy n-Pb scattering [19]. The pink and blue shaded regions are from A' searches (KLOE [21] and WASA [22]). A' limits applied to B are model-dependent, constraining possible leptonic B couplings. Limits shown here are for $\epsilon = 0.1 \times e g_B/(4\pi)^2$. The black contours are current exclusion limits from radiative light meson decays based on their total rate (assuming the QCD contribution is zero). The light purple shaded region shows where the B has a macroscopic decay length $c\tau > 1$ cm. The solid blue curve shows the projected 2σ sensitivity and the dashed blue curve shows the projected 5σ sensitivity for the JEF experimental reach. Dashed gray contours denote the upper bound on the mass scale Λ for new electroweak fermions needed for anomaly cancellation.

The experimental limits on the baryonic fine structure constant $\alpha_B = g_B^2/(4\pi)$ and B-boson mass m_B are shown in Fig. 1 along with the projected JEF exclusion limits. As shown in the

figure, the JEF experiment has the sensitivity to the baryonic fine structure constant α_B as low as 10^{-7}. The observation of a B-boson within the JEF limit would imply new fermions with masses around the TeV-scale or below. Although such new fermions may have escaped detection at colliders thus far, they are likely to be within the reach for discovery at the LHC or future high energy colliders.

4 Summary

A search for a GeV-scale leptophobic gauge boson (B) coupled to baryon number is complementary to ongoing searches for a dark photon. The JEF experiment at Jlab will search for B over the mass range of 0.14–0.54 GeV in the $\eta \to \gamma + B(\to \gamma + \pi^0)$ decay. This measurement will improve the existing bounds by two orders of magnitude, indirectly constraining the existence of anomaly cancelling fermions at the TeV-scale.

Acknowledgments

This project is supported by USA NSF awards PHY-1206043 and PHY-1506303.

References

[1] S. Tulin, Phys. Rev. D **89**, 114008 (2014).

[2] P. Langacker, Rev. Mod. Phys. **81**, 1199 (2009).

[3] G.R. Farrar and G. Zaharijas, Phys. Rev. Lett. **96**, 041302 (2006).

[4] M. Duerr and P.F. Perez, Phys. Lett. B **732**, 101 (2014).

[5] H. Davoudiasl *et al.*, Phys. Rev. Lett. **105**, 211304 (2010)

[6] K. Agashe and G. Servant, Phys. Rev. Lett. **93**, 231805 (2004)

[7] M.L. Graesser, I.M. Shoemaker, L. Vecchi, arXiv:1107.2666.

[8] A. E. Nelson and N. Tetradis, Phys. Lett. B **221**, 80 (1989).

[9] B. Holdom, Phys. Lett. B **166**, 196 (1986).

[10] R. Essig *et al.*, arXiv:1311.0029.

[11] T.D. Lee and C.N. Yang, Phys. Rev. **98**, 1501 (1955).

[12] R. Foot, G. C. Joshi, and H. Lew, Phys. Rev. D **40**, 2487 (1989).

[13] S. Rajpoot, Phys. Rev. D **40**, 2421 (1989); X.-G. He and S. Rajpoot, Phys. Rev. D **41**, 1636 (1990); C. D. Carone and H. Murayama, Phys. Rev. Lett. **74**, 3122 (1995); D. C. Bailey and S. Davidson, Phys. Lett. B **348**, 185 (1995); C. D. Carone and H. Murayama, Phys. Rev. D **52**, 484 (1995); A. Aranda and C. D. Carone, Phys. Lett. B **443**, 352 (1998); P. Fileviez Perez and M. B. Wise, Phys. Rev. D **82**, 011901 (2010).

[14] B. Dobrescu and C. Frugiuele, Phys. Rev. Lett. **113**, 061801 (2014).

[15] H. Davoudiasl and R.N. Mohapatra, New J. Phys. **14**, 095011 (2012); K.M. Zurek, Phys. Rept. **537**, 91 (2014); K. Petraki and R.R. Volkas, Int. J. Mod. Phys. A **28**, 1330028 (2013).

[16] M. Williams, C. Burgess, A. Maharana, and F. Quevedo, JHEP **1108**, 106 (2011).

[17] J. Beringer *et al.*, (Particle Data Group), Phys. Rev. D **86**, 010001 (2012).

[18] A. Aranda and C. D. Carone, Phys. Lett. B **443**, 352 (1998).

[19] R. Barbieri and T. E. O. Ericson, Phys. Lett. B **57**, 270 (1975).

[20] L. Gan *et al.*, Jlab proposal "Eta Decays with Emphasis on Rare Neutral Modes: The JLab Eta Factory (JEF) Experiment", *https://www.jlab.org/exp_prog/proposals/14/PR12-14-004.pdf*.

[21] D. Babusci *et al.*, Phys. Lett. B **720**, 111 (2013).

[22] P. Adlarson *et al.*, Phys. Lett. B **726**, 187 (2013).

Chapter 2

Contributed Posters

Effects of Hidden Photons during the Red Giant Branch (RGB) Phase

Adrián Ayala[1,2], *Oscar Straniero*[3], *Maurizio Giannotti*[4], *Alessandro Mirizzi*[5,6], *Inma Domínguez*[1]

[1]University of Granada, Granada, Spain
[2]University of Tor Vergata, Rome, Italy
[3]Instituto Nazionale di Astrofisica (INAF), Italy
[4]Barry University, Miami Shores, US
[5]University of Bari, Bari, Italy
[6]INFN, Bari, Italy

DOI: http://dx.doi.org/10.3204/DESY-PROC-2015-02/ayala_adrian

Features in the globular cluster luminosity functions (LF) of the post-main sequence stellar evolution can be used to investigate modifications of standard stellar models and to look for new physics fingerprints, like axions or hidden photons. Here, we investigate the possible effects of hidden photons during the red giant branch (RGB) phase. In a follow-up analysis, these results will be applied to discuss signatures and observational effects in the globular cluster LF.

1 Introduction

For decades stars have represented very efficient laboratories for testing new models of physics beyond the standard model [1], providing bounds often superseding what achieved by terrestrial experiments. Recent examples include axions [2, 3, 4, 5, 6], anomalous neutrino magnetic moment [7, 8, 9], extradimensions [10], and hidden photons [11, 12, 13, 14].

Here, we consider the case of the hidden photons and study their effects on the red giant branch (RGB). Hidden photons (HP) are described by the Lagrangian [11]

$$\mathcal{L} = -\frac{1}{4}F_{\mu\nu}^2 - \frac{1}{4}V_{\mu\nu}^2 - \frac{\chi}{2}F_{\mu\nu}V^{\mu\nu} + \frac{m_V^2}{2}V_{\mu\nu}V^{\mu\nu} \tag{1}$$

where F and V represent, respectively, the standard photon and the HP fields, m_V is the HP mass and χ is the coupling constant.

With the exception of [14], which studied the effects of low mass HP from the sun, all previous analyses of HP from stars have been performed on existent standard stellar models, therefore ignoring the feedback from the HP emission on the stellar evolution, particularly for RGB stars. In this case, the approach [12, 13] has been to consider a model of RGB near the He-flash and constraint the HP emission rate (averaged over the stellar core) to be less than 10 erg/g·s [13]. This simple criteria, however, ignores the possibility that the HP emission could modify the star evolution prior to the He-flash.

We present preliminary results of an attempt to study the full RGB evolution, including the new physics cooling channel in the evolutionary code.

2 Approach

In this first phase of the analysis, we plan to consider only HP masses from a few keV to a few 10 keV. This mass region seems to be the one where stars can overcome other constraints, particularly those derived from current dark matter experiments (see, e.g., [13]).

The HP emission rates (for transverse and longitudinal modes) can be found in [11, 12]. Here we consider only the longitudinal mode and use the emission rate in the resonant approximation [12]

$$\epsilon_L \simeq \frac{\chi^2 m_V^2}{4\pi\,\rho}\,\frac{\omega_{\rm pl}^2\sqrt{\omega_{\rm pl}^2 - m_V^2}}{e^{\omega_{\rm pl}/T}-1} \tag{2}$$

where $\omega_{\rm pl}$ is the plasma frequency. The resonant approximation represents an enormous simplification of the HP rate and, according to our numerical tests, is an excellent approximation of the longitudinal emission rate throughout the RGB evolution.

3 Preliminary Results

We have considered a model of a $0.82 M_\odot$ mass star, with metallicity $Z = 0.001$, representative of a typical globular cluster RGB star. The model has been evolved from pre-main sequence to the RGB *tip* (the point of maximum luminosity of the RGB phase, just before helium flash) using the FUNS (FUll Network Stellar evolution) stellar evolution code [15, 16, 17], with the additional cooling rate (2) for $m_V = 1$ keV.

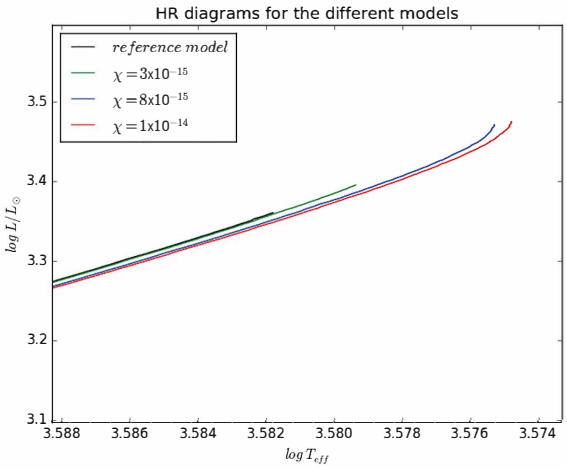

Figure 1: HR diagram for the RGB evolution for our reference models.

The HP emission plays no significant role during the main sequence evolution since, for the masses we are interested in, the resonant production of either transverse or longitudinal modes is forbidden in this early evolutionary stage.

However, assuming couplings $\chi \sim$ a few 10^{-15}, the additional emission provides an effective energy sink during the RGB evolution, increasing the mass of the helium core and the RGB tip brightness. The results are shown in the table below, where we report the χ value for each model, helium core mass M_{HeC}, evolutionary time up to the tip, the effective surface temperature, the luminosity at the tip (the maximum value of the luminosity) measured in I band magnitude, M_I, the difference of I magnitude between the tip and the bump (a small local luminosity minimum) ΔM_I and the differences of ΔM_I with respect to the reference model without hidden photon. It is evident

χ	M_{HeC}	t_{TIP} (Gy)	log T_{eff}	RGB tip M_I	ΔM_I	$\Delta M_I - [\Delta M_I]_{ref}$
0	0.5034	13.21	3.581	-3.997	-3.294	0
3×10^{-15}	0.5072	13.19	3.579	-4.075	-3.395	-0.101
8×10^{-15}	0.5238	13.10	3.576	-4.247	-3.734	-0.440
1×10^{-14}	0.5303	13.07	3.575	-4.255	-3.841	-0.547

Table 1: Results from the simulation. The luminosity is measured in I band magnitude (M_I)

that larger HP couplings produce brighter RGB tips.

The actual value of the RGB tip luminosity is a useful observable to test physics beyond the standard model. This method has been used recently to constrain the neutrino magnetic moment [3] and the axion electron coupling [8].

Comparing the results from our table (Table 1) with the recent analysis in [3, 8], we see that a value of $\chi \sim 10^{-14}$ seems to be excluded, a result somewhat stronger than the bound in [13].

One of the problem with this methodology, however, is the experimental identification of the RGB tip luminosity which depends, among other parameters, on the stellar distance. Noticeable, this was the source of the largest uncertainties in the recent studies [3, 8].

We therefore investigate another possible method: to measure the luminosity differences between the *tip* and the *bump* of the RGB. As shown in table 1 and Fig. 2, this observable increases monotonically with the coupling and becomes more than 0.5 magnitudes in the I band for $\chi = 10^{-14}$.

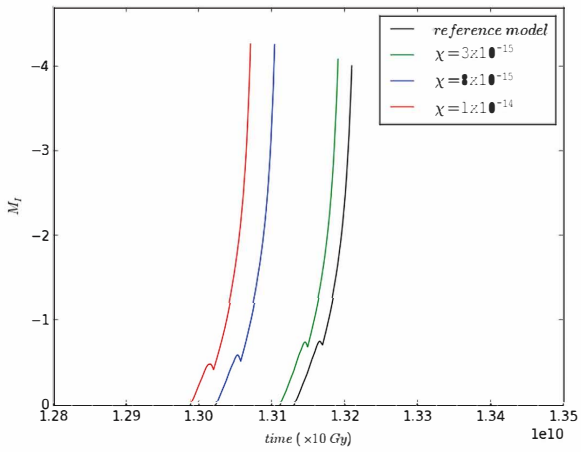

Figure 2: Luminosity (measured in I band magnitude) vs time, for the three models. Note the increase of the difference between the tip (maximum luminosity on the RGB band) and the bump (local luminosity decrease) with the coupling. See text for more explanation.

The exact threshold value for $\Delta M_I - [\Delta M_I]_{ref}$ to be confidently excluded has not been determined yet. Therefore, at this stage of the analysis, we are not ready to provide a clear constraint on the HP coupling. A complete study of this problem is currently in preparation.

4 Summary and conclusion

We reported on a preliminary study of the effects of HP emission on the evolution of RGB stars. In order to assess this impact, we modified the stellar evolution code to add the possibility of HP emission and studied the whole modified RGB evolution. At the moment, we have considered

only an example, with HP mass 1 keV, and confined our analysis to the case of resonant emission of the longitudinal mode.

Our results show that the HP can change the pre-He-flash evolution, as clear from the time shifts of the tracks in Fig. 2, confirming the need to use the modified code throughout the whole evolution.

Finally, we identified a possible observable, the luminosity difference (ΔM_I) between the tip and the bump in the RGB evolutionary tracks, which is less subject to systematics than the absolute luminosity of the RGB tip. Comparing the predicted values of ΔM_I with the observations could provide a promising way to constrain HP and other new physics candidates during the RGB evolution.

A full analysis, which will include a scan of masses between 1-10 keV and the off-resonant (longitudinal) rate, is in preparation.

References

[1] G. G. Raffelt, Chicago, USA: Univ. Pr. (1996) 664 p

[2] A. Friedland, M. Giannotti and M. Wise, Phys. Rev. Lett. **110**, 061101 (2013) [arXiv:1210.1271 [hep-ph]].

[3] N. Viaux, M. Catelan, P. B. Stetson, G. Raffelt, J. Redondo, A. A. R. Valcarce and A. Weiss, Phys. Rev. Lett. **111**, 231301 (2013) [arXiv:1311.1669 [astro-ph.SR]].

[4] A. Ayala, I. Dominguez, M. Giannotti, A. Mirizzi and O. Straniero, arXiv:1406.6053 [astro-ph.SR].

[5] A. Payez, C. Evoli, T. Fischer, M. Giannotti, A. Mirizzi and A. Ringwald, JCAP **1502**, no. 02, 006 (2015) [arXiv:1410.3747 [astro-ph.HE]].

[6] M. M. Miller Bertolami, B. E. Melendez, L. G. Althaus and J. Isern, JCAP **1410**, no. 10, 069 (2014) [arXiv:1406.7712 [hep-ph]].

[7] A. Heger, A. Friedland, M. Giannotti and V. Cirigliano, Astrophys. J. **696**, 608 (2009) [arXiv:0809.4703 [astro-ph]].

[8] N. Viaux, M. Catelan, P. B. Stetson, G. Raffelt, J. Redondo, A. A. R. Valcarce and A. Weiss, Astron. Astrophys. **558**, A12 (2013) [arXiv:1308.4627 [astro-ph.SR]].

[9] M. M. Miller Bertolami, Astron. Astrophys. **562**, A123 (2014) [arXiv:1407.1404 [hep-ph]].

[10] A. Friedland and M. Giannotti, Phys. Rev. Lett. **100**, 031602 (2008) [arXiv:0709.2164 [hep-ph]].

[11] J. Redondo, JCAP **0807**, 008 (2008) [arXiv:0801.1527 [hep-ph]].

[12] J. Redondo and G. Raffelt, JCAP **1308**, 034 (2013) [arXiv:1305.2920 [hep-ph]].

[13] H. An, M. Pospelov, J. Pradler and A. Ritz, Phys. Lett. B **747**, 331 (2015) [arXiv:1412.8378 [hep-ph]].

[14] N. Vinyoles, A. Serenelli, F. L. Villante, S. Basu, J. Redondo and J. Isern, arXiv:1501.01639 [astro-ph.SR].

[15] O. Straniero, R. Gallino and S. Cristallo, Nucl. Phys. A **777**, 311 (2006) [astro-ph/0501405].

[16] L. Piersanti, S. Cristallo and O. Straniero, arXiv:1307.2017 [astro-ph.SR].

[17] O. Straniero, S. Cristallo, and L. Piersanti, Astrophys. J. **785**, 77 (2014) [arXiv:1403.0819 [astro-ph.SR]].

Characterization of a Transition-Edge Sensor for the ALPS II Experiment

Noëmie Bastidon[1], *Dieter Horns*[1], *Axel Lindner*[2]

[1]University of Hamburg, Hamburg, Germany
[2]Deutsches Elektronen-Synchrotron (DESY), Hamburg, Germany

DOI: http://dx.doi.org/10.3204/DESY-PROC-2015-02/bastidon_noemie_poster

The ALPS II experiment, Any Light Particle Search II at DESY in Hamburg, will look for light ($m < 10^{-4}$ eV) new fundamental bosons (e.g., axion-like particles, hidden photons and other WISPs) in the next years by the mean of a light-shining-through-the-wall setup. The ALPS II photosensor is a Transition-Edge Sensor (TES) optimized for $\lambda = 1064$ nm photons. The detector is routinely operated at 80 mK, allowing single infrared photon detections as well as non-dispersive spectroscopy with very low background rates. The demonstrated quantum efficiency for such TES is up to 95% at $\lambda = 1064$ nm as shown in [1]. For 1064 nm photons, the measured background rate is $< 10^{-2}\,\mathrm{sec}^{-1}$ and the intrinsic dark count rate in a dark environment was found to be of $1.0 \cdot 10^{-4}\,\mathrm{sec}^{-1}$ [2]. Latest characterization results are discussed.

1 Single photon detection for ALPS II

The ALPS II experiment will be looking for new fundamental bosons. Such a light-shining-through-the-wall experiment requires a high quantum efficiency low background single-photon detector [3]. A Tungsten Transition-Edge Sensor, which is optimized for low-background high quantum efficiency single photon detection, has been developed by NIST (National Institute of Standards and Technology).

2 Detector setup

2.1 Tungsten Transition-Edge Sensor

TESs are superconductive microcalorimeters measuring the temperature difference ΔT induced by the absorption of a photon. They are operated in a strong negative electro-thermal feedback corresponding to a constant voltage bias.

When a 1064 nm photon is absorbed by the tungsten chip, the sensor temperature raises by 0.1 mK. Heating up of the detector brings it from its superconductive stage to close to its normal resistive stage with an increase of the resistance of $\Delta R \approx 1\Omega$. This leads to a decrease of the current with I ≈ 70 nA. TESs are inductively coupled to a SQUID (Superconducting Quantum Interference Device) that converts this current variation in a voltage difference of $\Delta V \approx -50$ mV.

The ALPS II detector module is constituted of two TESs coupled to a SQUID. Both detectors are 25×25 μm^2 large and 20 nm thick. A ceramic standard mating sleeve towers above each detector, allowing the coupling of a standard single-mode fiber.

2.2 Adiabatic Demagnetization

Transition-Edge Sensors are superconductive detectors. The detector needs to be placed in a bath at $T_{bath} = 80\,\text{mK} \pm 25\,\mu\text{K}$. In order to do so, the TES is placed in an Adiabatic Demagnetization Refrigerator (ADR).

ADR cryostats can reach two low-temperature levels [4]. A temperature baseline of 2.5 K at the colder stages of the cryostat is reached with the help of a compressor using helium and a pulse-tube cooler. The duration of this cool-down procedure is only limited by maintenance works and the necessary modifications of the setup. Within a cool-down, many phases at 80 mK can be reached in two hours through adiabatic demagnetization. Such a recharge lasts approximately 24 hours.

3 TES Characterization

3.1 Pulse shape

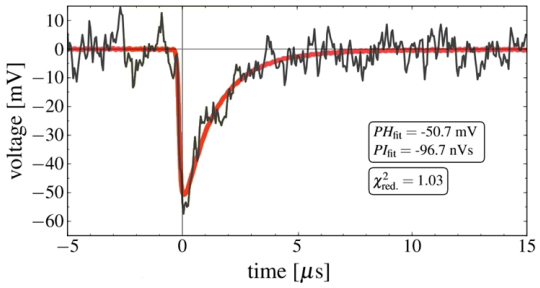

Figure 1: Infrared single-photon pulse shape.

The average pulse shape for 1064 nm photons shows a Peak Height of PH ≈ -50 mV and a Peak Integral of PI ≈ -100 nV (Fig. 1). A mask, corresponding to an average pulse, is fitted to the pulses for different scaling factors a and shift values j towards the trigger point [2].

3.2 Linearity and energy resolution

The linearity of the ALPS II W-TESs was tested by analysing the detector response to different photon energies. Four different lasers were used to that purpose (1064, 645, 532, 405 nm). In Figure 2, the average PH is shown depending on the energy of the photons absorbed by the detector. The sensors are linear in our region of interest (1.17 eV) [2]. The non-linearity at higher energies matches expectations (saturation of the detector). The energy resolution of the detectors for these different wavelengths was measured to be $\Delta E/E < 8\%$ [2].

3.3 Stability

Detection stability over time is essential for the ALPS II experiment where long-term measurements will be performed. Stability during a cool-down as well as between different cool-downs has been checked successfully. The most essential characteristic of the detector is its stability during a recharge-cycle corresponding to the data-taking period. The TES bias current (i.e. TES working point (Fig. 3)) has been measured to be reasonably stable with a maximum gradient $< 1.5\,\mu$A. This variation in the TES bias current corresponds to a variation in the peak height of $\Delta\mathrm{PH} < 3\%$. Finally, the results have been proven to be operator independent (adjustment method) [2].

4 Summary

Transition-Edge Sensors seem to ideally meet the ALPS II detector challenges. The characterization of the sensors provided by NIST has demonstrated a good detector energy resolution as well as a good stability of the pulse shape over long-term measurements. In addition to this, both detectors have shown a good linearity in the ALPS II region of interest (1.17 eV).

In the near future, optimization of the detector quantum efficiency as well as reduction of the background will be performed.

Acknowledgments

The authors are grateful to NIST, PTB and Entropy for their technical support. We would also like to thank J. Dreyling-Eschweiler and F. Januschek. Finally, we thank the PIER Helmholtz Graduate School for their financial travel support.

References

[1] A. E. Lita, A. J. Miller and S. W. Nam, "Counting near-infrared single-photons with 95% efficiency," Optics express **16**, 5 (2008).

[2] J. Dreyling-Eschweiler *et al.*, "Characterization, 1064 nm photon signals and background events of a tungsten TES detector for the ALPS experiment," J. Mod. Opt. **62**, 14 (2005) [arXiv:1502.07878 [hep-ex]].

[3] R. Bähre *et al.*, "Any light particle search II Technical Design Report," JINST **8**, (2013) [arXiv:1302.5647v2 [hep-ex]].

[4] G. K. White, P. J. Meeson, "Experimental techniques in low-temperature physics," Fourth Edition (2002).

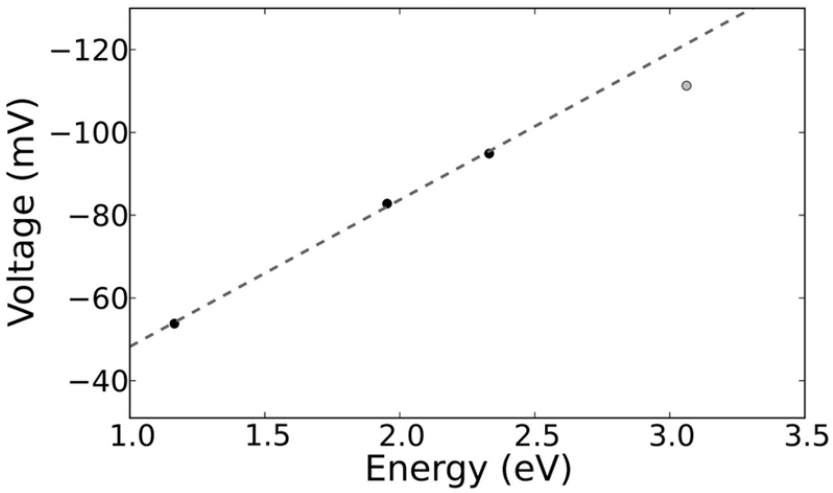

Figure 2: Average pulse height in units of voltage output as a function of photon energy for the TES. The dashed line is a fit to the first three points.

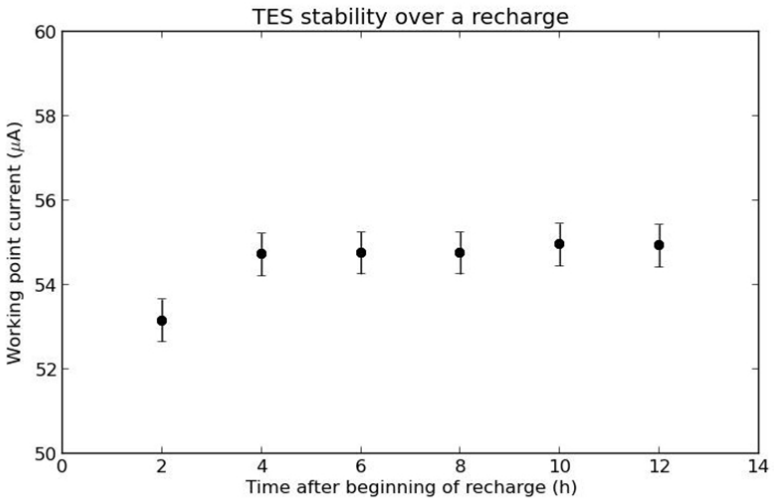

Figure 3: The TES working point current equivalent to $R_0 = 30\%\, R_{normal}$ as a function of time after the beginning of a recharge.

Receiver Electronics for Axion Experiment at CAPP

Seung Pyo Chang[1,2], *Young-Im Kim*[2], *Myeongjae Lee*[2], *Yannis K. Semertzidis*[1,2]

[1]Korea Advanced Institute of Science and Technology (KAIST), Daejeon, South Korea
[2]Center for Axion and Precision Physics Research (CAPP), Institute for Basic Science (IBS), Daejeon, South Korea

DOI: http://dx.doi.org/10.3204/DESY-PROC-2015-02/chang_seungpyo

The CAPP/IBS aims to do an axion search by detecting the axion using a resonant cavity. In this experiment, the axion signal should be amplified and down-converted because it is very weak (10^{-24} W) and the frequency is very high for digitization ($2 \sim 8$ GHz). In the radio frequency (RF) signal processing at room temperature, the amplifier and mixer play a crucial role. One of the amplifiers and the mixer is tested. Also the entire RF signal processing system is tested with a very weak artificial signal (10^{-19} W).

1 Introduction

The CAPP/IBS is searching for the cosmic axion using a resonant cavity. In this experiment, the extremely weak, axion signal is supposed to be generated in a resonant cavity inside a very high magnetic field ($> 8T$) and a very low temperature ($\sim$ 100 mK). After the axion signal exits from the cavity, it goes through the radio frequency (RF) signal processing system which amplifies the signal and downconverts the frequency from GHz to MHz at room temperature. The amplifier and the mixer have an important role in the RF signal processing system at room temperature (RT). The RF signal processing chain has been designed. The measurement results of the two components of the entire system are described in this paper. The entire RF signal processing system has been tested with a very weak artificial signal (10^{-19} W).

2 Measurement

The amplifier HMC-C059 and the mixer HMC-C009 have been tested with 8 GHz, 5 GHz signals respectively. These frequencies are chosen because they are at the middle of the available frequency range of each component. The input power range varies from -140 dBm to 10 dBm. For the mixer, the local oscillator (LO) frequency is set to 4.9 GHz and the intermediate frequency (IF) is 100 MHz. The entire RF signal processing system, which is composed of two amplifiers, a mixer, a band pass filter and a power splitter, has been tested with 2 signal generators and a signal analyzer. The test signal amplitude is set to -160 dBm at 6 GHz.

2.1 Amplifier

The gain is the ratio between the input and output amplifier's powers and can be defined as

$$\text{Gain [dB]} = 10\log(\mathrm{P_{out}}/\mathrm{P_{in}}). \quad (1)$$

The gain can be obtained by subtracting the input power and output power since the signal generator and signal analyzer shows the power in log scale. The basic set up for measuring the gain of an amplifier is shown in Figure 1. The output as a function of the input of an amplifier 'HMC-C009' is shown in Figure 2. The key parameters of an amplifier 'HMC-C059' are shown in Table 1 [1].

2.2 Mixer

The mixer is used for converting the frequency of RF signal. The conversion loss is the ratio between the input and output powers of a mixer. The conversion loss is defined as

$$\text{Conversion loss [dB]} = -10\log(\mathrm{P_{out}}/\mathrm{P_{in}}). \tag{2}$$

The basic set-up for measuring the conversion loss is shown in Figure 3. The left signal generator next to the mixer is used as input signal. Meanwhile, the signal generator below the mixer works as a local oscillator (LO). Finally, the signal analyzer is used for detecting the mixer's output signal. The quantitative relation between the RF, IF and LO frequency can be written as

$$f_{\mathrm{IF}} = f_{\mathrm{RF}} - f_{\mathrm{LO}}, \tag{3}$$

where f_{RF} and f_{IF} are respectively the frequencies of the input and output signals and f_{LO} is the frequency of a local oscillator. The Figure 4 shows the output of a mixer HMC-C009 as a function of the input. The key parameters of the mixer HMC-C009 are shown in Table 2 [2].

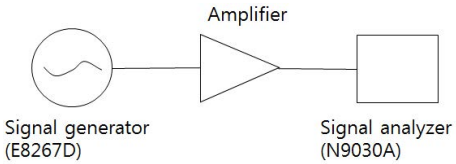

Figure 1: The set-up diagram for measuring the gain of an amplifier.

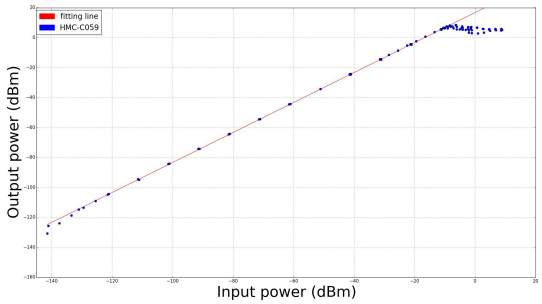

Figure 2: The input-output graph of an amplifier HMC-C059. The input frequency is 8 GHz.

Model	HMC-C059	
Freq. range (GHz)	1∼8	8∼12
Gain (dB)	16	14
DC voltage	V^+/V^- = +6/-5 V	

Table 1: Specifications of the HMC-C059 amplifier.

Model	HMC-C009
RF frequency (GHz)	4 ∼ 8
IF frequency (MHz)	100
LO power (dBm)	15
Conversion loss (dB)	7.5

Table 2: Specifications of the HMC-C009 amplifier.

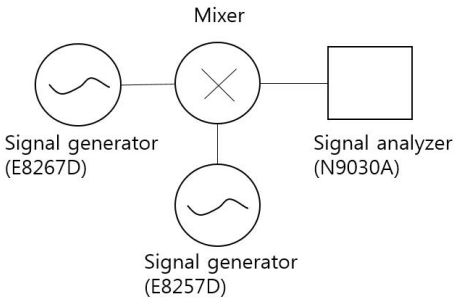

Figure 3: The diagram of set-up for measuring the mixer conversion loss.

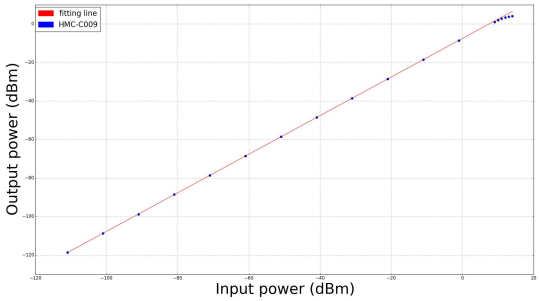

Figure 4: The input-output graph of an amplifier HMC-C009. The input frequency is 5 GHz.

2.3 RF signal processing system

The RF signal processing system is shown in Figure 5. The minimum input power which the signal generator can generate is - 160 dBm (10^{-19} W) with three 10 dB attenuators connected at the signal generator. This signal power is still stronger than the real axion signal - 210 dBm (10^{-24} W). This is reasonable to be tested because the axion signal would be amplified in the cryostat ($<$ 100 dB). Table 3 shows a summary of the gain/loss of this system. The screen shot of -160 dBm measurement of the signal analyzer is shown in Figure 6. The total system noise factor is 1.94 dB and the total system gain is 24. 3 dB. The performance of this electronics was measured using a spectrum analyser and running a VSA 89600 application. Figure 4 shows one of the results. The injected signal power is -160 dBm which is around 10^{-19} W. The expected noise floor with a 30 mHz resolution bandwidth is -163 dBm and the measured one is -156 dBm. The expected signal power is -135.7 dBm and the measured one is -129 dBm. The differences between the expected and measured values are possibly due to LO leakage and/or EMI.

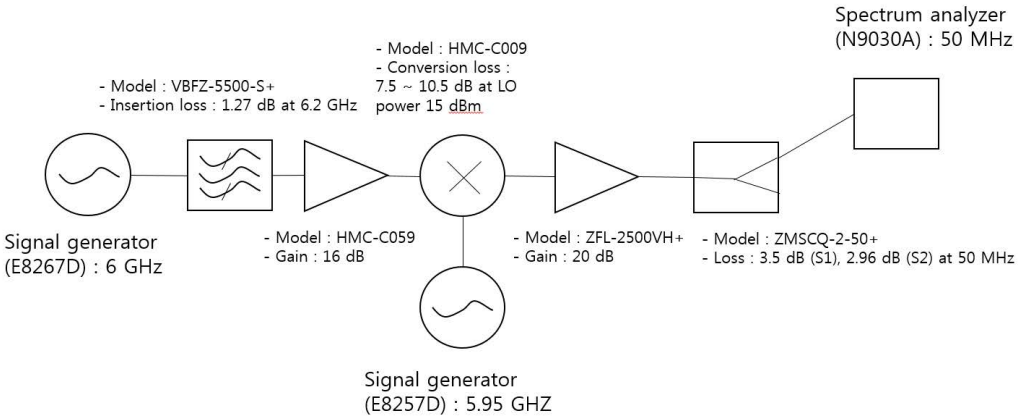

Figure 5: The diagram of the down conversion RF system. The model name and a short description is shown.

Model	VBFZ 5500-S+	HMC C059	HMC C009	ZFL 2500VH+	ZMSCQ 2-50+	Total
Gain/Loss (dB)	-1.3	+16	-10.5→-7.5	+20	-3.5	23.7

Table 3: The gain or loss of each component and the gain of the entire system. Those values are described in detail in their data sheet.

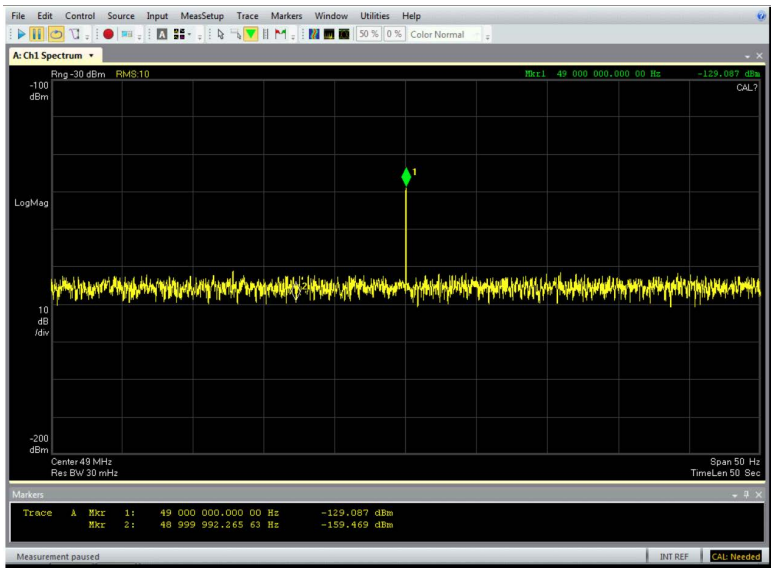

Figure 6: The screen shot of the signal analyzer : the input power is - 160 dBm. The measured output power is -129.087 dBm.

3 Conclusion

In the axion cavity experiment, the RF signal which is extreamly weak should be handled at room temperature. The RF signal processing system has been designed. Each individual component and the whole system have been tested. The gain or loss of each component matches well with data sheets. The entire RF processing system has been tested with a very weak signal (-160 dBm) and the gain of the whole system (25 dB) matches well with the expected value (23.73 dB).

References

[1] https://www.hittite.com/content/documents/data_sheet/hmc-c059.pdf

[2] https://www.hittite.com/content/documents/data_sheet/hmc-c009.pdf

Tm-Containing Bolometers for Resonant Absorption of Solar Axions

A.V. Derbin[1], *I.S. Drachnev*[1,2], *E.N. Galashov*[3], *V.N. Muratova*[1], *S. Nagorny*[2], *L. Pagnanini*[2], *K. Schaeffner*[4], *L. Pattavina*[4], *S. Pirro*[4], *D.A. Semenov*[1], *E.V. Unzhakov*[1]

[1] Petersburg Nuclear Physics Institute NRC Kurchatov Institute, Gatchina, Russia
[2] Gran Sasso Science Institute (INFN), L'Aquila, Italy
[3] Novosibirsk State University, Novosibirsk, Russia
[4] INFN Laboratori Nazionali del Gran Sasso, Assergi (AQ), Italy

DOI: http://dx.doi.org/10.3204/DESY-PROC-2015-02/derbin_alexander

A search for resonant absorption of solar axions by ^{169}Tm nuclei will be performed using the Tm-containing bolometers installed inside a low-background setup at the LNGS. The thulium crystals - $NaTm(WO_4)_2$ and $NaTm(MoO_4)_2$ have been grown and tested for the first time as bolometric detectors. The expected sensitivity of 1 kg Tm-bolometer to axion-photon $g_{A\gamma}$ and axion-electron g_{Ae} coupling constants for axions with mass in the range 10 eV to 8 keV is stronger than the present astrophysical limits.

1 Introduction

As a pseudoscalar particle, the axion should be subject to resonant absorption and emission in nuclear transitions of a magnetic type. In our experiments we chose the ^{169}Tm nucleus as a target [1, 2]. The energy of the first nuclear level ($3/2^+$) is equal to 8.41 keV. The resonant absorption should lead to the excitation of low-lying nuclear energy level: $A+^{169}\mathrm{Tm} \rightarrow ^{169}\mathrm{Tm}^* \rightarrow ^{169}\mathrm{Tm} + \gamma, e$ (8.41 keV). The level discharges through $M1$-type transition with $E2$-transition admixture value of δ^2=0.11% and internal conversion ratio $\eta = \gamma/e = 3.79 \times 10^{-3}$.

The cross-section of the resonant absorption for the axions with energy E_A is given by an expression similar to the one for γ-ray resonant absorption, but the ratio of the nuclear transition probability with the emission of an axion (ω_A) to the probability of magnetic type transition (ω_γ) has to be taken into account. The rate of solar axion absorption by ^{169}Tm nucleus will be

$$R_A = \pi\sigma_{0\gamma}\Gamma\frac{d\Phi_A}{dE_A}(E_A = 8.4)\left(\frac{\omega_A}{\omega_\gamma}\right), \quad (1)$$

where $\sigma_{0\gamma}$ is a maximum cross-section of γ-ray absorption ($\sigma_{0\gamma} = 2.56 \times 10^{-19}$ cm^2), Γ is a width of energy level (1.13×10^{-10} keV), and $d\Phi_A/dE_A$ is the axion flux at the energy 8.41 keV.

The ω_A/ω_γ ratio was calculated in the long-wave approximation in [3, 4]. In case of the

^{169}Tm nucleus the branching ratio can be rewritten as [1, 2],

$$\frac{\omega_A}{\omega_\gamma} = 1.03(g^0_{AN} + g^3_{AN})^2(p_A/p_\gamma)^3. \quad (2)$$

Here, g^0_{AN} and g^3_{AN} are dimensionless isoscalar and isovector coupling constants and p_γ and p_A are the photon and axion momenta. For ^{169}Tm nucleus, in contrast with ^{57}Fe (14.4 keV) [5] and ^{83}Kr (9.4 keV) [6] nuclei, the uncertainty of the flavor-singlet axial-vector matrix element S and light quark-mass ratio $z = m_u/m_d$ do not significantly change the value of (2).

Axions can be efficiently produced in the Sun by the Primakoff conversion of photons in the electromagnetic field of plasma. The resulting axion flux, $d\Phi_A/dE_A$, depends on $g^2_{A\gamma}$ and can be detected by the inverse Primakoff conversion of axions to photons in the laboratory magnetic fields [7]. The rate of Primakoff axion absorption by ^{169}Tm nucleus depends on $g_{A\gamma}$ and g_{AN} coupling constants [1],

$$R_A = 104 \times g^2_{A\gamma}(g^0_{AN} + g^3_{AN})^2(p_A/p_\gamma)^3 \mathrm{s}^{-1}, \quad (3)$$

where $g_{A\gamma}$ is in GeV^{-1} units.

Additional axions can be emitted by Compton $\gamma + e^- \to e^- + A$ and bremsstrahlung $e^- + Z \to e^- + Z + A$ processes in the hot solar plasma. The cross sections of both reactions depend on the axion-electron coupling constant g^2_{Ae}. The rate of Compton and bremsstrahlung axion absorption by ^{169}Tm nucleus can be written in a model-independent view [2],

$$R_A = 1.55 \times 10^5 g^2_{Ae}(g^0_{AN} + g^3_{AN})^2(p_A/p_\gamma)^3 \mathrm{s}^{-1}. \quad (4)$$

The amount of observed γ-rays that follow the axion absorption depends on the number of target nuclei N_{T_m}, measurement time T and detector efficiency ϵ, while the probability of 8.4 keV peak observation is determined by the background level B of the experimental setup.

2 Experimental setup

The Tm-containing crystals - $NaTm(WO_4)_2$ and $NaTm(MoO_4)_2$ have been grown in Novosibirsk State University. Their dimensions are about $5 \times 5 \times 5$ mm^3 and the thulium mass in one crystal is about 200 mg. The crystals are of light green color. The transmission and absorption spectra of such crystals were measured. Except for small portions of the spectrum at 360, 475 and 690 nm, the crystals are transparent in the range from 325 to 775 nm. At the moment, growing of larger crystals has started in a new growth vessel.

The Tm-crystals were installed in the ^{3}He/^{4}He dilution refrigerator in the Hall C of the underground laboratory of L.N.G.S. ($\approx$ 3650 m w.e.) and operated at a temperature of few mK. The crystals were housed in a highly pure copper structure, the same one described in [8]. The detectors were surrounded by a passive shield made of copper, lead and polyethylene.

A neutron Transmutation Doped (NTD) germanium thermistor was coupled to each Tm-bolometer. NTD acts as a thermometer recording the temperature rises produced by particle interaction in the absorbers and producing voltage pulses proportional to the energy deposition. These pulses are then amplified and fed into an 18-bit analog-to-digital converter. Software triggers ensure that every thermistor pulse is recorded. Details on our electronics and on the cryogenic set-up can be found elsewhere [9, 10].

The amplitude and the shape of the pulses are then determined by the off-line analysis. To maximize the signal-to-noise ratio, the pulse amplitude is estimated by means of the Optimum Filter (OF) technique [11, 12]. The heat channels were energy-calibrated by means of a X-ray (^{55}Fe) source. The relation between pulse amplitude and energy was parameterized with a first order polynomial fit.

3 Results

The background spectra collected during 135.2 h are presented in Fig. 1. One can see that the amplitude of the heat signal from $NaTm(MoO_4)_2$ crystals is higher than from $NaTm(WO_4)_2$ crystals.

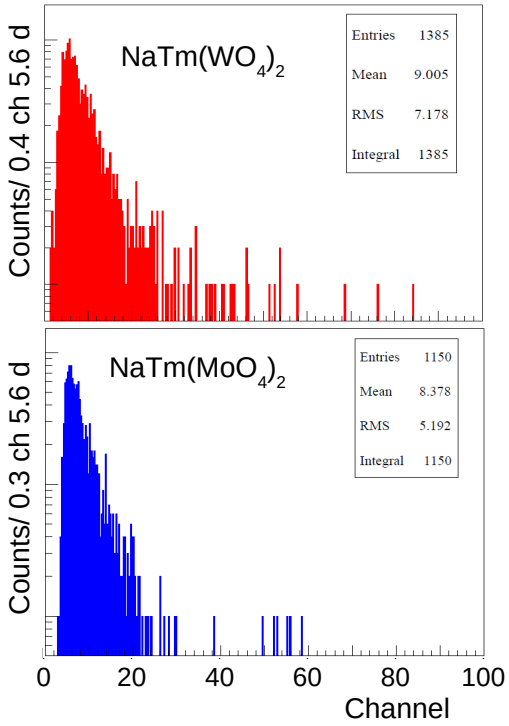

Figure 1: Energy spectra of $NaTm(WO_4)_2$ and $NaTm(MoO_4)_2$ bolometers.

There are no visible peaks in the spectra. In assumption of zero background in 8.4 keV region the upper limit on the excitation rate of ^{169}Tm by solar hadronic axions is defined as $R_{exp} = 2.44/N_{Tm}T$, where $N_{Tm} = 7.1 \times 10^{20}$ is the number of Tm nuclei in 0.2 g of thulium and $T = 4.87 \times 10^5$ s is the measurement time. The relation $R_A \leq R_{exp}$ limits the region of possible values of the coupling constants $g_{A\gamma}$, g_{Ae}, $(g^0_{AN} + g^3_{AN})$ and axion mass m_A.

Using relation (3) and (4) one can obtain the following constrains,

$$|g_{A\gamma}(g^0_{AN} + g^3_{AN})| \leq 8.2 \times 10^{-15}, \tag{5}$$

and

$$|g_{Ae}(g^0_{AN} + g^3_{AN})| \leq 2.1 \times 10^{-16}. \tag{6}$$

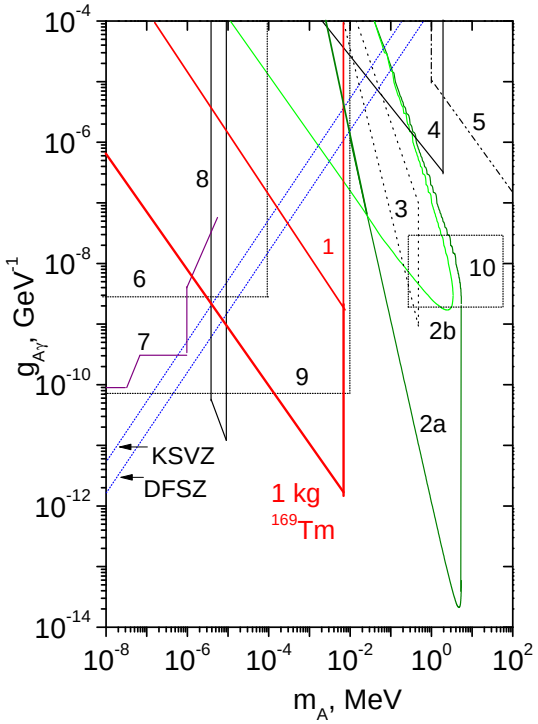

Figure 2: The sensitivity of 1 kg Tm-bolometer to $g_{A\gamma}$. 1 - ^{169}Tm resonant absorption [1], 2 - Borexino, 5.5 MeV axions, 3 - CTF, 478 keV axions, 4 - Reactor experiments, 5 - beam-dump experiments, 6 - Cosme, Solax, DAMA, 7 - CAST, 8 - Tokyo telescope, 9 - HB-stars, 10 - predictions of SUSY and mirror heavy axion models

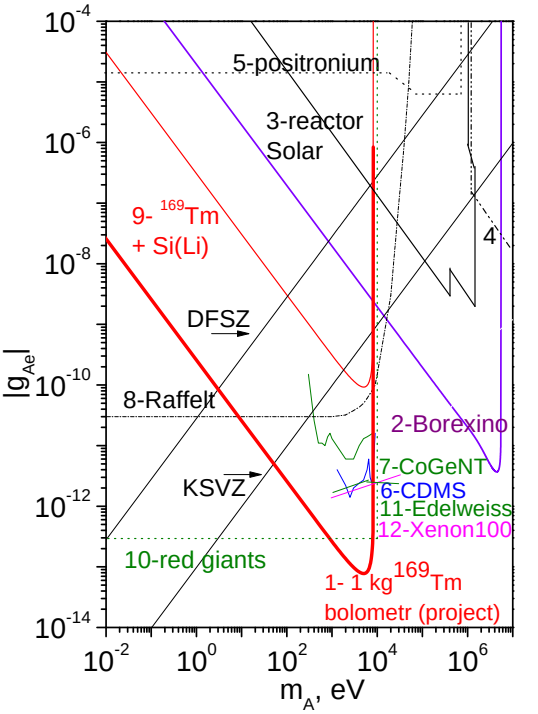

Figure 3: The sensitivity of 1 kg Tm-bolometer to g_{Ae} in comparison with the limits from others experiments

The limits (5), (6) are two orders of magnitude stronger than those obtained in our previous works [1, 2]. Since the coefficient of electron conversion for 8.4 keV transition in the nucleus ^{169}Tm is very large ($e/\gamma = 260$), the sensitivity of the experiment have been increased by $260/\epsilon = 10^4$ ($\epsilon \approx 0.02$ - detection efficiency of 8.4 keV gamma rays by Si(Li) detector [1]) for the case of registration of all particles (conversion and Auger electrons and γ- and X-rays) that follow this transition. For 1 kg detector with background level of 10 counts/day the enhancement factor can be about 2.5×10^6. The expected sensitivity of 1 kg Tm-bolometer to $g_{A\gamma}$ and g_{Ae} coupling constants are shown in Fig. 2 and Fig. 3.

Acknowledgements

The work is supported by the Russian Foundation of Basic Research (Grants No. 13-02-01199A, 13-02-12140-ofi-m and 15-02-02117A).

References

[1] A. V. Derbin *et al.*, Phys. Lett. B **678**, 181 (2009)

[2] A. V. Derbin *et al.*, Phys. Rev. D **83**, 023505 (2011)

[3] T. W. Donnelly *et al.*, Phys. Rev. D **18**, 1607 (1978)

[4] F. T. Avignone III *et al.*, Phys. Rev. D **37**, 618 (1988)

[5] A. V. Derbin *et al.*, Phys. At. Nucl. **74**, 596 (2011)

[6] Yu. M. Gavrilyuk *et al.*, JETP Letters **101**, 664 (2015)

[7] M. Arik *et al.*, (CAST coll.) Phys. Rev. D **92**, 021101 (2015)

[8] F. Alessandria *et al.*, Astropart. Phys. **35**, 839 849 (2012).

[9] S. Pirro *et al.*, Nucl. Instrum. Methods A **444**, 331 (2000).

[10] C. Arnaboldi *et al.*, Nucl. Instrum. Methods A 559, 826 (2006).

[11] E. Gatti, P. F. Manfredi, Riv. Nuovo Cimento **9**, 1 (1986).

[12] V. Radeka, N. Karlovac, Nucl. Instrum. Methods A **52**, 86 (1967).

The Optimization of Uniform Magnetic Field for an Experimental Search for Axion-mediated Spin-Dependent Interaction

Dongok Kim[1], *Yunchang Shin*[2], *Yannis K. Semertzidis*[1,2]

[1]Korea Advanced Institute of Science and Technology(KAIST), Daejeon 34141, South Korea,
[2]Center for Axion and Precision Physics Research(CAPP), Institute for Basic Science(IBS), Daejeon 34141, South Korea

DOI: http://dx.doi.org/10.3204/DESY-PROC-2015-02/kim_dongok

Possible interaction between unpolarized and polarized nuclei in long range may provide a new source for PT-violation. Moody and Wilczek proposed that such force might be mediated by the axion. A new idea of tabletop experiment searching for such interaction has been proposed from ARIADNE collaboration including SQUID NMR with polarized ^{3}He nuclei using the metastability-exchange optical pumping (MEOP) method. In this method, uniform magnetic field is required to produce the polarized ^{3}He gas with a laser at 1083 nm. We describe the finite element method (FEM) as well as the semi-analytical approach to generate uniform field to preserve polarization with a number of Helmholtz Coils compared with each other.

1 Introduction

Axion is a pseudo-scalar boson that explains the strong CP problem [1] and may mediate a new macroscopic force between nuclei [2]. Such interaction can be tested in laboratory experiments by employing polarized and unpolarized masses [3]. The nuclear spin of ^{3}He gas can be polarized with MEOP method and used to search for the spin-dependent interaction. In the experiment, the unpolarized mass affects the polarized ^{3}He gas in the presence of the PT-odd monopole-dipole interaction depending on the distance between them. The distance will be modulated by controlling the position of unpolarized mass. The nuclear spin of the polarized ^{3}He will precess off from the original polarization axis resonantly by the modulation. This signal can be detected with SQUID. The schematic design of experimental setup (a), (b) and polarization unit (c) for ^{3}He are shown in the Figure 1.

However, the polarized ^{3}He gas would be depolarized if they experience a magnetic field gradient. Therefore, it is necessary to have a uniform guide field to preserve the polarization while transporting the polarized ^{3}He gas from the polarization unit to the measurement cell as in the Figure 1 (c). In this paper, we present the magnetic field distribution optimized with the FEM software called the OPERA 3D [4]. The result was compared with analytically calculated field distribution from the Biot-Savart law to design guiding coils.

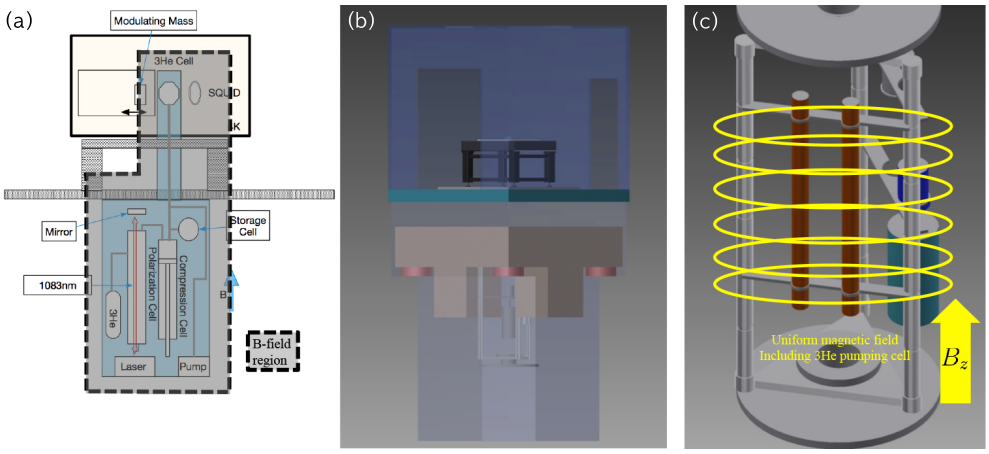

Figure 1: A conceptual design of the spin-dependent interaction experiment. The conceptual configuration (a), entire setup (b), and the polarization unit inside the magnetic field (c).

2 Optimization of the Field Distribution

Large enough square-shaped conducting coils were employed to generate guiding field, which allow better space utilization than circular-shaped or solenoid coils. It is necessary to optimize those conductors to generate guiding field uniformly distributed over wide range.

The variables for the uniform field generation are size, width, thickness, position, number of turns of the coil, and current. The size, width, and thickness of the coil were fixed at 1500 mm, 50 mm, and 1 mm respectively. The position and current density of conductor would be remaining parameters for the optimization. Each pair of opposite coils from the center should have the same parameters to generate symmetric field from the center.

2.1 Finite Element Method

The square-shaped conductor has 1500 mm length on each side with 1 mm thickness. The width of each coil was 50 mm. This geometry can be regarded as 50 turns of 1 mm^2 coil on the 1.5 m long square support.

The OPERA 3D [4] solver, TOSCA for a static magnetic field simulation, expands coefficients of the Legendre polynomial to calculate the variation level of the induced magnetic field in the spherical region. In this optimization, the radius was chosen 500 mm.

The conductors and induced field map are shown in the Figure 2. By the symmetric condition, we need only one octant instead of whole space to reduce calculation time as in the Figure 2.

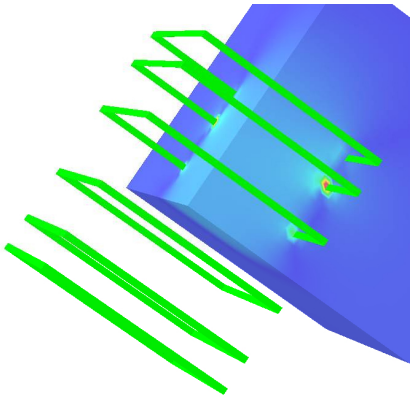

Figure 2: Simulation scheme for six conductors with OPERA 3D (TOSCA solver)

2.2 Analytic Calculation

The Biot-Savart law allows us to evaluate the magnetic field by integration. The induced field from square-shaped conductor is

$$B_z(z) = \frac{4\mu I}{\pi} \frac{d^2}{(d^2 + 4z^2)\sqrt{2d^2 + 4z^2}}. \quad (1)$$

The optimized parameters from the OPERA 3D will be assigned to this formula. The fields generated by the analytic calculation and finite element method will be compared with each other.

3 Result and Discussion

The optimization result of the positions and current densities from the OPERA 3D is as below Table 1:

Conductor	Position (mm)	Current density (A/mm^2)
1st pair	180	0.93
2nd pair	720	1.35
3rd pair	945	0.90

Table 1: The simulation output. The positions are distances from the center.

To produce uniform field along the central region, the second pair of coils plays a dominant role. They have the highest current density among three pairs of coils as 1.35 A/mm^2 at 720 mm distance from the center. The first pair makes the central part of the magnetic field more uniform. The third pair revises the field around the edge of the optimized range, 500 mm from the center. The superpositioned field distribution is shown in the Figure 3.

3.1 Field Distribution

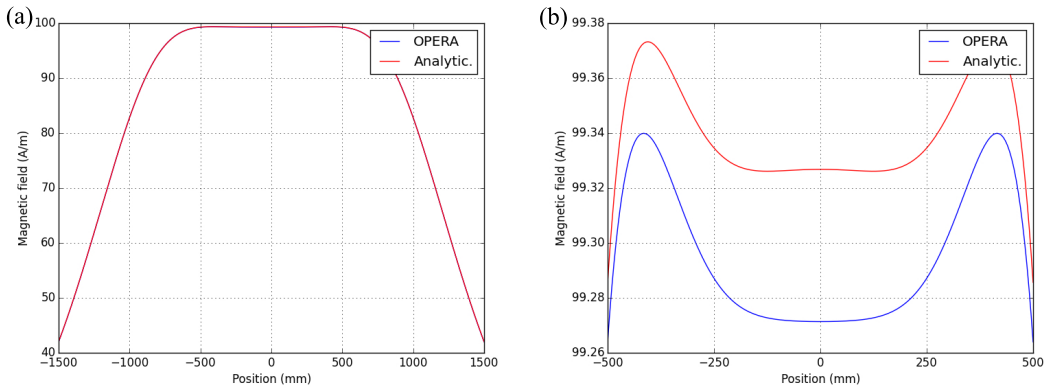

Figure 3: Field distribution along the z-axis (a) and magnified one for optimized range (b).

The difference between maximum and minimum values of uniform field distribution is order of 0.01 %. Also, the results from two approaches agree with each other.

3.2 Uniformity

The uniformity of the field can be tested by a rate of field value change, which is defined by the homogeneity

$$H(z) = \frac{B_z(z) - B_{\text{avg.}}}{B_{\text{avg.}}}. \tag{2}$$

The homogeneity is less than 0.1 % on the whole optimized range as in the Figure 4.

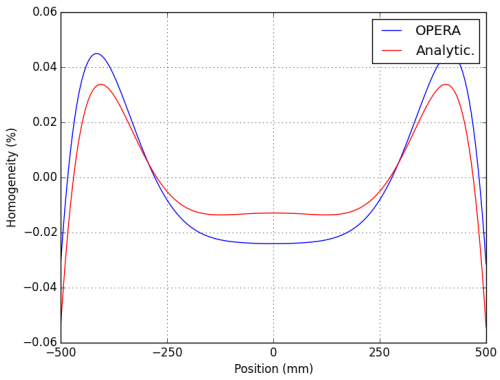

Figure 4: The homogeneity in the optimized range.

4 Summary

We designed and simulated the uniform guiding field of six square-shaped conductors to produce polarized ^{3}He gas in our setup. They are very useful to design optical polarization system of ^{3}He over large volume. We plan to build a proto-type coil system and integrate it into the ^{3}He gas optical pumping system.

Acknowledgement

This work was supported by the Institute for Basic Science under grant no. IBS-R017-D1-2015-a00.

References

[1] R. D. Peccei and R. Quinn, Phys. Rev. Lett. **38**, 1440 (1977)

[2] J. E. Moody and Wilczek, Phys. Rev. D **30**, 130 (1984)

[3] A. Arvanitaki and A. Geraci, Phys. Rev. Lett. **113**, 161801 (2014)

[4] Cobham plc., 2014. Opera-3d (17R1). [computer program] Cobham Technical Services.

Cylindrical Cavity Simulation for Searching Axions

Doyu Lee[1], *Woohyun Chung*[2], *Yannis Semertzidis*[1,2]

[1]Korea Advanced Institute of Science and Technology(KAIST), Daejeon, Republic of Korea,
[2]Center for Axion and Precision Physics(CAPP), Insititute for Basic science(IBS), Daejeon, Republic of Korea,

DOI: http://dx.doi.org/10.3204/DESY-PROC-2015-02/lee_doyu

The axion is an excellent candidate for cold dark matter. In 1983, Sikivie [1] proposed the scheme to detect axions using a resonant cavity inside a high magnetic field. In order to detect axions in his scheme, we need to scan a range of resonant frequencies of the cavity where the converted photon signal gets enhanced. This poster presents the ways to design a frequency tuning system with conducting and dielectric materials inside the cavity. The simulation software package COMSOL Multiphysics was used to evaluate the effects on the Q-factor and the form factor with different configurations and materials.

1 Introduction

The axion to photon conversion signal is extremely weak. To catch this signal, we need a 'good' cavity. 'Good' means with a broad frequency tuning range, high quality factor and form factor. We could optimize these conditions by real experiment but it would need a lot of resources. Here we want to find the optimal conditions for our microwave cavity using the COMSOL multiphysics simulation program.

2 Methods

The resonant frequency of the cavity could be changed by putting a different material inside. For a cylindrical cavity with TM010 mode, a conductor or dielectric rod inside the cavity could be used to tune the resonant frequency. The quality factor and form factor of the cavity are also changed according to the material and the position of the tuning rod. The simulation was performed to explore the best combinations for the axion search using the COMSOL Multiphysics program [2].

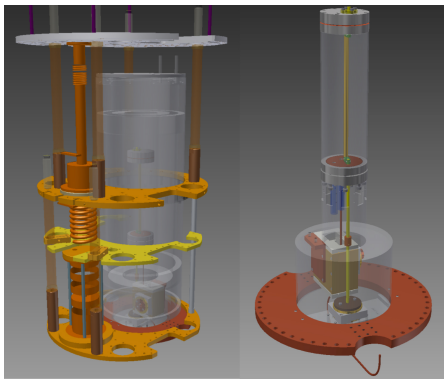

Figure 1: Drawing of the cavity tuning system. Drawn by Dr. Harry Therman(CAPP/IBS).

Figure 1 shows the cavity with a tuning system and when it was installed in the dilution refrigerator.

3 Results

3.1 Resonant frequency, quality factor and form factor

Figure 2 below shows the E-field distributions (cross sectional view) of TM010 mode with a tuning rod inside the cavity. The conductor rod pushes E-field and the dielectric rod pulls E-field. Based on these properties, we tune the resonant frequency of the cavity.

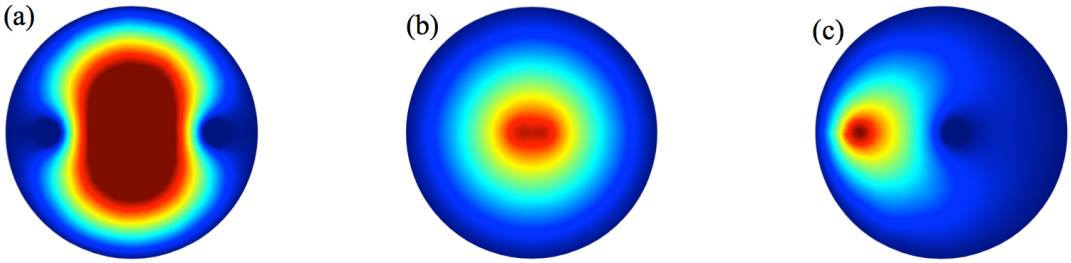

Figure 2: E field distribution in XY cross section for (a) two conductor rods (b) two dielectric rods (c) one conductor and one dielectric rod.

Depending on the position of the rod, the resonant frequency, quality factor, and form factor of the cavity are changed. In Fig. 3, the yellow horizontal line indicates an empty cavity. Introducing a conductor rod makes the resonant frequency go up and a dielectric rod makes it go down. The tuning range of the conductor rod is usually broader. Table 1 shows that the tuning range is about 1.7 GHz with two conductor rods, and 0.9 GHz with two dielectric rods. The quality factor and form factor vary with rod positions also.

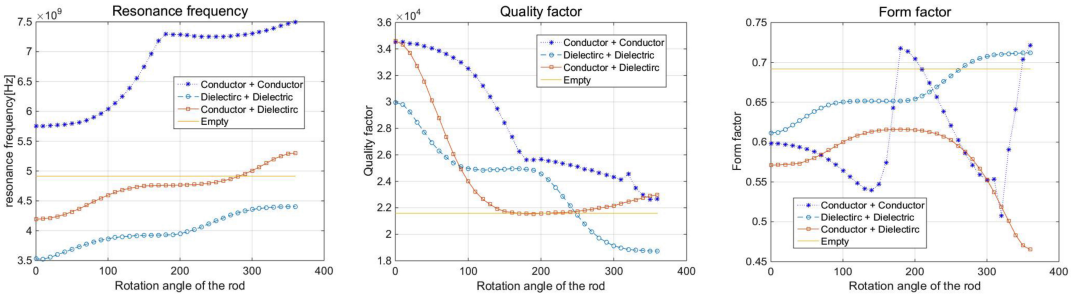

Figure 3: Resonance frequency, quality factor, and form factor of the cavity with different rod conditions.

	Frequency range	Quality factor	Form factor
Conductor + Conductor	5.8 GHz $\sim$ 7.5 GHz	$2.2\times10^4 \sim 3.4\times10^4$	0.59 $\sim$ 0.72
Conductor + Dielectric	4.2 GHz $\sim$ 5.3 GHz	$2.1\times10^4 \sim 3.4\times10^4$	0.46 $\sim$ 0.61
Dielectric + Dielectric	3.5 GHz $\sim$ 4.4 GHz	$1.8\times10^4 \sim 3.0\times10^4$	0.61 $\sim$ 0.71

Table 1: Resonance frequency, quality factor, and form factor range of the cavity with different rod conditions.

3.2 Gap problem in conducting rod case

When there is a gap between the rod and the cylinder, mode localization happens. Figure 4(a) shows the normal TM010 mode, but figure 4(b) shows a strange mode generated when a gap between the top or bottom of the cavity and the rod is introduced in the simulation model. In figure 4(c) we can see the location where mode localization shows up. One possible solution to solve this problem is changing the length of the cavity. The TM010 mode does not depend on the length, however the other strange mode depends on it. Figure 4(d) shows a mode crossing point according to the length of the cylinder. We can move the mode crossing points through this property, but cannot solve the, completely.

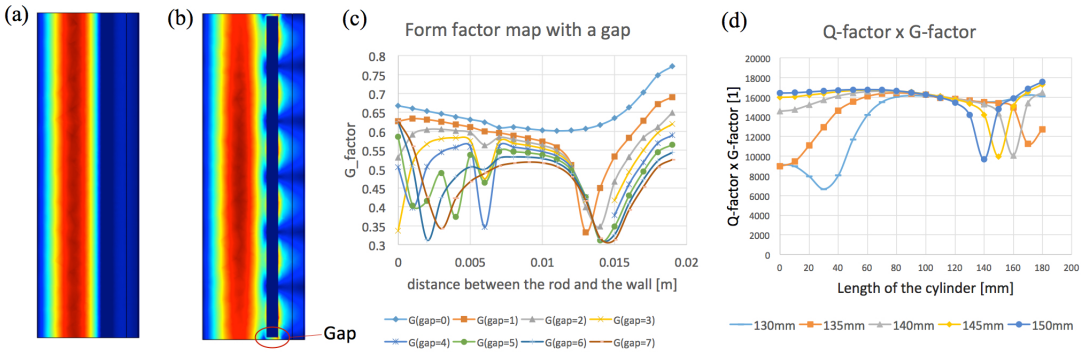

Figure 4: (a),(b) E-field norm of Y-Z cross section of the cylindrical cavity with conducting rod (a) without a gap, (b) with a gap. (c) Form factor graph with a cylindrical cavity which has various gap sizes (0mm-7mm). (d) Form factor and quality factor graph according to the length of the cylinder.

3.3 Cylindrical cavity with dielectric cap and high conductivity film

A high quality factor is required for higher axion conversion power. We change the conductivity of the cavity and introduce some dielectric material in the simulation to evaluate the effect. Figure 5 and Table 2 show results of many trials. If the conductivity of the cavity wall goes up, the quality factor goes up too. A dielectric cap at the top and bottom is harmful for the quality factor.

When the conductivity increase is N times larger, the Q factor is increase $\sqrt{N}$ times larger. To achieve a high Q factor, we consider the inner surface coating with superconducting film.

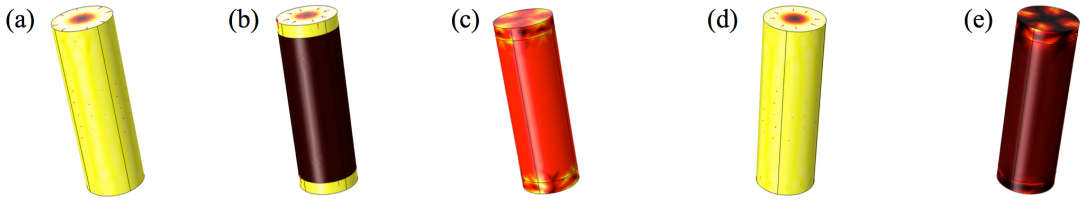

Figure 5: Heat map of surface loss for cylindrical cavity made with (a) copper only, (b) copper with high conductivity film on the wall side (the conductivity is 100 times higher than copper),(c) copper with high conductivity film on the wall side and dielectric cap on the top and bottom, (d) copper with high conductivity film on the whole cavity, (e) copper with high conductivity film on the whole cavity and dielectric cap on the top and bottom

	Quality factor
copper	21523.804
copper + high conductivity coating (wall)	66697.146
copper + high conductivity coating (wall) + dielectric cap	54158.212
copper + high conductivity coating (whole)	277928.43
copper + high conductivity coating (whole) + dielectric cap	247355.67

Table 2: Quality factor according to the various condition of the cavity.

4 Conclusion

The resonant frequency of the cylindrical cavity can be controlled by using the tuning rod. The use of a conductor rod can achieve wider frequency tuning range but has a mode localization problem. Employing one dielectric tuning rod seems a better option even with a bit narrower tuning range. The superconducting film coating looks very promising option to increase the quality factor of the cavity.

References

[1] P. Sikivie, Phys. Rev. Lett. **51** 1415 (1983).

[2] COMSOL Multiphysics (Version 5.1), 2015.

[3] Walter Wunsch, *An experiment to search for galactic axions.* PhD Thesis. University of Rochester, 1988.

Gamma-ray Spectra of Galactic Pulsars and the Signature of Photon-ALPs Mixing

Jhilik Majumdar, Dieter Horns

Institut für Experimentalphysik, Universität Hamburg, Germany

DOI: http://dx.doi.org/10.3204/DESY-PROC-2015-02/majumdar_jhilik

In many approaches to describe physics beyond the standard model, light Nambu-Goldstone bosons (named axion-like particles or ALPs) are predicted to exist. For ALPs with a mass of neV, photon-ALPs oscillation takes place in extra-galactic magnetic fields during the propagation of very high energy gamma-ray photons leading to excess radiation observed for optically thick sources. In order to verify this effect,gamma-ray spectra from strong galactic sources can be used. Here the photon-ALPs mixing would lead to an energy dependent suppression of the observed gamma-ray spectra. Here, we have used Fermi-LAT (Fermi-Large Area Telescope) observations of a sample of gamma-ray pulsars located at different line-of-sights to search for spectral signatures and compare the result with the predictions using particular models for the galactic magnetic field.

1 Introduction

Fermi-LAT observations for gamma ray pulsars.- The Fermi-LAT is a pair conversion telescope for gamma rays between 20 MeV to more than 300 GeV. 160 gamma ray pulsars have been discovered by Fermi-LAT. It has a wide field-of-view of 2.4 sr, a peak effective area of $\sim 7000c^2$ at 1 GeV on axis, and a 68 containment radius of 0.6 deg at 1 GeV for events converting in the front section of the LAT. The LAT is ~ 30 times more sensitive than its predecessor, the EGRET telescope.

Galactic magnetic field models.- The magnetic fields in galaxies are believed to be regenerated and maintained by dynamo actions in the interstellar medium. Here we have taken into account two models of magnetic fields: Jansson-Farrar and Pshirkov. Pshirkov's model of galactic magnetic fields consists of two different components: a disk and a halo field. According to directional dependence of this this model, this is categorized in two types: 1) ASS or axisymmetric model (the direction of the field in two different arms is the same) and 2) BSS or bi-symmetric model (the direction of the field in two different arms is opposite). The magnetic field along the line of sight of the pulsar J2021+3651 is shown in Fig. 1.

Axion-like particles.- Axions are considered to be an attractive dark matter candidate and also a solution to the strong CP problem of quantum chromodynamics. The equation of the Lagrangian of ALP-photon is,

$$\mathcal{L} = -\frac{1}{4} g_{\alpha\gamma} F_{\mu\nu} F^{\mu\nu} a = g_{\alpha\gamma} E \cdot B a, \tag{1}$$

where a is the axion-like field with mass $m_a, F_{\mu\nu}$ is the electromagnetic field-strength tensor,

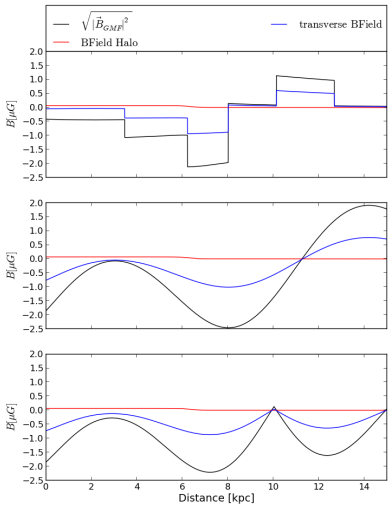

Figure 1: Magnetic field along the line of sight of the pulsar J2021+3651. Top panel for the model of Jansson-Farrar, middle panel for the model of Pshirkov in BSS, down in ASS mode.

and $g_{\alpha\gamma}$ is the ALP-photon coupling. Photons travelling through the external magnetic field couple to ALPs. The probability of the conversion after a distance z is

$$P_{\gamma\to a} = \frac{g_{\alpha\gamma}^2}{8}\left(\left|\int_0^z dz' e^{2\pi i z'/l_0} B_x(x,y,z')\right|^2 + \left|\int_0^z dz' e^{2\pi i z'/l_0} B_y(x,y,z')\right|^2\right) \tag{2}$$

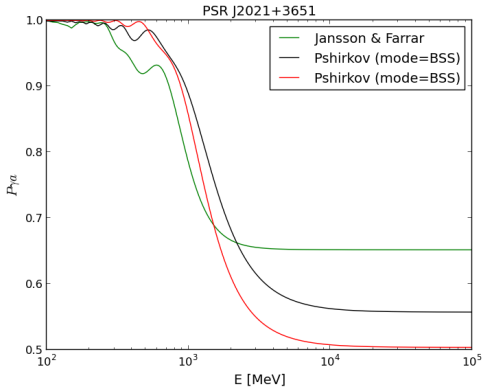

Figure 2: The conversion probability of the photon to axion as a function of energy.

Pulsar Name	χ^2
J2021+3651	139.845
J2021+4026	185.86

Table 1: Minimum value of χ^2 of pulsars as a power law of exponential decay

2 Fermi likelihood analysis

The detection, flux determination and spectral modeling of Fermi-LAT sources likelihood optimization technique is performed for the selected pulsar candidates. The spectrum of a pulsar can be modelled by a power law of exponential decay with the general form:

$$\frac{dN}{dE} = K.\left(\frac{E}{E_0}\right)^{-\tau} \exp\left(\frac{-E}{E_{cut}}\right) \tag{3}$$

We have also performed the same procedure for another pulsar source J2021+4026 as it is close to PSR-J2021+3651. So we can compare the spectra.

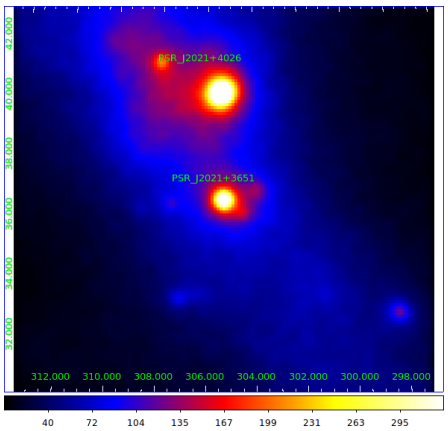

Figure 3: Event map of the PSRJ2021+3651 with color coding of photon events.

3 Pulsar spectrum

Determination of spectrum from the pulsar candidates.- We have adopted the energy range for the pulsar candidates from 100 MeV to 300 GeV and divided the entire range in 30 energy bins. The spectrum is derived for the data sets of front region of the tracking detector. The pulsar spectrum is determined for both sources PSR J2021+3651 and PSR J2021+4026 (Figure 4).

Best fit model of the pulsar - spectrum.-To investigate the signatures of the photon ALPs oscillations, a combination of power law with exponential cut-off energy and the survival probability to be adapted to the data points. For the fitting of the spectral data points, a χ^2 method is applied with the adjustment of free parameters like $g_{a\gamma}$ and m_a.

It can be said that the value of χ^2 decreases in adapting to the data points, taking into consideration larger distances.

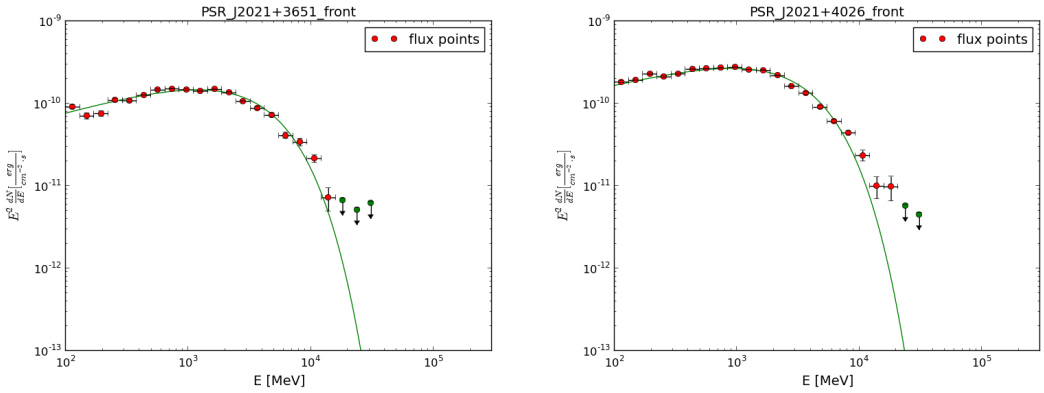

Figure 4: Model of the spectrum of PSR J2021+3651 (left) and PSR J2021+4026 (right) as a power law of exponential decay in accordance with the spectral data points

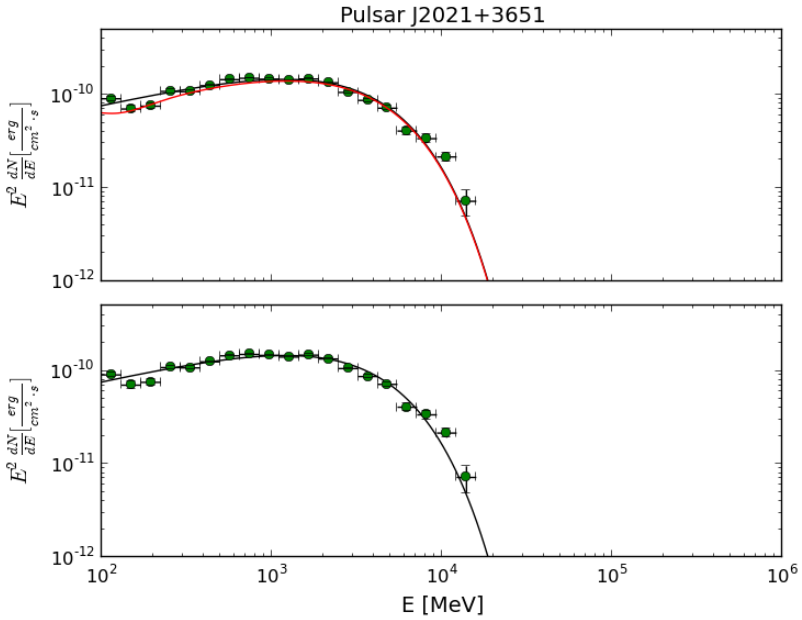

Figure 5: Best fitting model to the data points of the PSR J2021+3651.

References

[1] A. Mirizzi, G. G. Raffelt and P. D. Serpico, "Signatures of axion-like particles in the spectra of TeV gamma-ray sources," Phys. Rev. D **76**, 023001 (2007) [arXiv:0704.3044 [astro-ph]].

[2] M. Simet, D. Hooper and P. D. Serpico, "The Milky Way as a Kiloparsec-Scale Axionscope," Phys. Rev. D **77**, 063001 (2008) [arXiv:0712.2825 [astro-ph]].

Bfield-model	χ^2	$g_{a\gamma}$ [10^{-11}GeV^{-1}]	m_a [neV]
Jansson.Farrar	126.015	5.36939	3.27676
Pshirkov(BSS)	103.727	5.28798	4.74197
Pshirkov(ASS)	133.417	4.70924	3.7189

Table 2: Minimum value of χ^2 in accordance with the value of $g_{a\gamma}$ and m_a.

[3] M. Ackermann *et al.* [Fermi-LAT Collaboration], "The Fermi Large Area Telescope On Orbit: Event Classification, Instrument Response Functions, and Calibration," Astrophys. J. Suppl. **203**, 4 (2012) [arXiv:1206.1896 [astro-ph.IM]].

[4] R. Jansson and G. R. Farrar, "A New Model of the galactic Magnetic Field," Astrophys. J. **757**, 14 (2012) [arXiv:1204.3662 [astro-ph.GA]].

[5] M. S. Pshirkov, P. G. Tinyakov, P. P. Kronberg and K. J. Newton-McGee, "Deriving global structure of the galactic Magnetic Field from Faraday Rotation Measures of extragalactic sources," Astrophys. J. **738**, 192 (2011) [arXiv:1103.0814 [astro-ph.GA]].

WISPDMX: A Haloscope for WISP Dark Matter between 0.8-2 μeV

Le Hoang Nguyen[1], *Dieter Horns*[1], *Andrei Lobanov*[1,2], *Andreas Ringwald*[3]

[1] Institut für Experimentalphysik, Universität Hamburg, Germany
[2] Max-Planck-Institut für Radioastronomie, Bonn, Germany
[3] Deutsches Elektronen-Synchrotron (DESY), Hamburg, Germany

DOI: http://dx.doi.org/10.3204/DESY-PROC-2015-02/nguyen_lehoang

Weakly Interactive Slim Particles (WISPs), including the QCD axion, axion-like particles (ALPs), and hidden photons, are considered to be strong candidates for the dark matter carrier particle. The microwave cavity experiment WISPDMX is the first direct WISP dark matter search experiment probing particle masses in the 0.8-2.0 μeV range. The first stage of WISPDMX measurements has been completed at nominal resonant frequencies of the cavity. The second stage of WISPDMX is presently being prepared, targeting hidden photons and axions within 60% of the entire 0.8-2.0 μeV mass range.

1 Introduction

Weakly Interacting Slim (Sub-eV) Particles [1, 2, 3] are promising candidates for a dark matter (DM) particle and together with WIMPs, axions, and hidden photons are an attractive field for DM searches. The most favoured particle mass range for axion dark matter is between 10^{-7} and 10^{-3} eV which makes radio measurement at frequencies below 240 GHz a prime experimental tool for axion detection. Searches for the WISPs DM are cataloged into three types: purely laboratory experiments (Light-Shining Through Walls Experiments) using optical photons, helioscopes observing WISPs emitted by the Sun, and haloscopes which are searching for dark matter constituents.

The WISP Dark Matter eXperiment (WISPDMX) has been initiated at DESY and the University of Hamburg [4], aiming at covering the 0.8-2 μeV mass range, probing into the DM-favored coupling strengths. WISPDMX has three phases. Phase I: hidden photon searches at nominal resonances of the cavity; Phase II: cavity tuning for searches; and Phase III: Axion Like Particles searches with the adaption of HERA magnet.

The experiment utilises a 208-MHz resonant cavity (Fig. 1) used at the DESY HERA accelerator and plans to make use of the H1 solenoid magnet [5]. The cavity has a volume of 460 litres and a resonant amplification factor Q= 46,000 at the ground TM_{010} mode. The H1 magnet provides a field of 1.15 T in a volume of 7.2 m^3. The signal is amplified by a broad-band 0.2-1GHz amplifier with a system temperature of 100 K. Broad-band digitisation and FFT analysis of the signal are performed using a commercial 12-bit spectral analyser, enabling simultaneous measurements at several resonant modes. The cavity tuning can be provided with the use of a plunger assembly inserted into the cavity. The original plunger assembly used with the HERA cavity for the accelerator needs to be modified for the tuning.

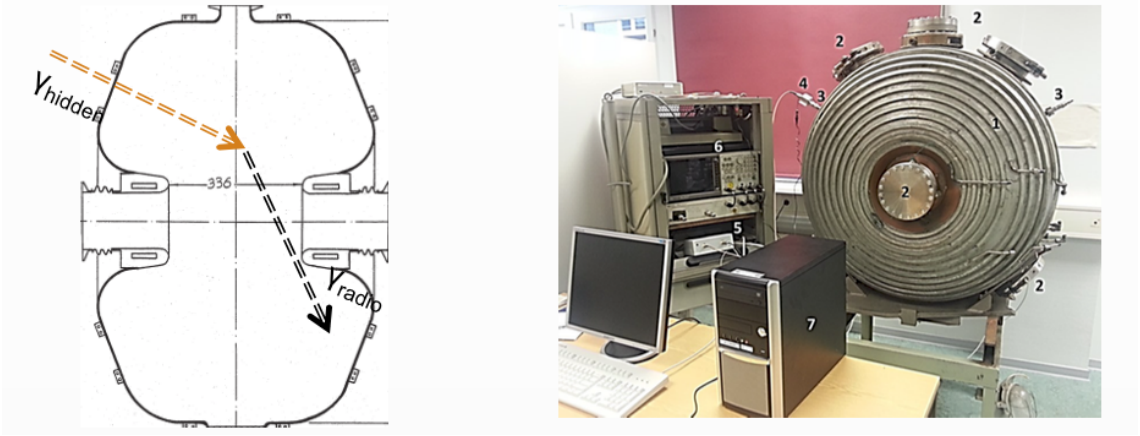

Figure 1: WISPDMX utilises a 208-MHz resonant cavity used at the DESY HERA accelerator and plans to make use of the H1 solenoid magnet. The cavity has a resonant amplification factor $Q = 46{,}000$ at the ground TM_{010} mode. The figure shows a simple sketch of the 208-MHz resonant cavity with possible conversion from HP to RF radiation (left) and the first stage's experiment setup of WISPDMX (right).

2 WISPDMX status.

2.1 Result from Phase I

In Phase I, we evaluated the broadband signal, by using a commercial ADC card (1.8 MSPS and 12 bits), measurements at the nominal frequencies at the resonant modes setting up the initial exclusion limits and obtaining the noise spectrum respectively shown in Fig. 2 and 3.

2.2 Phase II: Development and Preliminary Result.

2.2.1 Phase II, Experiment Setup.

In Phase II, we plan to perform simultaneous multiple mode measurements (with frequency calibration and broadband signal recording) with the help of tuning plungers. We will enhance the experiment with automatic tuning, continuous calibration and signal recording (Fig. 4).

The tuning plunger plays an important role in Phase II in searching for WISPs over a broad mass-range. The plunger assembly should provide effective coverage up to 56% of the 200-500 MHz range. The first plunger has been designed and manufactured, the second one is under construction. The tuning will be accomplished with a plunger assembly providing a 2 MHz tuning range of the ground mode and up to 30 MHz for the higher modes.

2.2.2 Phase II, Preliminary Result.

We study the reaction of the cavity to the temperature and atmospheric pressure changes by measuring the resonant modes of the cavity, and studying their dependence on changes with both of these quantities (see Fig. 5). This study has yielded a good calibration that can be

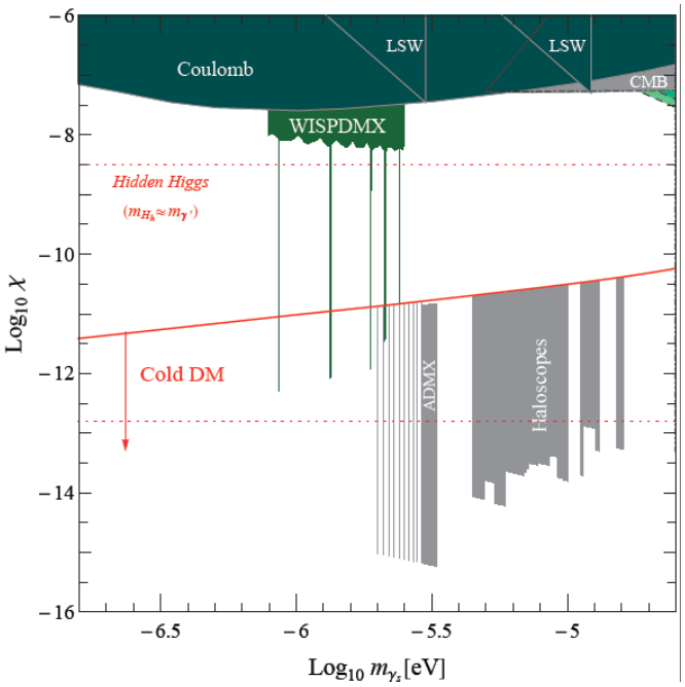

Figure 2: Current exclusion limit set by Phase I of WISPDMX [6], evaluating the broadband signal (600 MHz) under 40.3 dB amplification. The frecquency range is 180-600 MHz and the resolution is $\Delta\nu = 572$ Hz. The turquoise colour lines are exclusion limit set by ADMX.

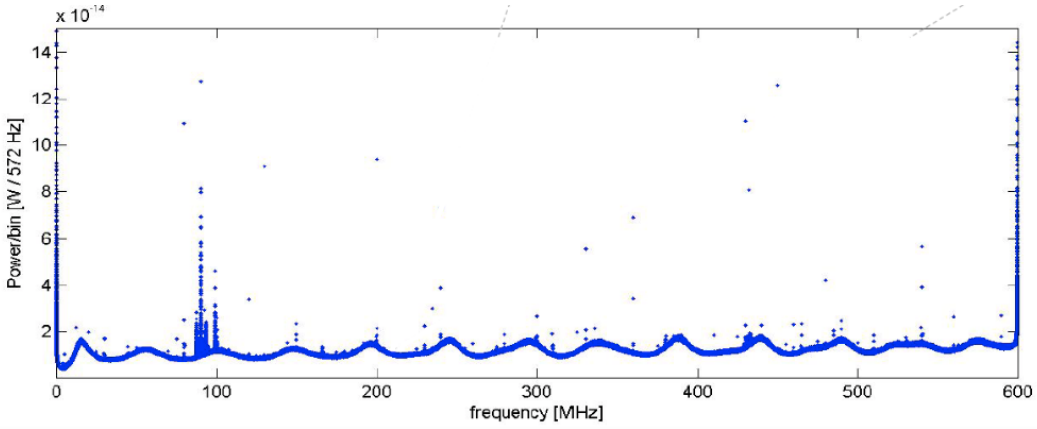

Figure 3: Broadband noise spectrum obtained from the Phase I of WISPDMX.

implemented into measurement with respect to the variability of temperature and atmospheric pressure.

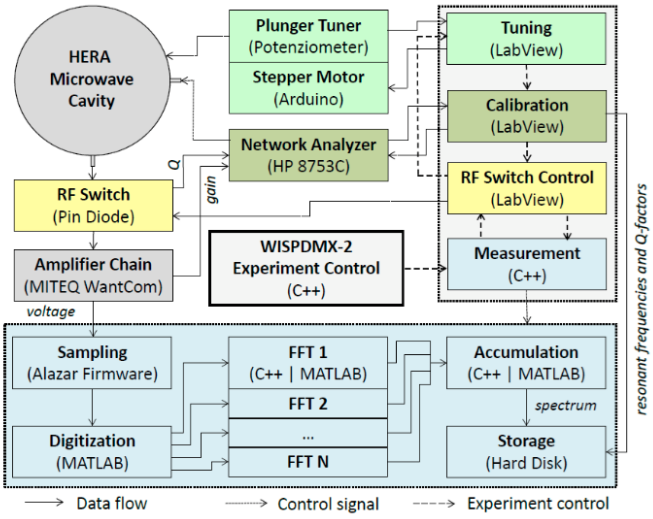

Figure 4: The flowchart illustrating the measurement procedures designed for Phase II of the WISPDMX. The tunning is made with a plunger driven by a stepper motor. The frequency calibration is performed with the help of a network analyser. The signal is amplified, digitised and analysed with a commercial digitised control by Matlab/C++ software. The overall experiment control is set within the Labview environment.

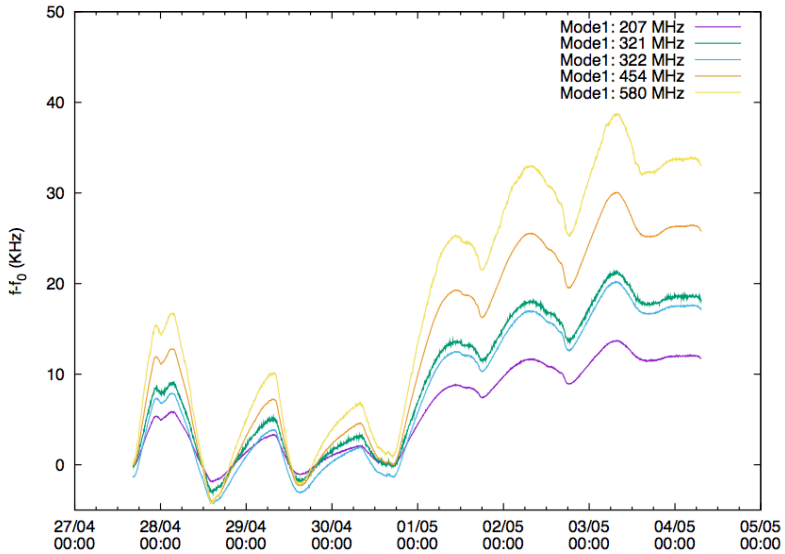

Figure 5: The shifting of 5 resonant modes due to the environment temperature. The frequency shift with respect to the temperature is 3 KHz/K.

3 Conclusion

The WISPDMX components and tools are 60% completed for the Phase II, with the second plungers for the cavity to be manufactured before the end of 2015 and software development to be ready for a preliminary run with one plunger. Further tests on the frequency calibration will be made in order to ensure frequency fidelity and accuracy at the desired spectral sensitivity in and out at the resonance.

References

[1] J. Jaeckel and A. Ringwald, *Ann. Rev. Nucl. Part. Sci.* **60**, 405 (2010), arXiv:1002.0329 [hep-ph].

[2] A. Ringwald, *Phys. Dark Univ.* **1**, 116 (2012), arXiv:1210.5081 [hep-ph].

[3] P. Arias, D. Cadamuro, M. Goodsell, J. Jaeckel, J. Redondo and A. Ringwald, *JCAP* **1206**, 013 (2012), arXiv:1201.5902 [hep-ph].

[4] D. Horns, A. Lindner, A. Lobanov and A. Ringwald, Proceeding at 10th Patras Workshop on Axions, WIMPs and WISPs (2014), arXiv:1410.6302 [hep-ex].

[5] A. Gamp, *Particle Accelerators* **29**, 65 (1990).

[6] S. Baum "WISPDMX - eine direkte Suche nach Dunkler Materie mit einer 208 MHz HERA-Kavität", University Hamburg, 2013.

Light Collection in the Prototypes of the ANAIS Dark Matter Project

J. Amaré, S. Cebrián, C. Cuesta[*], *E. García, M. Martínez*[†], *M.A. Oliván*[‡], *Y. Ortigoza, A. Ortiz de Solórzano, C. Pobes*[§], *J. Puimedón, M.L. Sarsa, J.A. Villar, P. Villar*

Laboratorio de Física Nuclear y Astropartículas, Universidad de Zaragoza, Pedro Cerbuna 12, 50009, Zaragoza, Spain,
Laboratorio Subterráneo de Canfranc, Paseo de los Ayerbe s/n, 22880 Canfranc Estación, Huesca, Spain

DOI: http://dx.doi.org/10.3204/DESY-PROC-2015-02/olivan_miguel_poster

The ANAIS experiment aims at the confirmation of the DAMA/LIBRA signal using the same target and technique at the Canfranc Underground Laboratory (LSC) in Spain. ANAIS detectors consist of large NaI crystals coupled to two photomultipliers (PMTs). In this work we present Single Electron Response (SER) data for several units of the Hamamatsu R12669SEL2 PMT model extracted from normal operation data of ANAIS underground prototypes and we compare them with PMT SER characterization previously done at surface lab before coupling them to NaI crystal. Moreover, total light collection for different ANAIS prototypes has been calculated, producing an excellent average result of 15 phe/keV, which has a good impact in both energy resolution and threshold.

1 Introduction

The ANAIS (Annual Modulation with NaI(Tl) Scintillators) experiment [1, 2] is intended to confirm the DAMA/LIBRA signal [3] using the same target and technique at the Canfranc Underground Laboratory. The ANAIS-25 set-up consisted of two NaI(Tl) detectors of 12.5 kg each manufactured by Alpha Spectra (named D0 and D1 in this work). It has been taking data since December 2012 in order to measure the internal contamination of the NaI(Tl) crystals and assess the performance of the detectors. A new Alpha Spectra detector (named D2 in this work) with lower internal background [4] was received in March 2015, added to ANAIS-25 modules to form the ANAIS-37 set-up. Every detector has been coupled to two Hamamatsu R12669SEL2 PMTs, the model selected for ANAIS [5]. In the following we will report on the PMT Single Electron Response (SER) data extracted from both set-ups on underground site and along normal operation. These results have also been compared with the SER characterization of the PMTs previously performed at Zaragoza (Section 2). Finally, we will inform about the estimates of the total light collection for all the available detectors (Sections 3 and 4).

[*]Present address: CENPA and Department of Physics, University of Washington, Seattle, WA, USA
[†]Present address: Univ. Roma La Sapienza, Roma, Italy
[‡]Corresponding author (e-mail: maolivan@unizar.es)
[§]Present address: Instituto de Ciencia de Materiales de Aragón, CSIC - Universidad de Zaragoza, Spain

2 SER extraction

First, the PMTs SER was measured at the Zaragoza test bench using UV LED illumination of very low intensity, and triggering in the excitation LED signal. This characterization was done for each PMT unit before mounting ANAIS detectors, and allowed to validate the SER determination onsite along normal operation of ANAIS detectors at the LSC. The SER has been studied thanks to a peak identification algorithm which allows us to select individual peaks at the end of the pulse of each PMT to avoid trigger bias and the pile-up of several photoelectrons (phe). An example of a pulse fulfilling these conditions can be seen in Figure 1a and the mean pulse of a selection of this kind of events is shown in Figure 1b. The phe area (proportional to charge) is integrated in a fixed time window around the peak maximum in order to obtain the single electron response charge distribution. The SER charge distribution extracted for the same PMT by these two methods is compared in Figure 1c showing full agreement between both.

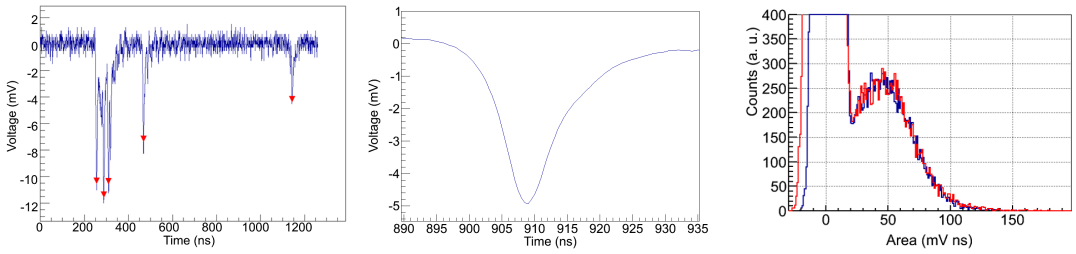

(a) (b) (c)

Figure 1: Pulse with a low number of phe; peaks identified by the applied algorithm are shown with red triangles (a), SER mean pulse (b) and SER charge distributions derived at PMT test bench (red) and along normal operation (blue) (c).

3 ANAIS-25

The light collected by each of the PMTs coupled to the ANAIS-25 modules was calculated by dividing the mean value of the charge distribution associated to a known energy deposition in the NaI crystal and the mean value of the SER charge distribution derived as aforementioned. The 22.6 keV line from a ^{109}Cd calibration source was used for this study. The result of the SER charge spectrum and the ^{109}Cd line Gaussian fits can be seen in Table 1 (PMT ij corresponds to PMT j of detector Di). These results and the global light collection of the two ANAIS-25 detectors are summarized in Table 2. The ^{109}Cd line resolution is also calculated and is shown in Table 3. These results confirm the prototypes outstanding light collection and its impact in resolution. The very good optical performance of the Alpha Spectra modules evidenced by these figures is very promising in order to reduce the energy threshold below 2 keVee [6].

PMT	SER mean mV·ns	SER σ mV·ns	22.6 keV mean mV·ns	22.6 keV σ mV·ns
00	35.47 ± 0.35	21.73 ± 0.25	6122 ± 2	669 ± 2
01	29.42 ± 0.21	18.81 ± 0.24	5057 ± 2	568 ± 2
10	41.20 ± 0.25	28.30 ± 0.21	7139 ± 4	809 ± 4
11	44.52 ± 0.29	24.36 ± 0.24	7570 ± 4	825 ± 3

Table 1: ANAIS-25 values for SER charge distribution and ^{109}Cd 22.6 keV line Gaussian fits.

PMT	PMT phe/keV	Detector phe/keV
00	7.64 ± 0.08	15.24 ± 0.09
01	7.61 ± 0.05	
10	7.67 ± 0.05	15.19 ± 0.07
11	7.52 ± 0.05	

Table 2: ANAIS-25 light collection.

PMT	PMT σ/E (%)	Detector σ/E (%)
00	10.93 ± 0.03	8.51 ± 0.03
01	11.24 ± 0.04	
10	11.33 ± 0.05	8.59 ± 0.04
11	10.90 ± 0.05	

Table 3: ANAIS-25 resolution at 22.6 keV.

4 ANAIS-37

The same procedure was repeated with ANAIS-37 setup data. In this setup the operating voltages of the D0 and D1 detectors were increased in order to better study the low energy region and for this reason the SER values are higher. The voltage of the new detector (D2) was selected to have a 10^6 gain value in both PMTs to explore the high energy region [6]. The results of the SER charge distribution and the ^{109}Cd 22.6 keV line Gaussian fits can be seen in Table 4. The light collection for every PMT and detector can be observed in Table 5. The newly extracted values for D0 and D1 are compatible with those obtained for ANAIS-25 (see previous section). Good values for the new D2 ($\sim$ 16 phe/keV) have also been measured having again a good impact in terms of energy threshold and resolution, crucial for the sensitivity to WIMPs annual modulation.

PMT	SER mean mV·ns	SER σ mV·ns	22.6 keV mean mV·ns	22.6 keV σ mV·ns
00	61.47 ± 0.36	35.02 ± 0.32	10257 ± 5	1126 ± 4
01	58.40 ± 0.71	43.06 ± 0.51	10425 ± 5	1166 ± 4
10	83.24 ± 0.55	46.52 ± 0.51	12820 ± 5	1463 ± 4
11	73.91 ± 0.74	42.04 ± 0.52	12740 ± 5	1404 ± 4
20	42.70 ± 2.10	25.42 ± 1.79	7928 ± 5	909 ± 6
21	44.57 ± 2.10	26.67 ± 1.95	8155 ± 6	930 ± 6

Table 4: ANAIS-37 values from SER charge distribution and ^{109}Cd 22.6 keV line Gaussian fits.

PMT	PMT phe/keV	Detector phe/keV
00	7.38 ± 0.04	15.26 ± 0.10
01	7.88 ± 0.09	
10	6.81 ± 0.05	14.44 ± 0.09
11	7.62 ± 0.08	
20	8.21 ± 0.40	16.31 ± 0.56
21	8.09 ± 0.38	

Table 5: ANAIS-37 light collection.

PMT	PMT σ/E (%)	Detector σ/E (%)
00	10.97 ± 0.04	8.73 ± 0.03
01	11.18 ± 0.04	
10	11.40 ± 0.03	8.80 ± 0.03
11	11.02 ± 0.03	
20	11.46 ± 0.07	8.99 ± 0.05
21	11.40 ± 0.08	

Table 6: ANAIS-37 resolution at 22.6 keV.

5 Conclusion

The PMTs single electron response was characterized along detectors normal operation and compared with the previous PMTs measurements showing a full compatibility among them. Using this extraction, an excellent light collection for the three ANAIS detectors, of the order of $\sim$15 phe/keV, has been measured. Thanks to this, an energy threshold for the ANAIS experiment at 1 keVee is at reach, depending now on improving the filtering protocols for PMT origin coincident events, which would significantly improve the sensitivity of the ANAIS Project in the search for the annual modulation effect in the WIMPs signal [6].

Acknowledgments

This work was supported by the Spanish Ministerio de Economía y Competitividad and the European Regional Development Fund (MINECO-FEDER) (FPA2014-55986), the Consolider-Ingenio 2010 Programme under grants MULTIDARK CSD2009-00064 and CPAN CSD2007-00042, and the Gobierno de Aragón (GIFNA and ARAID Foundation). P. Villar is supported by the MINECO Subprograma de Formación de Personal Investigador. We also acknowledge LSC and GIFNA staff for their support.

References

[1] J. Amaré *et al.* "Preliminary results of ANAIS-25". NIM A **742**, 197 (2014). [arXiv:1308.3478].

[2] J. Amaré *et al.* "From ANAIS-25 towards ANAIS-250". Physics Procedia **61**, 154-162 (2015) [arXiv:1404.3564].

[3] R. Bernabei *et al.* "Final model independent result of DAMA/LIBRA-phase1". Eur. Phys. J. C **73**, 2648 (2013) [arXiv:1308.5109].

[4] J. Amaré *et al.* "Background analysis and status of the ANAIS dark matter project". To appear in AIP Conference Proceedings, 2015 [arXiv:1506.03210].

[5] C. Cuesta. "ANAIS-0: Feasibility study for a 250 kg NaI(Tl) dark matter search experiment at the Canfranc Underground Laboratory". PhD thesis, Universidad de Zaragoza, 2013.

[6] J. Amaré *et al.* "Status of the ANAIS Dark Matter Project at the Canfranc Underground Laboratory". In this Proceedings volume.

Axion Dark Radiation and its Dilution

Hironori Hattori[1], *Tatsuo Kobayashi*[1], *Naoya Omoto*[1], *Osamu Seto*[2]

[1]Department of Physics, Hokkaido University, Sapporo, Japan
[2]Department of Life Science and Technology, Hokkai-Gakuen University, Sapporo, Japan

DOI: http://dx.doi.org/10.3204/DESY-PROC-2015-02/seto_osamu

Axions in the Peccei-Quinn (PQ) mechanism provide a promising solution to the strong CP problem in the standard model of particle physics. Coherently generated PQ scalar fields could dominate the energy density in the early Universe and decay into relativistic axions, which would conflict with the current dark radiation constraints. We show that a thermal inflation driven by a $U(1)$ gauged Higgs field dilutes such axions. We discuss an available baryogenesis mechanism for the $U(1)_{B-L}$ gauge symmetry.

1 Introduction

The standard model (SM) for elementary particles has been successful in describing high energy phenomena at colliders. One shortcoming of the SM is the strong CP problem. A mechanism introduced by Peccei and Quinn [1] with the corresponding global $U(1)$ symmetry, Peccei-Quinn (PQ) symmetry, elegantly solves this problem. Although the original model has been ruled out by the experimental results, so-called invisible axion models [2, 3] are promising and viable models. As a consequence of the global $U(1)$ PQ symmetry breaking, the axion field, which is its Nambu-Goldstone (NG) boson and becomes a pseudo-NG boson due to the QCD anomaly, appears.

Cosmology based on particle theory with the PQ symmetry would be interesting but not so simple. One appealing feature is, as it is well-known, that the axion is a promising candidate for dark matter in our Universe [4]. On the other hand, for example, one may imagine the following nontrivial evolution of the early Universe. The PQ scalar field could be produced in a coherent oscillation due to its scalar nature and temporally dominate the energy density of the Universe if its decay rate is very small because of suppressed couplings. The radial direction of the PQ scalar field[1] would mostly decay into axions or SM particles through loop processes. Those overproduced massless axions act as dark radiation which is nowadays stringently constrained [5].

Thermal inflation is a well-known mechanism to dilute unwanted relics [6] and is driven by a scalar field φ, often called the flaton. We show the condition of successful thermal inflation driven by a gauged $U(1)$ Higgs field to dilute axions generated by the late decay of the dominated PQ scalar [7]. If this flaton φ is a gauge singlet and has an (approximate) global $U(1)$, then the axions associated with the flaton could be produced again as shown in Ref. [8]. Thus, in order to avoid this problem, we consider that a flaton field is charged under a local $U(1)$ symmetry.

[1]From now on, we simply call it the PQ scalar.

We also discuss the implication in the case that this local $U(1)$ symmetry is identified with gauged $U(1)_{B-L}$ [9].

2 Thermal inflation in an axion-dominated Universe

We consider the scalar potential of the flaton φ as

$$V(\varphi) = V_0 - m^2|\varphi|^2 + \frac{|\varphi|^{2n}}{\Lambda^{2(n-2)}}. \tag{1}$$

A flaton field φ is assumed to be in thermal equilibrium through interactions with particles in the hot thermal bath and hence the thermal mass term,

$$\delta V = \frac{g_\varphi}{24} T^2 |\varphi|^2, \tag{2}$$

with T being the temperature of the thermal plasma, is added in the scalar potential. Here, g_φ is parametrizing the coefficient, while sometimes we may use an effective coupling with another particle $h \equiv \sqrt{g_\varphi}$ instead of g_φ in the rest of this paper.

The resultant number of e-fold in the axion-dominated Universe is estimated as

$$\begin{aligned} N_{2n} &= -\ln 4\sqrt{3} - \frac{1}{4}\ln\left(\frac{\pi^2}{30} g_*\right) + \frac{1}{2}\ln\frac{\Lambda}{M_P} h \\ &\quad -\frac{1}{4}\ln\frac{n^2}{4(n-1)} + \frac{1}{2}(n-2)\ln\left(\frac{M_P}{v}\right), \end{aligned} \tag{3}$$

with M_P being the reduced Planck mass. We list various physical quantities in Table 1.

Λ(GeV)	h	v(GeV)	T_i(GeV)	T_f(GeV)	N	ΔN_{eff}	T_R(GeV)
10^{16}	8.27×10^{-3}	10^8	2.79×10^3	1.03×10^3	1.00	0.05	5.9×10^3
10^{16}	8.27×10^{-2}	10^{10}	2.79×10^6	1.03×10^6	1.00	0.05	5.9×10^6
10^{16}	8.27×10^{-1}	10^{12}	2.87×10^9	1.03×10^9	1.00	0.05	5.9×10^9

Table 1: Quantities in thermal inflation by the potential (1).

3 Relic abundances

3.1 Axion dark radiation

As we have seen, if the PQ scalar field dominates the energy density of the Universe, its decay produces many axions, and the Universe ends up with relativistic axion domination. When the total energy density ρ_{total} from dominated axion ρ_a and subdominant radiation ρ_{rad} becomes comparable with $V(\varphi)$, $t = t_i$, the thermal inflation begins. After the thermal inflation, φ decays into SM particles and potentially non-SM particles again. The resultant axion dark radiation contribution is estimated in terms of ΔN_{eff} as

$$\Delta N_{eff} = \frac{43}{7}\left(\frac{43/4}{g_*}\right)^{1/3} \times \left.\frac{\rho_a}{\rho_{rad}}\right|_{H=\Gamma}. \tag{4}$$

3.2 Reheating temperature and possible baryogenesis scenarios

We adopt the reheating temperature after thermal inflation T_R under the assumption of the instantaneous reheating $\Gamma = H(t_f)$, which gives the highest reheating temperature. Available baryogenesis mechanisms depend on T_R.

For $T_R \gtrsim 10^9$ GeV, thermal leptogenesis by the lightest heavy RH neutrino decay of those with hierarchical masses is one of the simplest scenarios of baryogenesis [10, 11].

Nonthermal leptogenesis by RH neutrinos with hierarchical masses is available for a reheating temperature 10^9 GeV $\gtrsim T_R \gtrsim 10^6$ GeV [12]. If this local $U(1)$ is in fact the gauged $U(1)_{B-L}$ symmetry, φ is identified with the Higgs field to break this symmetry with the $B-L$ charge 2, and the decay φ into two RH neutrinos N_R is nothing but nonthermal production of N_R.

For $T_R \lesssim 10^6$ GeV, low-scale thermal leptogenesis requires an enhancement of CP violation. Here, for information, we note two examples. One is the so-called resonant leptogenesis, where two RH neutrino masses are strongly degenerated and CP violation is enlarged due to RH neutrino self-energy [13]. Another way is an extension of the Higgs sector, e.g., neutrinophilic Higgs model [14]. Another promising scenario would be electroweak baryogenesis [15].

3.3 Results

We summarize the viable parameter space and available baryogenesis mechanisms for some benchmark points. In order to have large enough CP violation $\varepsilon \gtrsim 10^{-6}$ in the N_R decay, we suppose $M_{N_R} \simeq 10^9$ GeV [16,17] and that the decay $\varphi \to N_R N_R$ is kinematically forbidden for $m_\varphi < 10^9$ GeV. We consider two cases of the PQ scalar VEV, $v = 10^{10}$ and 10^{12} GeV. We note that, for baryogenesis, the conclusion is the same for $v \lesssim 10^{10}$ GeV.

3.3.1 $n = 3, v = 10^{12}$ GeV case

For most of the parameter space, we have $T_R > 10^9$ GeV. Thermal leptogenesis could work.

3.3.2 $n = 3, v = 10^{10}$ GeV case

$T_R > 10^6$ GeV is realized, however, $m_\varphi \lesssim 10^9$ GeV. Nonthermal leptogenesis by the φ decay does not work because the φ decay is kinematically forbidden. A low-scale thermal leptogenesis with an enhanced CP violation or the electroweak baryogenesis with the extension of the Higgs sector is needed.

4 Summary

We have investigated scenarios with successful thermal inflation by a gauged $U(1)$ Higgs flaton field to dilute axions generated by late decay of the dominated PQ scalar field. We find that a promising viable baryogenesis is high- or low-scale thermal leptogenesis or the electroweak baryogenesis if this $U(1)$ symmetry is the gauged $U(1)_{B-L}$.

Acknowledgments

This work was supported in part by the Grant-in-Aid for Scientific Research No. 25400252 (T.K.) and on Innovative Areas No. 26105514 (O.S.) from the Ministry of Education, Culture,

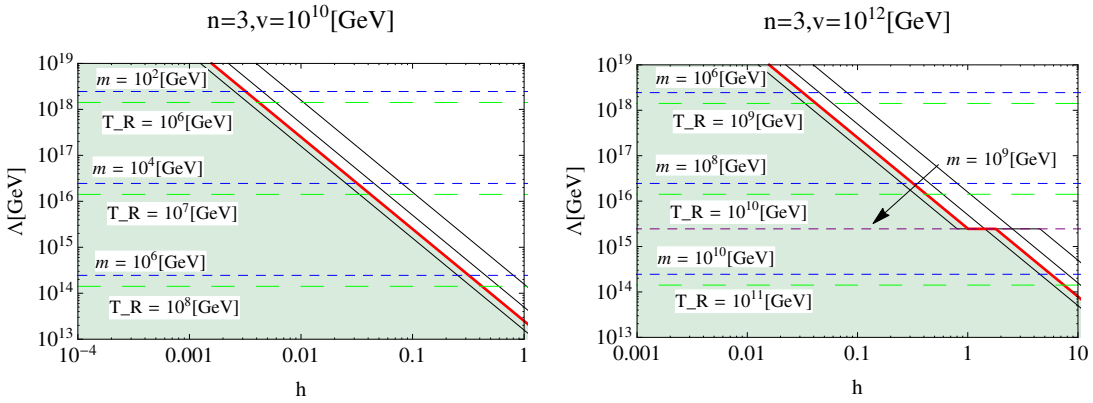

Figure 1: Contours of the resultant $\Delta N_{\rm eff} = 1, 0.4$ (thick red), 0.1, and 0.01 with solid lines from left to right, the mass of φ with dashed lines and the possible maximal reheating temperature after thermal inflation T_R with long dashed lines. The shaded region corresponds to $\Delta N_{eff} > 0.4$ which is disfavored by the Planck (2015) data.

Sports, Science and Technology in Japan.

References

[1] R. D. Peccei and H. R. Quinn, Phys. Rev. Lett. **38**, 1440 (1977).

[2] J. E. Kim, Phys. Rev. Lett. **43**, 103 (1979);
M. A. Shifman, A. I. Vainshtein and V. I. Zakharov, Nucl. Phys. B **166**, 493 (1980).

[3] M. Dine, W. Fischler and M. Srednicki, Phys. Lett. B **104**, 199 (1981);
A. R. Zhitnitsky, Sov. J. Nucl. Phys. **31**, 260 (1980) [Yad. Fiz. **31**, 497 (1980)].

[4] For a review, see, e.g., M. Kawasaki and K. Nakayama, Ann. Rev. Nucl. Part. Sci. **63**, 69 (2013).

[5] P. A. R. Ade *et al.* [Planck Collaboration], arXiv:1502.01589 [astro-ph.CO].

[6] D. H. Lyth and E. D. Stewart, Phys. Rev. Lett. **75**, 201 (1995);
D. H. Lyth and E. D. Stewart, Phys. Rev. D **53**, 1784 (1996).

[7] H. Hattori, T. Kobayashi, N. Omoto and O. Seto, Phys. Rev. D **92**, 023517 (2015).

[8] T. Asaka and M. Kawasaki, Phys. Rev. D **60**, 123509 (1999).

[9] R. N. Mohapatra and R. E. Marshak, Phys. Rev. Lett. **44**, 1316 (1980) Erratum [Phys. Rev. Lett. **44**, 1644 (1980)];
R. E. Marshak and R. N. Mohapatra, Phys. Lett. B **91**, 222 (1980).

[10] M. Fukugita and T. Yanagida, Phys. Lett. B **174**, 45 (1986).

[11] For a review, see, e.g., W. Buchmuller, P. Di Bari and M. Plumacher, Annals Phys. **315**, 305 (2005).

[12] T. Asaka, K. Hamaguchi, M. Kawasaki and T. Yanagida, Phys. Lett. B **464**, 12 (1999).

[13] A. Pilaftsis and T. E. J. Underwood, Nucl. Phys. B **692**, 303 (2004).

[14] N. Haba and O. Seto, Prog. Theor. Phys. **125**, 1155 (2011); Phys. Rev. D **84**, 103524 (2011).

[15] For a review, see, e.g., D. E. Morrissey and M. J. Ramsey-Musolf, New J. Phys. **14**, 125003 (2012).

[16] W. Buchmuller, P. Di Bari and M. Plumacher, Nucl. Phys. B **643**, 367 (2002) [Nucl. Phys. B **793**, 362 (2008)].

[17] S. Davidson and A. Ibarra, Phys. Lett. B **535**, 25 (2002).

Background Model of NaI(Tl) Detectors for the ANAIS Dark Matter Project

J. Amaré, S. Cebrián, C. Cuesta[*]*, E. García, M. Martínez*[†]*, M. A. Oliván, Y. Ortigoza, A. Ortiz de Solórzano, C. Pobes*[‡]*, J. Puimedón, M.L. Sarsa, J.A. Villar, P. Villar*[§]

Laboratorio de Física Nuclear y Astropartículas, Universidad de Zaragoza, Zaragoza, Spain and Laboratorio Subterráneo de Canfranc, Canfranc Estación, Huesca, Spain

DOI: http://dx.doi.org/10.3204/DESY-PROC-2015-02/villar_patricia

A thorough understanding of the background sources is mandatory in any experiment searching for rare events. The ANAIS (Annual Modulation with NaI(Tl) Scintillators) experiment aims at the confirmation of the DAMA/LIBRA signal at the Canfranc Underground Laboratory (LSC). Two NaI(Tl) crystals of 12.5 kg each produced by Alpha Spectra have been taking data since December 2012. The complete background model of these detectors and more precisely in the region of interest will be described. Preliminary background analysis of a new 12.5 kg crystal received at Canfranc in March 2015 will be presented too. Finally, the power of anticoincidence rejection in the region of interest has been analyzed in a 4×5 12.5 kg detector matrix.

1 The ANAIS experiment and background sources

The ANAIS project is intended to search for dark matter annual modulation with ultrapure NaI(Tl) scintillators at LSC in Spain, in order to provide a model-independent confirmation of the signal reported by the DAMA/LIBRA collaboration [1] using the same target and technique. Two prototypes of 12.5 kg mass each (referred as D0 and D1), made by Alpha Spectra, Inc. Colorado with ultrapure NaI powder, were taking data at LSC since December 2012 (ANAIS-25 set-up) and a new 12.5 kg module (referred as D2) also built by Alpha Spectra using improved protocols for detector production was added in March 2015 (ANAIS-37 set-up). The goal was the assessment of background and general performance of these detectors. Further description of the ANAIS experiment and these prototypes is given in [2].

The background model of the ANAIS-25 modules has been developed following the same procedure reported in [3]. External background sources from PMTs, copper encapsulation, quartz windows, silicone pads and archaeological lead have been quantified directly by HPGe spectrometry at LSC; also contribution from radon of the inner air volume of the shielding has been considered in the model. Internal contaminations in the NaI(Tl) crystals have been

[*]Present address: Department of Physics, Center for Experimental Nuclear Physics and Astrophysics, University of Washington, Seattle, WA, USA

[†]Present address: Università di Roma La Sapienza, Roma, Italy

[‡]Present address: Instituto de Ciencia de Materiales de Aragón, Universidad de Zaragoza-CSIC, Zaragoza, Spain

[§]Corresponding author (pvillar@unizar.es)

determined from ANAIS-25 and ANAIS-37 data [2] being ^{40}K (1.25 mBq/kg in all the modules) and ^{210}Pb (3.15 mBq/kg in D0/D1 and 0.58 mBq/kg in D2) the most relevant contributions in the region of interest. Also ^{129}I, as for DAMA/LIBRA crystals, has been included in the model. Cosmogenic contributions in the NaI(Tl) crystals have been quantified specifically for ANAIS-25 detectors in [4] and properly considered, being relevant in the long term that of ^{22}Na. The contribution of these background sources has been assessed by Monte Carlo simulation using the Geant4 code and results are presented in next sections.

2 ANAIS-25 detectors and the new ANAIS-37 module

A detailed description of the ANAIS-25 set-up including detectors, PMTs and shielding was included in the simulation and spectra at different conditions have been obtained for the different background components. Figure 1 compares the energy spectra summing all the simulated contributions described above with the measured data for ANAIS-25 detectors, considering anticoincidence data. A good agreement is obtained at high energy, but in the very low energy region some contribution seems to be missing. It was found that the inclusion in the model of an additional activity of $\sim$ 0.2 mBq/kg of ^{3}H in the NaI crystals significantly improves the agreement with data at low energy (see figure 2, left). This value is about twice the upper limit set for DAMA/LIBRA crystals, but lower than the saturation activity which can be deduced from the production rate at sea level of ^{3}H in NaI [5]. Figure 2 (right) summarizes the different contributions in the region from 1 to 10 keV according to the ANAIS-25 background model.

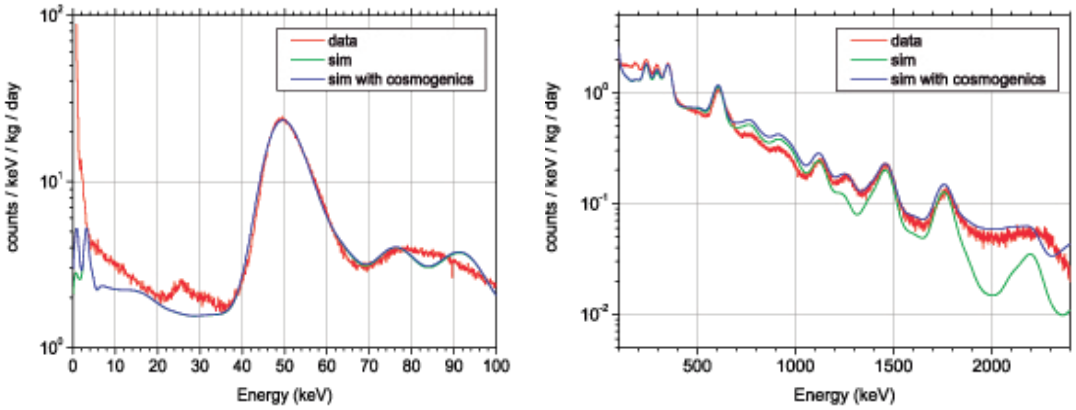

Figure 1: Comparison of the energy spectra summing all the simulated contributions (before and after adding the cosmogenics) with the measured data for ANAIS-25 considering anticoincidence data at low energy (left) and high energy (right).

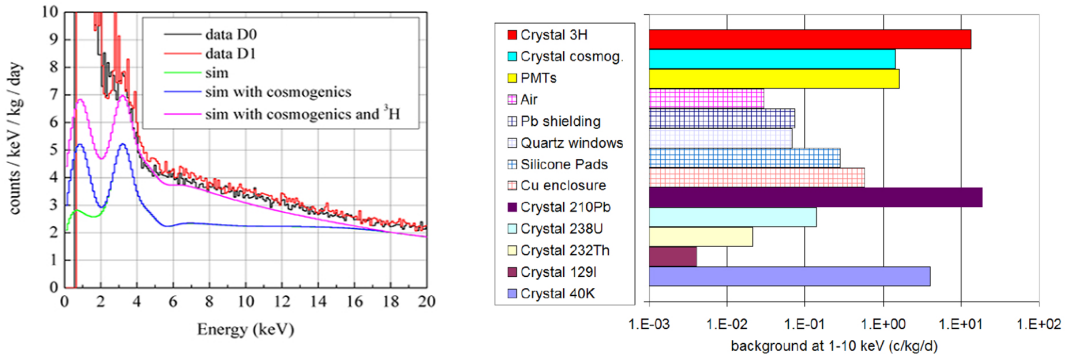

Figure 2: Effect of the inclusion of ^{3}H contribution in the very low energy spectrum (left) and different contributions in the region of 1–10 keV according to the ANAIS-25 background model (right).

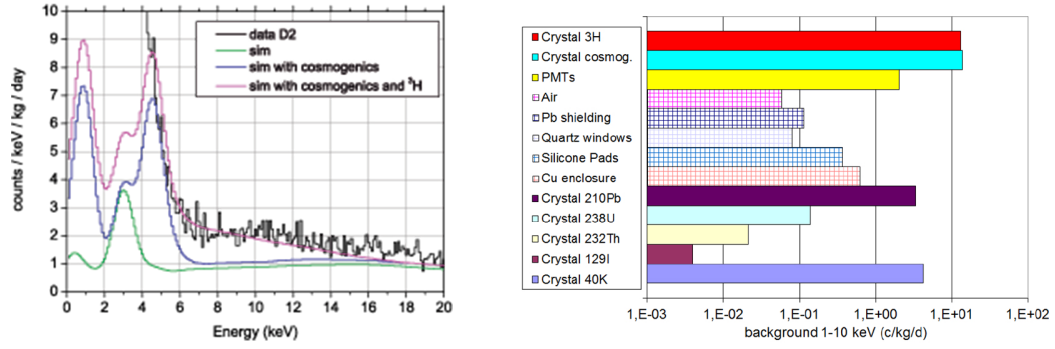

Figure 3: As figure 2, but for the new module D2 in ANAIS-37 set-up (considering ANAIS-25 activity). No event selection protocols (as those reported in [6]) have been applied to D2 data yet.

The new Alpha Spectra module grown under improved conditions in order to prevent radon contamination was mounted together with the previous ones forming the ANAIS-37 set-up. The new module (D2) is placed in between the two ANAIS-25 modules (D0 and D1) to maximize the coincidence efficiency for the potassium determination. Very preliminary results are presented here according to the first 50 days of live-time. A total alpha rate of 0.58 $\pm$ 0.01 mBq/kg in the new module D2, determined through pulse shape analysis, is a factor 5 lower than alpha rate in ANAIS-25 modules (3.15 mBq/kg). Data above 5 keV are well reproduced by our background model (see Figure 3 left) considering ^{210}Pb activity reduced with respect to D0-D1 in the same factor than alpha rate is reduced and considering the cosmogenic contribution in D2 is still important in the region of interest. Except ^{22}Na and tritium, these contributions should strongly decay in a few months.

3 Towards ANAIS

A good description of the measured background data of ANAIS-25 and ANAIS-37 prototypes has been achieved, being the main contributions in the region of interest the continua from ^{210}Pb and ^{3}H and the peaks from ^{40}K and ^{22}Na, all coming from the NaI(Tl) crystals. The latter (^{40}K and ^{22}Na) could be strongly reduced by profiting from anticoincidence. Anticoincidence rejection power of different experimental configurations is under study. Just as an example, figure 4 left illustrates the background reduction expected for the ^{40}K contribution in the region of interest in a 4×5 detector configuration. A full simulation of the 3×3 matrix of 12.5 kg NaI(Tl) scintillators to be used in the ANAIS experiment is underway, considering also the effect of a liquid scintillator veto (see figure 4, right).

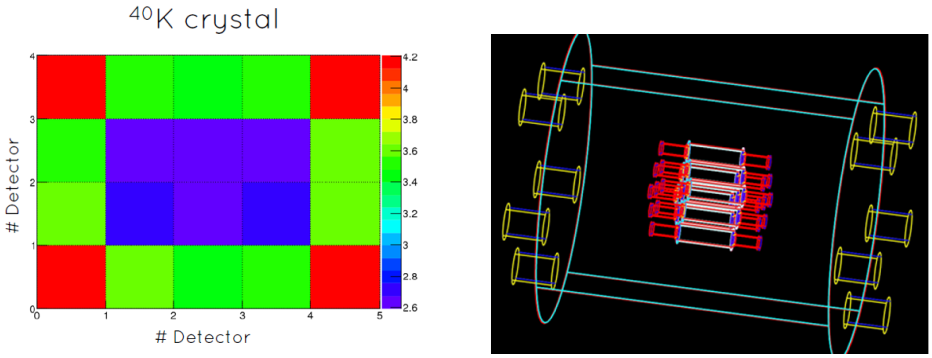

Figure 4: Distribution of background level below 10 keV (c/kg/d) in anticoincidence at each crystal for ^{40}K (ANAIS-25 activity) in a 4×5 detector configuration (left) and Geant4 (3×3) matrix of NaI(Tl) scintillators inside a liquid scintillator veto scheme (right).

Acknowledgements

This work was supported by the Spanish Ministerio de Economía y Competitividad and the European Regional Development Fund (MINECO-FEDER) (FPA2011-23749, FPA2014-55986-P), the Consolider-Ingenio 2010 Programme under grants MULTIDARK CSD2009-00064 and CPAN CSD2007-00042, and the Gobierno de Aragón (Group in Nuclear and Astroparticle Physics, ARAID Foundation). P. Villar is supported by the MINECO Subprograma de Formación de Personal Investigador. We also acknowledge LSC and GIFNA staff for their support.

References

[1] R. Bernabei *et al.*, Eur. Phys. J. C **73**, 2648 (2013).

[2] J. Amaré *et al.*, "Status of the ANAIS Dark Matter Project at the Canfranc Underground Laboratory," in these proceedings.

[3] S. Cebrián *et al.*, Astropart. Phys. **37**, 60 (2012).

[4] J. Amaré *et al.*, JCAP **02**, 046 (2015).

[5] J. Amaré *et al.*, to appear in AIP Conf. Proc. (Low Radioactivity Techniques 2015), arXiv:1505.06102.

[6] C. Cuesta *et al.*, Eur. Phys. J. C **74**, 3150 (2014).

Participants

Abdallah, Jalal	Academia SINICA/CERN
Abele, Hartmut	TU Wien
Arias, Paola	USACH
Avignone, Frank	University of South Carolina
Ayala, Adrián	Granada University
Azcoiti, Vicente	Universidad de Zaragoza
Balakin, Alexander	Kazan Federal University, Institute of Physics
Bastidon, Nomie	University of Hamburg
Beltrame, Paolo	University of Edinburgh
Brink, Paul	SLAC National Accelerator Laboratory
Butcher, Alistair	Royal Holloway - University of London
Cantatore, Giovanni	Universita' and INFN di Trieste
Carmona Bermudez, Adrian	ETH Zrich
Carmona, Jose Manuel	Universidad de Zaragoza
Caspers, Fritz	CERN
Cebrian, Susana	University of Zaragoza
Cerdeño, David G.	IPPP, Durham University
Chang, Seung Pyo	KAIST
Chattopadhyay, Swapan	Fermilab/NIU
Chowdhury, Partha	Kyung Hee University / University of Calcutta
Chung, Woohyun	CAPP/IBS
Colucci, Stefano	Universität Bonn
Creswick, Richard	University of South Carolina
Dafní, Theopisti	University of Zaragoza
Davenport, Martyn	CERN
Davoudiasl, Hooman	Brookhaven National Laboratory
de Jésus, Maryvonne	in2p3
Derbin, Alexander	Petersburg Nuclear Physics Institute
Desch, Klaus	University of Bonn
Doebrich, Babette	CERN
Ejlli, Damian	Laboratori Nazionali del Gran Sasso
Espriu, Domenec	Universitat de Barcelona
Flambaum, Victor	University of New South Wales
Follana, Eduardo	Universidad de Zaragoza
Galán, Javier	University of Zaragoza
Gan, Liping	University of North Carolina Wilmington
García, Eduardo	Universidad de Zaragoza
García Pascual, Juan Antonio	Universidad de Zaragoza
Gasparian, Ashot	NC A& State University
Geraci, Andrew	University of Nevada
Giannotti, Maurizio	Barry University
Gimeno Martinez, Benito	University of Valencia
Gomes Dias, Alex	UFABC
González-Díaz, Diego	Zaragoza/CERN

Gracia Garza, Javier	Universidad de Zaragoza
Grin, Daniel	University of Chicago
Hatzikoutelis, Athanasios	University of Tennessee Knoxville
Heisig, Jan	RWTH Aachen University
Hoof, Sebastian	Institute for Theoretical Physics, Heidelberg University
Iguaz Gutierrez, Francisco Jose	Universidad de Zaragoza
Inoue, Yoshizumi	ICEPP, the University of Tokyo
Irastorza, Igor	Universidad de Zaragoza
Jaeckel, Joerg	ITP Heidelberg
Kim, Dong-Ok	CAPP/KAIST
Ko, Byeong Rok	CAPP/IBS
Kodama, Hideo	High Energy Accelerator Research Organization (KEK)
Konikowska, Dominika	CAPP of IBS
Lee, Doyu	KAIST/CAPP
Lee, Yujung	Institute for Basic Science
Letessier Selvon, Antoine	CNRS - LPNHE
Liew, Seng Pei	University of Tokyo
Lindner, Axel	DESY
Lobanov, Andrei	MPIfR Bonn / Universität Hamburg
Lubashevskiy, Alexey	Max-Planck-Institut fr Kernphysik
Luzón, Gloria	Universidad de Zaragoza
Majumdar, Jhilik	University of Hamburg
Mescia, Federico	Universitat de Barcelona
Meyer, Manuel	Stockholm University
Miceli, Lino	Institute for Basic Science
Mirizzi, Alessandro	University of Bari
Münster, Andrea	Technische Universität Mnchen
Muratova, Valentina	Petersburg Nuclear Physics Institute
Nguyen, Le Hoang	Institut fr Experimentalphysik, Universität Hamburg
Obata, Ippei	Department of Physics, Kyoto University
O'Hare, Ciaran	University of Nottingham
Oliván, Miguel ?ngel	Universidad de Zaragoza
Ortolan, Antonello	INFN - LNL
Paredes, Angel	Universidade de Vigo
Pellen, Mathieu	RWTH Aachen
Peña Garay, Carlos	IFIC
Prescod-Weinstein, Chanda	M.I.T.
Raffelt, Georg	Max Planck Institute for Physics (MPP)
Rajendran, Surjeet	UC Berkeley
Rauch, Ludwig	Max-Planck-Institut fuer Kernphysik
Redondo, Javier	Universidad de Zaragoza

Roberts, Benjamin	University of New South Wales
Roncadelli, Marco	INFN - Pavia
Rybka, Gray	University of Washington
Sarsa Sarsa, Mara Luisa	University of Zaragoza
Satalecka, Konstancja	Universidad Complutense de Madrid
Schumann, Marc	AEC University of Bern
Semertzidis, Yannis	CAPP/IBS & KAIST
Servant, Geraldine	DESY & IFAE
Seto, Osamu	Hokkai-Gakuen University
Settimo, Mariangela	CNRS - LPNHE
Shin, Yunchang	(CAPP / IBS)
Sikivie, Pierre	University of Florida
Stadler, Julia	Max Planck Institute for Physics
Straniero, Oscar	INAF
Sulc, Miroslav	Technical University of Liberec
Sushkov, Alexander	Harvard University
Suzuki, Jun'ya	The University of Tokyo
Tanner, David	University of Florida
Tkachev, Igor	INR RAS
Tobar, Michael	The University of Western Australia
Troitsky, Sergey	INR
Tulin, Sean	York University
van Bibber, Karl	University of California Berkeley
Villar, Jose Angel	Universidad de Zaragoza
Villar, Patricia	Universidad de Zaragoza
Vinyoles Vergés, Núria	Institut de ciències de l'espai (CSIC-IEEC)
Weniger, Christoph	GRAPPA, University of Amsterdam
Wester, William	Fermilab
Woollett, Nathan	Lancaster University and The Cockcroft Institute
Youn, SungWoo	Institute for Basic Science
Zioutas, Konstantin	Univ. of Patras